Aromatic Hybrid Guanidine-Stabilized Copper Complexes and their Application as Tyrosinase Model Systems

Von der Fakultät für Mathematik, Informatik und Naturwissenschaften der RWTH Aachen University zur Erlangung des akademischen Grades einer Doktorin der Naturwissenschaften genehmigte Dissertation

vorgelegt von

Melanie Paul, M.Sc.

aus

Paderborn

Berichter: Univ.-Prof. Dr. rer. nat. Sonja Herres-Pawlis

Univ.-Prof. Dr. rer. nat. Iris Oppel

Tag der mündlichen Prüfung: 17.09.2021

Diese Dissertation ist auf den Internetseiten der Universitätsbibliothek verfügbar.

Eidesstattliche Versicherung

Ich, Melanie Paul, versichere hiermit an Eides Statt, dass ich die vorliegende Dissertation mit dem Titel

Aromatic Hybrid Guanidine-Stabilized Copper Complexes and their Application as Tyrosinase Model Systems

selbstständig und ohne unzulässige fremde Hilfe erbracht habe. Ich habe keine anderen als die angegebenen Quellen und Hilfsmittel benutzt. Für den Fall, dass die Arbeit zusätzlich auf einem Datenträger eingebracht wird, erkläre ich, dass die schriftliche und die elektronische Form vollständig übereinstimmen. Die Arbeit hat in gleicher oder ähnlicher Form noch keiner Prüfungsbehörde vorgelegen.

_____ _____

Ort, Datum Unterschrift

Belehrung

§ 156 StGB: Falsche Versicherung an Eides Statt

Wer von einer zur Abnahme einer Versicherung an Eides Statt zur zuständigen Behörde eine solche Versicherung falsch abgibt oder unter Berufung auf eine solche Versicherung falsch aussagt, wird mit Freiheitsstrafe bis zu drei Jahren oder mit Geldstrafe bestraft.

§ 161 StGB: Fahrlässiger Falscheid; fahrlässige falsche Versicherung an Eides Statt

(1) Wenn eine der in den §§ 154 bis 156 bezeichneten Handlungen aus Fahrlässigkeit begangen worden ist, so tritt Freiheitsstrafe bis zu einem Jahr oder Geldstrafe ein.

(2) Straflosigkeit tritt ein, wenn der Täter die falsche Angabe rechtzeitig berichtigt. Die Vorschriften des § 158 Abs. 2 und 3 gelten entsprechend.

Die vorstehende Belehrung habe ich zur Kenntnis genommen.

_____ _____

Ort, Datum Unterschrift

List of Publications, Projects, Presentations and Posters

Publications

1. J. Stanek, N. Sackers, F. Fink, M. Paul, L. Peters, R. Grunzke, A. Hoffmann, S. Herres-Pawlis, "*Copper Guanidinoquinoline Complexes as Entatic State Models of Electron-Transfer Proteins", Chem. Eur. J.* **2017**, *23*, 15738–15745.
2. M. Paul, F. Strassl, A. Hoffmann, M. Hoffmann, M. Schlüter, S. Herres-Pawlis, "*Reaction Systems for Bubbly Flows", Eur. J. Inorg. Chem.* **2018**, 2101–2124.
3. P. Steinhoff, M. Paul, J. P. Schroers, M.E. Tauchert, *"Highly Efficient Palladium-catalyzed Carbon Dioxide Hydrosilylation Employing PMP Ligands"*, *Dalton Trans.* **2019**, *48*, 1017–1022.
4. M. Paul, M. Teubner, B. Grimm-Lebsanft, C. Golchert, Y. Meiners, L. Senft, K. Keisers, P. Liebhäuser, T. Rösener, F. Biebl, S. Buchenau, M. Naumova, V. Murzin, R. Krug, A. Hoffmann, J. Pietruszka, I. Ivanović-Burmazović, M. Rübhausen, S. Herres-Pawlis, "*Exceptional Substrate Diversity in Oxygenation Reactions Catalyzed by a Bis(μ-oxo) Copper Complex", Chem. Eur. J.* **2020**, *26*, 7556–7562.
5. L. Laurini, M. Paul, A. Hoffmann, S. Herres-Pawlis, *"Control of the Formation and Reaction of Copper-Oxygen Adduct Complexes in Multiphase Streams*" in „*Reactive Bubbly Flows*", **2021**, Springer, Berlin, 7–38, DOI 10.1007/978-3-030-72361-3, ISBN 978-3-030-72361-3.
6. M. Paul, A. Hoffmann, S. Herres-Pawlis, "Room Temperature Stable Multitalent: Highly Reactive and Versatile Copper Guanidine Complexes in Oxygenation Reactions", *J. Biol. Inorg. Chem.* **2021**, *26*, 249–263.
7. M. Paul, M. Teubner, B. Grimm-Lebsanft, S. Buchenau, A. Hoffmann, M. Rübhausen, S. Herres-Pawlis, "*Influence of the Amine Donor on Hybrid Guanidine-Stabilized Bis(μ-oxido) dicopper(III) Complexes and their Tyrosinase-like Oxygenation Activity towards Polycyclic Aromatic Alcohols*", *J. Inorg. Biochem.* **2021**, *224*, 111541.
8. B. Grimm-Lebsanft, M. Teubner, M. Paul, S. Buchenau, A. Hoffmann, S. Herres-Pawlis, M. Rübhausen, "*Catecholate Formation after Phenolate Attack on a Catalytically Active Tyrosinase Model Complex – Low Temperature Operando Raman Studies*", manuscript in preparation.

DFG Projects

1. SPP1740 "*Reactive Bubbly Flows*", subproject "*Control of the Formation and Reaction of Copper-Oxygen Adduct Complexes in Multiphase Streams*"

Presentations

1. Annual Colloquium, DFG SPP1740 "*Reactive Bubbly Flows*", **2017**, Darmstadt, Germany: "*New Copper Hybrid Guanidine Complexes for the Activation of Oxygen*"
2. 4th Workshop "*Chemical Reaction Networks*", DFG SPP1740 "*Reactive Bubbly Flows*", **2017**, Aachen, Germany: "*New Copper Hybrid Guanidine Complexes for the Activation of Oxygen*"
3. 14th Coordination Chemistry Meeting, University of Heidelberg, **2018**, Heidelberg, Germany: "*Oxygen Activation with Aromatic Guanidine-Amine Hybrid Systems*"
4. Symposium of the International Research Training Program "*Selectivity in Chemo- and Biocatalysis (SeleCa)*", **2018**, Aachen, Germany: "*Oxygen Activation with Aromatic Guanidine-Amine Hybrid Systems*"
5. 2nd International Workshop of FERMaT and DFG SPP1740 "*Reactive Bubbly Flows*", **2018**, Hamburg, Germany: "*Aromatic Hybrid Guanidine Complexes for the Activation of Dioxygen*"
6. Annual Colloquium, DFG SPP1740 "*Reactive Bubbly Flows*", **2018**, Stuttgart, Germany: "*Aromatic Hybrid Guanidine Bis(μ-oxo)-Cu(III)-Complexes*"
7. 19th International Conference of Biological Inorganic Chemistry, University of Zurich, **2019**, Interlaken, Switzerland: "*Hybrid Guanidine-Stabilized Copper Complexes for the Activation of Dioxygen: Synthesis, Properties and Hydroxylation Catalysis*" (Flash presentation)
8. Annual Colloquium, DFG SPP1740 "*Reactive Bubbly Flows*", **2019**, Hamburg, Germany: "*N-Donor Stabilized Oxo and Peroxo Species and their Activity in Hydroxylation Reactions*"

Posters

1. 19th International Conference of Biological Inorganic Chemistry, University of Zurich, **2019**, Interlaken, Switzerland: "*Hybrid Guanidine-Stabilized Copper Complexes for the Activation of Dioxygen: Synthesis, Properties and Hydroxylation Catalysis*"

Abstract

The design of environmentally friendly and efficient catalysts for oxidation processes represents a longstanding research goal. The natural copper protein tyrosinase efficiently activates molecular oxygen, forming reactive copper-oxygen intermediates which catalyze phenolase and catecholase transformations. Inspired by nature, synthetic model systems are designed to imitate the active site of tyrosinase, exploring the structure-reactivity relationship of the copper protein.

This doctoral thesis deals with the development of tyrosinase model systems based on aromatic hybrid guanidine ligands. These tailored ligand systems combine strong σ-donor properties of the bulky guanidine moiety with spatially smaller, weaker amine donor moieties, which are bridged by an aromatic spacer to rigidify the ligand backbone. Five structurally related hybrid guanidine ligands were developed to examine correlations between ligand structure and reactivity of the corresponding copper complexes. 29 copper(I) and copper(II) species with weakly coordinating and halide anions were synthesized, of which 15 were structurally characterized by single crystal X-ray diffraction. Oxygenation of suitable copper(I) complexes resulted exclusively in the formation of bis(μ-oxido) dicopper(III) complexes, which were characterized by UV/Vis, resonance Raman and X-ray absorption spectroscopy, cryo-UHR-ESI mass spectrometry as well as DFT simulations. Additionally, the formation of the bis(μ-oxido) species was quantified by spectrophotometric titration with ferrocene monocarboxylic acid. Formation and thermal decay kinetics were studied extensively by UV/Vis spectroscopy to investigate the influence of the ligand system, present anions and different additives on the model system. Several decomposition products were successfully isolated.

The hybrid guanidine-stabilized bis(μ-oxido) dicopper(III) complexes are well-suited for tyrosinase-like oxygenation reactions of aromatic alcohols, as the hybrid ligands balance stabilization of the Cu_2O_2 core and accessibility for external substrates. A library of substrate classes was investigated to exceed the established substrate scope. Many new polycyclic aromatic alcohols including pyridinols, naphthols, quinolinols and indolols were introduced into tyrosinase chemistry. Substrates were hydroxylated and oxidized selectively to generate quinones which were captured exclusively as bent phenazine derivatives. The selectivity of the oxygenation reaction was confirmed by DFT calculations using the Fukui function, enabling a prognosis of the favored hydroxylation position. A simple salt metathesis of the catalyst allowed oxygenation reactions under mild conditions at room temperature, increasing the turnover of the system. Catalytic reactivity and selectivity of the model system were sustained despite enhancing the steric demand of the supporting ligand system. This systematic study opens the door to future developments on tyrosinase model systems to gain deeper insights into molecular mechanisms of the activation and transfer of dioxygen in biological systems.

Kurzzusammenfassung

Die Entwicklung von umweltfreundlichen und effizienten Katalysatoren für Oxidationsprozesse stellt ein langfristiges Forschungsziel dar. Natürlich vorkommende Kupferproteine wie Tyrosinase können Sauerstoff effizient aktivieren. Dabei bilden sie reaktive Kupfer-Sauerstoff-Intermediate, die Phenolase- und Catecholase-Transformationen katalysieren. Synthetische Modellsysteme werden entworfen, um das aktive Zentrum der Tyrosinase nach dem Vorbild der Natur zu imitieren und das Struktur-Wirkungsprinzip des Proteins zu erforschen.

Diese Dissertation beschreibt die Entwicklung von Tyrosinase-Modellen, die auf aromatischen Hybridguanidinliganden basieren. Die maßgeschneiderten Ligandensysteme verbinden starke σ-Donoreigenschaften der sterisch anspruchsvollen Guanidineinheit mit platzsparenden, schwächeren Amindonoren, die durch ein aromatisches Bindeglied verbrückt sind, um das Ligandenrückgrat zu versteifen. Fünf strukturell verwandte Hybridguanidinliganden wurden entwickelt, um die Ligandenstruktur mit der Reaktivität der entsprechenden Kupferkomplexe zu korrelieren. 29 Kupfer(I)- und Kupfer(II)komplexe mit schwach-koordinierenden und Halogenid-Anionen wurden hergestellt, von denen 15 kristallographisch charakterisiert wurden. Oxygenierungen geeigneter Kupfer(I)komplexe resultierten in der Bildung von Bis(μ-oxido)-dikupfer(III)komplexen, die durch UV/Vis-, Resonanz-Raman- und Röntgenabsorptionsspektroskopie, Kryo-ESI Massenspektrometrie sowie DFT-Simulationen analysiert wurden. Die Bildung wurde außerdem durch spektrophotometrische Titration mit Ferrocencarbonsäure quantifiziert. Die Bildungs- und Zerfallsreaktionen wurden umfangreich mittels UV/Vis-Spektroskopie studiert, um den Einfluss des Ligandensystems, der Anionen und verschiedener Additive auf das Modellsystem zu untersuchen. Mehrere Zerfallsprodukte wurden erfolgreich isoliert.

Die Hybridguanidin-stabilisierten Bis(μ-oxido)-Spezies sind sehr gut für Tyrosinase-ähnliche Oxygenierungsreaktionen von aromatischen Alkoholen geeignet, da die Hybridliganden die Stabilisierung des Cu_2O_2-Kerns und die Zugänglichkeit für externe Substrate geschickt balancieren. Zahlreiche Substrate verschiedener Klassen wurden untersucht, um das etablierte Substratspektrum zu erweitern. Viele neue polyzyklische aromatische Alkohole wie Pyridinole, Naphthole, Chinolinole und Indolole wurden in die Tyrosinase-Chemie eingeführt. Durch selektives Hydroxylieren und Oxidieren von Substraten wurden Chinone erzeugt, die ausschließlich als geknickte Phenazine derivatisiert wurden. Die Selektivität der Hydroxylierung wurde durch DFT-Rechnungen mithilfe der Fukui-Funktion prognostiziert. Eine simple Salzmethathese des Katalysators erlaubte Oxygenierungen unter milden Bedingungen, was mit einer erhöhten katalytischen Produktivität einherging. Die katalytische Reaktivität und Selektivität wurde trotz größerer Abschirmung des aktiven Zentrums durch das Ligandensystem aufrechterhalten. Diese systematische Studie öffnet die Tür für künftige Entwicklungen von Tyrosinase-Modellen, um einen tieferen Einblick in die molekularen Mechanismen der Sauerstoffaktivierung und dessen Transfer in biologischen Systemen zu erhalten.

Danksagung

An erster Stelle möchte ich mich bei Prof. Dr. Sonja Herres-Pawlis für die interessante Themenstellung meiner Dissertation bedanken. Die stetige Unterstützung und anregenden Diskussionen haben maßgeblich zum Gelingen dieser Arbeit beigetragen. Durch die Freiheiten bei der praktischen Durchführung des Projekts konnte ich meine eigenen Ideen und Interessen einbringen und mein Wissen vertiefen. Es war zudem eine persönliche Bereicherung, interdisziplinär mit Kooperationspartnern aus den Bereichen der Chemie, Verfahrenstechnik und numerischen Mathematik im Rahmen des DFG-Schwerpunktprogramms 1740 zusammenarbeiten zu dürfen. Außerdem bin ich sehr dankbar, dass ich an nationalen und internationalen Konferenzen sowie vertiefenden Kursen zur Röntgenstrukturanalyse teilnehmen durfte.

Weiterhin möchte ich Prof. Dr. Iris Oppel danken, dass sie das Zweitgutachten dieser Arbeit übernommen hat. Ich danke ihr außerdem für den sehr hilfreichen Input und die fruchtbaren Diskussionen rund um die Röntgenstrukturanalysen.

Bei Dr. Alexander Hoffmann möchte ich mich für praktische, präparative und organisatorische Hilfestellungen jeglicher Art bedanken. Außerdem danke ich ihm für die Durchführung, Analyse und Interpretation sämtlicher DFT-Rechnungen, für das Finalisieren der Kristallstrukturen sowie für das Korrekturlesen des experimentellen Teils dieser Arbeit.

Mein Dank geht außerdem an alle derzeitigen und ehemaligen Mitarbeiter des Arbeitskreises, die mich in Diskussionen inspiriert und mit konstruktiver Kritik weitergebracht haben. Besonders sind hier Angela Metz, Florian Strassl, Larissa Laurini und Rosalie Dalhoff zu nennen, die zudem stets für ein sehr angenehmes Arbeitsklima im Labor gesorgt haben. Außerdem möchte ich mich bei allen für die schöne Zeit und die zahlreichen Unternehmungen neben dem Laboralltag bedanken.

Zusätzlich möchte ich mich außerdem bei Claudia Nelleßen bedanken, die mir stets bei allen organisatorischen und bürokratischen Fragen mit Rat und Tat zur Seite gestanden hat.

Weiterhin bedanke ich mich bei meinen Bacheloranden, Forschungspraktikanten und Azubis, die maßgeblich zu dieser Arbeit beigetragen haben. Zu nennen sind hier Yannick Meiners, Maximilian Becker, Anke Braun, Christiane Golchert und Laura Kaufmann, die mit ihrer engagierten und motivierten Art den Arbeitsalltag bereichert haben.

Mein Dank gilt auch den Mitarbeitern der Institute für Anorganische und Organische Chemie der RWTH Aachen für die Durchführung analytischer Messungen. Hervorzuheben ist hier besonders Dr. Gerhard Fink, der mein Wissen rund um die NMR-Spektroskopie immens vertieft hat und immer für fachliche Diskussionen zu begeistern war. Außerdem danke ich Brigitte Pütz für die Durchführung zahlreicher Kryo-UHR-ESI Messungen. Prof. Dr. Ullrich Englert, Prof. Dr.

Iris Oppel, den Mitarbeitern ihrer Arbeitskreise, Tobias Storp, Florian Ritter und Henrika Hüppe danke ich für ihre Unterstützung rund um röntgenkristallographische Messungen.

Des Weiteren gilt mein Dank Prof. Dr. Ivana Ivanović-Burmazović und ihrem Arbeitskreis von der Friedrich-Alexander-Universität Erlangen-Nürnberg. Besonders Laura Senft möchte ich für die praktische Durchführung der Kryo-UHR-ESI Messungen und ihre rege Unterstützung rund um meinen Aufenthalt in Erlangen danken.

Ich bedanke mich bei Prof. Dr. Michael Rübhausen und seinem Arbeitskreis vom Center for Free-Electron Laser Science (CFEL) in Hamburg für die Kooperation im Bereich der Resonanz-Raman- und Röntgenabsorptionsspektroskopie. Besonders möchte ich mich bei Dr. Benjamin Grimm-Lebsanft, Melissa Teubner und Sören Buchenau bedanken, die nicht nur meinen Aufenthalt am DESY sehr angenehm gestaltet, sondern auch tapfer alle meine fachlichen Fragen beantwortet haben. Es ist schön, dass neben dem angenehmen Arbeitsklima auch Freundschaften entstanden sind.

Bei Prof. Dr. Jörg Pietruszka vom Forschungszentrum Jülich und Dr. Roxanne Krug möchte ich mich für die Reaktivitätsmessungen von Tyrosinase bedanken.

Besonderer Dank gilt auch meinen Freunden, die mich stets bedingungslos unterstützt haben. Es ist ein Privileg, wahre Freunde zu haben, die trotz teilweiser größerer Entfernung immer für mich da sind und mich immer wieder zum Lachen bringen.

Zuletzt möchte ich mich bei meinen Eltern bedanken, die mir vor der Promotion ein finanziell sorgenfreies Studium ermöglicht haben. Meiner Familie danke ich außerdem für die stetige Unterstützung im Leben, für die vielen Erinnerungen, nicht immer nur zu arbeiten, und den unermüdlichen Zuspruch für meine Ziele im Leben.

What you learn from a life in science is the vastness of our ignorance.

David Eagleman

American Neuroscientist

Abbreviations

aliph.	aliphatic
arom.	aromatic
ATR	attenuated total reflection
a.u.	atomic units
btmgp	bis(tetramethylguanidino)propylene
Bz	benzyl
calc.	calculated
CT	charge transfer
d	days, doublet (NMR)
DCM	methylene chloride
DFT	density functional theory
DMEG	*N,N,N',N'*-dimethylethyleneguanidine
DMF	*N,N*-dimethylformamide
DMorphG	dimorpholinylguanidine
DMPG	*N,N,N',N'*-dimethylpropyleneguanidine
DMSO	dimethyl sulfoxide
DPipG	dipiperidinylguanidine
D(TMPip)G	di(tetramethylpiperidinyl)guanidine
EA	elemental analysis
EI	Electron Ionization
Et	ethyl
EPR	Electron Paramagnetic Resonance
equiv.	equivalents
ESI	Electrospray Ionization
EXAFS	extended X-ray absorption fine structure
HRMS	High Resolution Mass Spectrometry
*i*Pr	*iso*-propyl
IR	Infrared
J	coupling constant (NMR)
L-Dopa	L-3,4-dihydroxyphenylalanine
m	multiplet (NMR), medium (IR)
Me	methyl

MeBIm	methylbenzimidazolyl
MeCN	acetonitrile
MeIm	methylimidazolyl
MeOH	methanol
MS	Mass Spectrometry
*n*Bu	*n*-butyl
NMR	Nuclear Magnetic Resonance
Ph	phenyl
ppm	parts per million
Py	pyridinyl
Pz	pyrazolyl
Qu	quinolinyl
R_f	retardation factor
rt	room temperature
s	singlet (NMR), strong (IR)
sept	septet (NMR)
t	triplet (NMR)
*t*Bu	*tert*-butyl
TEG	*N,N,N',N'*-tetraethylguanidine
THF	tetrahydrofuran
TMG	*N,N,N',N'*-tetramethylguanidine
TON	turnover number
tyr	tyrosine
UHR	Ultra-High Resolution
vs	very strong (IR)
vw	very weak (IR)
w	weak (IR)
XAS	X-ray Absorption Spectroscopy

List of Synthesized Ligands and Complexes

(*) These compounds were resynthesized according to literature. (#) These compounds were analyzed by single crystal X-ray diffraction.

Ligands

L1*,#	TMGbenza	**L4**	TMGbenzN*i*Pr$_2$
L2*,#	DMEGbenza	**L5***,#	DMEGanil
L3	TMGbenzNEt$_2$		

Cu(I) and Cu(II) complexes

C1	[Cu(**L1**)(MeCN)]PF$_6$	**C16***,#	[Cu(**L2**)I]$_2$
C2	[Cu(**L1**)(MeCN)]BF$_4$	**C17**#	[Cu(**L2**)Br]$_2$
C3	[Cu(**L1**)(MeCN)]OTf	**C18**#	{[Cu(**L2**)Br]·[CuBr]}$_2$
C4	[Cu(**L1**)(MeCN)]ClO$_4$	**C19**#	{[Cu(**L2**)Cl]·[CuCl]}$_2$
C5#	[Cu(**L1**)$_2$]PF$_6$	**C20**#	[Cu(**L1**)Cl$_2$]
C6#	[Cu(**L2**)$_2$]PF$_6$	**C21**#	[Cu(**L2**)Cl$_2$]
C7#	[Cu(**L2**)$_2$]OTf	**C22**	[Cu(**L3**)(MeCN)]PF$_6$
C8#	[Cu(**L1**)(PMe$_3$)]PF$_6$	**C23**	[Cu(**L3**)(MeCN)]BF$_4$
C9#	[Cu(**L1**)(PPh$_3$)]PF$_6$	**C24**	[Cu(**L3**)(MeCN)]OTf
C10#	[Cu(**L1**)I]	**C25**	[Cu(**L4**)(MeCN)]PF$_6$
C11#	[Cu(**L1**)Br]	**C26**	[Cu(**L4**)(MeCN)]BF$_4$
C12#	[Cu(**L1**)Cl]	**C27**	[Cu(**L4**)(MeCN)]OTf
C13	[Cu(**L1**)$_2$]I	**C28***,#	[Cu(**L5**)I]$_2$
C14	[Cu(**L1**)$_2$]Br	**C29**	[Cu(**L5**)(MeCN)]PF$_6$
C15	[Cu(**L1**)$_2$]Cl		

Bis(μ-oxido) dicopper(III) complexes

[**O1**]$^{2+}$	[Cu$_2$(μ-O)$_2$(**L1**)$_2$]$^{2+}$	[**O4**]$^{2+}$	[Cu$_2$(μ-O)$_2$(**L4**)$_2$]$^{2+}$
[**O2**]$^{2+}$	[Cu$_2$(μ-O)$_2$(**L2**)$_2$]$^{2+}$	[**O5**]$^{2+}$	[Cu$_2$(μ-O)$_2$(**L5**)$_2$]$^{2+}$
[**O3**]$^{2+}$	[Cu$_2$(μ-O)$_2$(**L3**)$_2$]$^{2+}$		

Decomposition products of the bis(μ-oxido) dicopper(III) complexes

[**H1**]$^{2+}$ #	[Cu$_3$(μ-O**L1**)$_2$(μ-OH)$_2$]$^{2+}$
[**H2**]$^{2+}$ #	[Cu$_2$(**L2**)$_2$(μ-OH)$_2$]$^{2+}$

Phenazines

P1	Benzo[a]phenazine	**P4**	Pyrrolo[3,2-a]phenazine
P2	Quinolino[3,4-b]quinoxaline	**P5**[#]	Pyrrolo[2,3-a]phenazine
P3[#]	Pyrido[3,2-a]phenazine		

Table of Contents

1. Introduction

Bioinorganic chemistry represents an interdisciplinary research field, which evaluates the role of metals in biological and bio-inspired systems. Studies on natural phenomena are of major interest in both biochemistry and inorganic chemistry, as many mechanisms of metalloproteins are not fully understood yet. The structural elucidation of biomimetic molecules contributes to the clarification of the structure-reactivity relationship of metalloproteins. The development of inorganic model systems imitating the behavior of the proteins is therefore an indispensable part of chemical research.

1.1. Copper-based Proteins

Copper is an essential trace element to numerous organisms including humans, plants and animals due to its key role in cytochrome c oxidase.[1] It is responsible for the flawless function of organs and metabolisms in the human body. Copper is found mainly in liver, muscles and bones with a total quantity of 1.4-2.1 mg per kilogram of body weight.[2,3] Therefore, it represents the third most common trace element in the human body after iron and zinc. A deficiency or excess of copper in the human body, which is regulated by nutritional ingestions, can cause health effects. Copper deficiency results in blood or immune diseases such as anemia and low white blood cell count.[4] An excess of copper in the body is reflected in symptoms of metal poisoning such as stomach upset, nausea and diarrhea.[5] Genetic diseases (e.g. Menkes disease and Wilsons disease) which are associated with improper copper content in the human body are rare.[6,7]

Possible oxidation states of copper range from 0 to +IV, of which copper(I) and copper(II) represent the most common forms. Copper(I) complexes are diamagnetic and mostly colorless. The d^{10} configuration of copper(I) is responsible for a flexible coordination geometry, ranging from linear over trigonal planar to tetrahedral depending on the coordination number (CN = 2-4). Copper(II) complexes are paramagnetic due to their d^9 configuration and exhibit a blue or green color. The coordination environment shows mostly a square-planar structure, but tetrahedral, trigonal-bipyramidal and distorted octahedral geometries are also possible. Copper(III) complexes are diamagnetic as a result of the d^8 configuration and feature a square-planar structure.[8]

1.1.1. Biological Systems

Many biological processes are based on copper proteins, whose copper center represents the catalytically active sites.[9–11] Copper proteins consist of one or more copper centers, which occur in different oxidation states during biological processes. They are distinguishable by their

spectroscopic and structural properties into three classical types of copper proteins (Figure 1), which are complemented by multinuclear copper proteins.[12–14] The protein scaffold consists of N-, O- or S-donor moieties of amino acids, which stabilize the copper centers in the oxidation states ranging from +I to +III.

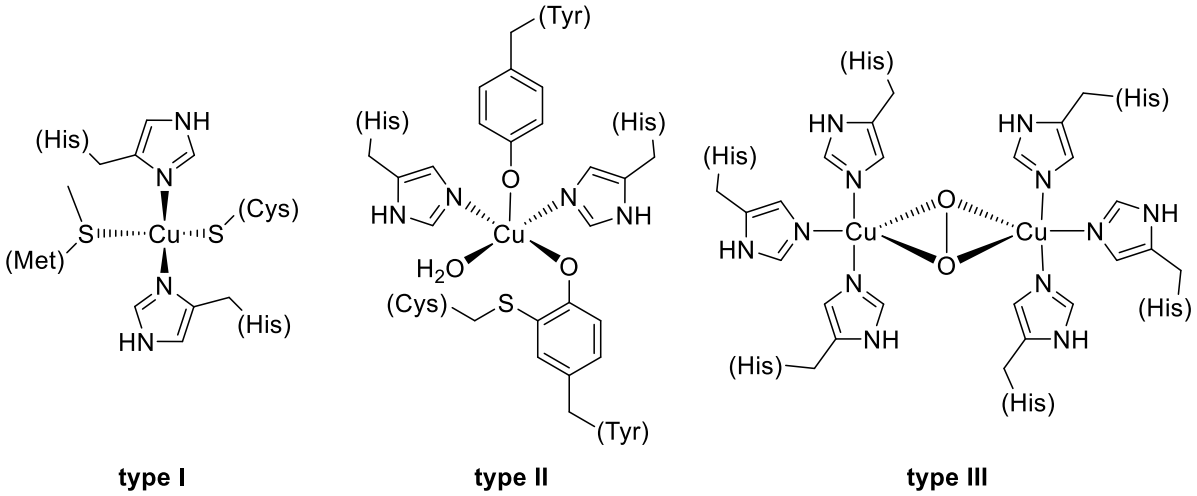

Figure 1: Active sites of copper proteins, exemplified by type I (plastocyanin), type II (galactose oxidase) and type III (tyrosinase).

Type I copper proteins, also known as blue copper proteins, feature an intense blue color, which is caused by strong absorption in the red spectral range near 600 nm. The central copper atom is coordinated by two histidine, one cysteine and one more flexible axially bound methionine residue in a distorted tetrahedral fashion. Blue copper proteins serve as electron transfer agents in biological systems, shuttling between copper(I) and copper(II) which is facilitated by the cysteine residue. Prominent examples are plastocyanin and azurin. Plastocyanin mediates the electron transfer in photosynthesis between cytochrome f and $P700^+$.[15] Azurin is responsible for electron transfer reactions in bacteria.[16]

Type II copper proteins are called normal or non-blue, whose copper center is coordinated by histidine (and tyrosine) residues in a square-planar structure. Since no S-donor ligand is present, they differ in their spectroscopic characteristics from type I copper proteins. A characteristic UV/Vis spectrum of type II copper proteins reveals only weak absorptions due to d-d transitions and no intensive LMCT absorptions are observed. Normal copper proteins are found in oxidation and oxygenation reactions.[17,18] Examples are galactose oxidase, superoxide dismutase and particulate methane monooxygenase. Galactose oxidase is involved in alcohol oxidation of D-galactose, which is found in fungi species.[19] Superoxide dismutase catalyzes the disproportionation of superoxido anions, displaying an important antioxidant in most living organisms.[20] Particulate methane monooxygenase (pMMO) is responsible for the oxidation of C–H bonds in alkanes, which occurs in some bacteria.[21]

In contrast to type I and type II copper proteins, type III copper proteins consist of two copper centers which are bridged by a peroxido unit. Each copper center is ligated by three histidine residues. Type III enzymes, such as hemocyanin, catechol oxidase and tyrosinase, are able to activate and transfer molecular oxygen.[10,14,22,23] Details of reaction mechanisms are presented in section 1.1.3.

Multinuclear copper proteins, comprised of Cu_A, Cu_B and Cu_Z centers, are also known. The binuclear Cu_A centers are stabilized by two histidines and one methionine and are bridged by two cysteine residues. Cu_B centers are coordinated by three histidine residues. The Cu_Z site represents a tetranuclear copper-sulfide cluster, which is stabilized by seven histidine residues. Cu_A, Cu_B and Cu_Z centers are present in nitrous-oxide reductase and cytochrome c oxidase, which are found in bacteria.[14] Cytochrome c oxidase is active in electron transfer reactions.[1] Nitrous-oxide reductase is responsible for denitrification of nitrous oxide to dinitrogen.[14]

1.1.2. Activation and Transfer of Dioxygen by Type III Copper Proteins

Activation and transfer of dioxygen is achieved by oxidases, monooxygenases, and dioxygenases. The type III copper proteins hemocyanin, catechol oxidase and tyrosinase are known for their activity towards dioxygen. Hemocyanin is a dioxygen transfer protein only found in mollusk and arthropod species.[24] While catechol oxidase is widely spread in various species of plants and fungi, tyrosinase is found in nearly all living organisms.[12,25–27] Tyrosinase catalyzes the *ortho*-hydroxylation of phenols to *ortho*-catechols, which is known as phenolase activity. Both tyrosinase and catechol oxidase oxidize *ortho*-catechols to *ortho*-quinones (catecholase activity). In this four-electron reduction reaction (converting two catechols per cycle), molecular oxygen is reduced to water. Tyrosinase is mainly involved in the biosynthesis of melanin from L-tyrosine (Scheme 1). Hydroxylation of L-tyrosine was determined by ^{18}O-labelled dioxygen, which was found in L-Dopa.[28] Subsequently, L-Dopa is oxidized into L-Dopaquinone by reducing dioxygen. The hydroxylation of L-tyrosine is significantly slower than the consecutive oxidation reaction.[29] Therefore, the rate-determining step of the reaction is the hydroxylation of L-tyrosine.

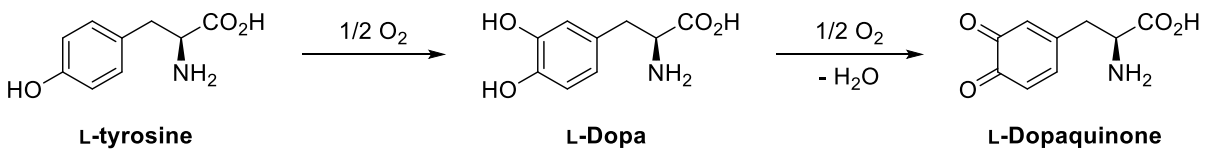

L-tyrosine **L-Dopa** **L-Dopaquinone**

Scheme 1: *Ortho*-hydroxylation of L-tyrosine to L-Dopa and oxidation of L-Dopa to L-Dopaquinone.

In subsequent condensation and oxidation steps, the pigment melanin formed which is responsible for browning processes of skin, feathers, and hair. Melanin protects organisms from UV radiation. Humans and animals who have very little or no melanin production in their

body suffer from albinism, which is a pigment disorder causing skin and hair to be very light and sensitive.[30,31] Tyrosinase is also involved in ripening processes of fruits and vegetables, which is accompanied by a change in taste and color.[32,33] Therefore, several industries including medicine, cosmetics, agriculture and food are focusing research on tyrosinase due to its high relevance.

1.1.3. Structure-Reactivity Relationship of Tyrosinase

The molecular structure of tyrosinase from *streptomyces castaneoglobisporus* was first reported in 2006 by Matoba and co-workers, revealing the structure of the μ-η^2:η^2-peroxido dicopper(II) core of the protein with a Cu···Cu distance of 3.4 Å in the oxy state of tyrosinase, as pictured in Scheme 2.[34] The deoxy state exhibited a Cu···Cu distance of 4.1 Å. They also observed two forms of the met state of tyrosinase, which were assigned as resting state due to their high stability.

Although the structure of the active site of catechol oxidase and tyrosinase are very similar, tyrosinase is able to both hydroxylate and oxidize, which results from the coordination sphere of the protein. One of the stabilizing histidine residues is disordered in tyrosinase, giving the protein a certain flexibility. In catechol oxidase, one of the stabilizing histidine residues is rigidified due to a thioether interaction.[34] The mechanism of phenolase and catecholase activity of tyrosinase was proposed by Tuczek and co-workers (Scheme 2).[35] Starting from the deoxy state, dioxygen is activated by two copper(I) centers to form a side-on peroxido dicopper(II) complex, which is the oxy state of tyrosinase. The oxy state converts both phenols and catechols in two different pathways. Reaction of phenols with tyrosinase led to the coordination of the substrate in axial position to a copper center. Hydroxylation in *ortho*-position of the phenol results in the D-met form of tyrosinase, a catecholate dicopper(II) complex. The D-met state reacts with protons to form an *ortho*-quinone under the release of water and the regeneration of the deoxy state.

Catecholase activity mediated by tyrosinase is achieved by transformation of catechols to *ortho*-quinones. Reaction of the oxy state of tyrosinase with catechols led to the formation of the D-oxy state, in which the central copper atoms are bridged by the catecholate. The catecholate is oxidized under the release of water to form an *ortho*-quinone. The concomitantly formed met state of tyrosinase shows two copper(II) centers, which are bridged by a hydroxido moiety. Incorporation of another catechol results in the formation of the D-met form of tyrosinase under the release of protons. Oxidation of the catecholate yields again an *ortho*-quinone, water and the reformed deoxy state of tyrosinase.

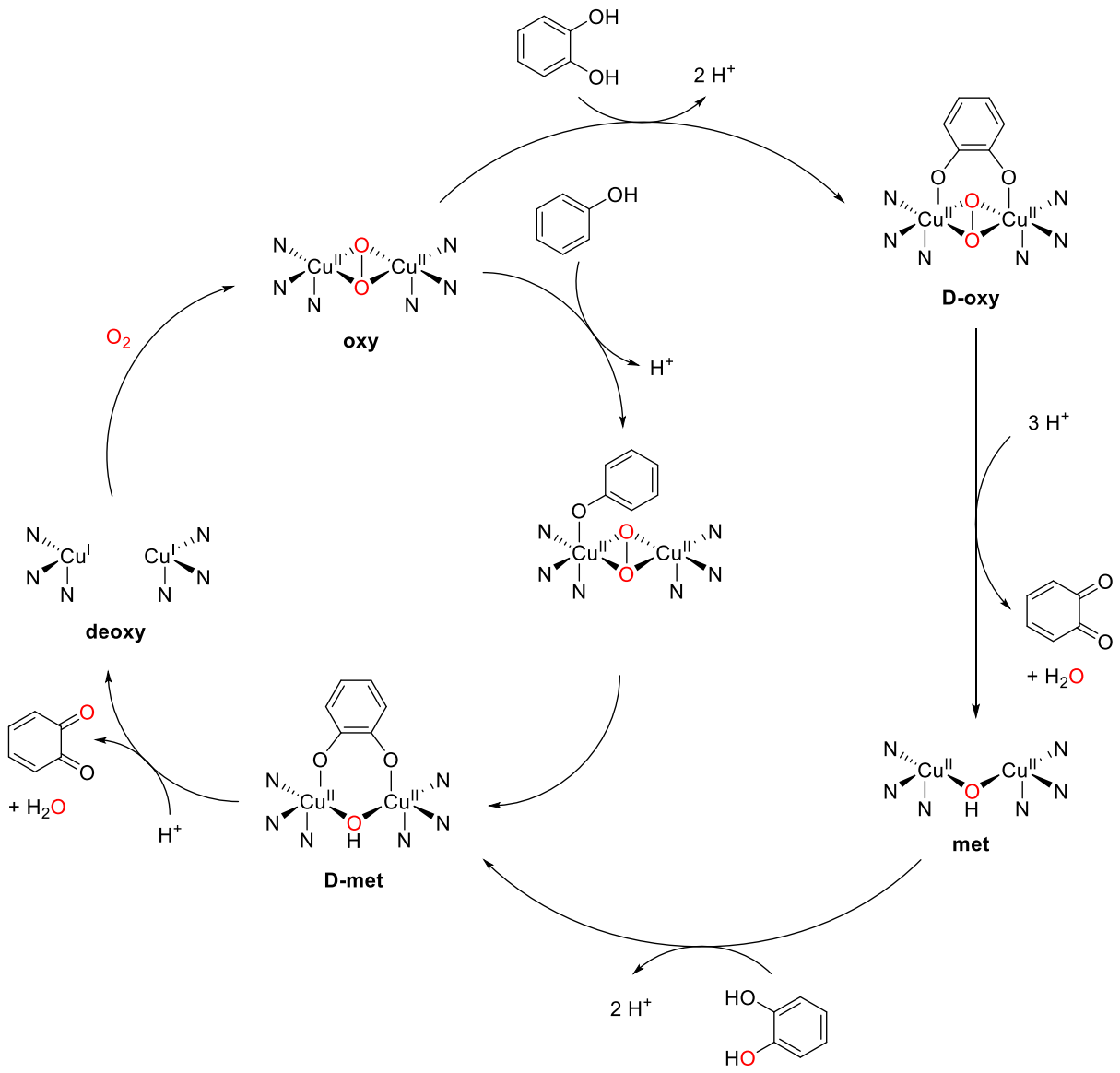

Scheme 2: Catalytic cycle of phenolase and catecholase activity of tyrosinase.[35]

The pathway from the oxy state of tyrosinase to the D-met state was discussed controversially.[9-11] The μ-η²:η²-peroxido dicopper(II) core is able to isomerize to the bis(μ-oxido) dicopper(III) form due to their small interconversion barrier (Scheme 3).[11,36–39] Therefore, it is still under debate when the O–O bond is cleaved reductively in regard of the consecutive electrophilic substitution.[11,14,47–49,22,40–46] Hedman, Hodgson, Solomon, Stack and co-workers reported in 2005 a sequential O–O bond cleavage and hydroxylation of their tyrosinase model system.[40] Thus, the early stage O–O bond scission has to be considered as a possible reaction mechanism besides the generally accepted concerted pathway or the late stage O–O bond scission.[11,14,22,41] Nevertheless, the structure of the catalytically active species is still under debate. Both motifs are considered to be possible for the enzymatic mechanism.[35] Recently, Rompel and co-workers contributed further knowledge to understand the phenolase activity, showing the impact of three surrounding histidine residues on the

phenolase activity of the reactive Cu_2O_2 center.[48,49] The flexible histidines are responsible for C–H activation of the substrate by functioning as bases and deprotonating the substrate.

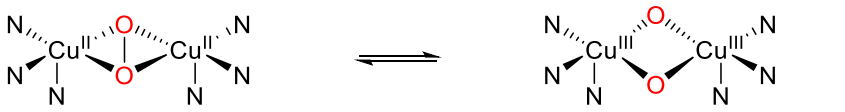

[P] **[O]**

μ–η²:η²-peroxido dicopper(II) core **bis(μ-oxido) dicopper(III) core**

Scheme 3: Equilibrium of the μ-η²:η²-peroxido dicopper(II) core and the bis(μ-oxido) dicopper(III) core.

1.2. Biomimetic Tyrosinase Model Systems

Understanding the mechanism of dioxygen activation and transfer of copper proteins in biological oxidation processes represents one major goal in chemical research. Nature serves as archetype as several proteins exhibit extraordinary efficiency in selective oxygenation and oxidation reactions. Synthetic model systems are developed to mimic the active site of the copper-based protein. They should feature similar structures and functions as the protein tyrosinase by being able to activate and transfer molecular oxygen to suitable substrates. The investigation of these model systems provides new insights into the molecular mechanisms to uncover the fundamental functionality of the activation of dioxygen.[50] This knowledge should be used in catalytic applications in industry to develop effective and environmentally friendly oxidation catalysts.[51]

1.2.1. Activation of Dioxygen by Copper(I) Complexes

Oxygenation of copper(I) species leads to copper-dioxygen species of different stoichiometries (Scheme 4). Reaction of copper(I) complexes with dioxygen in a $Cu:O_2$ ratio of 1:1 results in the formation of superoxido species, in which dioxygen is bound in different motifs. Dioxygen is incorporated in an end-on fashion in the η¹-superoxido copper(II) species. A side-on motif is also found in the η²-superoxido copper(II) complex, which can isomerize to a η²-peroxido copper(III) species. These species are highly reactive and therefore prone to react with another equivalent of the copper(I) species to form copper-dioxygen species in a ratio of 2:1, which are thermodynamically more stable. The η¹-superoxido species is transformed into a *trans*-μ-1,2-peroxido dicopper(II) species, whereas the η²-superoxido complex is converted to a μ-η²:η²-peroxido dicopper(II) species. The latter isomerizes to a bis(μ-oxido) dicopper(III) complex. The reaction of a μ-η²:η²-peroxido dicopper(II) or bis(μ-oxido) dicopper(III) species with another copper(I) species leads to the formation of a trinuclear bis(μ_3-oxido) species with one copper(III) and two copper(II) centers.[10,11,52]

The properties of copper-dioxygen species were studied extensively. The μ-η²:η²-peroxido dicopper(II) and bis(μ-oxido) dicopper(III) complexes with a Cu–O_2 ratio of 2:1 are well-characterized complexes.[10,11] The side-on peroxido species exhibits a Cu···Cu distance of 3.5 Å and averaged Cu–O bond lengths of 1.92 Å and an O–O bond length of 1.42 Å. The bis(μ-oxido) species has a smaller Cu···Cu distance of 2.8 Å, which is accompanied by a larger O···O distance of 2.3 Å and an averaged Cu–O bond length of 1.82 Å. The dicopper(III) species is a diamagnetic complex, whereas the side-on peroxido dicopper(II) species reveals antiferromagnetism.[11] The μ-η²:η²-peroxido dicopper(II) and bis(μ-oxido) dicopper(III) complexes are able to interconvert due to a very low energetic barrier resulting from very similar free energies (ΔG = 0.3-12.7 kcal mol^{-1}).[36–39]

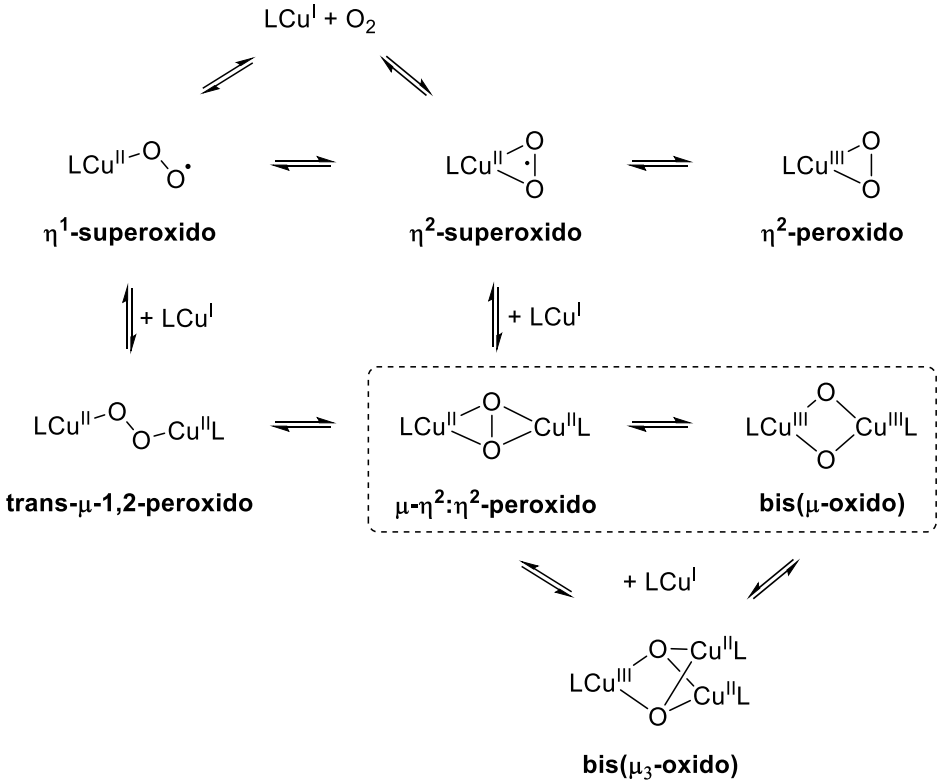

Scheme 4: Copper-dioxygen binding motifs of different stoichiometries.[10]

The equilibrium is influenced by the different factors such as ligand system, solvent, temperature and counterions. The ligand system controls the state of the equilibrium at first instance by means of steric and electronic properties. A sterically demanding ligand system supports the formation of μ-η²:η²-peroxido dicopper(II) species due to the smaller steric repulsion compared to bis(μ-oxido) dicopper(III) species.[53] A ligand system with high donor strength shifts the equilibrium towards the bis(μ-oxido) species as the higher oxidation state is better stabilized. Recently, Yoshizawa and co-workers investigated the influence of geometric effects of the ligand system on the equilibrium of μ-η²:η²-peroxido dicopper(II) and bis(μ-oxido) dicopper(III) species by using DFT calculations, showing perturbation effects in dependence of the N-donor distance of the used diamine ligand.[54] Polar solvents also promote the

stabilization of copper in a high oxidation state in favor of the bis(μ-oxido) dicopper(III) species. Mostly only one of the two species are observed as intermediate species.[14,22,23,35,55] Commonly, these copper-dioxygen species are synthesized by oxygenation of a copper(I) complex at low temperatures in the presence of weakly coordinating anions. The use of coordinating anions was rarely reported.[10,11] The solvents are usually aprotic, e.g. methylene chloride, tetrahydrofuran, acetone and acetonitrile. A temperature of –80 °C was established to stabilize reactive Cu_2O_2 intermediates. Even temperatures down to –145 °C were applied to increase the stability of the reaction intermediates.[56]

The μ-η^2:η^2-peroxido dicopper(II) and bis(μ-oxido) dicopper(III) complex possess different electronic structures, which makes them distinguishable by their spectroscopic properties (Figure 2).

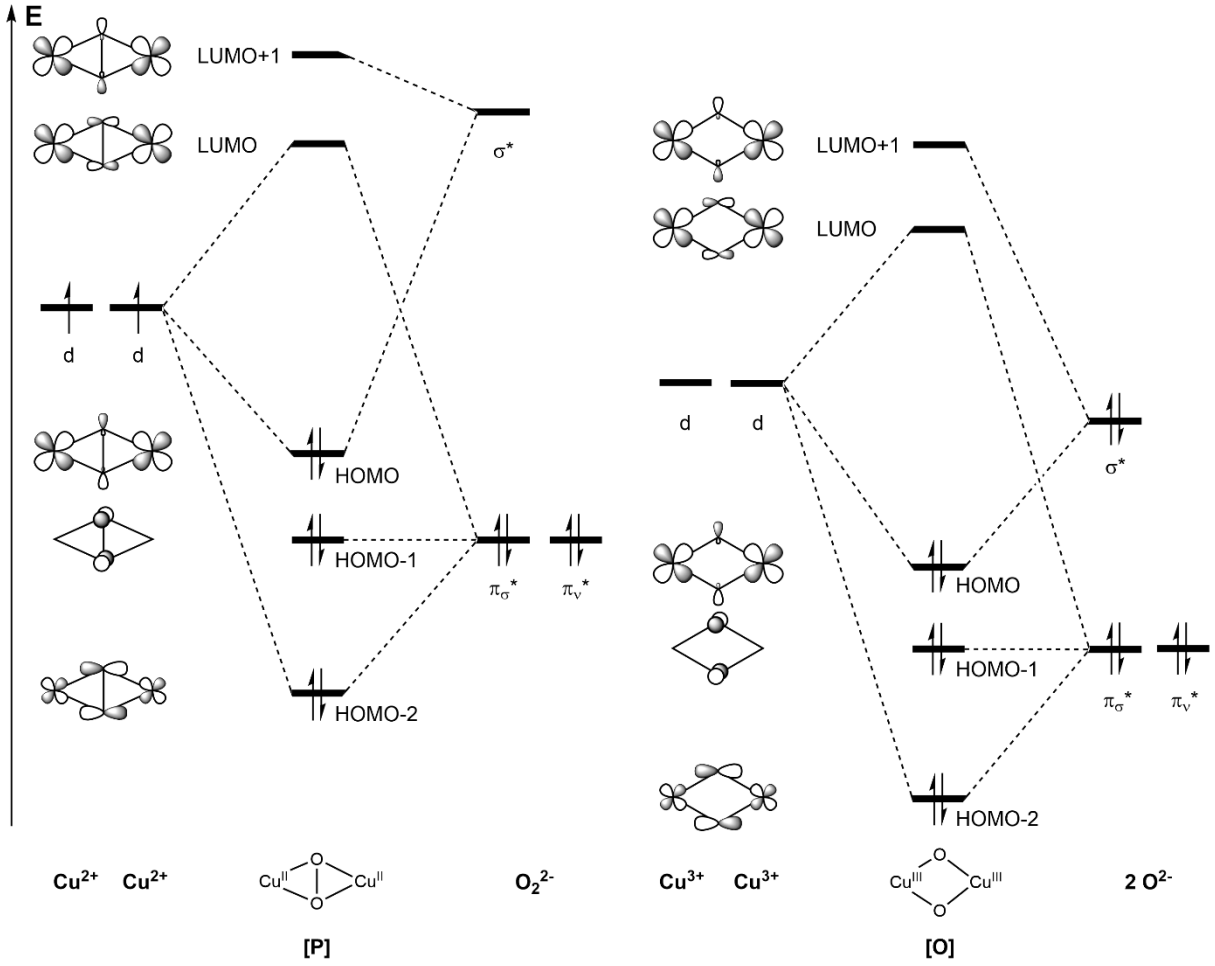

Figure 2: Molecular orbital diagram of μ-η^2:η^2-peroxido dicopper(II) complex (left) and bis(μ-oxido) dicopper(III) complex (right).[10]

The electronic changes upon isomerization are caused by transformed molecular orbitals. Formally, two electrons are transferred from the copper $d_{x^2-y^2}$ orbital to the oxygen σ* orbital of the [**P**] core, causing the O–O bond to cleave reductively under the formation of two oxido bridges.[22] The side-on peroxido species shows two characteristic LMCT absorption bands at

350 nm (20000 L mol^{-1} cm^{-1}) and 550 nm (1000 L mol^{-1} cm^{-1}) in the UV/Vis spectrum, which originate from the in-plane π_σ^* orbital to the copper d_{xy} orbital and the out-of-plane π_v^* orbital to the copper d_{xy} transition.[57] The bis(μ-oxido) species has LMCT bands at 300 nm (20000 L mol^{-1} cm^{-1}) and 400 nm (20000 L mol^{-1} cm^{-1}), which are caused by transitions of the in-plane π_σ^* orbital and σ* orbital to the d_{xy} orbital of copper.

Laser excitation around the charge transfer bands in the UV/Vis spectrum results in characteristic vibrations in the resonance Raman spectrum. The side-on peroxido species exhibits an O–O stretching vibration at 760 cm^{-1}. The bis(μ-oxido) species has a prominent breathing mode of the Cu_2O_2 core at 600 cm^{-1} along with an additional mode at 120 cm^{-1} of an asymmetrical stretch. The formal oxidation state of the copper centers is determined by Cu K-edge X-ray absorption spectroscopy (XAS). A typical pre-edge feature of the side-on peroxido dicopper(II) species is found at 8979 eV. The bis(μ-oxido) dicopper(III) species shows a transition at 8981 eV. EXAFS analysis provides information about interatomic distances, revealing significantly different Cu···Cu distances of 3.5 Å for the [**P**] core and 2.8 Å for the [**O**] core.

1.2.2. Design of Stabilizing Ligand Systems

In the last decades, several tyrosinase model systems were developed to activate molecular oxygen by binding in diverse motifs. In analogy to the deoxy state of tyrosinase, various copper(I) complexes were designed featuring different ligand systems with different coordination geometries. Reaction of copper(I) complexes with dioxygen results in different copper-dioxygen adduct species, which feature different structural properties in dependence of the ligand system. Therefore, the structure and oxidation state of the copper centers can be directed by tailored ligand systems. Commonly, tetradentate ligand systems support the formation of *trans*-μ-1,2-peroxido dicopper(II) species due to the propensity of copper(II) to be five-coordinated. Tri- and bidentate ligands are known for their greater flexibility allowing the coordination of dioxygen in the side-on motif. Therefore, they stabilize μ-η^2:η^2-peroxido dicopper(II) and bis(μ-oxido) dicopper(III) complexes. Most of the ligands were developed inspired by the histidine ligands of tyrosinase, which are N-donor ligands. Over the years, a variety of different N-donor ligands were reported, including imidazoles, pyrazoles, pyridines, amines, imines and guanidines.[10,11] O-, P- and S-donors are less common, as especially sulfur and phosphorus ligands tend to stabilize copper(I) complexes very well, which decelerates or even inhibits the reaction with molecular oxygen. O-donor ligands, such as alkoxides and aryloxides, are frequently used to investigate copper-dioxygen-based oxidation catalysts for the conversion of methane to methanol.[58,59] Alkoxide-stabilized systems also showed their activity in oxidase and oxygenase reactions.[60] While neutral ligand systems are most common to stabilize $Cu–O_2$ species in a 2:1 ratio, monoanionic ligands promote the formation of highly

reactive Cu–O_2 species in a 1:1 ratio. In general, chelate ligands creating a five- or six-membered ring with the metal center are favored. The steric demand of the ligand is also crucial as high steric demand correlates with elongated structures of Cu–O_2 species.

1.2.3. Historical Milestones

Important historical milestones in copper-dioxygen chemistry are summarized in the following. The first example of a copper-dioxygen species was reported in 1984 by Karlin and co-workers (Scheme 5).[61] Oxygenation of a dicopper(I) species **1** stabilized by ligand $XylO^-$ resulted in the formation of peroxido dicopper(II) complex **2**.

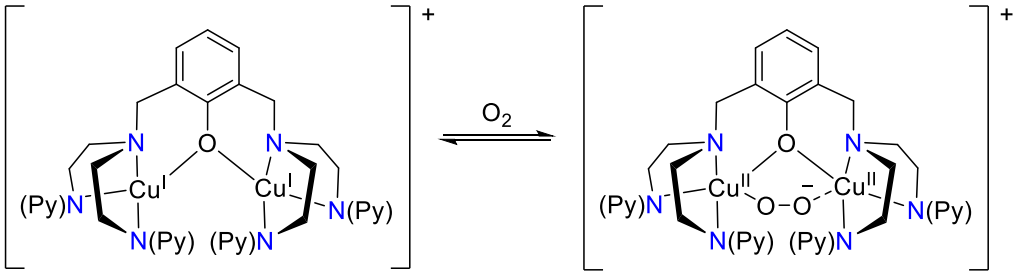

Scheme 5: First example of dioxygen activation by copper(I) complexes by Karlin and co-workers in 1984.

In 1989, Kitajima and co-workers described the first μ-η^2:η^2-peroxido dicopper(II) complex **3**, which was characterized crystallographically (Figure 3).[62] The purple complex **3** was synthesized at -78 °C in acetone. The two copper(II) centers were each stabilized by a tris(pyrazolyl)-borate ligand. The reactive Cu_2O_2 core exhibited a Cu···Cu distance of 3.56 Å, a O–O bond length of 1.41 Å and averaged Cu–O bond lengths of 1.91 Å. Complex **3** showed characteristic absorption bands at 349 nm (21000 L mol^{-1} cm^{-1}) and 551 nm (800 L mol^{-1} cm^{-1}) in the UV/Vis spectrum and a typical resonance Raman feature at 741 cm^{-1}, which shifted by 43 cm^{-1} upon utilization of $^{18}O_2$.[10,62]

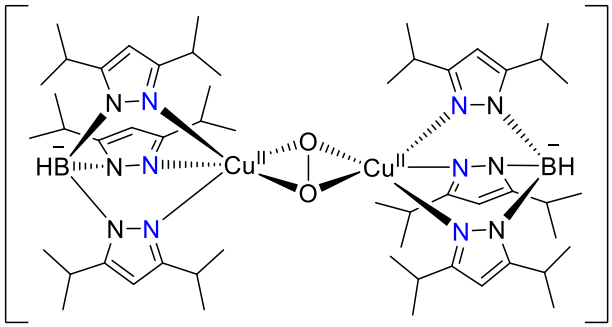

Figure 3: First example of a μ-η^2:η^2-peroxido dicopper(II) complex by Kitajima and co-workers in 1989.

The first example of a bis(μ-oxido) dicopper(III) complex (**4**) was crystallographically characterized in 1996 by Tolman and co-workers (Figure 4).[55] Complex **4** was formed in methylene chloride at -78 °C. A sterically demanding tris(amine) ligand was used to stabilize the copper(III) centers, which were distanced by 2.79 Å. The average Cu–O bond length was determined to 1.80 Å. The O···O distance of 2.29 Å clearly showed a complete cleavage of the dioxygen bond resulting in two μ-oxido bridges. Complex **4** depicted characteristic absorption bands at 318 nm (12000 L mol^{-1} cm^{-1}) and 430 nm (14000 L mol^{-1} cm^{-1}) in the UV/Vis spectrum and a resonance Raman feature at 603 cm^{-1}, which shifted by 23 cm^{-1} upon oxygenation with $^{18}O_2$.

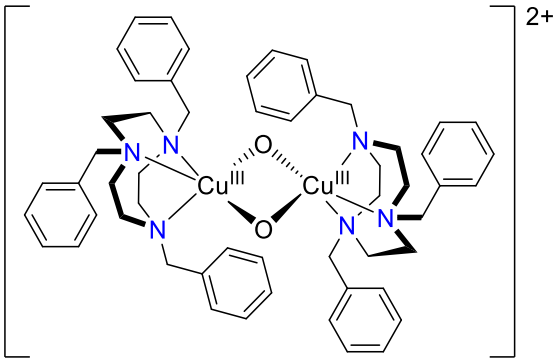

4

Figure 4: First example of a bis(μ-oxido) dicopper(III) complex by Tolman and co-workers in 1996.

The most stable μ-η^2:η^2-peroxido dicopper(II) species (**5**) was to date reported by Scarborough and co-workers in 2016 (Figure 5).[63] They described a sterically demanding tris(amine) ligand with *tert*-butyl substituents which was able to stabilize a μ-η^2:η^2-peroxido dicopper(II) species with a half-life of 14 h in methanol and 9.6 days in aqueous Na_2HPO_4 at room temperature. They correlated the enormous steric bulk of the ligand system with no co-existing bis(μ-oxido) isomer.

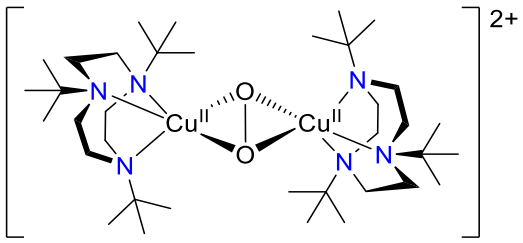

5

Figure 5: The most stable μ-η^2:η^2-peroxido dicopper(II) species was to date reported by Scarborough and co-workers.

The highest stability of an isomeric bis(μ-oxido) dicopper(III) complex was to date published by Herres-Pawlis, Henkel, Rübhausen, Meyer-Klaucke and co-workers in 2009 (Figure 6).[64] They developed a very bulky piperidinyl-substituted bis(guanidine) ligand system, which

stabilized an unreactive bis(μ-oxido) species (**6**) for several days in acetonitrile at room temperature.

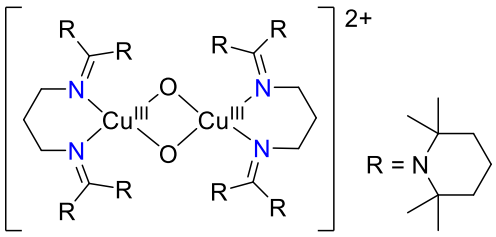

6

Figure 6: The most stable bis(μ-oxido) dicopper(III) complex was to date reported by Herres-Pawlis, Henkel, Rübhausen, Meyer-Klaucke and co-workers.

The special role of bis(μ-oxido) dicopper(III) complexes as biomimetic systems for copper enzymes lies in their potential reactivity towards external substrates, as they represent powerful oxidants but they are largely prone to thermal decomposition due to the intramolecular hydroxylation of the ligand system.[10,11] The group of Stack focusses on the development of small and simple histidine-derived ligand systems, intending to enhance the reactivity of the Cu_2O_2 core with exogenous substrates due to the increased core accessibility.[38,65,66] However, the oxygenation of Cu(I) complexes stabilized by small and simple ligand systems (such as primary amines) yields a multitude of $Cu–O_2$ species even at –125 °C due to the high reactivity of initially formed adducts. To overcome this problem, they introduced the “core capture” method, a ligand exchange process of a tetramethyl propylenediamine-supported bis(μ-oxido) species, which is robust at –80 °C, with stronger donating ligand systems at lower temperatures. Thus, the selective formation of bis(μ-oxido) species ligated by primary amines such as propylenediamine was possible at –125 °C.[67] This “core capture” method was also applied to synthesize histamine-stabilized bis(μ-oxido) species.[68] Moreover, preformed bis(μ-oxido) species were used to enable the full formation of μ-η^2:η^2-peroxido dicopper(II) species supported by Nτ-ligation of imidazoles at very low temperatures (–145 °C).[56] The minimized steric demand of imidazole ligands in τ-position over those in π-position facilitate the accessibility of the Cu_2O_2 core and accelerate the reaction with exogenous substrates.[56] A permethylated bis(amine) ligand promoted the stabilization of the bis(μ-oxido) species at –125 °C in methylene chloride and was able to selectively oxidize primary alcohols and amines, which was limited to stoichiometric conversions.[65] The substitution of the tertiary amines by imidazole ligands led to an increased stability of the corresponding bis(μ-oxido) complexes.[68,69] But until now, the catalytic reactivity of biomimetic bis(μ-oxido) dicopper(III) species remains still challenging. The relevance of the bis(μ-oxido) species was also studied previously in the context of model systems for pMMO.[68,70] Understanding the mechanism of $Cu–O_2$ oxidation chemistry will not only be beneficial for C–H functionalization reactions (such as the oxidation of methane to methanol) but also for the

development of oxidation catalysts applicable to industrial scale (such as Cu/O-based zeolites).[58,59,71]

1.2.4. Transfer of Dioxygen in Hydroxylation Reactions

Many structural model systems were developed mimicking the active site of tyrosinase. Since the beginning of the 1990s, efforts were made to design model systems which feature tyrosinase-like monophenolase and catecholase reactivity towards exogenous substrates. The reaction of aromatic alcohols with reactive Cu_2O_2 species results in different products (Scheme 6). Monophenolase reactivity towards phenol **7** yields the *ortho*-hydroxylation product **8** (pathway (a)). Catechol **8** is oxidized to the *ortho*-quinone **9** (catecholase, pathway (b)). Quinones are highly reactive species prone to side reactions, as they are known to be unstable and volatile.[72,73] O*rtho*-quinone **9** can be attacked nucleophilically by phenol **7**, leading to C–O coupled intermediate **10** (pathway (c)) which isomerizes to the C–O coupled catechol **11** (pathway (d)).[74,75] Catechol **11** is also oxidizable to form the C–O coupled quinone **12** (pathway (e)).[76,77] In addition, C–C coupling reactions can occur via a radical mechanism, in which phenoxy radicals dimerize in *ortho*-position to form C–C coupled biphenols **13** (pathway (f)).[41]

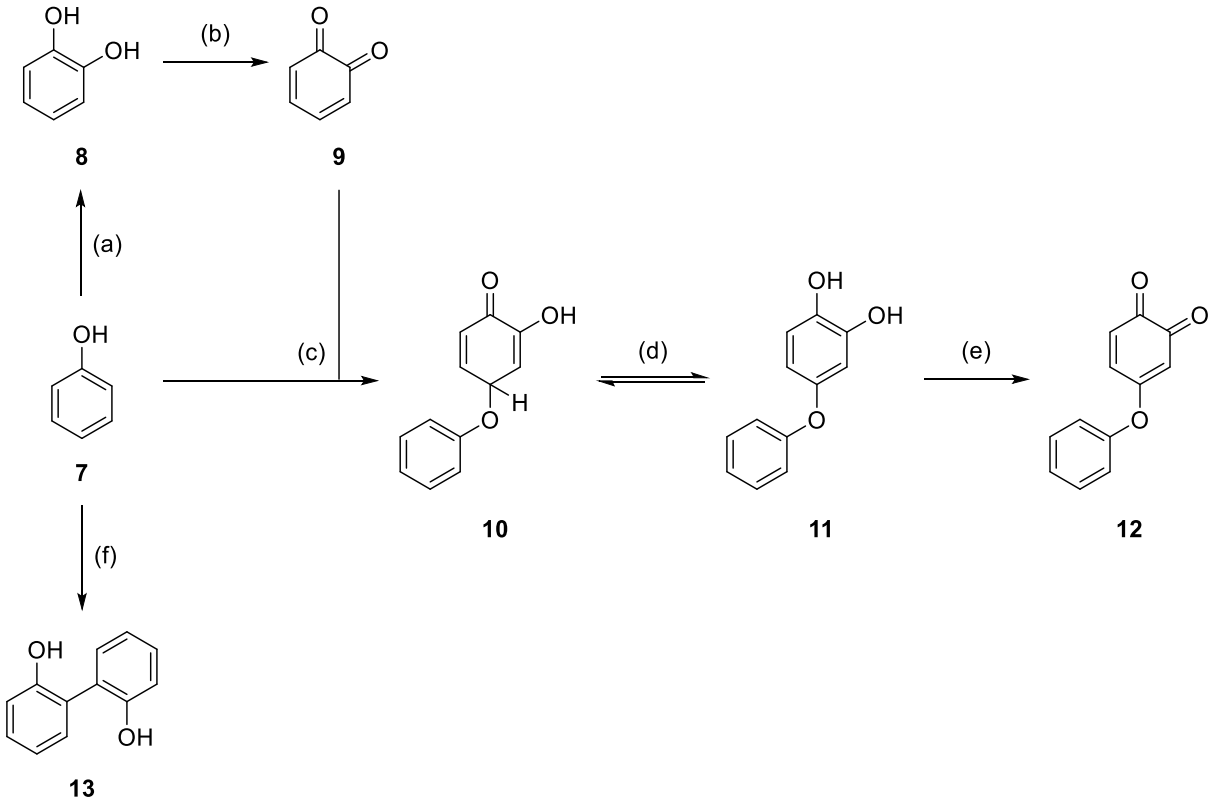

Scheme 6: Possible reaction pathways in oxygenation reactions of aromatic alcohols: (a) *ortho*-hydroxylation, (b) oxidation, (c) oxidative C–O coupling reaction, (d) isomerization, (e) oxidation, (f) C–C coupling reaction.

The isolation of *ortho*-quinones **9** is challenging due to their instability. Nevertheless, it is of fundamental interest as *ortho*-quinones **9** represent an important intermediate in melanin biosynthesis. One way to transform reactive *ortho*-quinones **9** into stable derivatives is the condensation reaction with *ortho*-phenylenediamine (**14**) to form phenazines (**15**), enabling the synthesis of various phenazine derivatives (Scheme 7).[78–84]

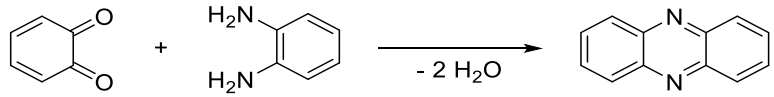

9 **14** **15**

Scheme 7: Condensation of *ortho*-quinones with *ortho*-diamines to form phenazines.

Phenazines (**15**) are planar tricyclic aromatic heterocycles, which often feature a yellow color. In nature, phenazine compounds are produced by bacteria.[79] Modifications lead to a variety of phenazine derivatives with different biological activities. Many derivatives were found to show inter alia antibiotic, antitumor and antimalarial properties, which makes them especially attractive for medicinal research.[85,86] Moreover, the fully conjugated aromatic π-system provides optical and redox properties. Absorption and emission spectra of phenazines exhibit bands in the region of 400 nm to 700 nm, making them useful as fluorescent tracers for applications in molecular imaging.[87] Phenazines are also frequently used as starting material for dyes such as neutral red, safranine and mauveine.[88] In addition, they are important starting materials for the industrial production of pesticides.[89]

1.2.4.1. Substrate Scope of Catalytically Active Systems

A multitude of tyrosinase model systems were reported, which showed stoichiometric hydroxylation activity.[9,11,35,90,91] To date, very few model systems are known that allow the catalytic hydroxylation of exogenous substrates.[90] Applied substrates are derived from phenol, as tyrosinase naturally converts L-tyrosine into L-Dopaquinone (see Scheme 1). In addition to different substituted phenols (**7**, **16-19**), which were used standardly, conversion of N-acetyl tyrosine ethyl ester (**20**), 8-quinolinol (**21**) and estrone (**22**) were published so far (Figure 7).

Turnover numbers (TON) were determined via UV/Vis spectroscopy by using the absorption band of the quinone products. Their characteristic absorbance A was used to calculate the amount of quinone formed with the help of the Lambert-Beer law (1).

$$A = c \cdot d \cdot \varepsilon \quad (1)$$

(c = concentration [M^{-1}], d = optical path length [cm], ε = extinction coefficient [M^{-1} cm^{-1}])

The product concentration of the quinone was then correlated to the concentration of the catalyst to obtain the turnover number.

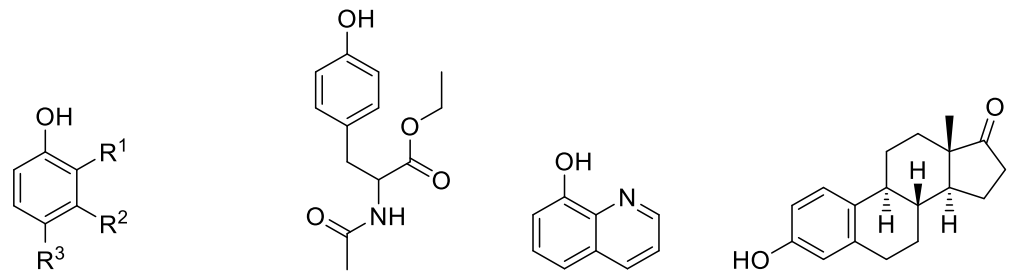

7 (R^1 = H, R^2 = H, R^3 = H)
16 (R^1 = H, R^2 = H, R^3 = OMe)
17 (R^1 = H, R^2 = H, R^3 = Me)
18 (R^1 = H, R^2 = *t*Bu, R^3 = H)
19 (R^1 = *t*Bu, R^2 = H, R^3 = *t*Bu)

20 **21** **22**

Figure 7: Substrate scope of tyrosinase-like catalytic oxygenation reactions.

Ligand systems, which promote catalytic conversion of substrates, are summarized in Figure 8. The first catalytically active model system was reported in 1990 by Réglier and co-workers.[92] The binucleating hybrid imine pyridine ligand **23** stabilized the formation of a [**P**] complex, which was able to convert 2,4-di-*tert*-butyl phenol (**19**) into the corresponding quinone with a turnover number of 16 in one hour. The group of Casella published in 1991 another model system supported by benzimidazole ligand **24** with an aromatic spacer, which also showed catalytic activity towards phenolic substrate **19** with a TON of 1.22.[93] Nearly 20 years later, Tuczek and co-workers showed in 2010 that copper(I) complexes of the small hybrid imine pyridine ligand **31** are capable of the hydroxylation of phenol **19** in the presence of dioxygen with a TON of 18 within 24 hours.[94] Herres-Pawlis and co-workers reported in 2013 the synthesis of [**P**] species supported by bis(pyrazolyl)methane ligand **26**.[95] The catalyst was able to transform a variety of substrates including 4-methoxy phenol (**16**, TON = 15, 24 h), *N*-acetyl tyrosine ethyl ester (**20**, TON = 15, 16 h), 8-quinolinol (**21**, TON = 8, 16 h) and estrone (**22**, TON = 4, 6 h), thus expanding the substrate scope. The number of catalytically active tyrosinase model systems was significantly increased since then.[74,75,103–106,77,96–102] Small molecule changes of the ligand system caused substantial differences in the catalytic performance. Most active ligand systems were bidentate chelate ligands. Few examples featured tridentate support, but none of them revealed fourfold denticity. Most systems were bridged by a spacer to form a five- or six-membered ring with the metal center. Three-membered spacers were most frequently used, which enable a larger bite angle than two-membered spacers. Many of them are connected to heterocyclic donor moieties, which only allow a certain degree of flexibility of the ligand backbone. The steric demand of active ligand systems varied significantly. On the one hand, bulky substituents such as *tert*-butyl groups were implemented in many systems to shield the catalytically active center. On the other hand, very small and simple ligand systems also supported catalytic reactivity. Therefore, the structure-reactivity relationship of tyrosinase model systems remains still unclear.

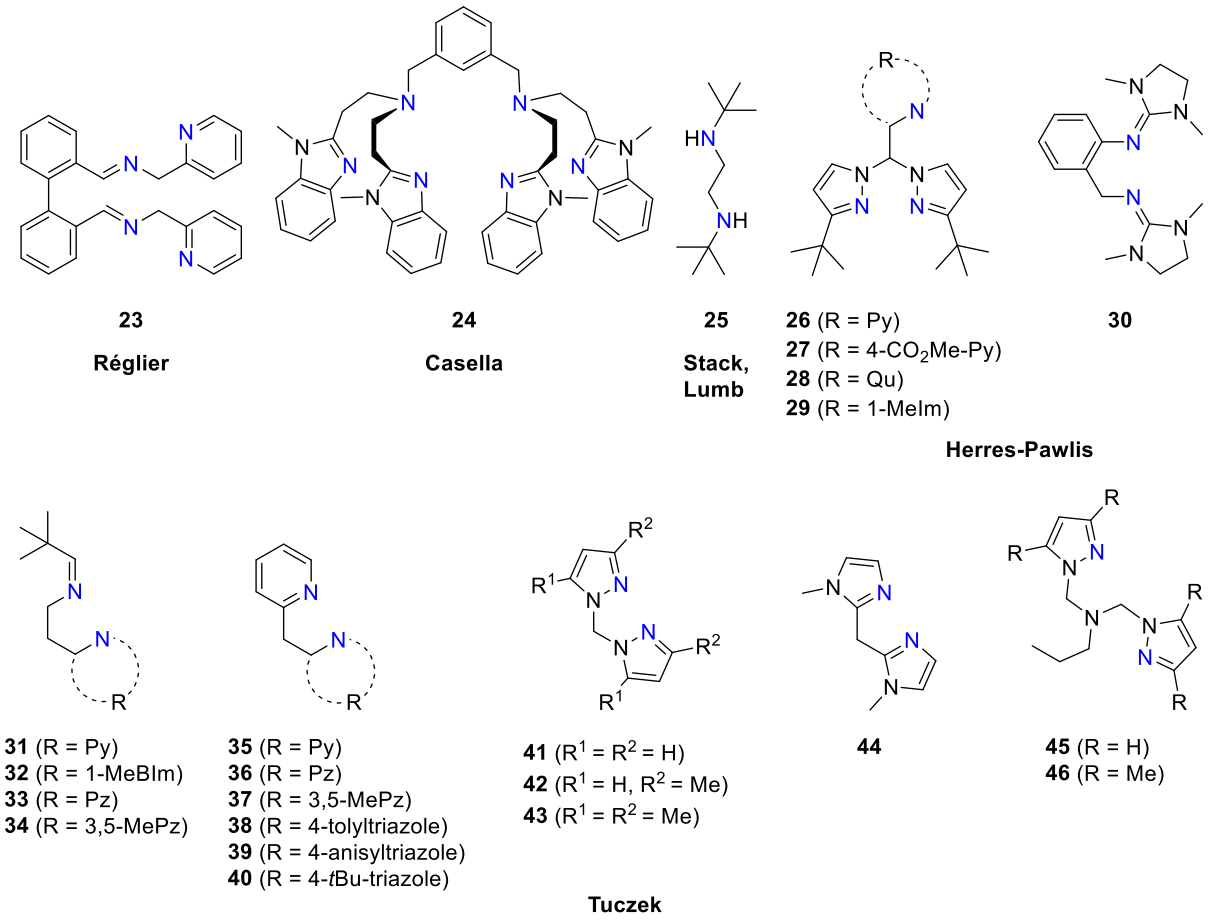

Figure 8: Ligand systems promoting catalytic hydroxylation reactions.

1.3. Guanidine-stabilized Tyrosinase Model Systems

1.3.1. Guanidines Ligands

The reactive center of the protein tyrosinase is supported by histidine ligands, which permit the activation and transfer of dioxygen. Inspired by these natural N-donor ligands, related N-donor moieties are suitable ligands to mimic the imine-donor moiety of histidine. Metal centers with high oxidation states are optimally stabilized by strong organic bases. Guanidines provide very high basicity due to the delocalization of the positive charge of the guanidinium cation (Figure 9).

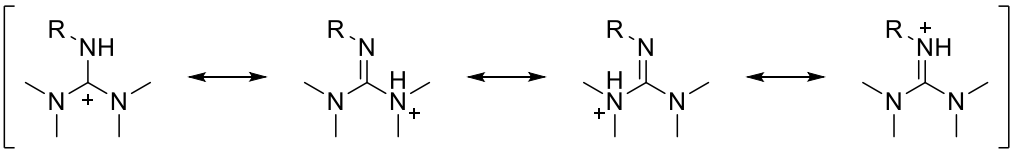

Figure 9: Charge delocalization of the guanidinium cation.

Guanidines are found in nature in amino acids (e.g. arginine, isocytosine and creatinine), on which most proteins are based. Besides their natural occurrence, guanidine ligands are widely spread in the field of coordination chemistry.[107] Guanidine-based metal complexes were used successfully as catalysts in atom transfer radical polymerizations[108–111] and ring-opening polymerization of lactide.[112–117] Furthermore, copper complexes stabilized by guanidine ligands showed high potential as entatic state model systems.[118–120]

1.3.2. Characteristics of Bis(guanidines) and Hybrid Guanidines

Guanidine ligands can be classified into poly(guanidines) and hybrid guanidines (Figure 10). Poly(guanidines) feature at least two guanidine moieties which are bridged by a spacer. A ligand with multiple guanidine moieties allows the stabilization of highly reactive metal centers by both strong σ-donor abilities and shielding of the metal due to high steric demand. Bis- and tris(guanidine) ligands are prominent examples which are used frequently in coordination chemistry and copper-dioxygen chemistry.[107,121–124] Hybrid guanidines consist of a guanidine moiety and at least one different donor function. The combination of different donor moieties enables the design of a tailored ligand system suitable for their purpose. Balancing donor strength and steric demand of the ligand system allows not only proper support of the metal center but also tunes the accessibility of the metal center for organic transformation reactions. The design of the bridging spacer is responsible for the steric and electronic properties of the ligand system. Depending on the branched structure of the spacer, multidentate guanidine ligands are feasible. Besides the control of the denticity of the ligand, the bite angle can also be tailored by the choice of the spacer. Aliphatic spacers provide a flexible ligand backbone, whereas aromatic spacers enhance the rigidity of the system. In addition, aromatic spacers facilitate the detection of metal complexes by using spectroscopic methods due to the implemented π-electron system.

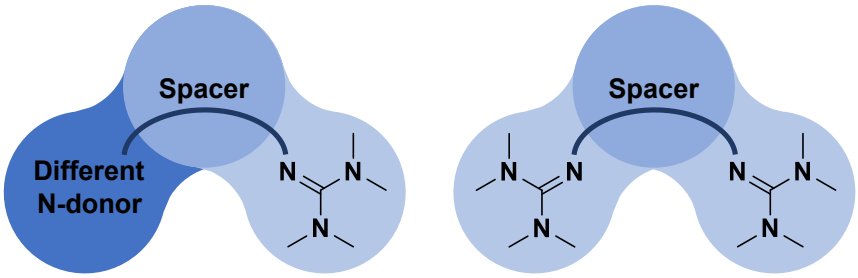

Figure 10: Schematic design of hybrid guanidines (left) and bis(guanidines) (right).

1.3.3. Synthesis of Guanidines

Guanidines are accessible by various synthetic methods. The first method was developed by Strecker in 1861 via oxidative degradation of guanine.[125] A very efficient method for the design of both poly(guanidines) and hybrid guanidines was presented by Kantlehner and co-workers

in 1984, which was modified by Sundermeyer, Herres-Pawlis and co-workers (Scheme 8).[102-105]

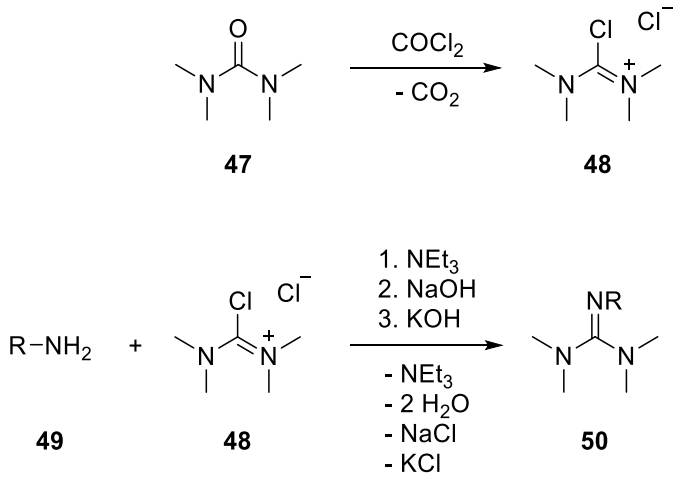

Scheme 8: Synthesis of guanidines via condensation reaction.

Guanidines (**50**) are synthesized by condensation of a primary amine (**49**) with a Vilsmeier salt derivative (**48**) in several hours. Vilsmeier salts (**48**) are formed by reaction of urea compounds (**47**) with phosgene, enabling the design of very different building blocks.[126]

The mechanism of the guanidine synthesis is illustrated in Scheme 9. The reaction of a primary amine and a Vilsmeier salt results in the formation of a guanidinium hydrochloride in the presence of the auxiliary base triethylamine. The concomitantly formed hydrochloride salt is deprotonated by equimolar amounts of sodium hydroxide. The stable guanidinium cation is deprotonated by 50% potassium hydroxide to form the free base. This method enables the isolation of guanidines in high yields. Guanidines are highly hygroscopic compounds. Purification of guanidines is achieved by distillation or column chromatography if necessary. Guanidine compounds are primarily soluble in polar organic solvents. Guanidine derivatives often also show good solubility in nonpolar solvents.

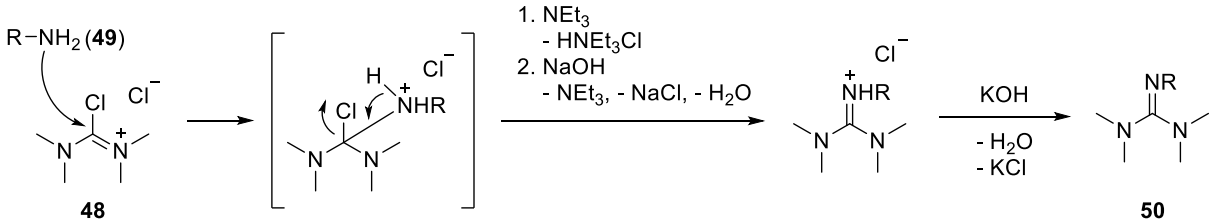

Scheme 9: Mechanism of the condensation reaction of a Vilsmeier salt and a primary amine.

One major advantage of using this method is the versatility of the system. On the one hand, the formation of different Vilsmeier salts allows the synthesis of guanidine moieties with suitable steric demand and donor strength (Figure 11).[128] On the other hand, poly(guanidines) and hybrid guanidines offer a toolbox for various applications.

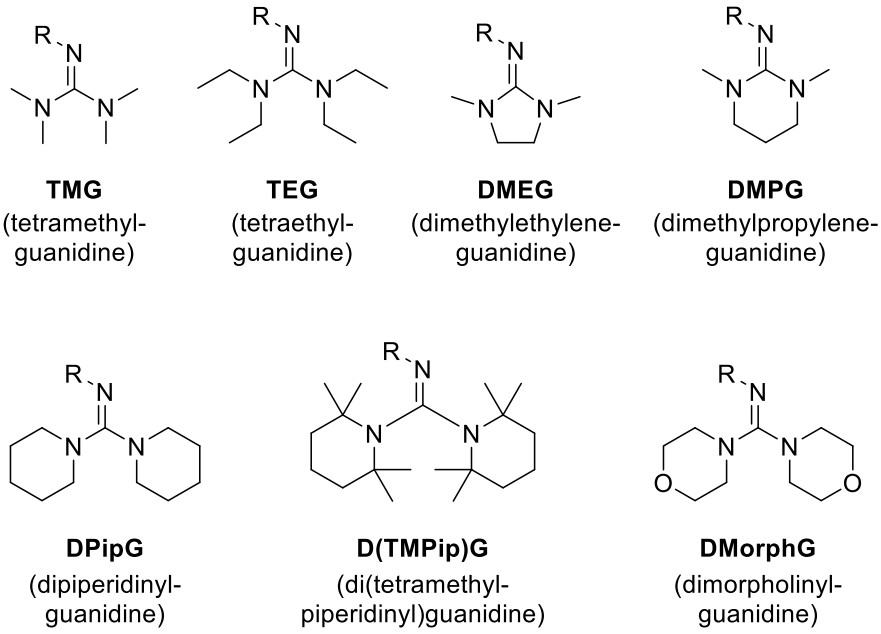

Figure 11: Different structures of guanidine moieties.[128]

1.3.4. Activation and Transfer of Dioxygen by Guanidine-stabilized Copper Complexes

Guanidine ligands have a long history in copper-dioxygen chemistry. Hybrid guanidine, bis(guanidine) and tri(guanidine) ligands **30**, **51**-**54** exhibited their suitability as model systems for copper enzymes, which are illustrated in Figure 12. The ligands **30**, **51**, **53** and **54** possess two N-donor groups, which are bridged by a C_3-chain to form a six-membered ring upon metal coordination, thus stabilizing the metal center in a bidentate fashion. Tris(guanidine) ligands, such as **52**, consist of three guanidine moieties which are connected by a spacer, such as a tertiary amine moiety, thus supporting a metal center in a tetradentate manner.

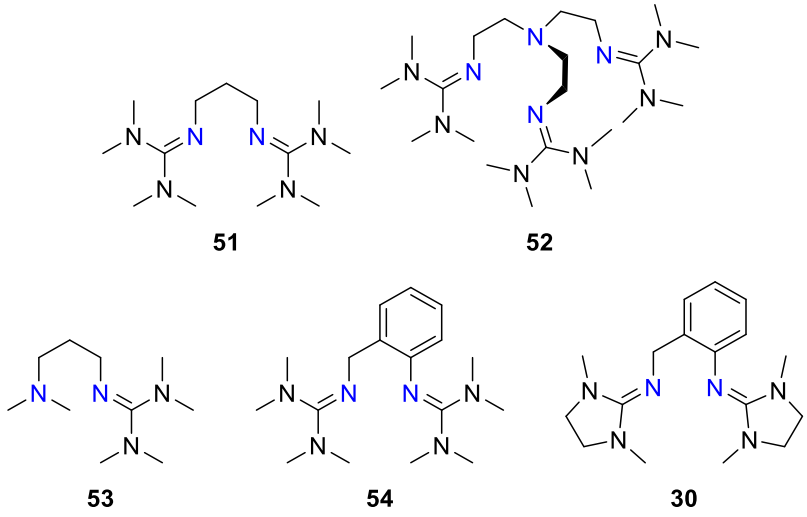

Figure 12: Guanidine ligand systems for the activation and transfer of dioxygen.

Ligand **51** was developed in 2000 and contains two guanidine moieties, which are sterically demanding und possess strong donor abilities to stabilize copper centers.[130,131] Their corresponding copper(I) complexes are air- and moisture-sensitive. In 2005, the activation of dioxygen was achieved at –80 °C to form a reactive bis(μ-oxido) dicopper(III) complex **55**, which was characterized by UV/Vis and resonance Raman spectroscopy. Complex **55** decayed at temperatures above -40 °C and was found to form alkoxido-bridged and hydroxido-bridged decomposition products.[132,133]

One year later, much attention was attracted by the tris(guanidine) ligand **52**, which was developed by Sundermeyer and co-workers in 2001, as the strong base was able to stabilize a variety of transition metals (Mn, Fe, Zn).[134] A breakthrough was achieved when copper(I) complexes of ligand **52** were found to react with dioxygen in acetone at -70 °C to form end-on superoxido copper(II) complexes.[122] The 1:1 Cu/O_2 adduct was characterized by resonance Raman, UV/Vis spectroscopy and DFT calculations. The formation of the end-on superoxido copper(II) complex was completely reversible, as warming up of the reaction solution to room temperature resulted in the release of dioxygen and repeated cooling down led again to the formation of the end-on superoxido copper(II) complex. Two years later, a crystal structure of the 1:1 Cu/O_2 adduct was obtained successfully.[124] The end-on superoxido copper(II) complex was also found to react with exogenous substrates in oxygenation reactions, leading to C–H and O-H functionalized substrates.[121]

In 2009, hybrid guanidine ligand **53** was introduced as supporting ligand system in copper-dioxygen chemistry. The ligand **53** consists of a guanidine and an amine moiety, balancing steric demand and donor strength. Its respective copper(I) complexes form reactive bis(μ-oxido) species **56** in the presence of dioxygen at –80 °C, which showed high stability at low temperatures and were characterized spectroscopically.[47]

The reactivity of the bis(μ-oxido) complexes **55-57** stabilized by ligands **51**, **53** and the related bis(amine) ligand were compared towards the substrates 2,4-di-*tert*-butylphenolate and 2,4-di-*tert*-butylphenol (Figure 13).[47] The bis(guanidine)-supported complex **55** revealed no reactivity towards both substrates, whereas the bis(amine)-stabilized species **57** exhibited radical coupling reactivity to form bisphenol products. The hybrid guanidine-amine promoted complex **56** showed hydroxylation reactivity towards phenolates to form catechols and radical coupling chemistry towards phenols. These fascinating differences were explained by the immense stabilizing effect of guanidine moieties due to their high basicity. As a result, the bis(μ-oxido) complex **55** is sufficiently stabilized to eliminate the oxidative power of the copper(III) centers, thus inhibiting outer-sphere oxidation. Another possibility represents the minor accessibility of the reactive core due to the high steric demand of the guanidine groups, as no conversion of a substrate was observed even after some hours. More oxidative power was ascribed to the hybrid guanidine-amine ligated system **56** and even far more to the

bis(amine) ligated system **57**. The latter revealed fast outer-sphere one-electron oxidation reactivity towards phenolates forming phenoxyl radicals. This reactivity is attenuated by the guanidine moiety in complex **56**, allowing the coordination of the phenolate to the Cu_2O_2 core to perform hydroxylation reactions.

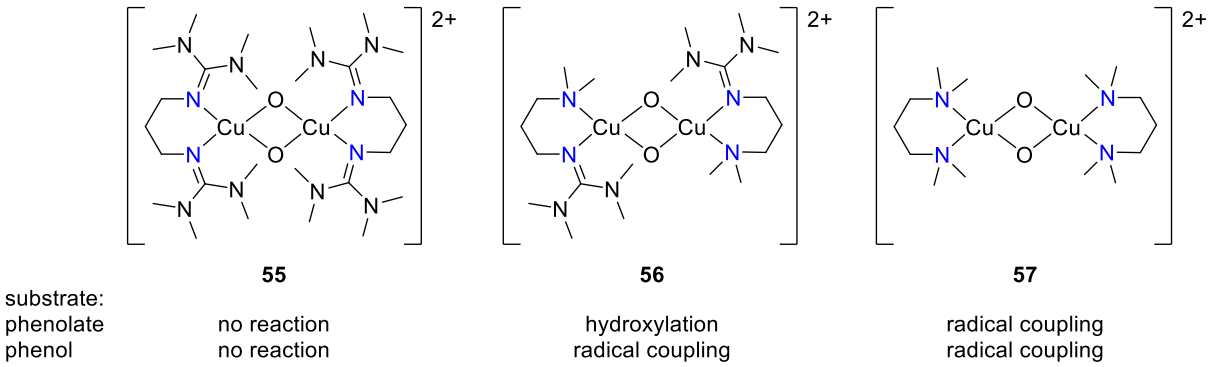

55 **56** **57**

substrate:			
phenolate	no reaction	hydroxylation	radical coupling
phenol	no reaction	radical coupling	radical coupling

Figure 13: Reactivity of bis(μ-oxido) dicopper(III) complexes stabilized by bis(guanidine), hybrid guanidine amine and bis(amine) ligands towards 2,4-di-*tert*-butylphenolate and 2,4-di-*tert*-butylphenol.

In analogy to ligand **51**, a related bis(guanidine) system **54** was developed in 2017, which features a benzylene-spacer (Figure 12).[135] The aromatic spacer allows enhanced fluorescence activity due to the π-electron system. Activation of dioxygen resulted in the formation of a bis(μ-oxido) complex **58**, which was formed very quickly at –80 °C and decayed at temperatures above -40 °C. Complex **58** was characterized by spectroscopic methods and simulated by DFT calculations. A closely related bis(μ-oxido) species **59** stabilized by ligand **30** was developed in 2018, which exhibited catalytic activity towards 8-quinolinol.[99]

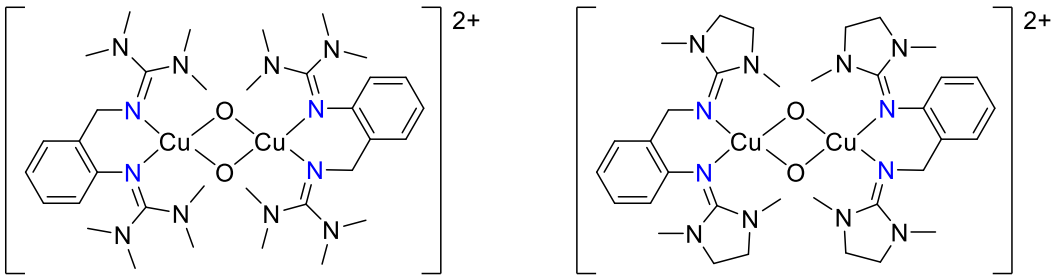

58 **59**

Figure 14: Bis(μ-oxido) dicopper(III) complexes stabilized by aromatic bis(guanidine) ligands.

1.3.5. Application in Bubbly Flows

The use of dioxygen as readily available oxidizing agent is envisioned for industrial applications in multiphase systems. Selective oxidation catalysts remain challenging with respect to sustainability. A prominent example is the Baeyer-Villiger oxidation, in which ketones are oxidized to esters by using peracids. The industrial oxidation of cyclohexanone to caprolactone, which is a monomer for biodegradable polymers, is performed by peracids, such as peracetic acid[136] or perbenzoic acid[137], although the oxidation was already successfully conducted by dioxygen and benzaldehyde in lab-scale in the early 1990's.[138,139] This example

shows the difficulty of scaling up reaction processes and the associated complications due to mass transfer effects. The DFG priority program 1740 focusses on developing solutions to overcome the challenges of mass transfer and hydrodynamics of bubbly flows in multiphase systems.[140] Oxygenation of organic compounds in gas-liquid systems in large reactors is desirable to ultimately understand the behavior of bubble swarms. The synthesis of many bulk chemicals often requires close proximity between gaseous starting materials and a continuous liquid phase. The application of dioxygen as oxidant for producing oxygenated products is envisioned as dioxygen is cheap and readily available. Bubble columns are frequently applied to transport dioxygen efficiently from the gaseous phase into the liquid phase. Large bubble column reactors represent a promising device, working in a continuous flow of a multiphase system.[140] Reactive bubbly flows enable large reaction volumes in bubble column reactors, but they are also minimizable in small reactors to investigate mixing behavior in different time and space scales. The efficiency of bubble column reactors is determined by several factors, e.g. bubble size distribution, bubble rise velocity, back-mixing, and phase interfaces.[141,142] Nevertheless, the determination of these parameters is still challenging due to the complexity of the apparatuses. Therefore, small-sized set ups are used to reduce the parameters affecting the system to a minimum.

Oxygenation reactions of copper(I) complexes and organic substrates represent gas-liquid systems, which are suitable for applications in bubbly flows because they enable insights into mass transfer and hydrodynamic behavior during the reaction. For this purpose, suitable reaction systems are necessary, of which the chemical characteristics are foremost understood forming the basic conditions of applying a reaction system in bubbly flows. Especially bis(guanidine) systems **30**, **51** and **54** exhibited promising potential in the application of bubbly flows due to their easy and quantitative synthesis in a short period of time. The starting material is cheap and easy to handle. Oxygenation reactions of copper(I) complexes supported by **51** were already followed in different bubbly column reactors, such as the SuperFocus mixer setup[143], Taylor flow systems[144] and most recently Hele-Shaw cells.[145] Such applications contribute to a better understanding of occurring processes on the route to optimized bubbly column reactors for oxidation processes in industrial scale.

2. Objective and Outline

2.1. Objective

The design of environmentally friendly, selective and efficient oxidation catalysts is one major goal in chemical research.[51,146–148] The activation of molecular oxygen was impressively demonstrated by copper proteins, forming catalytically active copper-dioxygen species.[22] Bioinorganic chemistry provided a deep insight into the mechanisms of these enzymes by modelling of the active site with the aid of tailored synthetic small-molecule systems. However, only few examples of these well-characterized model systems depicted catalytic reactivity towards exogenous substrates, underlining the difficulty of understanding the structure-reactivity relationship of the active sites.[10,11,90]

This thesis aims to develop stabilized copper complexes serving as tyrosinase model systems which are able to activate and transfer dioxygen. Inspired by aliphatic hybrid guanidine-supported copper complexes which showed excellent activation abilities and promising phenolase reactivity[47], the design of new hybrid guanidine ligands and their corresponding copper complexes represents a primary target of this work. In search of functional N-donor ligands suitable for the stabilization of high oxidation states of transition metals, the choice was made in favor of aromatic hybrid guanidine ligands as they enable the beneficial interplay between electronic and steric factors with respect to stability of the reactive Cu_2O_2 core and its accessibility towards exogenous substrates. Moreover, the aromatic spacer enhances the fluorescence behavior of the ligand system due to the additional π-electron system. An important topic is the comprehensive characterization of the copper(I) complexes to correlate structure and reactivity. For the same reason, the activation of dioxygen mediated by systematically varied copper(I) complexes has to be investigated. Studies on the structure of generated copper-dioxygen species and their consecutive reactions provide information about the molecular mechanisms, which are still under debate. Moreover, the lack of active oxidation catalysts in hydroxylation reactions impede the investigation of the structure-reactivity relationship to correlate ligand design and suitable substrates. To fill this gap, the potential of the catalysts has to be evaluated in oxygenation reactions by screening the applicable scope of substrate classes.

2.2. Outline

The results of this thesis are divided into four parts. Ligands used in this study are aromatic hybrid guanidine ligands, in which the guanidine moiety is either bound to the phenyl ring (benza ligands, Figure 15) or bound to the methylene moiety of the spacer (anil ligands). Each chapter deals with a ligand system and their corresponding copper complexes, followed by

their reactivity towards dioxygen and their activity in oxygenation reactions of aromatic alcohols.

Chapter 3.1 describes the development of two hybrid guanidines of the benza ligand group. The ligands were used in combination with copper salts to synthesize copper(I) complexes with weakly coordinating anions. Structural features of these complexes are discussed comprehensively. Suitable copper(I) complexes are evaluated in oxygen activation reactions at low temperatures. In this context, the influence of different weakly coordinating anions on the properties of the generated bis(μ-oxido) dicopper(III) complexes is analyzed. The bis(μ-oxido) species are characterized by spectroscopic methods, cryo-UHR-ESI mass spectrometry and DFT calculations. Stability studies are performed, and decomposition products are evaluated. A mechanism of the decomposition reaction is proposed and discussed. Additionally, catalytic hydroxylation reactions of aromatic alcohols are investigated, which are combined with the condensation of generated quinones in a one-pot reaction to obtain various phenazine derivatives. This is related to the introduction of the Fukui function into tyrosinase chemistry to predict the hydroxylation position of a phenolic substrate with two accessible *ortho*-positions next to the hydroxyl group. Multiple substrates of different classes are screened, including phenols, pyridinol, naphthols, quinolinols and indolols. The applicable substrate scope is compared to the reactivity of the enzyme itself.

benza ligands **anil ligands**

Figure 15: Aromatic hybrid guanidine ligands, in which the guanidine moiety is either bound to the phenyl ring (benza ligands) or bound to the methylene moiety of the spacer (anil ligands).

Chapter 3.2 is devoted to copper halide complexes supported by benza ligands. Various copper(I) and copper(II) complexes are synthesized and characterized. The reactivity of suitable copper(I) complexes towards dioxygen was examined at different temperatures by UV/Vis spectroscopy and cryo-UHR-ESI mass spectrometry. The influence of different additives on the bis(μ-oxido) complex form the main focus of discussion. Moreover, DFT calculations provide deeper insights into the impact of the iodide anion on the molecular orbitals and spectroscopic features of the bis(μ-oxido) species. Also, the achieved room temperature stability of the bis(μ-oxido) species is exploited to evaluate tyrosinase-like oxygenation reactions under mild conditions.

Chapter 3.3 focusses on the impact of varying the amine moieties of the benza ligands on the corresponding copper(I) complexes with weakly coordinating anions. The modification of the amine moiety allows a deeper insight into structural and electronic effects. For this purpose, two new ligands and their copper(I) complexes are synthesized. Suitable copper(I) complexes

are evaluated regarding their reactivity towards dioxygen. The impact of the ligand modifications on the formation and stability of the bis(μ-oxido) complex is discussed. UV/Vis and resonance Raman spectroscopy provide further information regarding the correlation of the spectroscopic properties of the bis(μ-oxido) complex and the donor strength of the ligand system. DFT calculations help to elucidate the impact of the electronic und steric abilities of the bis(μ-oxido) species on a molecular basis. Moreover, the activity of these reactive copper-dioxygen species in catalytic oxygenations is investigated and compared to related systems.

Chapter 3.4 deals with the synthesis and characterization of anil ligands. The reactivity of the corresponding copper(I) complexes towards dioxygen in the presence of coordinating and weakly coordinating anions is investigated by UV/Vis spectroscopy and cryo-UHR-ESI mass spectrometry to evaluate the formed copper-dioxygen species.

3. Results and Discussion

The synthesized hybrid guanidine ligands are bidentate chelate ligands whose second N-donor unit consists of a peralkylated amine. The guanidine and amine moiety are connected by an aromatic spacer, enabling a more rigid ligand backbone, which was inspired by the propylene-bridged hybrid guanidine ligand **53** published in 2009 by Herres-Pawlis, Stack and co-workers (see section 1.3.4).[47] In a benzylene-bridged hybrid guanidine ligand, the guanidine moiety can either be bound to the phenyl ring (benza ligands, see section 3.1-3.3) or to the aliphatic methylene unit (anil ligands, see section 3.4). The aromatically linked guanidine ligands possess peralkylated amine donor units which are varied regarding their steric demand and donor strength.

3.1. TMGbenza- and DMEGbenza-stabilized Copper Complexes with Weakly Coordinating Anions

Parts of this chapter are already published in:

[1] M. Paul, M. Teubner, B. Grimm-Lebsanft, C. Golchert, Y. Meiners, L. Senft, K. Keisers, P. Liebhäuser, T. Rösener, F. Biebl, S. Buchenau, M. Naumova, V. Murzin, R. Krug, A. Hoffmann, J. Pietruszka, I. Ivanović-Burmazović, M. Rübhausen, S. Herres-Pawlis, *Chem. Eur. J.* **2020**, *26*, 7556–7562.

[2] M. Paul, *Master Thesis* **2017**, RWTH Aachen University.

3.1.1. Ligand Synthesis

The permethylated amine moiety of the benza ligands represents the spatially smallest, but strongest amine donor among the ligands used within this study. The guanidine moiety is varied by using tetramethylguanidine (TMG) or dimethylethyleneguanidine (DMEG) groups. The benza ligands are synthesized in a three-step reaction according to Scheme 10. First, 2-nitrobenzyl bromide (**60**) is substituted nucleophilically with a dialkylamine to give *N,N*-dialkyl-(2-nitrophenyl)methanamine. The nitro group is then reduced by hydrazine monohydrate to form the primary amine **62**. Finally, the guanidine synthesis is achieved by condensation of the amine with the Vilsmeier salts chlorido-*N,N,N′,N′*-tetramethylformamidinium chloride or chlorido-*N,N′*-dimethylethyleneformamidinium chloride. A detailed mechanism of the guanidine synthesis is discussed in the introduction (Scheme 9). The guanidines were deprotonated and purified by vacuum distillation to give the free base as light-yellow oils. The overall yield of the ligand synthesis is determined to be 64% for **L1** and 66% for **L2**. The ligands were stored in a glovebox under nitrogen atmosphere due to their moisture- and/or air-sensitivity.

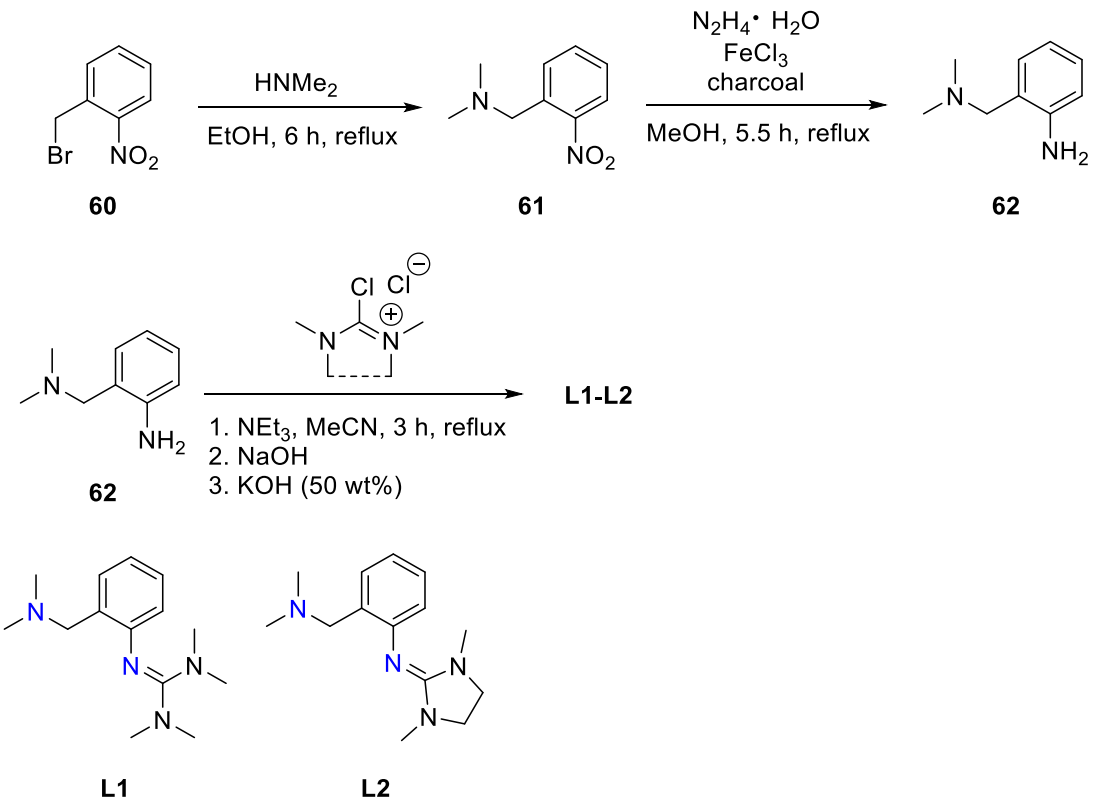

Scheme 10: Synthesis of benza ligands **L1** and **L2**.

The ligands **L1** and **L2** were analyzed by NMR and IR spectroscopy as well as mass spectrometry. The differences of the chemical shifts of **L1** and **L2** in the ^{1}H NMR and ^{13}C{^{1}H} NMR spectra are insignificantly small. An exception is the central carbon atom of the guanidine unit of **L1** and **L2**, which revealed a shift of 4.0 ppm due to the different guanidine moieties TMG and DMEG (**L1**: 159.5 ppm, **L2**: 155.5 ppm). This shift was also observed for related bis(guanidine) ligands.[99,135] The IR spectrum showed the characteristic vibrations of the C=N bond of the guanidine unit at 1606 cm^{-1} for **L1** and 1658 cm^{-1} for **L2**, which are consistent with other guanidine ligands.[47,99,135] It is noteworthy to mention that the hybrid guanidine ligands are prone to protonation, which is identified by precipitation of colorless to light-yellow solids. The free base is restorable by deprotonation with potassium hydroxide and subsequent vacuum distillation. The ligands can be stored in a glovebox under nitrogen or argon atmosphere for several months.

The ligands **L1** and **L2** were crystallized from a saturated pentane solution at -32 °C and analyzed by single crystal X-ray diffraction (Figure 16). Crystallographic details are provided in Table 41 in the appendix and key structural parameters are summarized in Table 1. Both ligands crystallize in the monoclinic space group $P2_1/n$ with Z = 4. The ligand **L1** showed C–N single bond lengths which range from 1.377(2) to 1.383(2) Å, which are closely related to the values of **L2** (1.384(2) to 1.386(2) Å). The C=N bond of **L1** is significantly elongated compared to the C=N double bond of **L2**.

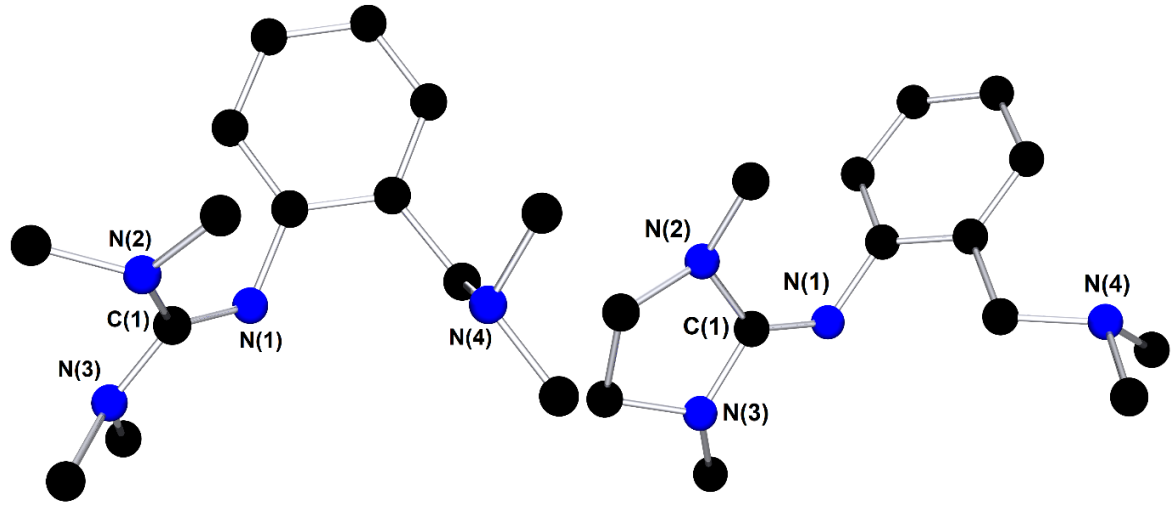

Figure 16: Molecular structures of TMGbenza (**L1**, left) and DMEGbenza (**L2**, right) in the solid state. Hydrogen atoms were omitted for clarity.

The guanidine twist describes the averaged angle between the $C_{imine}N_3$-plane and the $N_{amine}C_3$-planes within the guanidine unit. In **L1**, the guanidine twist amounts to 31°, which is characteristic for TMG-based guanidine ligands.[47,132,133,135] The torsion angle of the heterocyclic guanidine unit in **L2** is with an averaged value of 6° significantly restricted due to the lack of free rotation of the rigid heterocycle. Similarly, the N(2)–C(1)–N(3) angle within the imidazole ring of **L2** (108.3(1)°) is decreased in comparison to the ideal 120° bond angle. The structural parameter ρ allows a statement about the charge delocalization within the guanidine moiety.[127] An ideal C_3-symmetric guanidine has an intrinsic value ρ of 1. The ligands **L1** and **L2** showed values of 0.94 to 0.93, which is ascribed to a clear localization of the guanidine double bond, which is also obvious by the different C–N bond lengths.

Table 1: Selected bond lengths [Å], angles [°] and the structure parameter ρ of **L1** and **L2**.

	L1	**L2**
C(1)–N(1)	1.298(2)	1.286(2)
C(1)–N(2)	1.377(2)	1.384(2)
C(1)–N(3)	1.383(2)	1.386(2)
N(1)–C(1)–N(2)	126.2(1)	131.4(2)
N(1)–C(1)–N(3)	119.5(1)	122.6(1)
N(2)–C(1)–N(3)	114.4(1)	108.3(1)
$\sphericalangle(CN_3;NC_3)_{av}$	30.6	5.8
ρ	0.94	0.93

ρ = 2a/(b+c)[127] with a = C(1)–N(1), b = C(1)–N(2) and c = C(1)–N(3).

3.1.2. Cu(I) Complexes

The synthesis of monochelate copper(I) complexes was achieved by mixing equimolar amounts of a hybrid guanidine ligand and a copper salt $[Cu(MeCN)_4]X$ ($X^- = PF_6^-$, BF_4^-, OTf^-, ClO_4^-) in acetonitrile at room temperature in a glovebox under inert conditions (Scheme 11).

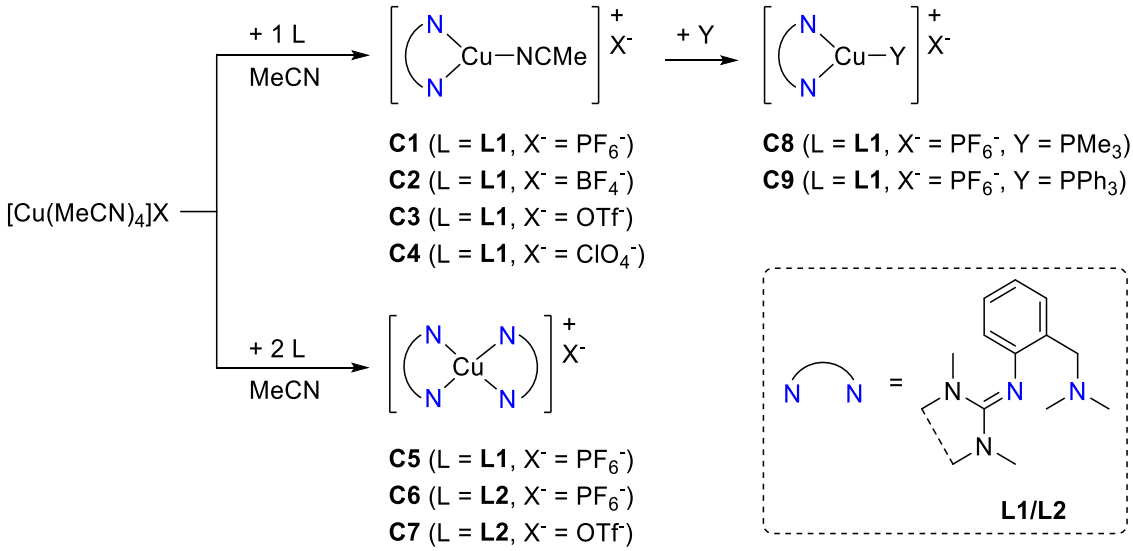

Scheme 11: Synthesis of monochelate and bischelate copper(I) complexes stabilized by the ligands **L1** and **L2**.

The colorless, air- and moisture sensitive complexes **C1**-**C4** must be synthesized highly diluted in acetonitrile in order to suppress the formation of a bischelate complex. The complexes **C1**-**C4** were characterized via NMR, IR, and UV/Vis spectroscopy as well as mass spectrometry. The ^1H and $^{13}C\{^1H\}$ NMR spectra of the complexes **C1**-**C4** are almost identical, showing no influence of the weakly coordinating anions PF_6^-, BF_4^-, OTf^- and ClO_4^- on the complex cation. The UV/Vis spectrum of **C1** displayed an absorption band at 280 nm, originating from π to π* transitions of the aromatic backbone of the ligand system.

Suitable crystals for X-ray diffraction to resolve the molecular structure of the monochelate complexes **C1**-**C4** could not be obtained until now. Instead, the molecular structure of the corresponding bischelate species **C5** was obtained. Similar observations were made by using the ligand **L2**, generating the bischelate complexes **C6**-**C7**. The colorless complexes **C5**-**C7** were crystallized by slow diffusion of pentane into the tetrahydrofuran solution of the complex. The molecular structures of **C5**-**C7** are shown in Figure 17. For **C6** and **C7**, the molecular structures differ in terms of the present weakly coordinating anion. Therefore, the structure of $[Cu(\mathbf{L2})_2]^+$ is exemplified by the complex cation of **C6**. Selected bond lengths and angles of **C5**-**C7** are listed in Table 2 (for crystallographic details of **C5**-**C7**, see Table 43 in the appendix).

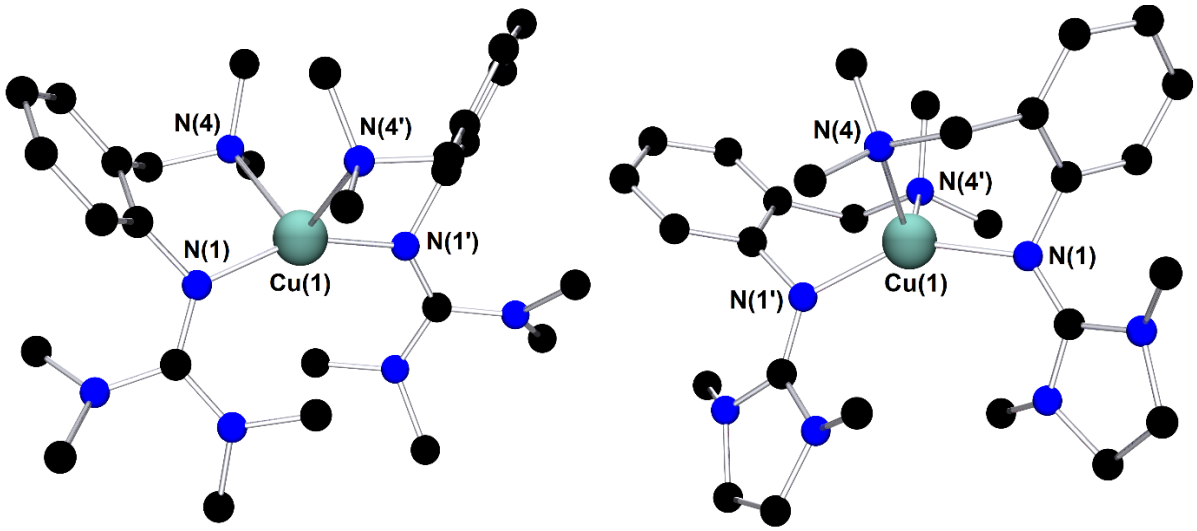

Figure 17: Molecular structures of the complex cation [Cu(**L1**)]$^+$ in crystals of **C5** (left) and the complex cation [Cu(**L2**)]$^+$ in crystals of **C6** and **C7** (right) in the solid state. **C6** and **C7** contain the same complex cation in the presence of different anions PF_6^- and OTf^-. Therefore, only one complex cation is shown. Hydrogen atoms and anions were omitted for clarity.

Table 2: Selected bond lengths [Å], angles [°] and the structure parameters of **C5**-**C7**.

	C5	**C6**	**C7**
Cu(1)–N(1)	1.980(4)	2.049(3)	2.046(5)
Cu(1)–N(4)	2.406(4)	2.214(3)	2.211(6)
Cu(1)–N(1')	1.980(4)	2.049(3)	2.046(5)
Cu(1)–N(4')	2.406(4)	2.214(3)	2.211(6)
N(1)–Cu(1)–N(4)	91.8(2)	94.0(2)	94.5(2)
$\sphericalangle(CN_3;NC_3)_{av}$	35.9	8.1	7.1
ρ	0.97	0.96	0.96
τ_4	0.68	0.70	0.70

ρ = 2a/(b+c)[127] with a = C(1)–N(1), b = C(1)–N(2) and c = C(1)–N(3).

τ_4 = [360°-(α+β)]/141°[149] with α and β being the biggest two $\sphericalangle(CuN_2)$ angles.

Compound **C5** crystallizes in the orthorhombic space group *P*ccn with four asymmetric units in the unit cell, whereas the complexes **C6** and **C7** crystallize in the orthorhombic space group $P2_12_12$ with two complex molecules in the unit cell. All three bischelate complexes adopt a distorted tetrahedral geometry of the central copper atom with τ_4 values between 0.68 and 0.70. The structure parameter describes the coordination geometry of complexes with four donor moieties (τ_4 = 0 square-planar, τ_4 = 1 tetrahedral).[149] All three complexes display shorter Cu–N_{gua} bond lengths compared to the Cu–N_{amine} bond lengths, revealing the stronger N-donor features of the guanidine moiety with respect to the amine moiety. The π-electrons of the guanidine unit are well delocalized in complexes **C5-C7** with ρ values between 0.96 and

0.97. The guanidine twist of the TMG-based complex **C5** is with 35.9° greater than the twist of the DMEG-based complexes **C6** and **C7** with 7.1-8.1°. Obviously, the hybrid guanidine ligands **L1** and **L2** both support the formation of bischelate copper(I) species, which is caused by their limited bite angle and small steric encumbrance, comparable to the propylene derivative TMGdmap.[47,150] Thus, coordinating solvent molecules such as acetonitrile are apparently not strong enough to stabilize the monochelate copper(I) species in the solid state.

Aiming to avoid the formation of bischelate complexes, the free coordination site was saturated with a co-ligand to stabilize the monochelate copper(I) species. Suitable co-ligands are organophosphorus compounds (e.g. trimethyl phosphine, triphenyl phosphine). Phosphorus ligands feature many properties similar to nitrogen ligands.[151,152] The phosphine-stabilized copper(I) complexes **C8**-**C9** were synthesized by adding equimolar amounts of the co-ligand to a solution of the copper(I) complex **C1** in acetonitrile and isolated as colorless solids in high yields (Scheme 12). The resulting complexes **C8** and **C9** were analyzed by NMR and IR spectroscopy as well as mass spectrometry.

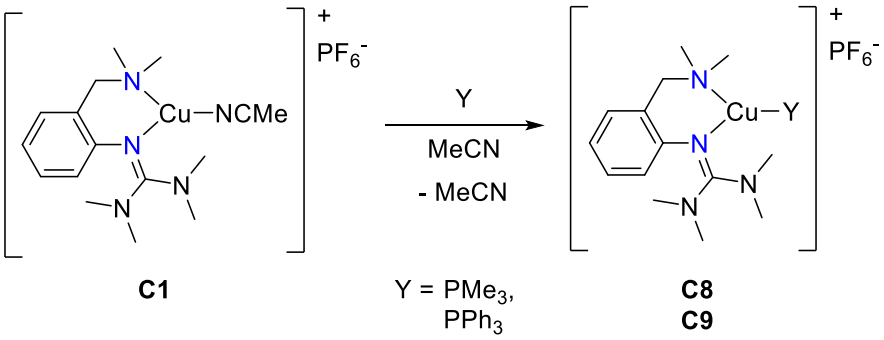

Scheme 12: Synthesis of monochelate copper(I) complexes with a phosphine as co-ligand.

Single crystals, suitable for X-ray diffraction, were obtained by slow diffusion of pentane into the tetrahydrofuran solution of the colorless complexes **C8**-**C9**. The compound **C8** crystallizes in the orthorhombic space group *P*bca with eight molecules in the asymmetric unit, whereas the complex **C9** crystallizes in the triclinic space group $P\bar{1}$ with two complex molecules in the unit cell. The molecular structures of **C8** and **C9** are depicted in Figure 18 and selected bond lengths and angles of both complexes are summarized in Table 3 (for crystallographic details of **C8** and **C9** see Table 44 in the appendix). The central copper atom of the complexes **C8** and **C9** is coordinated in a distorted trigonal-planar fashion by the hybrid guanidine ligand **L1** and a phosphine as third donor. The Cu–N_{gua} bond lengths are considerably shorter than the Cu–N_{amine} bond lengths, underlining the superior N-donor strength of the guanidine moiety compared to the amine moiety. The phosphine donor function is bound to the central copper atom with bond lengths between 2.160(1) Å and 2.176(1) Å, displaying the strong electron-donating abilities of aryl and alkyl phosphines to the copper(I) center caused by backbonding of the metal in low oxidation states.[151–153] Both complexes **C8** and **C9** depict an approximately

Y-shaped geometry with N(1)–Cu(1)–P(1) bond angles of 136.7(1)-137.3(1)°, revealing a deviation from the ideal 120° angle due to the restricted bite angle of **L1** (97-98°). The guanidine twist is with 28-30° comparable to other TMG-based guanidine copper complexes.[47,135] The structure parameter ρ of **C8** and **C9** evidences a well delocalized double bond within the guanidine unit, which is significantly more delocalized compared to the bischelate complexes **C5-C7** (Table 2) and which is similar to other **L1**-stabilized monochelate complexes **C10-C12** (Table 16).

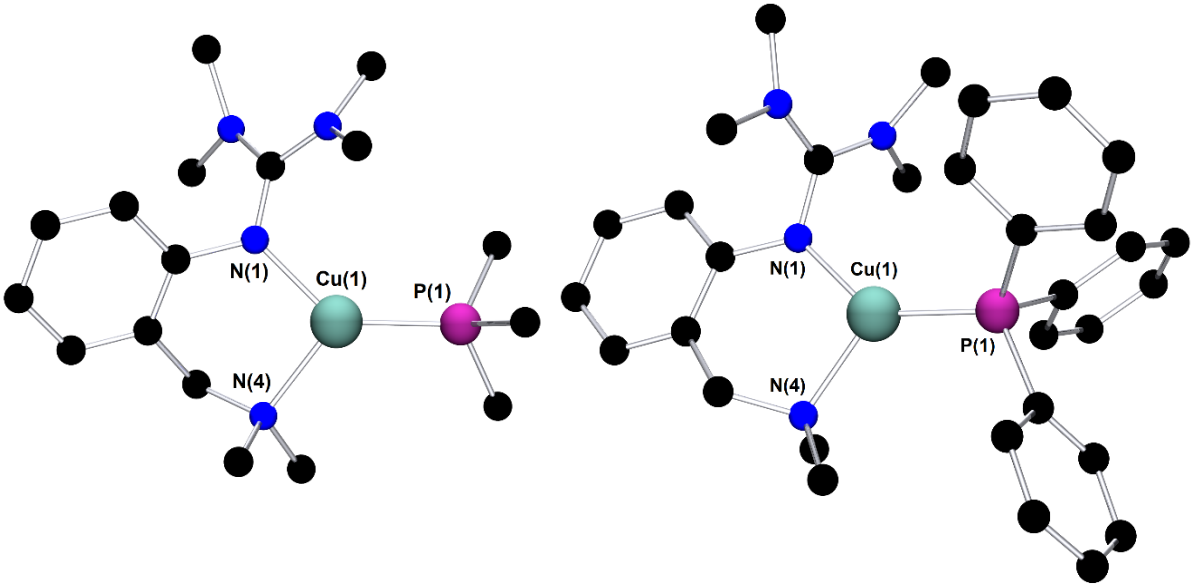

Figure 18: Molecular structures of the complex cation $[Cu(\mathbf{L1})(PMe_3)]^+$ of **C8** (left) and the complex cation $[Cu(\mathbf{L1})(PPh_3)]^+$ of **C9** (right) in the solid state. Hydrogen atoms and anions were omitted for clarity.

Table 3: Selected bond lengths [Å], angles [°] and the structure parameter ρ of **C8** and **C9**.

	C8	**C9**
Cu(1)–N(1)	1.988(2)	1.963(1)
Cu(1)–N(4)	2.095(2)	2.041(1)
Cu(1)–P(1)	2.176(1)	2.160(1)
N(1)–Cu(1)–N(4)	97.1(1)	97.9(1)
N(1)–Cu(1)–P(1)	136.7(1)	137.3(1)
N(4)–Cu(1)–P(1)	125.0(1)	124.8(1)
$\sphericalangle(CN_3;NC_3)_{av}$	29.7	27.7
ρ	0.98	1.00

ρ = 2a/(b+c)[127] with a = C(1)–N(1), b = C(1)–N(2) and c = C(1)–N(3).

3.1.3. Dioxygen Activation

While the oxygenation of tetradentate tris(guanidine)-supported copper(I) complexes results in the formation of end-on superoxido copper(II) species, the oxygenation of copper(I) complexes stabilized by bidentate hybrid guanidine and bis(guanidine) ligands leads to the formation of copper-dioxygen species with a bis(μ-oxido) dicopper(III) core due to the high basicity and strong N-donor ability of the guanidine moiety (see section 1.3.4).[47,64,99,122,124,128,132,133,135,150] Characterization of these copper-dioxygen species with different spectroscopic methods allows an evaluation of these complexes as biomimetic tyrosinase models.[10,11] The mechanism of dioxygen activation by copper(I) complexes is described in section 1.2.1. Bidentate hybrid guanidine ligands have already proven their suitability for the stabilization of reactive copper-dioxygen motifs at low temperatures.[47,150] The aromatic hybrid guanidine ligands TMGbenza (**L1**) and DMEGbenza (**L2**) were successfully tested in the oxygenation reactions of the corresponding copper(I) complexes in the presence of the weakly coordinating anions PF_6^- and OTf^- as a part of the master thesis.[154] Ligand **L1** and **L2** revealed a comparable behavior regarding the stabilization of bis(μ-oxido) dicopper(III) complexes, so that the following dioxygen activation measurements are focused on ligand **L1**.

The oxygenation reactions of the complexes **C1-C4** employed besides the anions PF_6^- and OTf^- further weakly coordinating anions BF_4^- and ClO_4^- to investigate the influence of the counterion on the bis(μ-oxido) species. The synthesis of the bis(μ-oxido) species [**O1**]X_2 (X^- = PF_6^-, BF_4^-, OTf^-, ClO_4^-) were performed at –90 °C in tetrahydrofuran by bubbling dioxygen through a precooled tetrahydrofuran solution and subsequently injecting the acetonitrile solution of the copper(I) species **C1**-**C4** into the oxygenated tetrahydrofuran (Scheme 13, Figure 20 and Table 4).

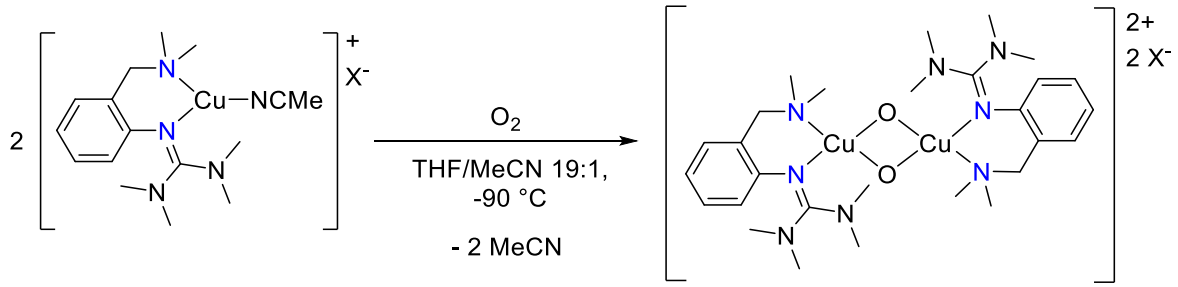

Scheme 13: Oxygenation of copper(I) complexes **C1-C4**.

The oxygenation of the monochelate complex **C1** led to an immediate color change to green (khaki). The formation of the bis(μ-oxido) complex [**O1**]$(PF_6)_2$ was followed by UV/Vis spectroscopy (Figure 19). Compound [**O1**]$(PF_6)_2$ was formed within three minutes and exhibited ligand-to-metal charge transfer bands at 280 nm (40000 M^{-1} cm^{-1}) and 390 nm (21000 M^{-1} cm^{-1}) in the UV/Vis spectrum, which are characteristic for bis(μ-oxido) dicopper(III) complexes.[10,11] The

UV/Vis features originate from the transition of the oxygen in-plane π_{σ^*} and σ* orbital to the copper d_{xy} orbital.[9–11] The high extinction at 280 nm results from an overlap of the in-plane π_{σ^*} → d_{xy} charge transfer transition and π → π* transition of the aromatic backbone of **L1**. The incorporated dioxygen of [**O1**](PF$_6$)$_2$ was resistant to cycles of evacuation and purging with nitrogen.

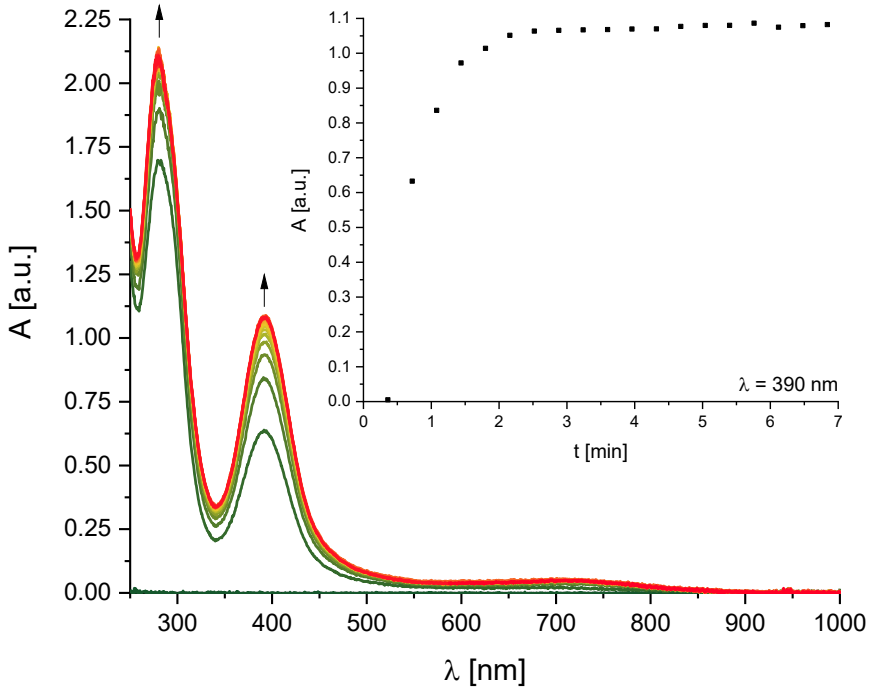

Figure 19: UV/Vis spectra of the formation of the bis(μ-oxido) complex [**O1**](PF$_6$)$_2$ (0.5 mM) in tetrahydrofuran at –90 °C (Inset: time-resolved formation of [**O1**](PF$_6$)$_2$ monitored at 390 nm).

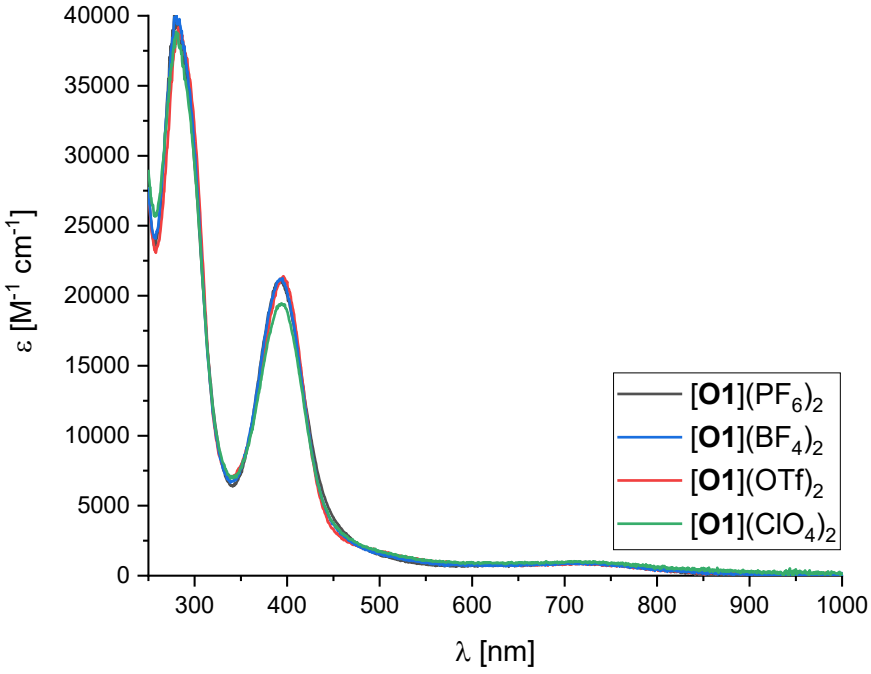

Figure 20: UV/Vis spectra of the bis(μ-oxido) complexes [**O1**](X)$_2$ (X$^-$ = PF$_6^-$, BF$_4^-$, OTf$^-$, ClO$_4^-$; 0.5 mM) in tetrahydrofuran at –90 °C.

The complex [**O1**]$(PF_6)_2$ was also formed at –80 °C, showing a slightly less intense absorption band at 390 nm (-5%), which was assigned to the competitive thermal decay of [**O1**]$(PF_6)_2$ while forming. The temperature sensitivity of [**O1**]$(PF_6)_2$ was demonstrated by a significant loss in quantity of [**O1**]$(PF_6)_2$ (-24%) upon formation at –74 °C. Similar bis(μ-oxido) species [**O1**]X_2 (X^- = BF_4^-, OTf^-, ClO_4^-) were formed by the oxygenation of the complexes **C2-C4**, which showed very similar UV/Vis features (Table 4).

Table 4: UV/Vis features of [**O1**]$(X)_2$ (X^- = PF_6^-, BF_4^-, OTf^-, ClO_4^-) in tetrahydrofuran at –90 °C.

X	λ [nm]	ε [M^{-1} cm^{-1}]	λ [nm]	ε [M^{-1} cm^{-1}]	color
PF_6	280	40000	392	21000	green
BF_4	280	40000	392	21000	green
ClO_4	281	38000	393	19000	green
OTf	284	39000	396	21000	orange

The formation of [**O1**]$(PF_6)_2$ was quantified by the spectrophotometric titration of [**O1**]$(PF_6)_2$ with ferrocene monocarboxylic acid (FcCOOH), which provides one proton and one electron.[47] The bis(μ-oxido) complex [**O1**]$(PF_6)_2$ is fully reduced by two equivalents of FcCOOH to generate the corresponding bis(μ-hydroxido) dicopper(II) species (Scheme 14).

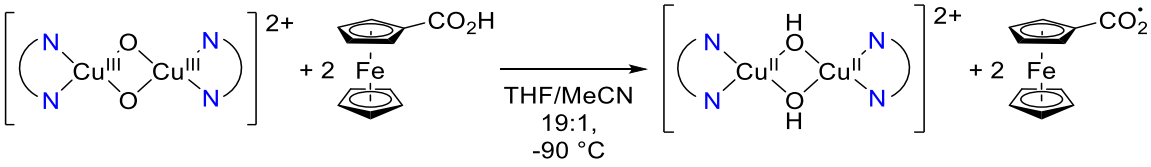

Scheme 14: Spectrophotometric titration of [**O1**]$(PF_6)_2$ with ferrocene monocarboxylic acid.

The complex [**O1**]$(PF_6)_2$ was generated at –90 °C in tetrahydrofuran and titrated with FcCOOH in 0.2 equivalent steps after the removal of remaining dioxygen. The addition of the first aliquot of FcCOOH resulted in the decay of the absorption band of [**O1**]$(PF_6)_2$ at 390 nm, which was followed by UV/Vis spectroscopy (Figure 21). After the stabilization of the optical spectrum, the next aliquot of FcCOOH was added. The titration experiment revealed a nearly linear dependency of the absorbance of [**O1**]$(PF_6)_2$ at 390 nm and the added amount of the titrant. The bis(μ-oxido) complex [**O1**]$(PF_6)_2$ was formed in >90% quantity, as more than 1.8 equivalents of FcCOOH were required under anaerobic reaction conditions.

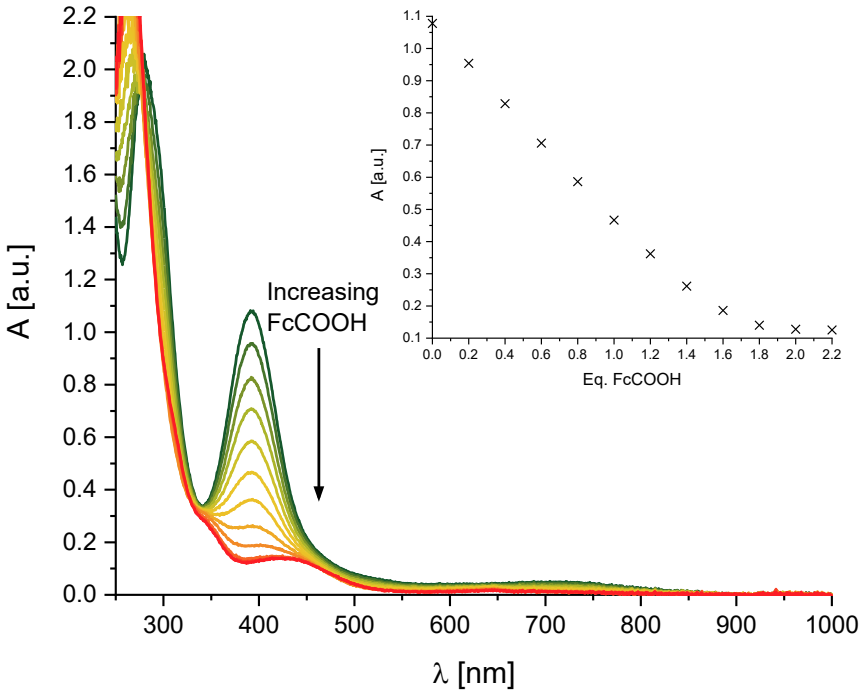

Figure 21: UV/Vis spectra of the titration of [**O1**](PF$_6$)$_2$ (0.5 mM) with ferrocene monocarboxylic acid in tetrahydrofuran at –90 °C (inset: absorbance of [**O1**](PF$_6$)$_2$ during the titration of [**O1**](PF$_6$)$_2$ with FcCOOH (0 to 2.2 equivalents) monitored at 390 nm).

The bis(μ-oxido) complex [**O1**](PF$_6$)$_2$ was further characterized via resonance Raman spectroscopy in a tetrahydrofuran/acetonitrile mixture at low temperatures below –90 °C in cooperation with the group of Prof. Dr. Michael Rübhausen at the CFEL in Hamburg (Figure 22).

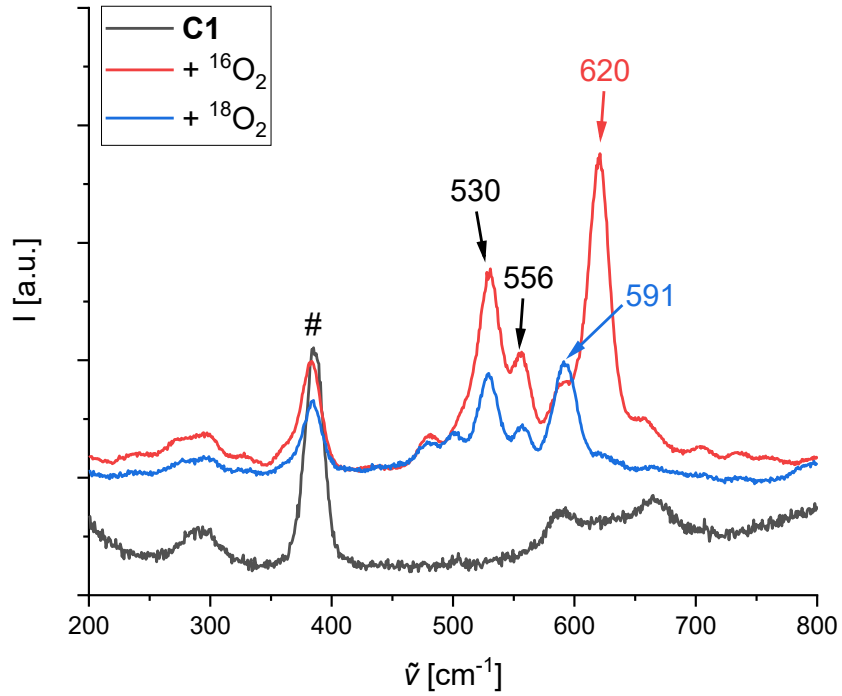

Figure 22: Resonance Raman spectra of [**O1**](PF$_6$)$_2$ in tetrahydrofuran with excitation at 420 nm (black: **C1**, red: $^{16}O_2$, blue: $^{18}O_2$, #: solvent). The resonance Raman spectrum was recorded by the group of Prof. Dr. Michael Rübhausen at the CFEL in Hamburg.

The resonance Raman spectrum of [**O1**](PF$_6$)$_2$ displays a characteristic vibration at 620 cm^{-1} which was attributed to the symmetric expansion of the Cu$_2$O$_2$ core. This breathing mode is typically observed in bis(μ-oxido) dicopper(III) complexes.[9–11] $^{16}O_2/^{18}O_2$ isotope exchange measurements revealed a shift of 29 cm^{-1} to 591 cm^{-1}, which is in good agreement with theoretical studies (Table 8). One additional vibration found at 530 cm^{-1} results from the Cu–N_{amine} vibration and was confirmed by the calculated Raman modes. DFT calculations predicted the breathing mode at 636 cm^{-1}, which shifts similarly by 29 cm^{-1} to 607 cm^{-1} upon isotope exchange with $^{18}O_2$.

In the next step, Cu K-edge X-ray absorption spectroscopy (XAS) provides deeper insights into the electronic structure of [**O1**](PF$_6$)$_2$ as the molecular structure of bis(μ-oxido) dicopper(III) complexes is difficult to access via crystallization due to their temperature sensitivity. XAS measurements were performed in cooperation with the group of Prof. Dr. Michael Rübhausen at the CFEL in Hamburg. X-ray absorption near-edge spectroscopy (XANES) provides details about the oxidation state and the coordination sphere of the copper centers (Figure 23).

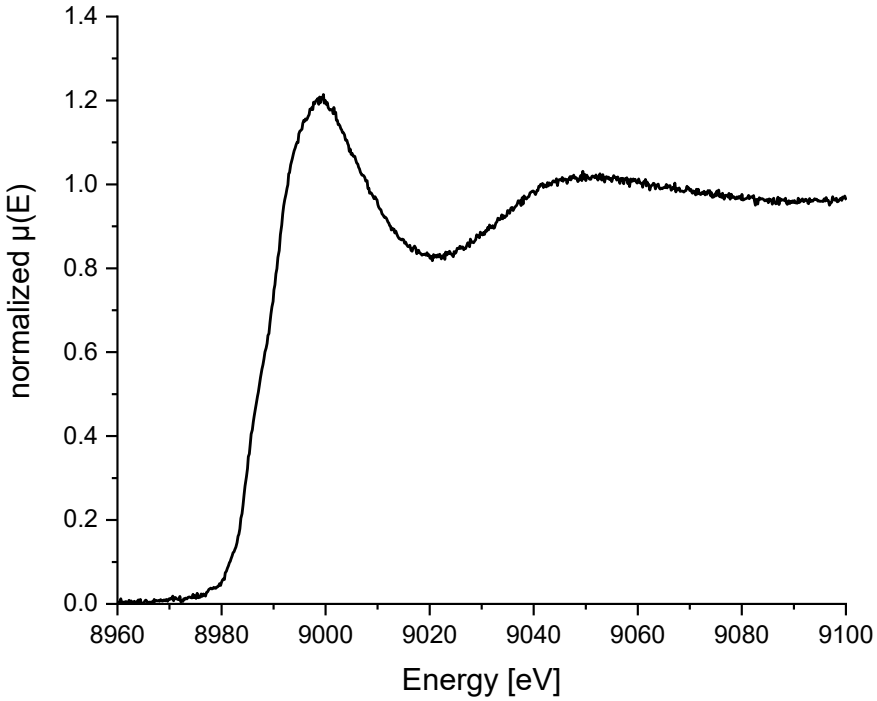

Figure 23: Normalized Cu K-edge XANES of [**O1**](PF$_6$)$_2$. Integration time of the spectrum was 300 s. The XANES spectrum was recorded by the group of Prof. Dr. Michael Rübhausen at the CFEL in Hamburg.

The measured Cu K-edge (defined as 50% of the edge jump) for complex [**O1**](PF$_6$)$_2$ is found at 8987.0 eV, which is indicative for a 1s → 3d transition within a Cu(III) center.[9–11] The shoulders at 8987.3 eV and 8992.0 eV in the rising edge of [**O1**](PF$_6$)$_2$ reveal typical 1s → 4p and simultaneous shakedown transitions, which were also reported for [Cu(III)$_2$(μ-O)$_2$(L_{ME})$_2$]$^{2+}$ by Hodgson and co-workers.[155]

The extended X-ray absorption fine structure (EXAFS) analysis provides information about the distances to neighboring atoms. The phase-corrected Cu K-edge Fourier transformed EXAFS spectrum of [**O1**](PF$_6$)$_2$ including the k^3-weighted Cu K-edge EXAFS fit (inset) is shown in Figure 24. Selected structural parameters are listed in Table 5.

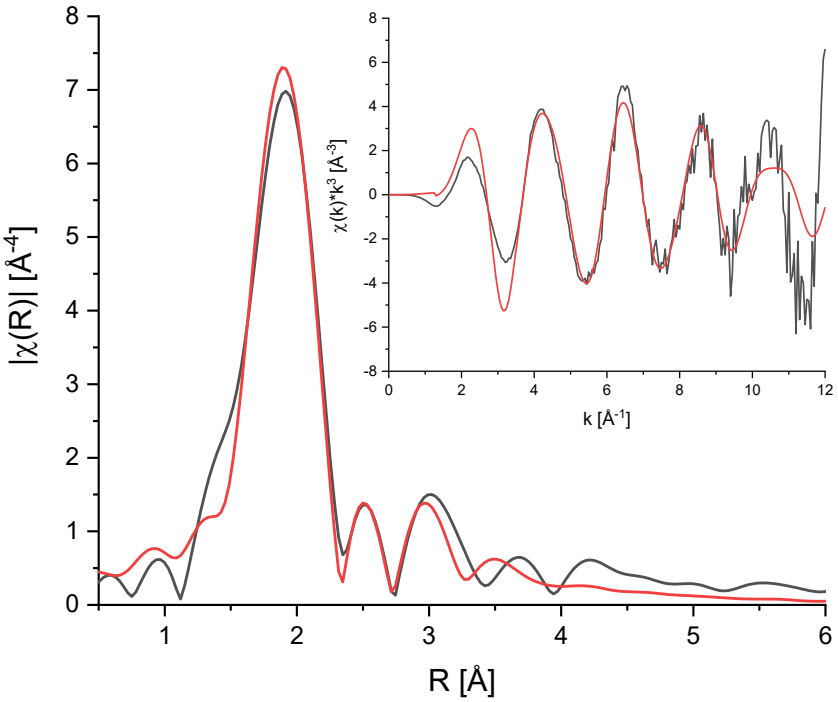

Figure 24: Phase-corrected Cu K-edge Fourier transformed EXAFS of [**O1**](PF$_6$)$_2$ (Inset: k^3-weighted Cu K-edge EXAFS fit; black: experimental, red: calculated fit). The spectra were recorded by the group of Prof. Dr. Michael Rübhausen at the CFEL in Hamburg.

Table 5: Cu–X distances of [**O1**](PF$_6$)$_2$ from the DFT model (R_{eff}) and the best fit results (R) from Artemis.[156] Calculations and fits were performed by the group of Prof. Dr. Michael Rübhausen at the CFEL in Hamburg.

X	**N**	**S_0^2**	**σ^2**	**ΔE_0**	**Δr**	**R_{eff}**	**R**
O	2.00000	0.94000	0.00014	6.38400	0.09116	1.80190	1.89306
N	1.00000	0.94000	0.00014	6.38400	0.09682	1.91380	2.01062
N	1.00000	0.94000	0.00014	6.38400	0.09939	1.96460	2.06399
Cu	1.00000	0.94000	0.01342	6.38400	-0.08663	2.75020	2.66357
C	1.00000	0.94000	0.00014	6.38400	0.06966	2.70640	2.77606
C	1.00000	0.94000	0.00014	6.38400	0.07117	2.76530	2.83647
C	1.00000	0.94000	0.00014	6.38400	0.07349	2.85550	2.92899
C	1.00000	0.94000	0.00014	6.38400	0.07433	2.88790	2.96223
C	1.00000	0.94000	0.00014	6.38400	0.07572	2.94190	3.01762

N = Number of neighbor atoms; S_0^2 = amplitude; σ^2 = Debye-Waller-like factor to account for disorder; ΔE_0 = deviation to E_0; Δr = R-R_{eff}.

From the best fit, which describes the data with the smallest χ^2, an averaged Cu–O distance of 1.89 Å and Cu–N distances of 2.01 Å and 2.06 Å were determined. A short Cu···Cu distance of 2.66 Å is consistent with other bis(μ-oxido) dicopper(III) complexes.[9–11] The occurrence of a μ-η^2:η^2-Cu_2O_2 core can be excluded as their characteristic Cu···Cu distance of 3.6 Å was not observed.[9–11] Experimental data derived from EXAFS analysis are in good accordance with Cu–X distances calculated from the DFT model.

Theoretical analyses of [**O1**]$(PF_6)_2$ were performed by Dr. Alexander Hoffmann to evaluate the structure of the theoretical Cu_2O_2 species. Calculations are based on the hybrid meta GGA functional TPSSh[157–159] combined with the triple-valence basis set def2-TZVP[160–163] and empirical dispersion correction with Becke-Johnson damping GD3BJ.[164–167] The calculated energies, geometric and spectroscopic parameters of the theoretical Cu_2O_2 species are listed in Table 6, Table 7 and Table 8.

Table 6: Energies of the theoretical Cu_2O_2 species (TPSSh/def2-TZVP, GD3BJ, THF-PCM).

	S^2	**ΔE [kcal mol^{-1}]**
Bis(μ-oxido)		0.00
Peroxido		11.61
Peroxido BS	0.41	10.12

BS = Broken Symmetry

Table 7: Geometric parameters of the theoretical Cu_2O_2 species (TPSSh/def2-TZVP, GD3BJ, THF-PCM). The structure of the bis(μ-oxido) species is illustrated in Figure 25. Bond lengths to the same copper atom are separated by comma, otherwise by semicolon.

	Cu···Cu [Å]	**Cu–O [Å]**	**O–O [Å]**	**Cu–N_{gua} [Å]**	**Cu–N_{amine} [Å]**
Bis(μ-oxido)	2.750	1.800, 1.806; 1.801, 1.804	2.331	1.914; 1.915	1.963; 1.965
Peroxido	3.527	1.900, 1.921; 1.900, 1.928	1.473	1.932; 1.931	1.998; 2.000
Peroxido BS	3.542	1.938, 1.905; 1.909, 1.931	1.487	1.932; 1.932	2.000; 1.997

BS = Broken Symmetry

The DFT calculations predict a thermodynamically favored bis(μ-oxido) species over the related side-on peroxido isomer by 10 kcal mol^{-1} in free energy, which is consistent with the obtained experimental data.

Table 8: Spectroscopic parameters of the theoretical bis(μ-oxido) species [**O1**]$^{2+}$ (TPSSh/def2-TZVP, GD3BJ, THF-PCM).

	$\tilde{\nu}$ ($^{16}O_2$) [cm^{-1}]	$\tilde{\nu}$ ($^{18}O_2$) [cm^{-1}]	$\tilde{\nu}$ (N_{amine}–Cu in $Cu_2{}^{16}O_2$) [cm^{-1}]	$\tilde{\nu}$ (N_{amine}–Cu in $Cu_2{}^{18}O_2$) [cm^{-1}]
Raman	636	607	517	516
IR	681	652	512	511

The DFT optimized structure of the theoretical bis(μ-oxido) complex of [**O1**]$^{2+}$ is illustrated in Figure 25. The calculated bond lengths are in good agreement with the experimentally obtained data. The Cu–O bond lengths and the Cu···Cu distance are characteristic for bis(μ-oxido) dicopper(III) complexes and similar to guanidine-stabilized systems reported previously.[99,135] The Cu–N bond lengths of the guanidine donor unit are significantly shorter than the Cu–N bond lengths of the amine donor moiety, revealing the higher donor strength of the guanidine with respect to the amine as expected.

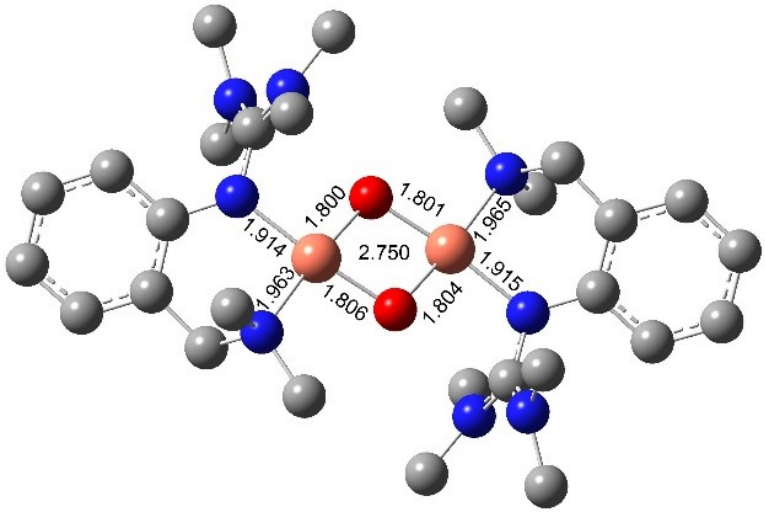

Figure 25: DFT model of [**O1**]$^{2+}$ (TPSSh/def2-TZVP, THF-PCM), selected bond lengths [Å] and a Cu···Cu vector [Å].

The copper-dioxygen stoichiometry of [**O1**]$(PF_6)_2$ was evaluated by using cryo-UHR-ESI mass spectrometry (Figure 26). The mass spectra were recorded in cooperation with the group of Prof. Dr. Ivana Ivanović-Burmazović at the University of Erlangen-Nürnberg. Figure 26 illustrates the isotopic pattern and the corresponding m/z values of the monocationic species [**O1**]$(PF_6)^+$ with a Cu–O_2 ratio of 2:1. The experimental values agree well with the calculated m/z values. Similar results were obtained for the bis(μ-oxido) complex [**O1**]$(OTf)_2$ (Figure 68 in the appendix).

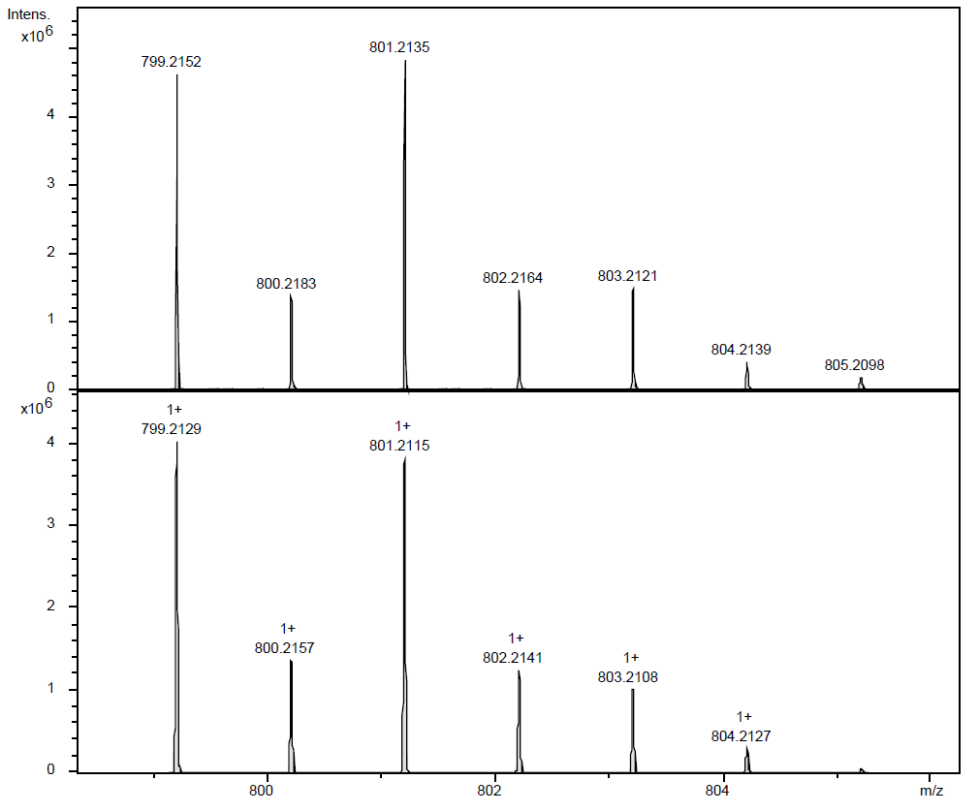

Figure 26: Cryo-UHR-ESI mass spectrometry of [**O1**](PF$_6$)$^+$ in tetrahydrofuran at –80 °C (top: experimental, bottom: calculated spectra). This mass spectrum was recorded by the group of Prof. Dr. Ivana Ivanović-Burmazović at the University of Erlangen-Nürnberg.

The stability of bis(μ-oxido) complex [**O1**](PF$_6$)$_2$ was investigated via UV/Vis spectroscopy. Although the typically used formation temperature of different copper-dioxygen species is –80 °C[9–11], a temperature of –90 °C was required to achieve the quantitative formation of complex [**O1**](PF$_6$)$_2$. At this temperature, the bis(μ-oxido) complex [**O1**](PF$_6$)$_2$ was stable for at least 90 minutes. Increasing the temperature to –80 °C reduced the stability to less than 20 minutes. A significantly lower stability of [**O1**](PF$_6$)$_2$ was observed at –74 °C, which underlines the temperature sensitivity of the bis(μ-oxido) complex. The decay of the absorption band of [**O1**](PF$_6$)$_2$ at 390 nm followed first-order kinetics (Figure 27). Thermal decay parameters k_1 were determined via an exponential fit at the chosen temperature (Table 9). The half-life $t_{1/2}$ of the complex is defined as $\frac{ln\,2}{k_1}$ and was calculated for both temperatures. A small change of the temperature from –80 °C to –74 °C resulted in a more than ten times faster decomposition of [**O1**](PF$_6$)$_2$. Thus, the temperature control during experiments is crucial for the reliability of the results.

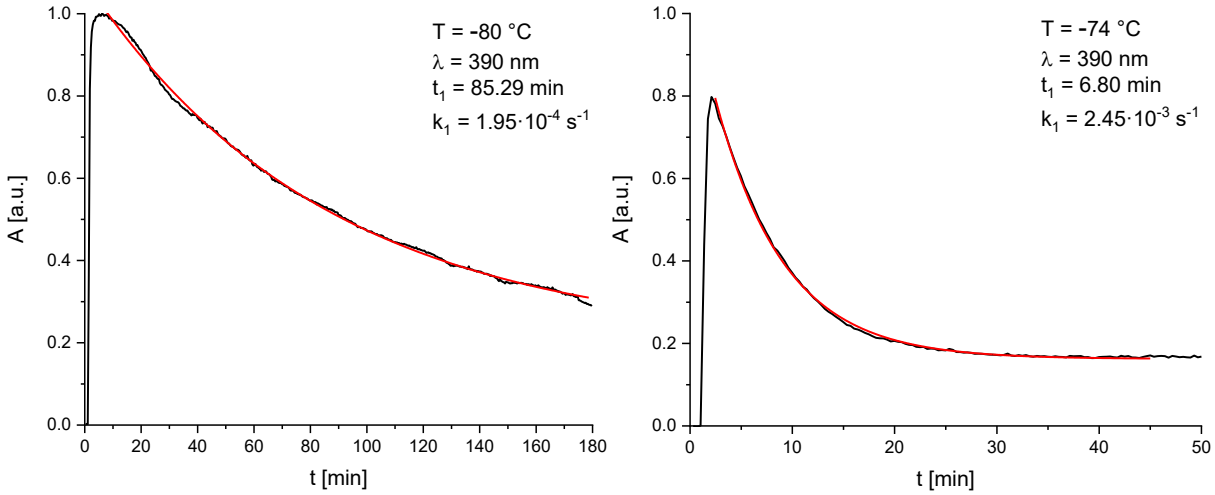

Figure 27: Thermal decay of [**O1**]$(PF_6)_2$ in tetrahydrofuran at –80 °C (left) and –74 °C (right) monitored at 390 nm (black: experimental, red: calculated fit).

Table 9: Thermal decay parameters of [**O1**]$(PF_6)_2$ in tetrahydrofuran at –80 °C and –74 °C.

T	**k_1**	**$t_{1/2}$**
[°C]	**[s^{-1}]**	**[min]**
–80	$1.95 \cdot 10^{-4}$	59.1
–74	$2.45 \cdot 10^{-3}$	4.7

The bis(μ-oxido) complex [**O1**]$(PF_6)_2$ displayed a certain stability towards other solvents such as tetrahydropyran, methylene chloride and methanol. But these solvents are less suitable for experiments than tetrahydrofuran, as the complex was resistant to tetrahydrofuran at the longest, which was also reported for other hybrid guanidine-stabilized Cu_2O_2 species.[47,150] The bis(μ-oxido) species [**O1**]$(PF_6)_2$ showed a moderate stability towards bases such as triethylamine, which is important for the oxygenation reactions of exogenous substrates as presented in section 3.1.4.

In the next step, the observed thermal sensitivity of the bis(μ-oxido) complex [**O1**]$(PF_6)_2$ led to the investigation of possible decomposition products. Mostly, decomposition products are identified to be the thermodynamically stable bis(μ-hydroxido) dicopper(II) species.[47,56,66,168–174] They often result from the intramolecular hydroxylation of C–H bonds in α- or β-position to N-donor groups.[175–179] Concomitant stoichiometric formation of the bis(μ-alkoxido) dicopper(II) species was also reported, implying a μ-alkoxido μ-hydroxido dicopper(II) complex as reaction intermediate, as proposed by mechanistic studies on the intramolecular hydroxylation of the supporting ligand by Itoh, Tolman and co-workers.[175,176,180] The stoichiometric combination of bis(μ-hydroxido) dicopper(II) species and bis(μ-alkoxido) dicopper(II) species was observed previously, which were stabilized by bis(guanidine) ligands.[132,181] Only a few examples of a μ-alkoxido μ-hydroxido copper(II) complex were reported by Karlin, Ghosh, Pérez and

co-workers so far.[61,182,183] The decomposition products of the bis(μ-oxido) complex [**O1**](PF$_6$)$_2$ were analyzed by warming up of the reaction solution to room temperature and crystallization under ambient conditions to evaluate the possible mechanisms of the decomposition (Scheme 15). Single crystals, suitable for X-ray diffraction, were obtained by slow diffusion of diethyl ether into a saturated acetonitrile solution of the mixture or by slow diffusion of acetonitrile into toluene. After a few days, the crystallization of blue and light-yellow blocks in a greenish solution was observed. The blue blocks showed the molecular structure of a dicationic μ-alkoxido μ-hydroxido tricopper(II) complex [**H1**](PF$_6$)$_2$, whereas the light-yellow blocks were identified as the protonated ligand [**L1**H$_2$]$^{2+}$. Same observations were made by the decomposition of [**O1**](BF$_4$)$_2$ leading to the μ-alkoxido μ-hydroxido tricopper(II) complex [**H1**](BF$_4$)$_2$ and the protonated ligand [**L1**H$_2$]$^{2+}$.

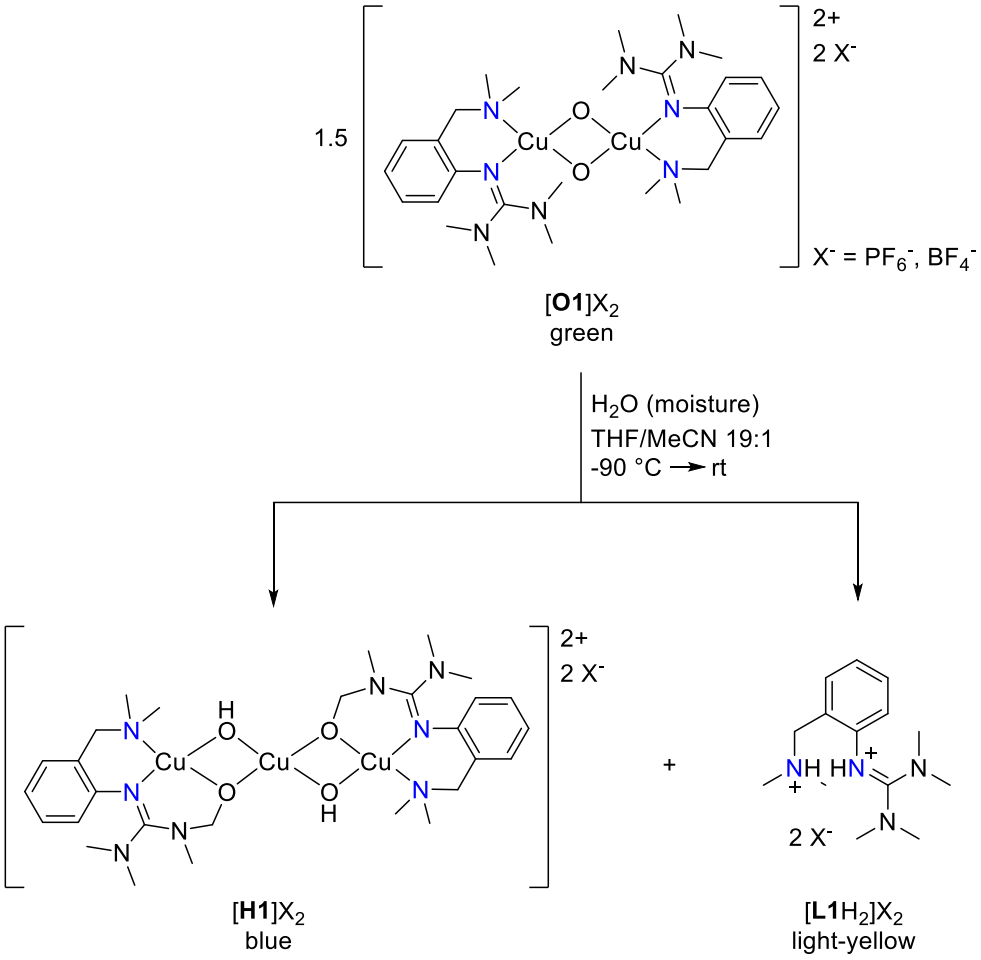

Scheme 15: Decomposition of [**O1**]X$_2$ and formation of tricopper μ-alkoxido μ-hydroxido complex [**H1**]X$_2$ and protonated ligand [**L1**H$_2$]X$_2$ (X$^-$ = PF$_6^-$, BF$_4^-$).

The molecular structures of [**H1**](PF$_6$)$_2$ and [**H1**](BF$_4$)$_2$ are displayed in Figure 28. Selected interatomic distances, bond lengths and angles are summarized in Table 10. Crystallographic details are provided in Table 49 in the appendix. The compound [**H1**](PF$_6$)$_2$ crystallizes in the monoclinic space group $P2_1/n$ with two molecules in the asymmetric unit, whereas the complex [**H1**](BF$_4$)$_2$ crystallizes in the triclinic space group $P\bar{1}$ with one complex molecule in the unit cell.

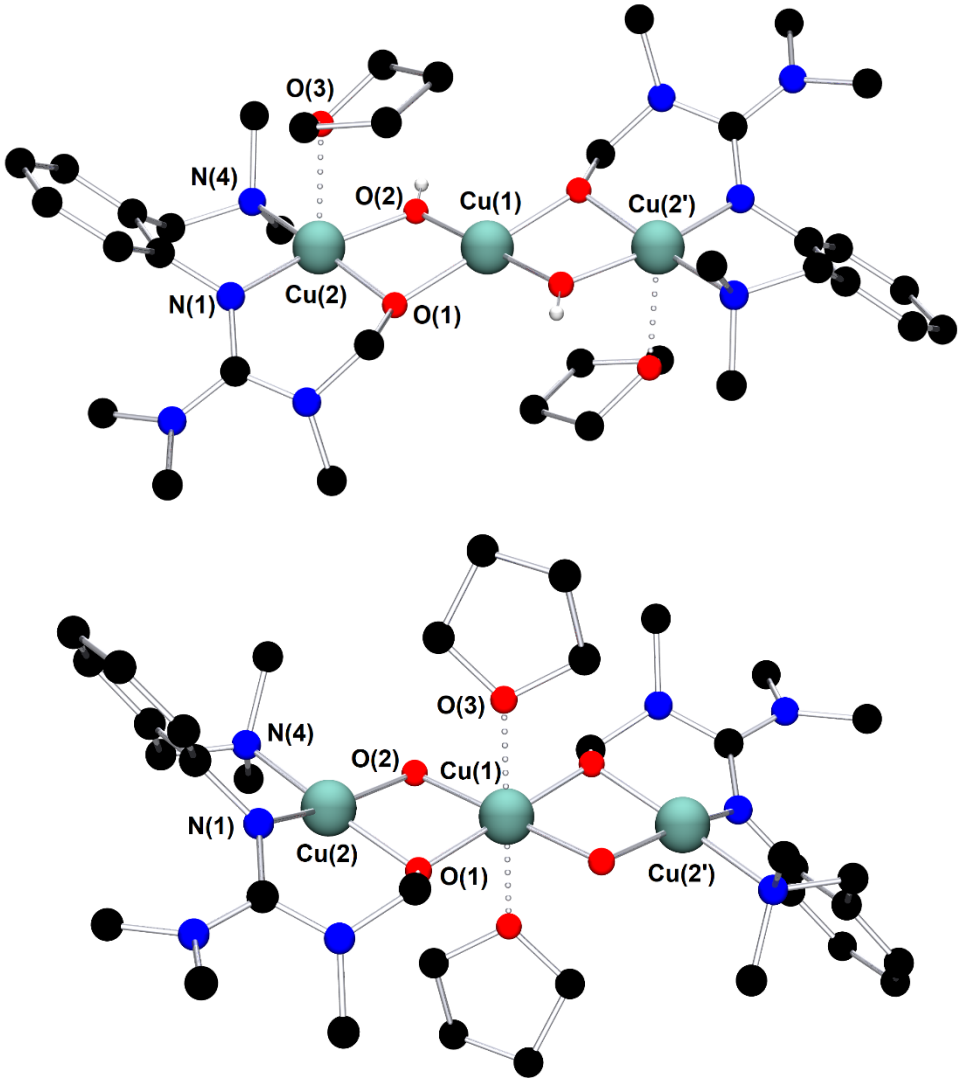

Figure 28: Molecular structures of the complex cation $[\mathbf{H1}]^{2+}$ in crystals of $[\mathbf{H1}](PF_6)_2$ (top) and $[\mathbf{H1}]^{2+}$ in crystals of $[\mathbf{H1}](BF_4)_2$ (bottom) in the solid state. The anions and hydrogen atoms, except for hydroxy moieties if available, were omitted for clarity. It was not possible to locate the hydrogen atoms of the hydroxido groups in $[\mathbf{H1}](BF_4)_2$.

The Cu···Cu distance of $[\mathbf{H1}](PF_6)_2$ is with 2.953(1) Å slightly elongated compared to a distance of 2.919(2) Å within complex $[\mathbf{H1}](BF_4)_2$. The central copper atom Cu(1) resides on a crystallographically imposed inversion center. In both complexes, each copper ion is coordinated in a distorted square-planar fashion. The averaged Cu–O bond length of the Cu_3O_4 core of $[\mathbf{H1}](PF_6)_2$ is with 1.92 Å slightly shorter compared to that in $[\mathbf{H1}](BF_4)_2$, which is 1.93 Å. Both complexes contain shorter averaged Cu–O bond lengths than a μ-phenolato μ-hydroxido dicopper(II) complex reported by Karlin and co-workers.[61] This trend correlates to a stronger interaction of additional tetrahydrofuran molecules with $[\mathbf{H1}](BF_4)_2$ with respect to $[\mathbf{H1}](PF_6)_2$, as the Cu–O(3) bond length is significantly shorter in $[\mathbf{H1}](BF_4)_2$ than in $[\mathbf{H1}](PF_6)_2$. Surprisingly, the tetrahydrofuran molecules are orientated differently in $[\mathbf{H1}](PF_6)_2$ and $[\mathbf{H1}](BF_4)_2$, which is presumably caused by the smallest Cu···F distance to the counterions PF_6^- and BF_4^-. The nearest fluoride atom of the anion BF_4^- is with 2.541(4) Å considerably

closer located towards the complex cation compared to that of PF_6^- with 4.003(7) Å. Consequently, the two tetrahydrofuran molecules both support the central copper atom in [**H1**]$(BF_4)_2$, whereas Cu(2) and Cu(2') in [**H1**]$(PF_6)_2$ are stabilized by one solvent molecule each. The guanidine twist is with 32-33° comparable to other TMG-based guanidine copper complexes, showing no effect of the geometric constraint of the μ-alkoxido bridge.[47,135] The structure parameter ρ of [**H1**]$(PF_6)_2$ and [**H1**]$(BF_4)_2$ evidences a well delocalized double bond within the guanidine unit.

Table 10: Selected interatomic distances [Å], bond lengths [Å], angles [°] and the structure parameter ρ of [**H1**]$(PF_6)_2$ and [**H1**]$(BF_4)_2$.

	[H1](PF$_6$)$_2$	**[H1](BF$_4$)$_2$**
Cu(1)–O(1)	1.912(2)	1.904(4)
Cu(1)–O(2)	1.893(2)	1.961(4)
Cu(1)–O(3)	-	2.253(4)
Cu(2)–O(1)	1.923(2)	1.902(5)
Cu(2)–O(2)	1.932(2)	1.961(4)
Cu(2)–O(3)	2.556(2)	-
Cu(1)···Cu(2)	2.953(1)	2.919(2)
Cu(2)–N(1)	1.986(2)	1.953(5)
Cu(2)–N(4)	2.019(3)	2.007(6)
Cu(2)···F	4.003(7)	2.541(4)
N(1)–Cu(2)–N(4)	94.9(1)	96.1(2)
O(1)–Cu(1)–O(2)	78.0(1)	80.3(2)
O(1)–Cu(2)–O(2)	76.8(1)	80.4(2)
Cu(2)–O(1)–Cu(1)	100.7(1)	100.2(2)
Cu(2)–O(2)–Cu(1)	101.1(2)	96.2(2)
Cu(2)–Cu(1)–Cu(2')	180.0	180.0
$\sphericalangle(CN_3;NC_3)_{av}$	32.0	33.0
ρ	0.99	0.99

ρ = 2a/(b+c)[127] with a = C(1)–N(1), b = C(1)–N(2) and c = C(1)–N(3).

In analogy to the decomposition of the bis(μ-oxido) species [**O1**]$(PF_6)_2$, the decay product of the related **L2**-stabilized complex [**O2**]$(OTf)_2$ was also analyzed by warming up of the reaction solution to room temperature and crystallization under ambient conditions (Scheme 16). Single crystals, suitable for X-ray diffraction, were obtained by slow diffusion of diethyl ether into a saturated benzene solution. Crystallization of green needles in a dark green solution was

observed after several hours. The green needles revealed the molecular structure of a dicationic bis(μ-hydroxido) dicopper(II) complex [**H2**](OTf)$_2$ in the solid state, which is illustrated in Figure 29. Selected interatomic distances, bond lengths and angles are summarized in Table 11. Crystallographic details are provided in Table 49 in the appendix.

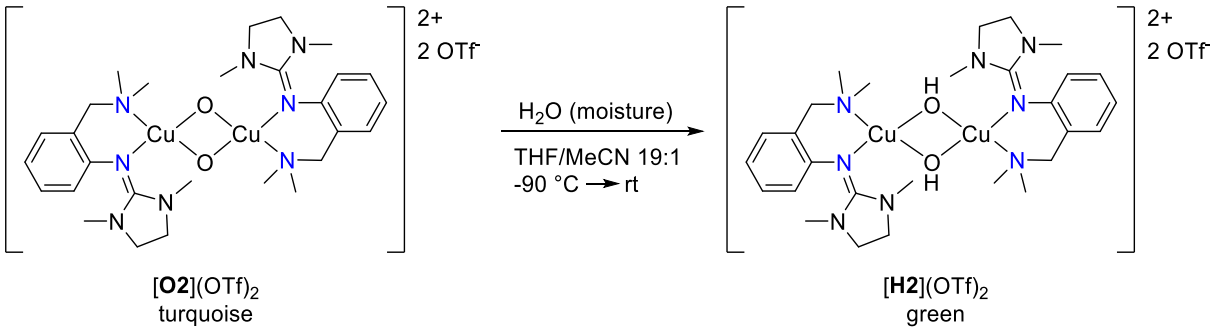

Scheme 16: Decomposition of [**O2**](OTf)$_2$ and formation of bis(μ-hydroxido) dicopper(II) complex [**H2**](OTf)$_2$.

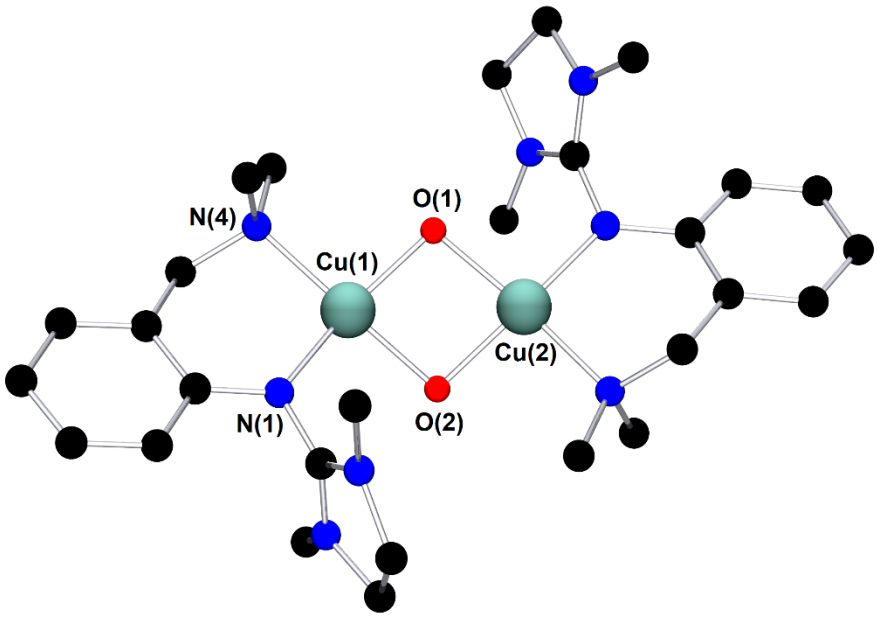

Figure 29: Molecular structure of the complex cation [**H2**]$^{2+}$ in crystals of [**H2**](OTf)$_2$ in the solid state. Hydrogen atoms, triflate anions, and non-coordinating solvent molecules (benzene) were omitted for clarity. It was not possible to locate the hydrogen atoms of the hydroxido groups in [**H2**](OTf)$_2$.

The decomposition product [**H2**](OTf)$_2$ crystallizes in the monoclinic space group $P2_1/c$ with four molecules in the unit cell. The Cu···Cu distance of [**H2**](OTf)$_2$ is with 2.900(1) Å comparable to the **L1**-supported decomposition products [**H1**](PF$_6$)$_2$ and [**H1**](BF$_4$)$_2$. Both central copper atoms of [**H2**](OTf)$_2$ are coordinated in a distorted square-planar fashion. The average of the Cu–O bond lengths of the Cu$_2$O$_2$ core within [**H2**](OTf)$_2$ is with 1.95 Å elongated compared to that in [**H1**](PF$_6$)$_2$ and [**H1**](BF$_4$)$_2$. It is also worth to mention that each triflate anion with the smallest Cu···O distance of 2.603(5) Å and 2.757(5) Å interacts with one of the two copper centers for additional stabilization. The bite angle of **L2** within [**H2**](OTf)$_2$ (92.5(3)°) is

slightly smaller than that of **L1** in [**H1**](PF$_6$)$_2$ and [**H1**](BF$_4$)$_2$ (94.9(1)-96.1(2)°). The guanidine twist is with 2.0° significantly smaller than in the **L1**-based complexes [**H1**](PF$_6$)$_2$ and [**H1**](BF$_4$)$_2$. The geometric constraint of the DMEG-based ligand causes a more rigid ligand sphere, which presumable contributes to the stabilization of the bis(μ-hydroxido) complex. The structure parameter ρ of [**H2**](OTf)$_2$ exhibits a completely delocalized double bond within the guanidine unit.

Table 11: Selected interatomic distances [Å], bond lengths [Å], angles [°] and the structure parameter ρ of [**H2**](OTf)$_2$.

	[H2](OTf)$_2$
Cu(1)–O(1)	1.949(5)
Cu(1)–O(2)	1.955(5)
Cu(2)–O(1)	1.935(5)
Cu(2)–O(2)	1.958(5)
Cu(1)···Cu(2)	2.900(1)
Cu(1)···O(OTf)	2.603(5)
Cu(2)···O(OTf)	2.757(5)
Cu(1)–N(1)	1.983(7)
Cu(1)–N(4)	2.009(7)
N(1)–Cu(1)–N(4)	92.5(3)
O(1)–Cu(1)–O(2)	82.1(2)
O(1)–Cu(2)–O(2)	82.4(2)
Cu(2)–O(1)–Cu(1)	96.6(2)
Cu(2)–O(2)–Cu(1)	95.7(2)
∢(CN$_3$;NC$_3$)$_{av}$	2.0
ρ	1.02

ρ = 2a/(b+c)[127] with a = C(1)–N(1), b = C(1)–N(2) and c = C(1)–N(3).

Interestingly, the decomposition products [**H1**]X$_2$ (X$^-$ = PF$_6^-$, BF$_4^-$), which are stabilized by **L1**, are the first examples of a μ-alkoxido μ-hydroxido tricopper(II) species. The complex [**H2**](OTf)$_2$ revealed the more common structure of a bis(μ-hydroxido) dicopper(II) species, although the two ligands **L1** and **L2** are structurally closely related. A probable mechanism of the decomposition of the bis(μ-oxido) dicopper(III) complexes [**O1**]$^{2+}$ and [**O2**]$^{2+}$ is proposed in Scheme 17. The mechanism suggests different pathways of ligand hydroxylation resulting in various decomposition products. Starting from the bis(μ-oxido) dicopper(III) complex, ligand hydroxylation can occur either in a concerted manner via intermediate B or via hydrogen atom abstraction followed by a fast rebound-step to generate intermediate D. The hydroxylation at

the α-carbon position of compound D is followed by fast dealkylation reaction to form a secondary amine and a ketone or aldehyde.[178,184] Alternatively, intermediate D can be rearranged to form a dinuclear μ-alkoxido μ-hydroxido dicopper(II) complex (E), which dissociates into two mononuclear fragments (F). On the one hand, these fragments can reassociate to generate bis(μ-hydroxido) species and bis(μ-alkoxido) species, as reported previously.[132] On the other hand, hydrolysis of the dissociated fragments leads to an aggregation of these fragments stabilized by a water molecule (G). The transition state G might be further stabilized by the solvent shell, as tetrahydrofuran features coordinating properties. The spatial proximity of water and the guanidine ligand results in the protonation of the basic guanidine ligand. Thereby, the hydroxido moiety is bound to the central copper atom. The present tetrahydrofuran molecules are expected to stabilize the trinuclear copper(II) complex, so that the protonated ligand is split off (H). None of the transition states on the route to the observed decay products could be isolated or detected so far. The μ-alkoxido μ-hydroxido tricopper(II) complex [**H1**]$^{2+}$ and protonated ligand [**L1**H]$^{+}$ were isolated in a ratio of 1:1, which agrees well with the proposed mechanism. The mechanism is also applicable to the hydroxylation of the peralkylated amine moiety, which was observed previously upon stabilization by hybrid guanidine ligands[150], but the chemoselective attack of the equatorially located methyl groups of the guanidine unit is seemingly favored over the aminomethyl groups. Similarly, Tolman and co-workers described a predominant hydroxylation of C–H bonds of equatorially disposed ligand substituents, underlining the geometric rationale of C–H bond activation and oxygenation upon the comparison of C–H bonds of similar strength.[178,184]

Many factors must be considered to explain the different decomposition products. On the one hand, the rigidity of the guanidine moiety in [**H2**](OTf)$_2$ causes a preorientation of the methyl groups of the DMEG-based unit, which can lead to the hydroxylation of DMEG-based ligands during the decomposition of the bis(μ-oxido) species as reported before.[181] On the other hand, [**H2**](OTf)$_2$ is stabilized by triflate anions, which are significantly stronger coordinating in comparison to BF_4^- and PF_6^- anions. Thus, the support by the triflate anions might enable the stabilization of a dinuclear complex, whereas the complexes [**H1**](PF$_6$)$_2$ and [**H1**](BF$_4$)$_2$ demand further support from solvent molecules forming a trinuclear complex. Another factor represents the solvent used for crystallization, which might direct the reaction pathway. Complex [**H2**](OTf)$_2$ was crystallized from benzene, which is non-coordinating. Therefore, the reaction intermediate **G** might not be stabilized enough during the process. The crystallization of complexes [**H1**](PF$_6$)$_2$ and [**H1**](BF$_4$)$_2$ includes coordinating solvents such as tetrahydrofuran and acetonitrile, allowing the formation of **G**. Nevertheless, the pathway of the decomposition of the bis(μ-oxido) complex [**O1**]$^{2+}$ and [**O2**]$^{2+}$ remains unclear and needs to be further analyzed.

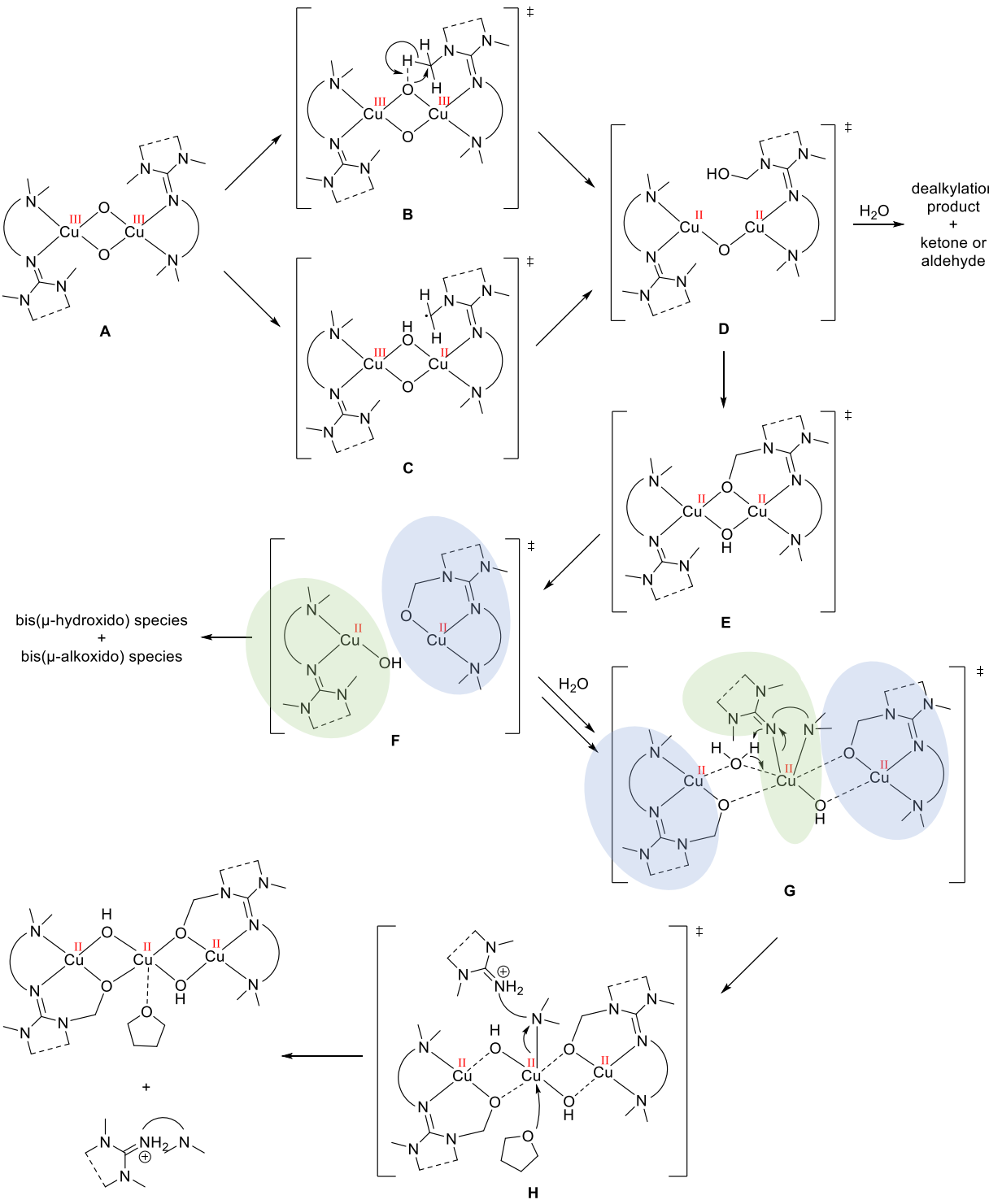

Scheme 17: Proposed mechanism of the decomposition of a hybrid guanidine-stabilized bis(μ-oxido) species.

3.1.4. Catalytic Oxygenation Reactions

In the preceding chapter, the copper-dioxygen species [**O1**](PF$_6$)$_2$ was already identified as a bis(μ-oxido) dicopper(III) complex which is discussed as potential active intermediate of tyrosinase.[38,47,65,66,69,70,150] The investigation of the functionality of [**O1**](PF$_6$)$_2$ towards exogenous substrates helps to complete this picture. The Cu_2O_2 complex mimics the active site of the enzyme, which naturally catalyzes the *ortho*-hydroxylation of L-tyrosine to L-dopa as well as the subsequent oxidation to L-dopaquinone in melanin biosynthesis (see section 1.1.3). A detailed mechanism of the phenol hydroxylation is described in Scheme 2. Aiming to expand the commonly used substrate scope of substituted phenols, the reactivity of [**O1**](PF$_6$)$_2$ was investigated towards a variety of challenging substrate classes, including phenols, pyridinols, naphthols, quinolinols and indolols. Different aromatic alcohols were hydroxylated by [**O1**](PF$_6$)$_2$. The resulting quinones, which are known for their instability and high reactivity[72,73], were transformed in a condensation reaction into more stable phenazine derivatives by using 1,2-phenylenediamine (Scheme 18).

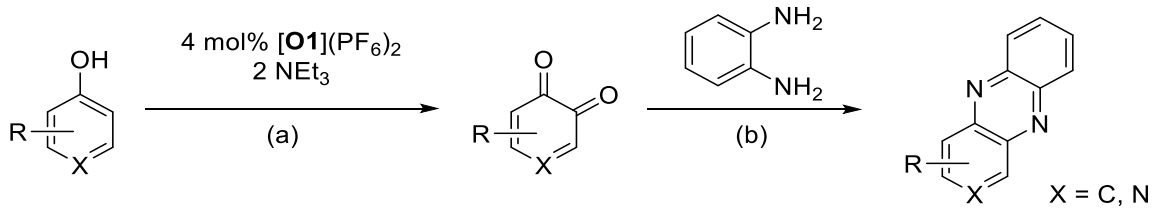

Scheme 18: Catalytic oxygenation of aromatic alcohols mediated by bis(μ-oxido) complex [**O1**](PF$_6$)$_2$ (a) and subsequent condensation of the quinones with 1,2-phenylenediamine to generate phenazines (b).

The experiments were carried out by following an adapted protocol, which was established by Bulkowski and modified by Tuczek and co-workers.[94,185] A catalyst concentration of 4 mol% referred to the full formation of the bis(μ-oxido) complex [**O1**](PF$_6$)$_2$ was chosen, which corresponds to 25 equivalents of the substrate. Triethylamine was used as auxiliary base in two equivalents with respect to the substrate to deprotonate the substrate. The hydroxylation reaction was monitored by UV/Vis spectroscopy in tetrahydrofuran at –90 °C for one hour (Reaction (a) in Scheme 18), as optical spectra remained constant after that time. This small-scale experiment ensures UV/Vis spectra within the Lambert-Beer limitations. Generated quinones were transformed in a one-pot reaction by adding 1,2-phenylenediamine and warming up to room temperature (Reaction (b) in Scheme 18).

3.1.4.1. Conversion of Monocyclic Aromatic Alcohols

Simple monocyclic aromatic alcohols were tested in the catalytic oxygenation reaction mediated by bis(μ-oxido) species [**O1**](PF$_6$)$_2$, as substituted phenols are primarily used for tyrosinase-like reactions in literature.[90,91] In addition to phenols, pyridinols were also evaluated (Table 12).

Table 12: Reaction of monocyclic aromatic alcohols with bis(μ-oxido) species [**O1**](PF$_6$)$_2$ (Scheme 18).

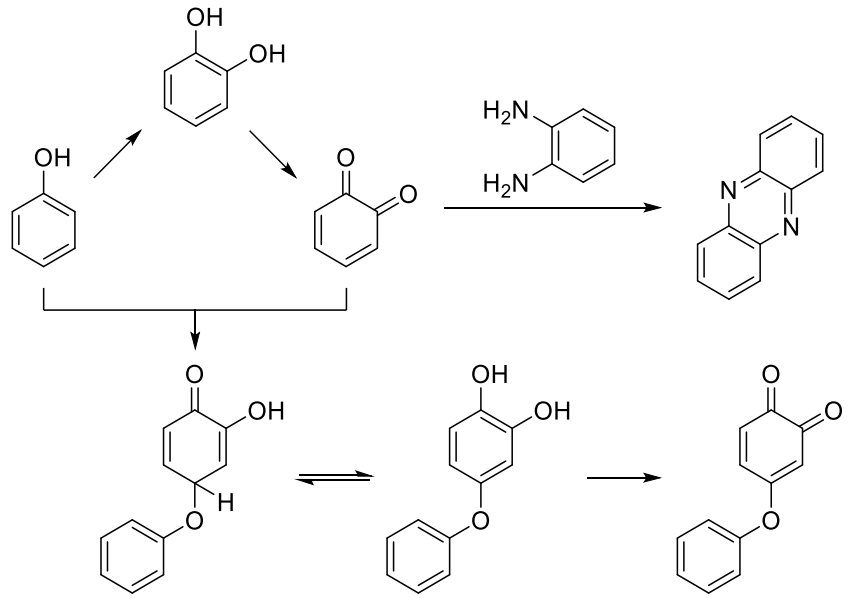

Entry	Substrate	Conv. [%]	Coupling Product (CP)
1	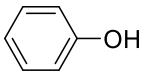	> 99	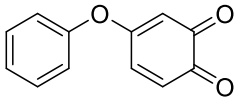 (**CP1**)
2	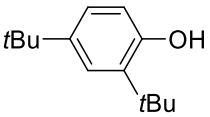	0	
3	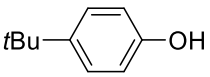	> 99	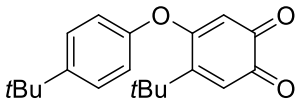 (**CP2**)
4	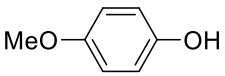	> 99	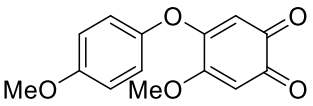 (**CP3**)
5	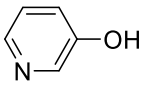	> 99	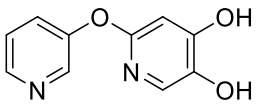 (**CP4**)
6	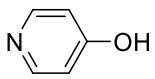	> 99	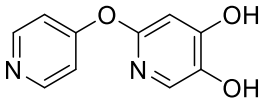 (**CP5**)

[a] Conditions: THF, -90 °C, 1 h. [b] Conditions: THF, -90 °C, then rt, overnight.

The catalyst [**O1**](PF$_6$)$_2$ exhibited besides the expected hydroxylation activity towards (substituted) phenols also C–O coupling chemistry (see Scheme 6). Surprisingly, no phenazine products were observed. Cryo-UHR-ESI spectra of the reddish-brown reaction solution using

phenol (Table 12, entry 1) depicted an m/z value of 201.0885 (calculated 201.0546) for $[M+H]^+$, which was attributed to the C–O coupled quinone **CP1**, and 223.1690 (calculated 223.0366) for $[M+Na]^+$. In case of 2,4-di-*tert*-butyl phenol (entry 2), a substrate which is widely used in tyrosinase chemistry[90,91], a conversion was observed neither at –90 °C nor at room temperature. This can be explained by the high steric demand of the two *tert*-butyl groups, which presumably interfere with the large guanidine moiety of the ligand system. Reaction of 4-*tert*-butyl phenol and 4-methoxy phenol (entries 3-4) led to a likewise reddish-brown reaction solution. Cryo-UHR-ESI measurements revealed the formation of the C–O coupled quinone in both cases (**CP2**: $[M+H]^+$ (found 313.1276, calculated 313.1325), $[M+HNEt_3]^+$ (found 414.3005, calculated 414.3003); **CP3**: $[M+Na]^+$ (found 283.1440, calculated 283.0577), $[M+HNEt_3]^+$ (found 364.2704, calculated 364.2118).

In contrast to comprehensive studies on phenols, no conversion of pyridinols in a tyrosinase-like reaction was reported so far. When 3- and 4-pyridinol were used (entries 5-6), an immediate formation of an absorption band at 375 nm was observed, similar to that in the reaction of 3- and 4-quinolinol (see Figure 75 in the appendix for comparison), indicating the formation of 3,4-pyridoquinone. A rapid drop in intensity illustrates the high reactivity of the quinone even at –90 °C. No turnover numbers were determined because no extinction coefficients of the respective quinones are listed elsewhere. Theoretical studies revealed lesser stability of 3,4-pyridoquinone with respect to the most stable 2,5-isomer.[186] Cryo-UHR-ESI measurements of the reaction solution using 3-pyridinol revealed a m/z value of 205.1530 (calculated 205.0608) for $[M+H]^+$, which was assigned to the C–O coupled catechol **CP4**, and 306.2537 (calculated 306.1812) for $[M+HNEt_3]^+$. Conversion of 4-pyridinol led to a likewise formation of the C–O coupled catechol **CP5** (found 205.1529, calculated 205.0608 for $[M+H]^+$).

Considering the detected coupling products via cryo-UHR-ESI measurements and the immediate color change of the reaction solution after the addition of a monocyclic aromatic alcohol, these results underline the massive oxidative strength of bis(μ-oxido) complex [**O1**]$(PF_6)_2$ causing undesired side reactions even at –90 °C. Also, the reaction rate of the C–O coupling reaction of the quinone with remaining phenol is seemingly faster than the condensation reaction of the quinone with 1,2-phenylenediamine. Therefore, lowering of the reaction temperature to –125 °C in 2-methyltetrahydrofuran or even to –145 °C in an eutectic mixture of tetrahydrofuran and 2-methyltetrahydrofuran (1:4)[56] might allow the observation of the quinone in the future.

3.1.4.2. Conversion of Bicyclic Aromatic Alcohols

In contrast to monocyclic aromatic alcohols, the conversion of bicyclic substrates such as naphthols, quinolinols and indolols is more complicated. These bicyclic aromatic alcohols are significantly larger, which should influence the time needed to orientate the substrate molecule

accordingly for the hydroxylation reaction. Moreover, many substrates offer two accessible *ortho*-positions next to the hydroxy group, providing two possible quinone products. The corresponding quinones can be transformed into bent and/or linear phenazine derivatives (Scheme 19).

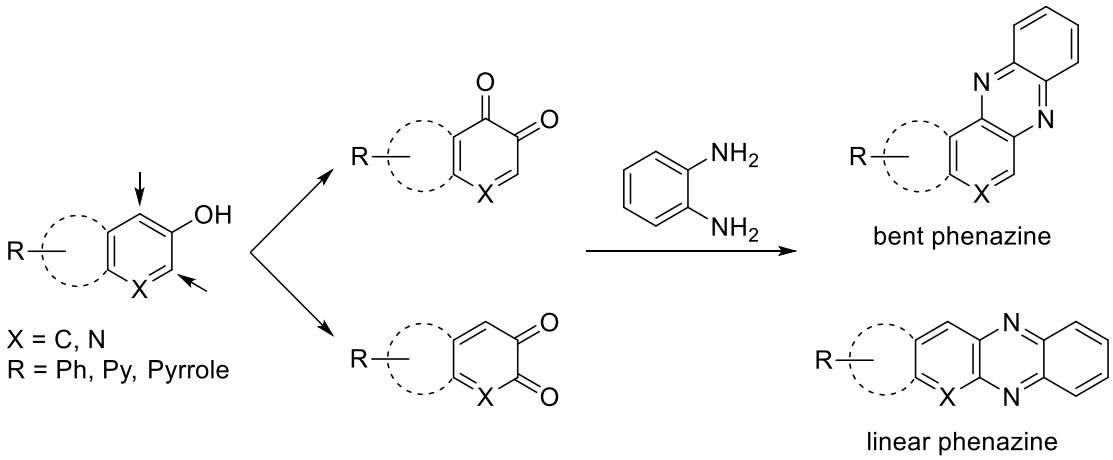

Scheme 19: Oxygenation of bicyclic aromatic alcohols and subsequent condensation of the corresponding quinones with 1,2-phenylenediamine.

Theoretical studies were performed by Dr. Alexander Hoffmann to predict the preferred position of hydroxylation for substrates with two accessible *ortho*-positions next to the hydroxy group. The Fukui function uses the concept of frontier orbitals and describes a change in electron density at a given position of a molecule to allow a prognosis of the most electrophilic and nucleophilic positions.[187] The electron density $\delta\rho(r)$ is displayed by the Fukui function in dependency of the number of electrons $\mathrm{N_{electron}}$ (equation (2)).

$$\mathrm{f}(r) = \frac{\delta\rho(r)}{\delta N_{\mathrm{electron}}} \tag{2}$$

There is a positive and a negative version of the Fukui function, depending on whether an electron is added to or removed from the molecule. The positive Fukui function (3) representing the electron density of a molecule for a nucleophilic reaction is defined as follows:

$$f_+(r) = \rho_{N+1}(r) - \rho_N(r) \tag{3}$$

In analogy, the negative Fukui function (4) describes the electron density of a molecule for an electrophilic reaction.

$$f_-(r) = \rho_N(r) - \rho_{N-1}(r) \tag{4}$$

With respect to the preferred position, at which the aromatic alcohol is hydroxylated, the negative Fukui function was applied because the hydroxylation reaction follows an electrophilic reaction mechanism.[9–11,90,91] The location of the electrophilic attack at a C atom of the molecule is identified by a large value of the negative Fukui function. DFT calculations based on the hybrid meta GGA functional TPSSh[157–159] in combination with the triple-valence basis set def2-TZVP[160–163] and empirical dispersion corrections with the Becke-Johnson damping

GD3BJ[164–167] were performed by Dr. Alexander Hoffmann. The calculated electron densities at different positions of the substrate molecules are summarized in Table 13 and illustrated in section 7.3 in the appendix. In all cases of bicyclic aromatic alcohols studied herein, including 2-naphthol, 3- and 6-quinolinol as well as 5- and 6-indolol, the electrophilic attack is predicted to be at the C–H position next to the neighboring aromatic ring, which leads to a bent phenazine.

Table 13: Summary of the calculated negative Fukui function (f_-) of phenolic substrates with two possible products.

Entry	Substrate	f_-	C atom position
1	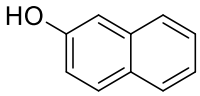	21.14 0.74	1 3
2	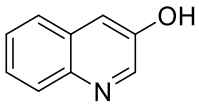	1.38 15.17	2 4
3	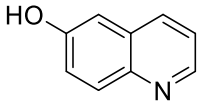	23.93 0.91	5 7
4	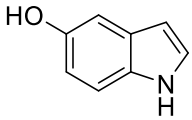	19.93 1.05	4 6
5	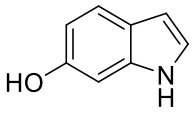	2.03 11.99	5 7

Validation experiments of the prognoses via Fukui function were performed according to the protocol described above to evaluate the selectivity of the hydroxylation reaction in comparison to the theoretical calculations. The reactivity studies on the bis(μ-oxido) complex [**O1**]$(PF_6)_2$ were also conducted on a larger scale to quantify the reaction products, if UV/Vis and NMR spectra indicated the conversion of the substrate. Flame-dried molecular sieve (3 Å) was added to intercept water molecules produced during the reaction to avoid the decomposition of the catalyst. After the acidic work-up, the crude product was purified via column chromatography and/or sublimation to isolate the respective phenazine. The tested substrates of bicyclic aromatic alcohols including naphthols, quinolinols and indolols are summarized in Table 14.

The oxygenation of naphtholic substrates, such as 1-naphthol and 2-naphthol, in the presence of an oxidation catalyst was already reported previously.[188–190] When the bis(μ-oxido) complex [**O1**]$(PF_6)_2$ was used as an oxidation catalyst, both naphthols were converted into the corresponding quinone, which led to the formation of benzo[a]phenazine (**P1**) upon treatment

with 1,2-phenylenediamine (Table 14, entries 1-2). **P1** was purified via column chromatography and isolated in 22-31% yield. Consistent with observations made by Krohn and co-workers, no formation of the linear phenazine was observed, but they obtained besides **P1** a Michael adduct species, which resulted from the reaction of unreacted substrate with the reactive quinone intermediate.[190] No Michael adduct species was observed during [**O1**]$(PF_6)_2$ catalysis, which might be a result of a shorter reaction time and/or lower temperatures compared to Krohn and co-workers, inhibiting the undesired side reaction. A control reaction was performed to enforce the formation of the linear phenazine by using 1-methyl 2-naphthol (entry 3), as the 1-position is occupied by the methyl substituent. No conversion of the substrate was observed, confirming the prognosis via Fukui function.

The catalytic hydroxylation of quinolinols has a long history as 8-quinolinol was converted previously by various catalysts, but the reaction product was mostly only observed via UV/Vis spectroscopy.[90] While 7,8-quinolinedione (**Q1**) was formed with 14 turnovers (entry 7), methyl-substitution in 2-position led to a slight decrease of the TON to 12 (**Q2**, entry 8). However, the formation of the respective phenazine was observed in neither case, presumably due to the smaller Fukui function f_+ at the respective C atoms of **Q1** and **Q2** (Table 56 in the appendix). A conversion of the other quinolinols was not reported before in literature. 3- and 4-quinolinol were transformed into their quinone (absorption band at 370 nm) and isolated as quinolino[3,4-b]quinoxaline (**P2**) (entries 4-5). 6-Quinolinol was oxygenated to 5,6-quinolinedione (entry 6), which showed absorption bands at 325, 340 and 370 nm. Pyrido[3,2-a]-phenazine (**P3**) was isolated in 15 turnovers after column chromatography and sublimation. Single crystals, suitable for X-ray diffraction, were obtained from a concentrated DMSO solution of phenazine **P3** (Figure 30). Crystallographic details of **P3** are listed in Table 50 in the appendix.

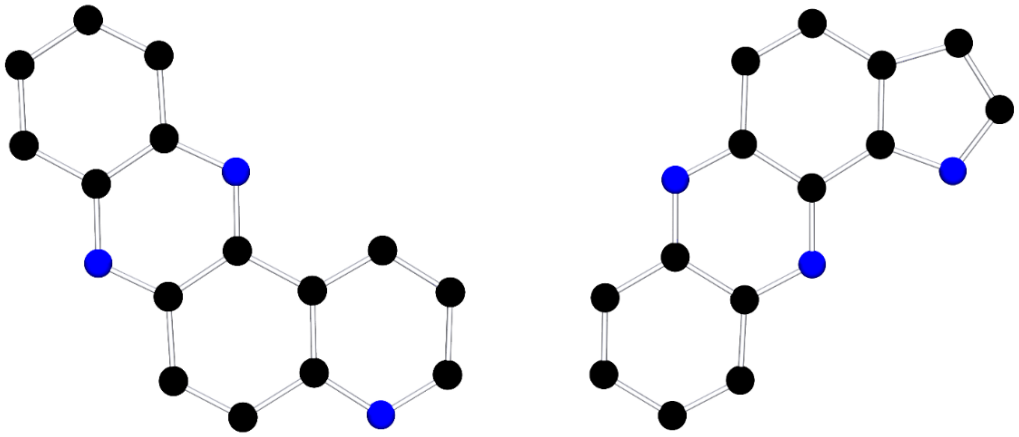

Figure 30: Molecular structures of **P3** (left) and **P5** (right) in the solid state. Hydrogen atoms were omitted for clarity.

Table 14: Catalytic oxygenation of bicyclic aromatic alcohols mediated by [**O1**]$(PF_6)_2$ (a) and subsequent condensation of the generated quinone by using 1,2-phenylenediamine (Scheme 18).

Entry	Substrate	Conv.[c] [%]	Product Quinone (Q) / Phenazine (P)		Yield[d] [%]
1	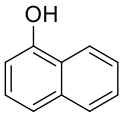	80	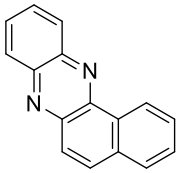	(**P1**)	22
2	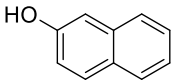	89		(**P1**)	31
3	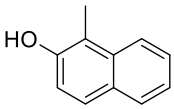	0			0
4	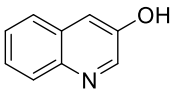	95	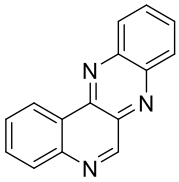	(**P2**)	32
5	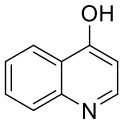	87		(**P2**)	22
6	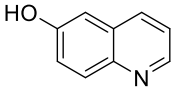	> 99	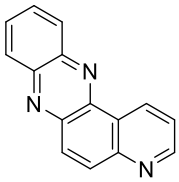	(**P3**)	30
7	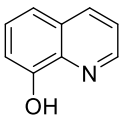	28	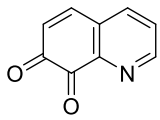	(**Q1**)	[e]
8	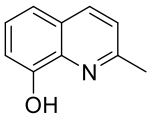	24	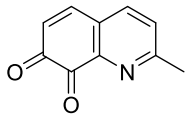	(**Q2**)	[e]
9	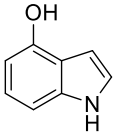	81	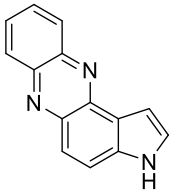	(**P4**)	19
10	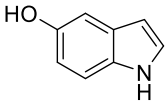	88		(**P4**)	26
11	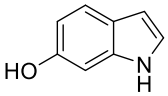	92	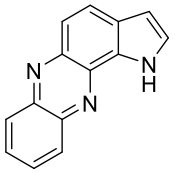	(**P5**)	27
12	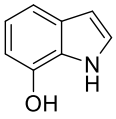	84		(**P5**)	31

[a] Conditions: THF, -90 °C, 1 h. [b] Conditions: THF, -90 °C, then rt, overnight. [c] Conversion of the substrate determined by ^{1}H NMR spectroscopy. [d] Isolated yield of the phenazine after column chromatography. [e] No phenazine product observed. TON of 14 for **Q1** and 12 for **Q2** determined after reaction (a) via UV/Vis spectra and based on the concentration of [**O1**]$(PF_6)_2$.

Although indolols possess an easily accessible pyrrole ring, C–H functionalization of the neighboring phenyl ring remains challenging.[191] The substrates 4- and 5-indolol were converted into 4,5-indoledione, which was captured as pyrrolo[3,2-a]phenazine (**P4**) in 19-26% yield after column chromatography (entries 9-10). Similarly, 6- and 7-indolol were transformed into pyrrolo[2,3-a]phenazine (**P5**, 27-31% isolated yield). Single crystals, suitable for X-ray diffraction, were obtained from a saturated hexane solution of phenazine **P5** (entries 11-12 and Figure 30), confirming the formation of **P5**. The oxygenation of 6-indolol was also conducted in the presence of oxygenated copper salt $[Cu(MeCN)_4]PF_6$ to evaluate the necessity of a stabilizing ligand system. Here, no oxygenation activity on 6-indolol was observed, which underlines the supporting effects of ligand **L1**.

In summary, nine out of twelve substrates were converted successfully into their corresponding phenazine derivative. Five of them provide two possible phenazine products, of which the bent phenazine was formed selectively. The linear phenazine was observed in neither case. The high selectivity of the hydroxylation reaction validates the prognosis of the theoretical studies via Fukui function, thus introducing a new predictive tool into tyrosinase chemistry applicable on a variety of substrate classes. Nevertheless, the maximum yield achieved during the one-pot reaction of catalytic oxygenation and condensation is limited to 32%. It is noteworthy that the optically determined duration of the hydroxylation reaction of one hour might be too short, as the conversion of these challenging bicyclic substrates takes significantly longer than the conversion of simple substituted phenols. Therefore, the use of UV/Vis spectroscopy might be misleading for slow reactions. A remaining amount of starting material was observed for all tested substrates except for 6-quinolinol after acidic workup in the ^{1}H NMR spectrum. Thus, future studies should evaluate longer reaction times, which might also influence the selectivity of the reaction.

3.1.4.3. Reactivity of Tyrosinase (*A. oryzae*)

The reactivity of tyrosinase from *A. oryzae* was studied by the group of Prof. Dr. Jörg Pietruszka at the IGB-1 in Jülich according to a published procedure[192] to compare the substrate scope of the enzyme with the scope of the tyrosinase model system [**O1**]$(PF_6)_2$. For this purpose, the enzyme (with a volumetric activity of 43 U mL^{-1}) was dissolved in Tris·HCl buffer (pH 6) and treated with an acetonitrile solution of a phenolic substrate in the presence of CH-acidic cyclopentanone-2-carboxylic acid methyl ester at room temperature (Scheme 20).

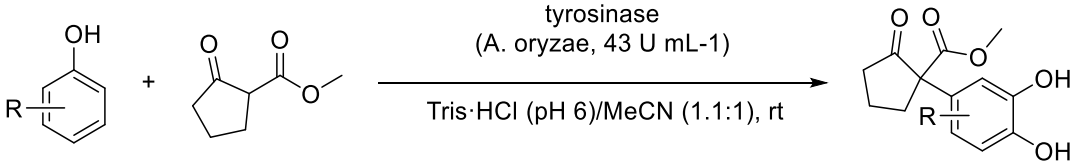

Scheme 20: Oxygenation of phenolic substrates mediated by tyrosinase (*A. oryzae*) and subsequent Michael addition to form a cyclopentanone ester.

The reaction was followed by thin-layer chromatography and NMR spectroscopy. Conversion of phenol mediated by tyrosinase led to the arylation product in 65% isolated yield (Table 15, entry 1).[192] However, using the same batch of tyrosinase, even after three days, 1- and 2-naphthol as well as 6-quinolinol were not transformed into the corresponding arylation products (entries 2-4).

The reactivity of tyrosinase towards phenolic substrates was also studied in the presence of 1,2-phenylendiamine at room temperature to give a phenazine product (Scheme 21). However, the conversion of phenol yielded no formation of phenazine after several days (Table 15, entry 5). Only polymer traces were detected. By using different indolols, only the formation of various side products to a lesser extent was observed via NMR spectroscopy (entries 6-9).

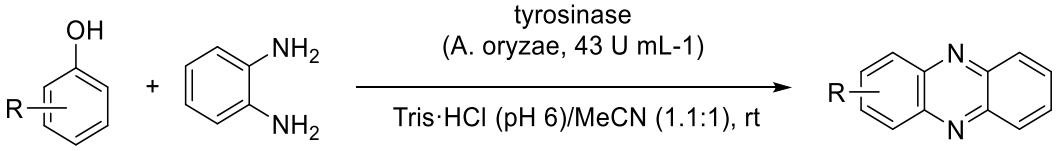

Scheme 21: Oxygenation of phenolic substrates mediated by tyrosinase and subsequent condensation with 1,2-phenylenediamine.

Table 15: Reactivity studies of tyrosinase (from *A. oryzae*), performed by the group of Prof. Dr. Jörg Pietruszka at the IGB-1 in Jülich.

entry	substrate	additive	time [d]	yield [%]
1	phenol	cyclopentanone ester (1.2 eq)	1	65
2	1-naphthol	cyclopentanone ester (1.2 eq)	3	0
3	2-naphthol	cyclopentanone ester (1.2 eq)	3	0
4	6-quinolinol	cyclopentanone ester (1.2 eq)	3	0
5	phenol	1,2-phenylenediamine (1.2 eq)	several	0
6	4-indolol	1,2-phenylenediamine (1.2 eq)	3	traces[a]
7	5-indolol	1,2-phenylenediamine (1.2 eq)	3	traces[a]
8	6-indolol	1,2-phenylenediamine (1.2 eq)	3	traces[a]
9	7-indolol	1,2-phenylenediamine (1.2 eq)	3	traces[a]

[a] Detection of undefined products in traces.

To conclude, the enzyme tyrosinase oxidizes phenol quantitatively but exhibited no reactivity towards naphthols, quinolinols and indolols, neither in the presence of a cyclopentanone ester nor in the presence of 1,2-phenylenediamine. In comparison to tyrosinase model system [**O1**]$(PF_6)_2$, which depicted an exceptional broad substrate scope, the enzyme itself gave no access to that scope, underlining the oxidative strength of the hybrid guanidine-stabilized bis(μ-oxido) complex.

3.2. TMGbenza- and DMEGbenza-stabilized Copper Complexes with Coordinating Anions

Hybrid guanidine ligands demonstrated their suitability as tyrosinase model system in the presence of weakly coordinating anions. The bis(μ-oxido) complex showed a moderate stability at low temperatures and an exceptional activity in tyrosinase-like oxygenation reactions towards a library of polycyclic aromatic alcohols. This chapter deals with the synthesis and characterization of hybrid guanidine-stabilized copper(I) halide complexes. The reactivity towards molecular oxygen of copper(I) halide complexes is examined. In addition, the influence of additives on the properties of the bis(μ-oxido) species is discussed and the reactivity in tyrosinase-like oxygenation reactions is evaluated.

Parts of this chapter are already published in:

[1] M. Paul, A. Hoffmann, S. Herres-Pawlis, *J. Biol. Inorg. Chem.* **2021**, *26*, 249–263.
[2] M. Paul, *Master Thesis* **2017**, RWTH Aachen University.

3.2.1. Cu(I) Complexes

Hybrid guanidine-stabilized copper(I) halide complexes possess different coordination geometries depending on the features of the ligand system and copper salts. The synthesis of TMGbenza-stabilized copper(I) halide complexes can be accomplished depending on the copper salt to ligand ratio (Scheme 22).

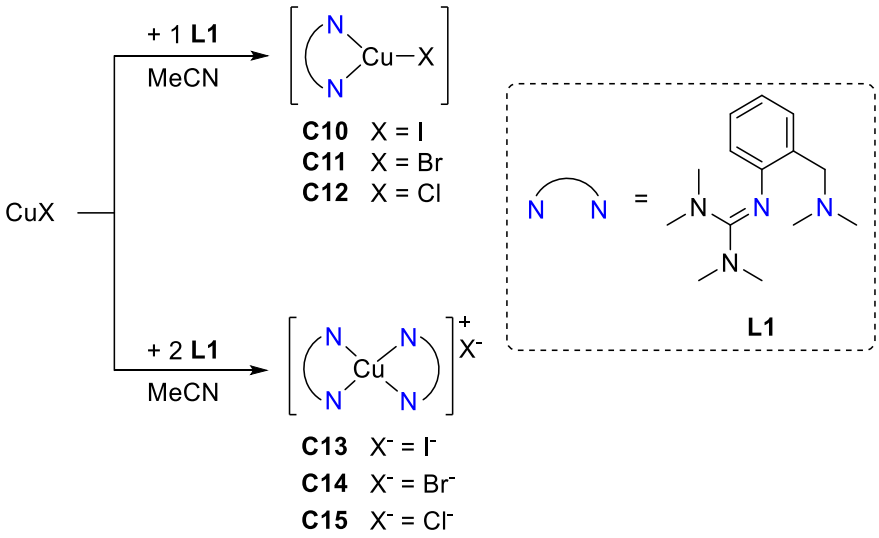

Scheme 22: Synthesis of TMGbenza-stabilized monochelate and bischelate copper(I) halide complexes **C10**-**C12** and **C13**-**C15**.

The reaction of equimolar amounts of copper(I) halides CuX (X = I, Br, Cl) with ligand **L1** resulted in the formation of the neutral monochelate copper(I) complexes [Cu(**L1**)I] (**C10**), [Cu(**L1**)Br] (**C11**), and [Cu(**L1**)Cl] (**C12**) in high yields. The colorless complexes were analyzed

by NMR, IR, and UV/Vis spectroscopy as well as mass spectrometry. Interestingly, chemical shifts in the aromatic and aliphatic region of the ^{1}H NMR spectra are broadened from **C10** to **C12**, which was attributed to the increasing ionic character of the Cu–X bond (from I to Cl). The UV/Vis spectra of **C10**-**C12** possess an absorption band at 290 nm, originating from π to π* transitions of the aromatic backbone of the ligand system. Single crystals of **C11**-**C12**, suitable for X-ray diffraction, were grown by slow diffusion of diethyl ether into a saturated solution of the complex in acetonitrile (Figure 31). The molecular structure of **C10** was reproduced from the master thesis.[154] Selected bond lengths and angles are summarized in Table 16. Crystallographic details are provided in Table 45 in the appendix.

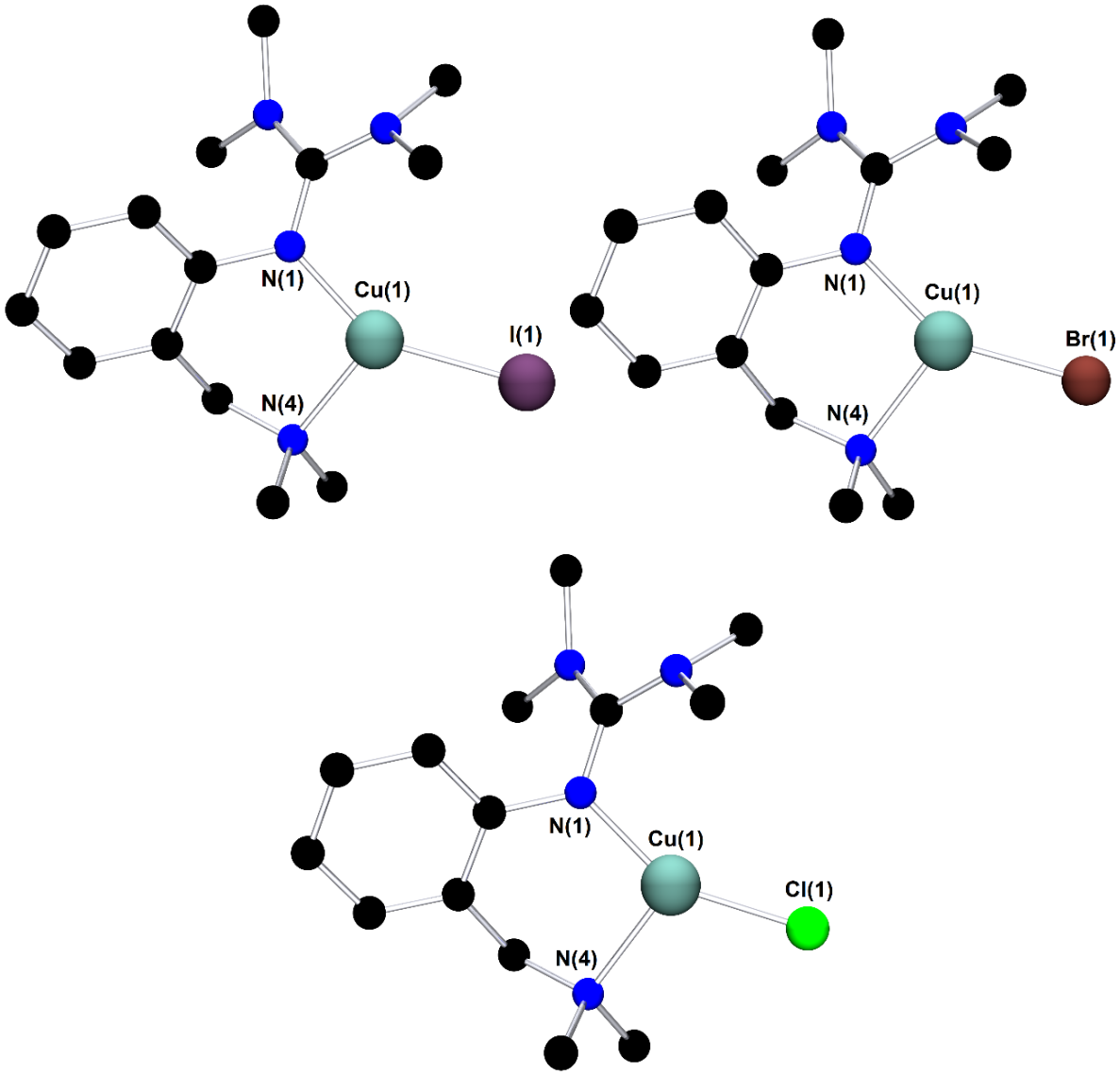

Figure 31: Molecular structures of **C10**[154] (top left), **C11** (top right) and **C12** (bottom) in the solid state. Hydrogen atoms were omitted for clarity.

The colorless blocks of **C10**-**C12** crystallize in the orthorhombic space group *P*bca with eight molecules in the asymmetric unit. The central copper atom Cu(1) is coordinated in a distorted trigonal-planar fashion by the bidentate hybrid guanidine ligand **L1** and one halide donor. The

Cu–N(4) bond lengths are significantly elongated compared to the Cu–N(1) bond lengths, revealing the higher σ-donor character of the guanidine unit compared to the amine donor function. The decreasing Cu–X bond length from complex **C10** to **C13** correlates with an increasing Cu(1)–N(4) bond length. Similarly, a correlation between an increasing N(1)–Cu(1)–X bond angle and a decreasing Cu(1)–N(1) and Cu(1)–X bond lengths is observed. Complex **C10** depicts an approximately Y-shaped geometry with an N(1)–Cu(1)–X bond angle of 147.6(1)°, which deviates from the ideal 120° angle due to the restricted bite angle of **L1** (97°-99°). The coordination geometry in **C11** and **C12** is slightly more distorted Y-shaped, which was also observed in other trigonal-planar guanidine complexes.[99,135,193] The guanidine twist of the $C_{imine}N_3$-plane and the $N_{amine}C_3$-plane is with 28-29° comparable to other TMG-based guanidine copper(I) complexes.[47,135] The structure parameter ρ was calculated from the C–N bond lengths within the guanidine moiety, showing a good delocalization of the double bond within the guanidine unit.

Table 16: Selected bond lengths [Å], angles [°] and the structure parameter ρ of **C10**-**C12**.

	C10[154]	**C11**	**C12**
Cu(1)–N(1)	1.958(2)	1.943(3)	1.941(2)
Cu(1)–N(4)	2.108(3)	2.130(3)	2.151(2)
Cu(1)–X(1)	2.449(1)	2.282(1)	2.159(1)
N(1)–Cu(1)–N(4)	99.3(1)	98.7(1)	97.8(1)
N(1)–Cu(1)–X	147.6(1)	149.7(1)	151.7(1)
N(4)–Cu(1)–X	113.0(1)	111.5(1)	110.4(1)
$\sphericalangle(CN_3;NC_3)_{av}$	29.3	28.5	28.3
ρ	0.98	0.98	0.99

ρ = 2a/(b+c)[127] with a = C(1)–N(1), b = C(1)–N(2) and c = C(1)–N(3).

Bischelate copper(I) halide complexes [Cu(**L1**)$_2$]I (**C13**), [Cu(**L1**)$_2$]Br (**C14**), and [Cu(**L1**)$_2$]Cl (**C15**) can also be formed due to the restricted bite angle of TMGbenza, as observed previously in the presence of weakly coordinating anions (see section 3.1.2). The diffusion constant *D* of a molecule allows to distinguish between monochelate, bischelate and dimeric complexes in solution. For this purpose, ^{1}H DOSY NMR measurements were performed to determine the diffusion constants *D* of the compounds in dependence of the temperature *T* in acetonitrile according to the Stokes-Einstein equation (5).

$$D(T) = \frac{k_B}{6\pi\eta R_0} \cdot T \tag{5}$$

The Boltzmann constant is abbreviated with k_B, whereas η denotes the dynamic viscosity and R_0 the hydrodynamic radius of the diffusing particles. The diffusion constant is a measure of

the mobility of the particles in dependence of the temperature. In general, the diffusion constant is non-linearly depending on the temperature as the viscosity of the solvent is temperature dependent. For a small range of temperature, the correlation of $D(T)$ and T is approximately linear if viscosity effects are negligibly small. The calculated diffusion constants D of ligand **L1**, monochelate complex **C10**, bischelate complex **C13** and acetonitrile are summarized in Figure 32.

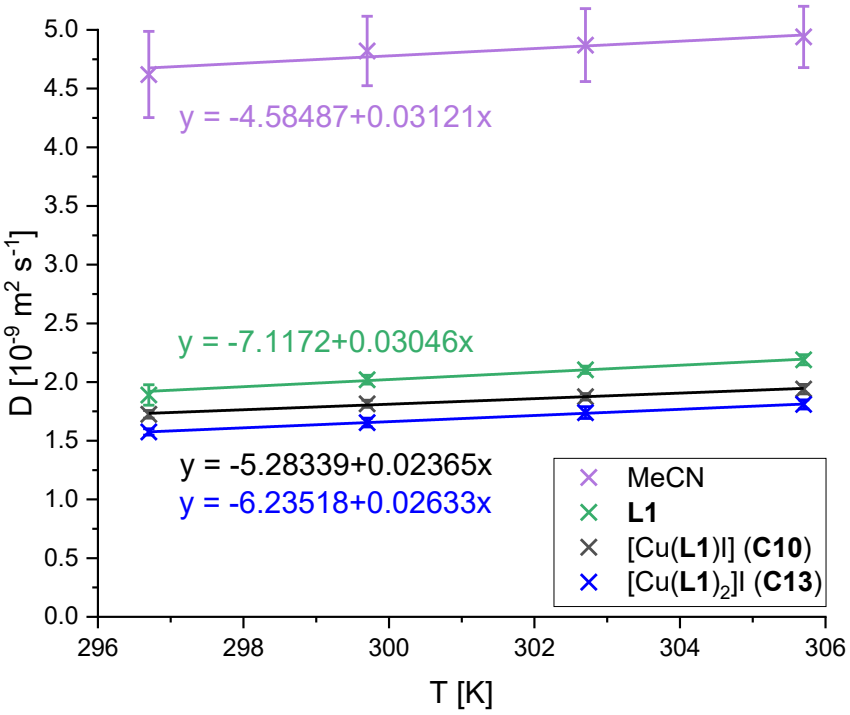

Figure 32: Diffusion constant D of acetonitrile (violet), ligand **L1** (green), monochelate complex **C10** (black) and bischelate complex **C13** (blue) in dependence of temperature T (derived from ^{1}H DOSY NMR spectra).

The measurements were conducted at different temperatures to exclude possible temperature effects. Figure 32 shows a linear dependency of the diffusion constant and the temperature within the temperature range used. Monochelate species **C10** depicted a significantly higher diffusion constant than its related bischelate species **C13** within the error tolerances (D(**C10**) = (1.81±0.03) 10^{-9} m^2 s^{-1} and D(**C13**) = (1.65±0.04) 10^{-9} m^2 s^{-1} at 299.7 K), revealing a higher dynamic behavior of **C10** due to its smaller molecule size and the geometric constraints of the bischelate complex. Therefore, the presence of a dimeric species of **C10** was ruled out because the dimeric species would show a smaller diffusion constant. Free ligand **L1** exhibits with D(**L1**) = (2.02±0.04) 10^{-9} m^2 s^{-1} at 299.7 K a higher diffusion constant compared to the copper(I) complexes (as expected). The extinction coefficient of acetonitrile was determined to D(MeCN) = (4.82±0.30) 10^{-9} m^2 s^{-1} at 299.7 K, revealing an error of approximately 10% which is significantly higher than the error of the diffusion coefficient of the complexes and ligand. As a result, the temperature range used is not optimal for acetonitrile

as the solvent molecules move too quickly. It is noteworthy that the calculated fits pass through the origin in neither case, showing a minor viscosity effect during the measurements.

When the hybrid guanidine ligand DMEGbenza (**L2**) was used, no mononuclear complexes were formed upon the reaction of equimolar amounts of **L2** and a copper(I) halide. Instead, the corresponding dimeric DMEGbenza-supported copper(I) halide complexes were obtained (Scheme 23).

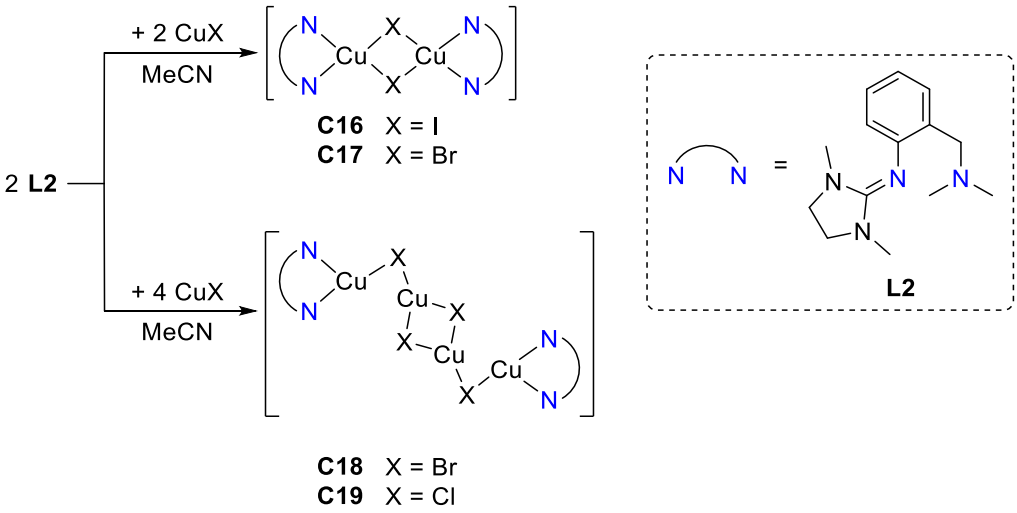

Scheme 23: Synthesis of DMEGbenza-stabilized dimeric copper(I) halide complexes [(**L2**)CuX]$_2$ (**C16**-**C17**; X = I, Br) and [(**L2**)CuX·CuX]$_2$ (**C18**-**C19**; X = Br, Cl).

Single crystals of **C17**, suitable for X-ray diffraction, were grown by slow diffusion of pentane into a saturated solution of the complex in tetrahydrofuran (Figure 33). The molecular structure of **C16** was reproduced from my master thesis for comparison.[154] Selected bond lengths and angles are summarized in Table 17. Crystallographic details are provided in Table 46 in the appendix.

The colorless blocks of **C16**-**C17** crystallize in the triclinic space group $P\bar{1}$ with one molecule in the asymmetric cell. The two copper atoms Cu(1) and Cu(1') are coordinated in a distorted tetrahedral fashion by the bidentate hybrid guanidine ligand **L2** and two bridging halides. The chelate ligands are orientated in *anti*-position. The center of the Cu_2X_2-plane of **C16**-**C17** resides on a crystallographically imposed inversion center. The angles between the CuN_2 and CuX_2 plane of both complexes **C16**-**C17** are very similar (85.7(1)° for **C16** and 85.3(1)° for **C17**), deviating from the ideal tetrahedron (90°). This is also displayed in the value τ_4 for both complexes (0.84-0.88). The bite angle N(1)–Cu(1)–N(4) of **L2** in dimeric complexes **C16**-**C17** (95°) is narrowed compared to the **L1**-stabilized monomeric complexes **C10**-**C11** (98-99°).

The Cu–N(1) bond lengths are significantly shorter than the Cu–N(4) bond lengths in both complexes **C16**-**C17**, revealing the higher σ-donor strength of the guanidine unit compared to the amine donor function. The Cu–X bond lengths of **C16**-**C17** are elongated in comparison to the mononuclear complexes **C10** and **C11**, which results from the higher coordination number

in **C16**-**C17**. The Cu(1)···Cu(1') distance of complex **C16** is significantly longer than the distance in **C17**, which is consistent with the longer Cu–X bond lengths and the larger X(1)–Cu(1)–X(1') bond angle of complex **C16**.

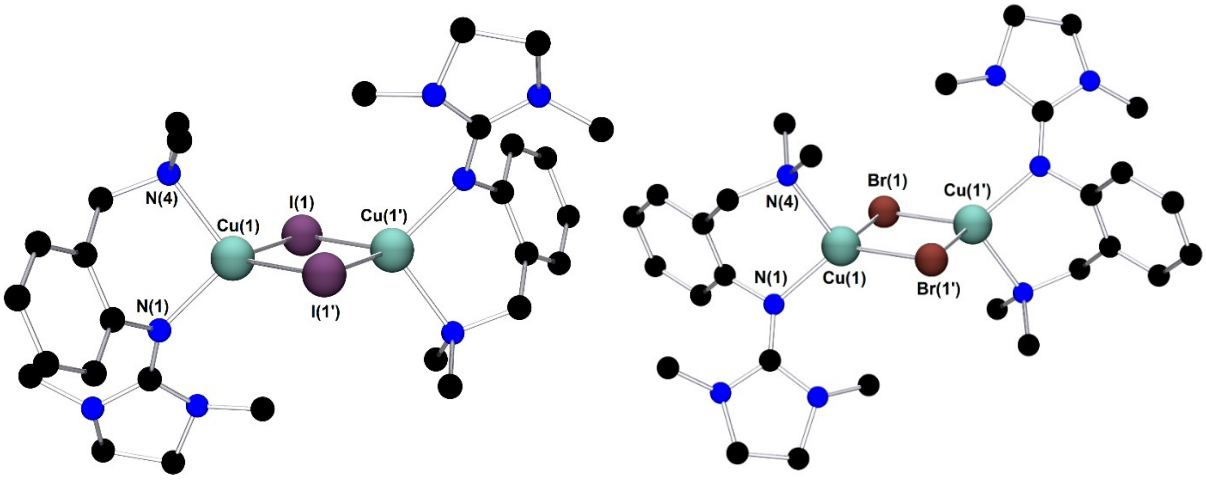

Figure 33: Molecular structures of **C16** (left) and **C17** (right) in the solid state. Hydrogen atoms were omitted for clarity.

Table 17: Selected interatomic distances [Å], bond lengths [Å], angles [°] and structure parameters of **C16** and **C17**.

	C16[154]	**C17**
Cu(1)–N(1)	2.092(2)	2.058(4)
Cu(1)–N(4)	2.182(2)	2.176(4)
Cu(1)–X(1)	2.671(1)	2.478(1)
Cu(1)–X(1')	2.652(1)	2.505(1)
Cu(1)···Cu(1')	3.312(1)	3.204(2)
X(1)–Cu(1)–X(1')	103.1(1)	100.0(1)
Cu(1)–X(1)–Cu(1')	76.9(1)	80.0(1)
Cu(1)–X(1')–Cu(1')	76.9(1)	80.0(1)
N(1)–Cu(1)–N(4)	96.0(1)	95.5(2)
$\sphericalangle(CuN_2;CuX_2)_{av}$	85.7(1)	85.3(1)
$\sphericalangle(CN_3;NC_3)_{av}$	7.1	6.5
ρ	0.96	0.95
τ_4	0.88	0.84

ρ = 2a/(b+c)[127] with a = C(1)–N(1), b = C(1)–N(2) and c = C(1)–N(3).

τ_4 = [360°-(α+β)]/141°[149] with α and β being the biggest two $\sphericalangle(CuR_2)$ angles.

The guanidine twist between the $C_{imine}N_3$-plane and the $N_{amine}C_3$-plane is with 6-7° comparable to other DMEG-based guanidine copper(I) complexes.[99] The structure parameter ρ was

calculated from the C–N bond lengths within the guanidine moiety, showing a good delocalization of the double bond within the guanidine unit.

Mixing of hybrid guanidine ligand **L2** and copper salt CuX (X = Br, Cl) in a ratio of 1:2 led to the formation of dimeric copper(I) salt adduct complexes [(**L2**)CuX·CuX]$_2$ (**C18**-**C19**, Scheme 23). Single crystals of **C18**-**C19**, suitable for X-ray diffraction, were grown by slow diffusion of pentane into a saturated solution of the complex in tetrahydrofuran (Figure 34). Selected bond lengths and angles are summarized in Table 18. Crystallographic details are provided in Table 47 in the appendix.

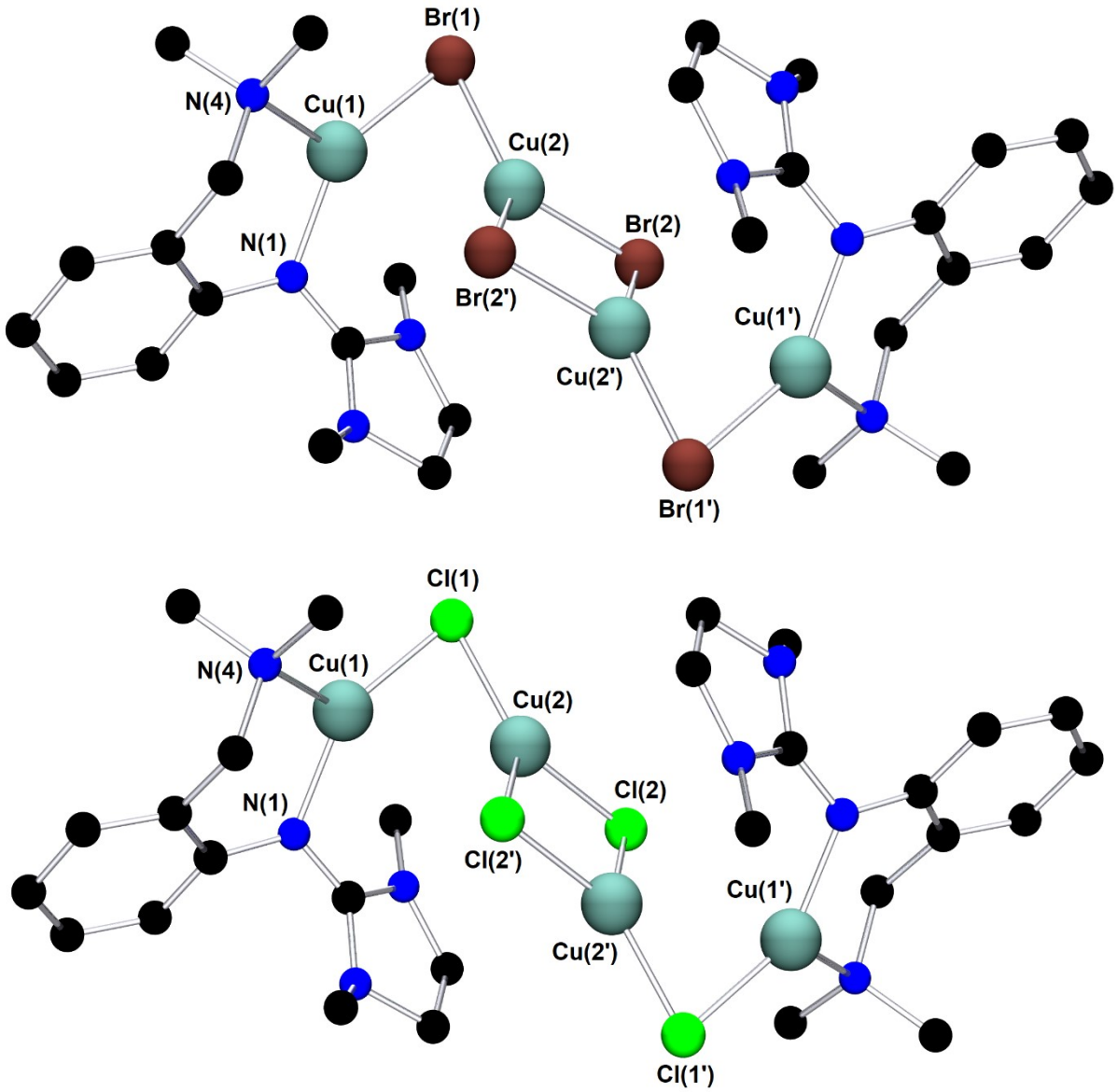

Figure 34: Molecular structures of **C18** (top) and **C19** (bottom) in the solid state. Hydrogen atoms were omitted for clarity.

The colorless blocks of **C18**-**C19** crystallize in the triclinic space group $P\bar{1}$ with one molecule in the asymmetric cell. The two copper atoms Cu(1) and Cu(1') are coordinated in a distorted trigonal fashion by the bidentate hybrid guanidine ligand **L2** and a halide. The chelate ligands

are orientated in *anti*-position. The center of the Cu_2X_2-plane of **C18**-**C19** resides on a crystallographically imposed inversion center. The bite angle N(1)–Cu(1)–N(4) of **L2** in dimeric complexes **C18**-**C19** (100°) is widened compared to the **L1**-stabilized monomeric complexes **C11**-**C12** (98-99°). The Cu–N(1) bond lengths are significantly shorter than the Cu–N(4) bond lengths in both complexes **C18**-**C19,** revealing the higher σ-donor strength of the guanidine unit compared to the amine donor function. The Cu(1)–X(1) bond lengths of **C18**-**C19** are elongated in comparison to the mononuclear complexes **C11** and **C12**, which results from the adduct complex formation. The Cu(1)···Cu(2) distance of complex **C18** (2.721(2) Å) is slightly longer than the distance in **C19** (2.707(1) Å), which is consistent with the longer Cu(1)–X(1) and Cu(2)–X(1) bond lengths of complex **C18**. The Cu···Cu distances in both complexes **C18**-**C19** are significantly larger than usual bonds between two copper(I) centers.[194] Interestingly, complexes **C18**-**C19** are the first examples of a tetranuclear copper(I) halide adduct species. The guanidine twist of the $C_{imine}N_3$-plane and the $N_{amine}C_3$-plane of the complexes **C18**-**C19** is with an average value of 7° comparable to other DMEG-based guanidine copper(I) complexes.[99] The structure parameter ρ was calculated from the C–N bond lengths within the guanidine moiety, showing a good delocalization of the double bond within the guanidine unit.

Table 18: Selected interatomic distances [Å], bond lengths [Å], angles [°] and the structure parameter ρ of **C18** and **C19**.

	C18	**C19**
Cu(1)–N(1)	1.967(8)	1.975(5)
Cu(1)–N(4)	2.111(8)	2.091(6)
Cu(1)–X(1)	2.332(2)	2.211(2)
Cu(2)–X(1)	2.375(2)	2.220(2)
Cu(2)–X(2)	2.408(2)	2.280(2)
Cu(1)···Cu(2)	2.721(2)	2.707(1)
Cu(2)···Cu(2')	2.774(3)	2.857(2)
X(1)–Cu(2)–Cu(2')	170.1(1)	174.1(1)
X(2)–Cu(2)–X(2')	110.2(1)	103.7(1)
Cu(2)–X(2)–Cu(2')	69.8(1)	76.3(1)
N(1)–Cu(1)–N(4)	100.5(3)	99.6(2)
N(1)–Cu(1)–X(1)	141.9(2)	143.6(2)
N(4)–Cu(1)–X(1)	117.1(2)	115.9(2)
$\sphericalangle(CN_3;NC_3)_{av}$	7.3	6.8
ρ	0.99	0.99

ρ = 2a/(b+c)[127] with a = C(1)–N(1), b = C(1)–N(2) and c = C(1)–N(3).

3.2.2. Cu(II) Complexes

Hybrid guanidine ligands also coordinate copper(II) halides. Conversion of **L1** and **L2** with equimolar amounts of copper(II) chloride in acetonitrile resulted in the formation of neutral monochelate copper(II) species [Cu(L)Cl_2] (**C20-C21**). Single crystals of **C20**-**C21**, suitable for X-ray diffraction, were grown by slow diffusion of diethyl ether into a saturated solution of the complex in acetonitrile (Figure 35). Selected bond lengths and angles are summarized in Table 19. Crystallographic details are provided in Table 48 in the appendix.

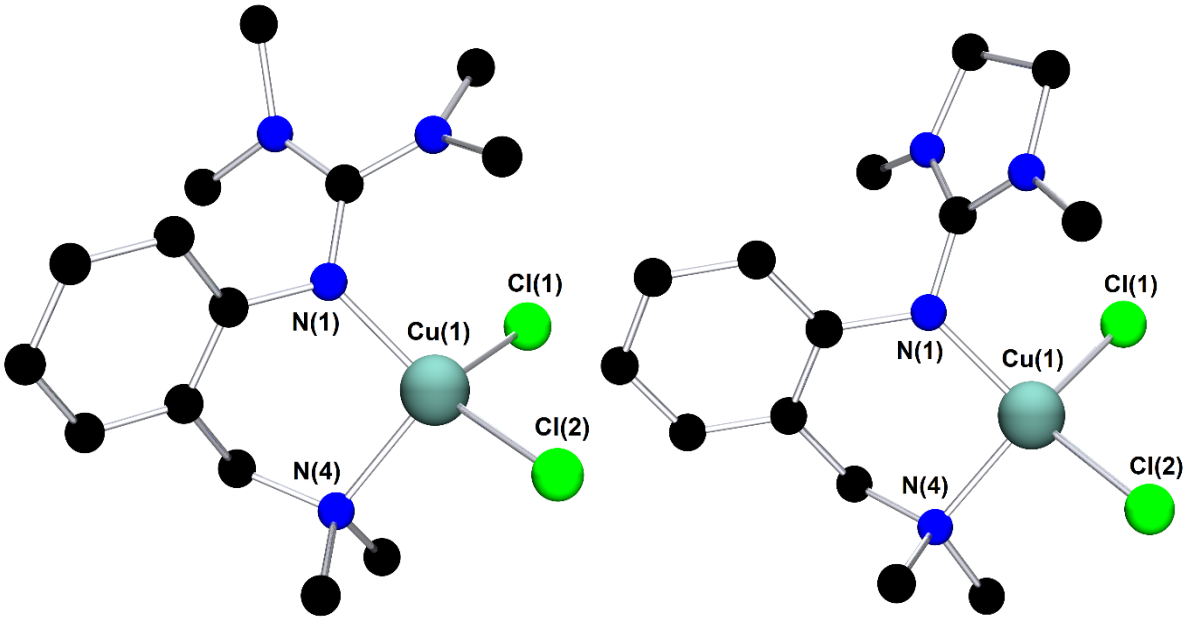

Figure 35: Molecular structures of **C20** (left) and **C21** (right) in the solid state. Hydrogen atoms were omitted for clarity.

The complexes crystallize in the monoclinic space group $P2_1/c$ (**C20**) and $P2_1/n$ (**C21**) with four molecules in the asymmetric unit. The central copper atom Cu(1) of the complexes **C20-C21** is coordinated in a distorted tetrahedral fashion by the bidentate hybrid guanidine ligands **L1** and **L2** and two halide donor moieties, which is described by the structural parameter τ_4 (0.60-0.70). The tetrahedral distortion is also reflected in the angle between the CuN_2- and $CuCl_2$-planes (56.7(1)-66.8(1)°), which deviates clearly from an ideal angle of 90°. Both complexes agree well with other guanidine copper(II) chloride complexes.[99,135] The Cu–N(1) and Cu–N(4) bond lengths of complexes **C20** and **C21** are similar within the error limits. The Cu–N(4) bond lengths are significantly elongated compared to the Cu–N(1) bond lengths, revealing the higher σ-donor character of the guanidine unit compared to the amine donor function. The differences in the Cu–Cl bond lengths and the N(1)–Cu(1)–N(4) bite angle between the complexes **C20** and **C21** are negligibly small. The guanidine twist of the $C_{imine}N_3$-plane and the $N_{amine}C_3$-plane is with 31° for the TMG-based complex **C20** significantly larger than the angle of the DMEG-based complex **C21** (5°). The structure parameter ρ was

calculated from the C–N bond lengths within the guanidine moiety, showing a full delocalization of the double bond within the guanidine unit.

Table 19: Selected bond lengths [Å], angles [°] and structure parameters of **C20** and **C21**.

	C20	**C21**
Cu(1)–N(1)	1.959(2)	1.959(2)
Cu(1)–N(4)	2.059(2)	2.028(2)
Cu(1)–X(1)	2.274(1)	2.249(1)
Cu(1)–X(2)	2.224(1)	2.247(1)
N(1)–Cu(1)–N(4)	96.0(1)	94.5(1)
$\sphericalangle(CuN_2;CuCl_2)_{av}$	66.8(1)	56.7(1)
$\sphericalangle(CN_3;NC_3)_{av}$	30.9	5.3
ρ	1.00	1.00
τ_4	0.70	0.60

ρ = 2a/(b+c)[127] with a = C(1)–N(1), b = C(1)–N(2) and c = C(1)–N(3).

τ_4 = [360°-(α+β)]/141°[149] with α and β being the biggest two $\sphericalangle(CuR_2)$ angles.

3.2.3. Dioxygen Activation

Previous studies on guanidine ligand-stabilized copper(I) halide complexes showed that they are capable of activating molecular oxygen to form reactive bis(μ-oxido) dicopper(III) species.[64,99,132,133,135] The applied copper(I) halide complexes only involve iodide as co-ligand. Herres-Pawlis and co-workers reported in 2005 a bis(guanidine)-stabilized bis(μ-oxido) iodide species, which decayed to form bis(μ-hydroxido) and bis(μ-alkoxido) species.[132] The latter revealed an additional iodide-bridge between the two copper centers in the molecular structure. These findings indicate the stabilization of the bis(μ-oxido) species by an iodide-bridge when iodide anions are present (*vide infra*). Moreover, no study investigated the behavior of bromide and chloride co-ligands with respect to the activation of dioxygen, although halide ligands including iodide, bromide and chloride should show similar properties being easily abstractable X-type ligands.

The aromatic hybrid guanidine ligands TMGbenza (**L1**) and DMEGbenza (**L2**) were already tested in the oxygenation reactions of the corresponding copper(I) iodide complexes as a part of the master thesis. Both copper(I) iodide complexes showed their activity towards dioxygen.[154] Therefore, the reactivity of copper(I) halide complexes **C10-C12** towards dioxygen was analyzed systematically to evaluate the influence of different halide co-ligands on the formation of bis(μ-oxido) dicopper(III) species. Activation of molecular oxygen was achieved by bubbling dioxygen through a tetrahydrofuran solution and subsequently injecting

a solution of the copper(I) species **C10-C12** in acetonitrile (Scheme 24). The oxygenation reaction was followed by UV/Vis spectroscopy.

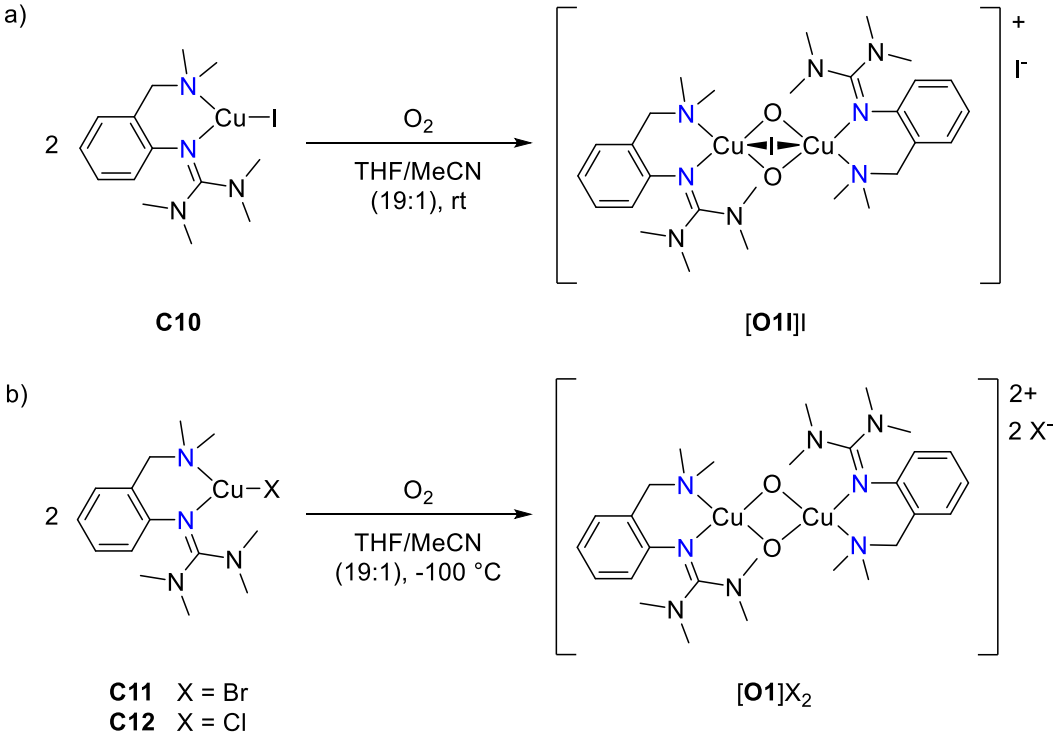

Scheme 24: Oxygenation of monochelate copper(I) complexes **C10**-**C12**.

The oxygenation of monochelate species **C10** was repeated to validate previous results. The reaction was performed in a tetrahydrofuran/acetonitrile mixture at room temperature for three hours, leading to an immediate color change from colorless to reddish-brown. Selected UV/Vis spectra of the reaction are depicted in Figure 36 for clarity. The UV/Vis spectrum displays two ligand-to-metal charge transfer bands at 290 nm and 370 nm, which are in the characteristic range of bis(μ-oxido) species.[10,11] The high extinction at 290 nm is caused by overlapping in-plane π_{σ^*} to d_{xy} and π to π* transitions of the aromatic backbone of **L1**. Additionally, the weaker CT bands at 450 nm and 570 nm were assigned to the guanidine π-system, causing the red color of the bis(μ-oxido) species [**O1I**]$^+$, which was also observed for other bis(μ-oxido) species.[47] Complex **C10** was also oxygenated at –80 °C, showing similar UV/Vis features in comparison to the formation at room temperature (Figure 77). The absorption band at 370 nm documents a blueshift by 20 nm relative to the related system [**O1**]$(PF_6)_2$, which shows spectral features at 280 nm (40000 M^{-1} cm^{-1}) and 392 nm (21000 M^{-1} cm^{-1}, see section 3.1.3). The blueshift was assigned to a possible coordinating iodide anion, which influences the complex cation and therefore its spectral features.

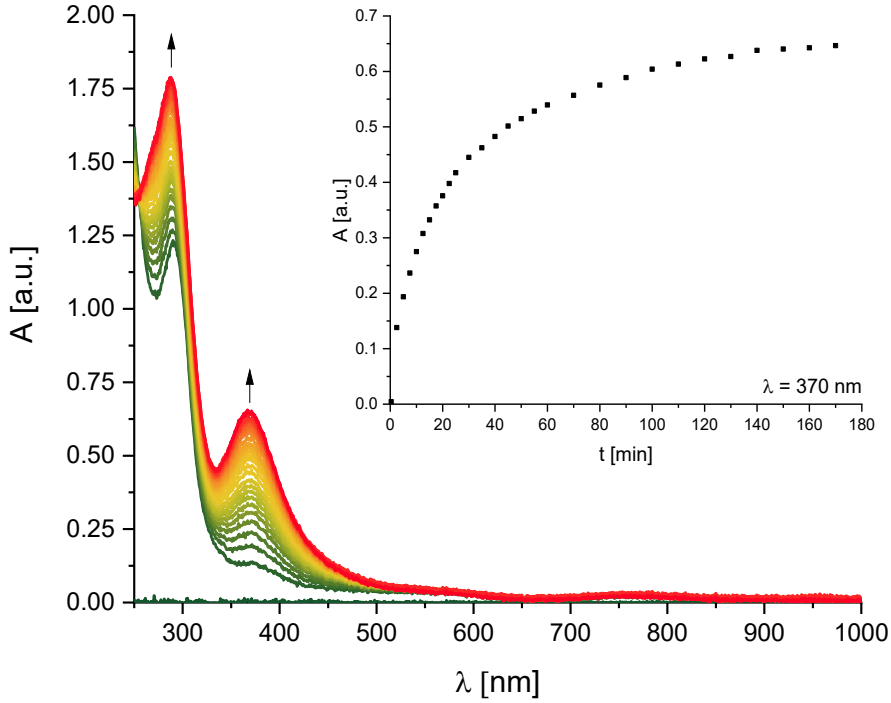

Figure 36: Selected UV/Vis spectra of the oxygenation of **C10** to give the bis(μ-oxido) complex [**O1I**]$^+$ (0.5 mM) in tetrahydrofuran at room temperature (Inset: time-resolved formation monitored at 370 nm).

In comparison to the bis(μ-oxido) complex [**O1**](PF$_6$)$_2$, however, it is conspicuous that the extinction of the absorption bands is significantly lower than expected from previous data, indicating an incomplete formation of the bis(μ-oxido) species (65%). Since copper iodide species are known for the formation of iodidocuprate clusters [Cu$_y$I$_{x+y}$]$^{x-}$[195–197] several titration experiments were performed to investigate the formed bis(μ-oxido) species and its potential anions (Figure 37). For this purpose, the bis(μ-oxido) species [**O1I**]$^+$ was synthesized and subsequently titrated with different additives. Upon titration of [**O1I**]$^+$ with hybrid guanidine ligand **L1** the absorption bands of [**O1I**]$^+$ remained constant, revealing no effect of additional ligand on the bis(μ-oxido) species (Figure 37a). Similarly, unchanged UV/Vis features were observed upon titration with iodide source tetrabutylammonium iodide, showing no influence of the amount of iodide on [**O1I**]$^+$ (Figure 37b). The titration of [**O1I**]$^+$ with one and two equivalents of copper salt [Cu(MeCN)$_4$]PF$_6$ resulted in a marginal decrease of the absorption band at 370 nm (Figure 37c), resulting from a slight diluting effect during the addition of copper salt.

When bis(μ-oxido) species [**O1I**]$^+$ is titrated with equivalents of copper iodide (Figure 37d), a slight color change to deeper reddish-brown was observed. The absorption band at 370 nm increased significantly upon addition of one as well as two equivalents of copper iodide and remained approximately constant upon addition of a third equivalent of copper iodide. Consequently, two equivalents of copper iodide are necessary to achieve quantitative formation of the bis(μ-oxido) species, which indicates the formation of iodidocuprate anions with a copper-to-iodine ratio of 1:2 in the outer sphere of the complex cation [**O1I**]$^+$. Therefore,

the complete formation of the bis(μ-oxido) complex is accompanied by the presence of small iodidocuprate anions with the stoichiometry twice $[CuI_2]^-$ or $[Cu_2I_4]^{2-}$.

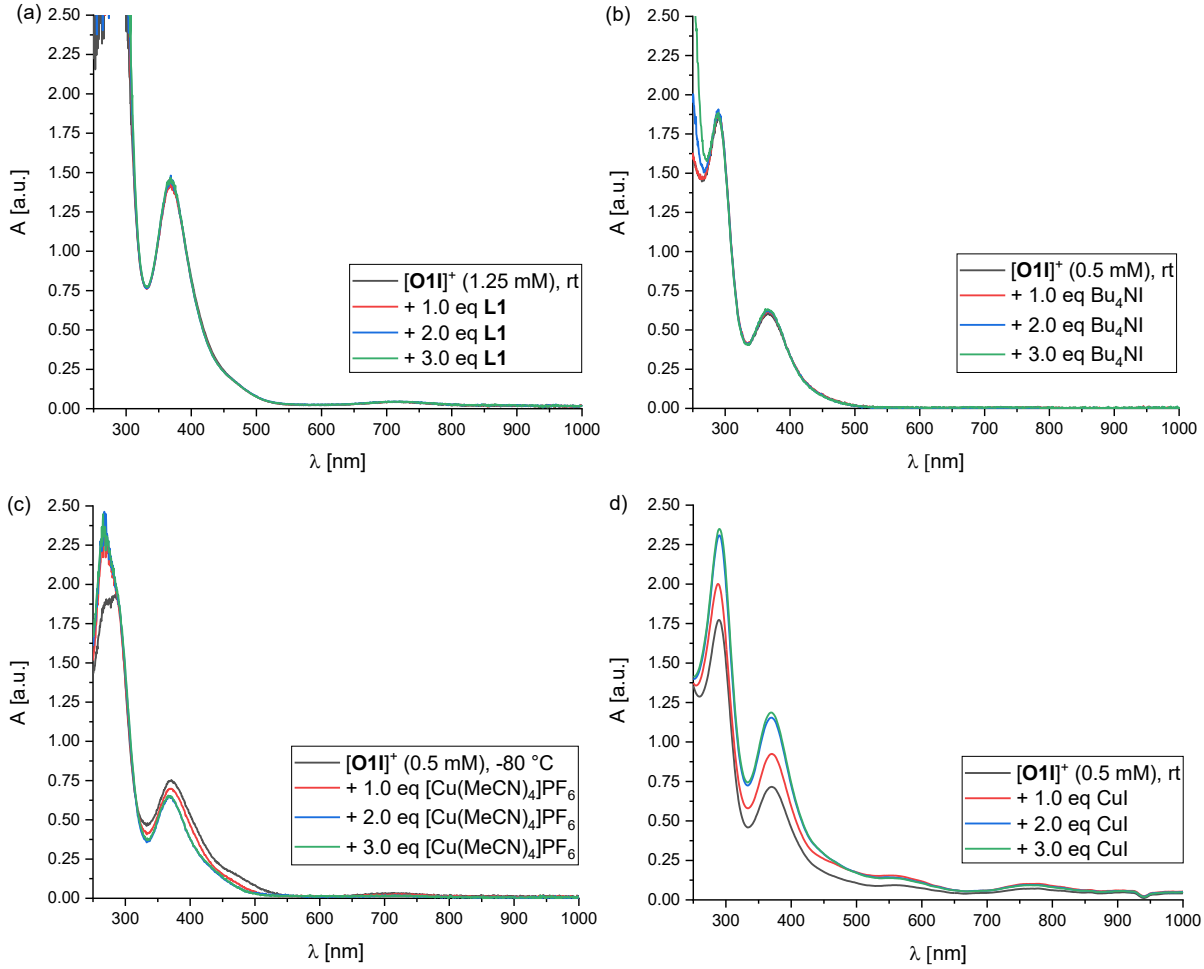

Figure 37: UV/Vis spectra of the titration experiments of **[O1I]**$^+$ with the titrant (a) **L1**, (b) Bu_4NI, (c) $[Cu(MeCN)_4]PF_6$ and (d) CuI.

Direct oxygenation of the copper(I) adduct **C10**·CuI confirmed these findings, showing similar absorption features at 290 nm (50000 M^{-1} cm^{-1}) and 370 nm (22000 M^{-1} cm^{-1}) in the UV/Vis spectrum (Figure 76 in the appendix). The extinction coefficient of **[O1I]**(CuI_2) is slightly higher than the one of **[O1]**$(PF_6)_2$, which is in line with the introduction of an iodide bridge, modifying the bis(μ-oxido) cation and therefore the extinction coefficient. The absorption bands at 450 nm (4300 M^{-1} cm^{-1}) and 570 nm (1700 M^{-1} cm^{-1}) were more intense compared to the oxygenation of **C10**, which is in accordance with the more intense red color of the reaction solution, caused by the interaction of the iodidocuprate anion and the guanidine π-system (see DFT section, *vide infra*). ^{1}H NMR measurements depicted only marginal differences between **C10** and **C10**·CuI (Figure 82 in the appendix), which is ascribed to a very similar chemical environment enabling the formation of the same bis(μ-oxido) complex **[O1I]**(CuI_2). The LMCT bands of **[O1I]**(CuI_2) were stable for at least seven days which is remarkable as most bis(μ-oxido) complexes are only stable at very low temperatures.[10,11] The stability of a bis(guanidine)-stabilized bis(μ-oxido) complex was limited to temperatures below -40 °C, although iodide co-

ligands were involved and the decomposition product was identified as iodide-bridged bis(μ-alkoxido) species in the molecular structure.[132,133] Herres-Pawlis, Rübhausen, Meyer-Klaucke and co-workers reported in 2009 a bis(μ-oxido) complex stabilized by a bulky piperidinyl-substituted bis(guanidine) ligand in the presence of iodide counterions.[64] The bis(μ-oxido) complex also exhibited the extraordinary room temperature stability, which was redirected to the sterically demanding ligand system and to the inhibited intramolecular hydroxylation due to the missing protons in α-position to the guanidine donor groups.[64] Both arguments disagree with ligand system **L1** because the ligand is significantly smaller than the reported system from 2009 and possible intramolecular hydroxylation of the ligand was exemplified by [**O1**]$(PF_6)_2$ and [**O1**]$(BF_4)_2$ (see Figure 28 and Scheme 17 for comparison). Therefore, the high stability of bis(μ-oxido) complex [**O1I**](CuI_2) presumably results from the support of the iodidocuprates formed and/or the iodide bridge.

For the investigation of the properties of the formed bis(μ-oxido) species in the presence of halide co-ligands, the copper(I) halide complexes **C11-C12** were oxygenated to form the bis(μ-oxido) complexes [**O1**]X_2 (X^- = Br^-, Cl^-) in tetrahydrofuran at –100 °C. The reaction was followed by UV/Vis spectroscopy (Figure 38).

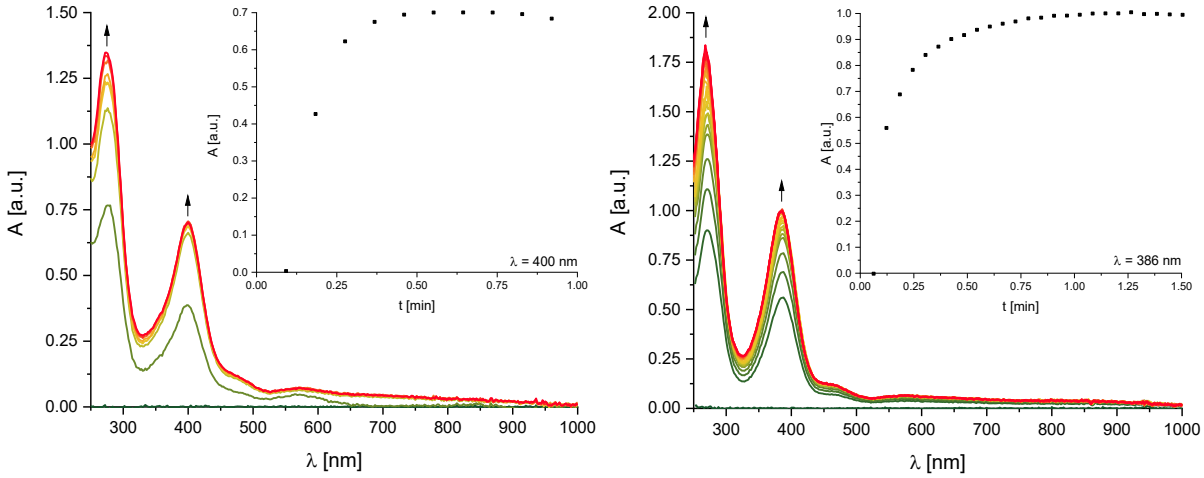

Figure 38: UV/Vis spectra of the oxygenation of **C11** (left) and **C12** (right) to give the bis(μ-oxido) complex [**O1**]X_2 (X^- = Br^-, Cl^-; 0.5 mM) in tetrahydrofuran at –100 °C (Inset: time-resolved formation of [**O1**]Br_2 and [**O1**]Cl_2 monitored at 400 nm and 386 nm).

After the injection of complexes **C11-C12** the reaction solution turned green immediately, which was also observed upon the formation of [**O1**]$(PF_6)_2$ (see section 3.1.3). The bis(μ-oxido) complexes [**O1**]Br_2 and [**O1**]Cl_2 were formed within seconds at –100 °C and decayed very quickly afterwards, which reveals the high reactivity of these species. Complex [**O1**]Br_2 exhibited LMCT bands at 270 nm (50000 M^{-1} cm^{-1}) and 399 nm (21000 M^{-1} cm^{-1}) in the UV/Vis spectrum. Here, no quantitative formation of [**O1**]Br_2 (70%) was observed due to a faster decay rate compared to the formation rate. For a complete formation of [**O1**]Br_2, the reaction should be performed at lower temperatures to inhibit the competitive decomposition reaction. Compound [**O1**]Cl_2 depicted comparable UV/Vis features at 270 nm (50000 M^{-1} cm^{-1}) and

386 nm (21000 M^{-1} cm^{-1}). Upon thermal decomposition of the species [**O1**]Br_2 and [**O1**]Cl_2, the reaction solution discolored to yellow. The properties of [**O1**]$(X)_2$ (X^- = PF_6^-, Br^-, Cl^-) and [**O1I**](CuI_2) are summarized in Table 20. The spectral features of complexes [**O1**]Br_2 and [**O1**]Cl_2 agree well with the properties of [**O1**]$(PF_6)_2$, revealing no hint for a halide-bridged species. Therefore, they differ significantly from the iodide-bridged species [**O1I**](CuI_2), which presumably results from the smaller anion size of bromide and chloride compared to iodide. All these findings indicate that the stabilization of the bis(μ-oxido) species by the iodide-bridge is more significant than by the formed iodidocuprates.

Table 20: UV/Vis features of [**O1**]$(X)_2$ (X^- = PF_6^-, Br^-, Cl^-) and [**O1I**](CuI_2) in tetrahydrofuran.

	λ [nm]	**ε [M^{-1} cm^{-1}]**	**λ [nm]**	**ε [M^{-1} cm^{-1}]**	**color**
[**O1**]$(PF_6)_2$	392	21000	280	40000	green
[**O1I**](CuI_2)	370	22000	290	50000	reddish-brown
[**O1**]Br_2	399	21000	270	50000	green
[**O1**]Cl_2	386	21000	270	50000	green

In contrast to monochelate copper(I) complexes, bischelate copper(I) complexes should be resistant to molecular oxygen due to their saturated coordination sites. The formation of bischelate complexes stabilized by **L1** and **L2** was already observed in the presence of weakly coordinating anions, caused by the restricted bite angle of the ligand (see section 3.2.1). Therefore, a solution of bischelate copper(I) halide complexes **C13**-**C15** was oxygenated to evaluate the reactivity of bischelate copper(I) complexes towards dioxygen at low temperatures with the help of UV/Vis spectroscopy. The formed species showed similar UV/Vis features with respect to the oxygenated monochelate copper(I) complexes **C10**-**C12**. An exception was the obtained extinction, which was with a maximum of approximately 50% quantity significantly lower. The observations made during the oxygenation process of bischelate species indicate a predominant dynamic equilibrium between monochelate and bischelate copper(I) species in solution (Scheme 25). The proposed mechanism of the dynamic equilibrium is illustrated in Scheme 25. In a first step (a), the neutral monochelate species forms ion pairs in the polar solvent acetonitrile. The excess of acetonitrile forms a solvation shell around the complex cation so that the solvent saturates the free coordination site of the copper center (step (b)). Next, two fragments rearrange to form a more stable bischelate copper(I) complex and a copper(I) halide (step(c)). The rearrangement is favored due to a suitable bite angle of the ligand **L1** and a preferred coordination number of copper(I) species of four (over three). Additionally, the amine and guanidine donor moieties function as stronger Lewis bases compared to acetonitrile. The released copper(I) halide is presumably solvated by acetonitrile. In the next step (d), the copper(I) halide interacts with the central

copper atom of the bischelate species, reducing the electron density at the copper atom of CuX. Finally, the halide reacts with the polarized CuX to form a halidocuprate anion (Lewis acid-base reaction), which supports the bischelate complex. If only a monochelate complex reacts with dioxygen, the equilibrium is forced to adjust constantly. The equilibrium is assumed to adjust slowly for X^- = I^-, as the formation of [**O1I**](CuI_2) took several hours. For X^- = Br^-, Cl^-, the equilibrium apparently exhibits a very dynamic behavior, which is concluded from the fast formation kinetics of [**O1**]Br_2 and [**O1**]Cl_2.

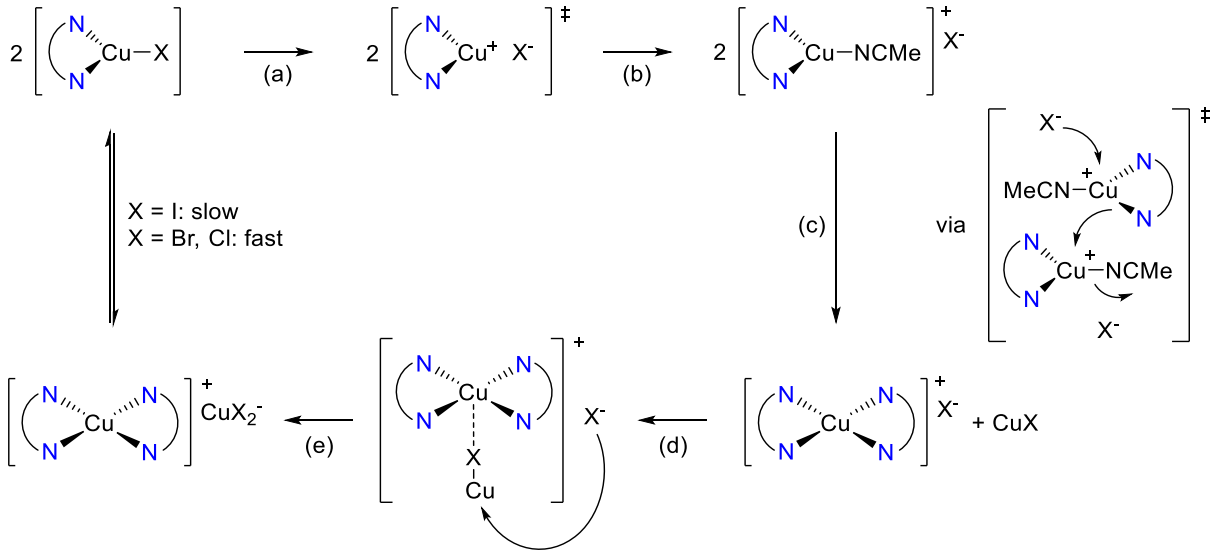

Scheme 25: Proposed mechanism of the dynamic equilibrium between monochelate and bischelate copper(I) halide complexes in solution.

The dynamic equilibrium between monochelate and bischelate copper(I) halide complexes in solution was further investigated by using cryo-UHR-ESI mass spectrometry to observe intermediate species of the proposed mechanism. Oxygenation reactions of **C10**-**C12** were measured at –100 °C immediately after the injection of copper(I) complex solution and again after approximately three minutes. When complexes **C10**-**C12** were oxygenated, the isotopic pattern and corresponding m/z value of $[Cu(\mathbf{L1})_2]^+$ were found immediately after the injection in all three mass spectra in the positive mode. Accordingly, the isotopic pattern and corresponding m/z values of $[CuX_2]^-$ were observed in the negative mode in all cases. The intensity of these signals declined after a few minutes and the formation of the bis(μ-oxido) species [**O1**]$(X)^+$ was observed. The intensity of the observed monochelate species $[Cu(\mathbf{L1})]^+$ and $[Cu(\mathbf{L1})(MeCN)]^+$ was very low during both measurement times for all three oxygenation reactions. In addition, the mass spectra of the oxygenation reactions of both **C10** and **C10**·CuI revealed the isotopic pattern of the monocationic species [**O1I**]$^+$ and [**O1**]$(CuI_2)^+$ in the positive mode (Figure 39). In the negative mode, the isotopic pattern and respective m/z values of $[CuI_2]^-$ and iodide were observed in both oxygenation reactions. Similarly, the isotopic pattern and corresponding m/z values of the oxygenation of **C11** and **C12** were obtained, exhibiting the mass spectrum of the monocationic species [**O1**]$(Br)^+$ and [**O1**]$(Cl)^+$ in the positive mode

(Figure 69 and Figure 70 in the appendix). Interestingly, solely bromido- and chloridocuprate anions were detected in the negative mode during both measurement times when oxygenating **C11** and **C12**. Bromide and chloride were observed in neither case.

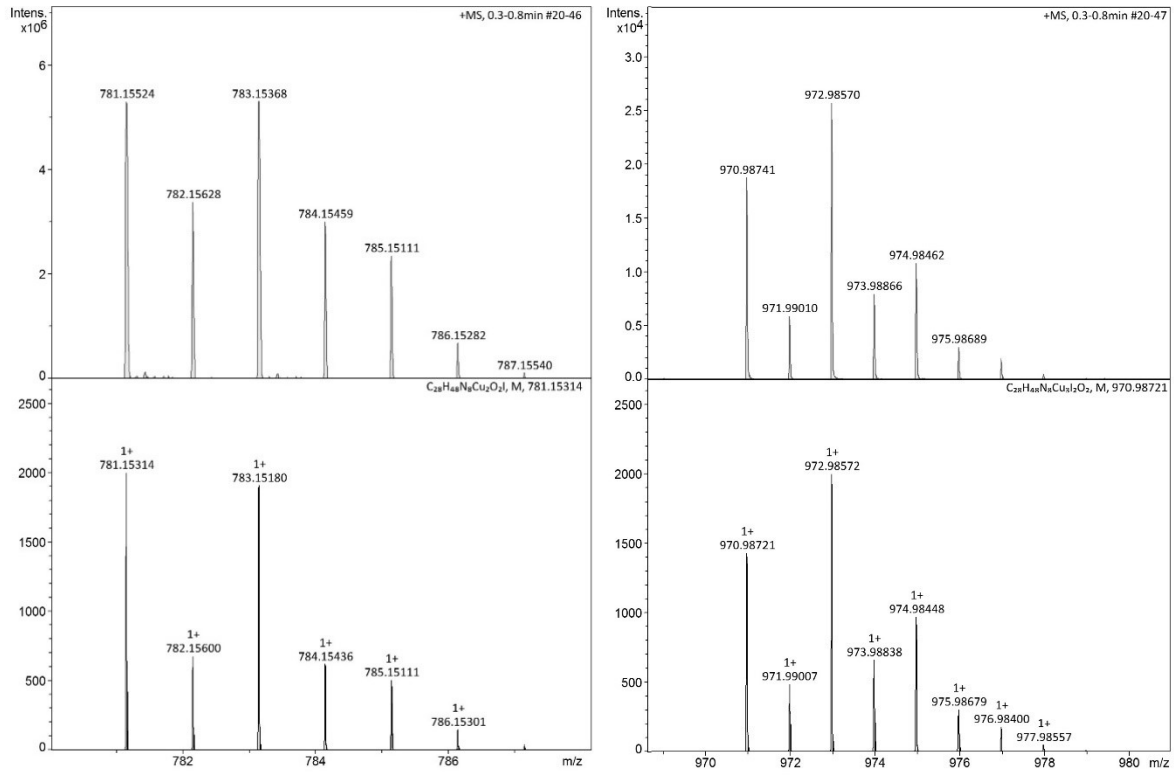

Figure 39: Cryo-UHR-ESI mass spectrometry of [**O1I**]$^+$ (left) and [**O1**](CuI$_2$)$^+$ (right) in tetrahydrofuran at –80 °C, which were observed in the oxygenation of **C10** and **C10**·CuI (top: experimental, bottom: calculated spectra).

These findings support the interpretation of an occurring predominant dynamic equilibrium (Scheme 25). The decreasing amount of bischelate complex cation found and the increasing intensity of bis(μ-oxido) species [**O1I**]$^+$ and [**O1**](X)$^+$ (X$^-$ = Br$^-$, Cl$^-$) correlates to a constantly adopting equilibrium, in which the monochelate species is consumed. This is also in accordance with a constantly small amount of monochelate species observed. Moreover, the related mass spectra of the oxygenation reactions of **C10** and **C10**·CuI show a similar oxygenation process. The occurrence of iodidocuprate anions which stabilize the bis(μ-oxido) core was encouraged in both cases. For the oxygenated species **C11** and **C12**, the high intensity of [Cu(**L1**)$_2$]$^+$ and still very fast formation of the bis(μ-oxido) species [**O1**]Br$_2$ and [**O1**]Cl$_2$ underline the highly dynamic behavior of the equilibrium for X$^-$ = Br$^-$, Cl$^-$. The occurrence of solely [CuX$_2$]$^-$ anions (X$^-$ = I$^-$, Br$^-$, Cl$^-$) can be referred to the higher stability of monomeric halidocuprates in solution as larger clusters of halidocuprates were often observed in the solid state.[197,198] Moreover, it is also possible that the used electrospray ionization method is more efficient in generating gas phase ions [CuX$_2$]$^-$ compared to larger anions.

Considering the formation characteristics, the UV/Vis features, and the obtained mass spectra, the bis(μ-oxido) complexes [**O1**]Br_2 and [**O1**]Cl_2 are apparently very similar to [**O1**]$(PF_6)_2$. It is conspicuous that [**O1I**](CuI_2) stands out for its stability, color, and spectroscopic properties, which is likely caused by the present iodide-bridge stabilizing the bis(μ-oxido) complex. The difference in behavior in dependence of the present halide can be explained by the bonding character of the halide to the copper atom due to the different ionic radii [199] and therefore different anion sizes, which also influence the formation of a halide bridge. On the one hand, the Cu–I bond reveals the highest covalency within the copper halides analyzed, which impedes iodide dissociation (Scheme 25, step (a)). Thus, the major occurrence of the monochelate species is favored, which slowly reacts with dioxygen to the bis(μ-oxido) dicopper(III) complex containing an additional iodide-bridge.[132] It is also possible that the slow formation of the bis(μ-oxido) bridge in complex [**O1I**]$^+$ occurs via an iodide-bridged dicopper(I) intermediate, so that dioxygen has to orientate itself accordingly prior to the reaction. Bromide and chloride, on the other hand, are significantly smaller than iodide and reveal a more ionic bond character to the copper(I) center, which facilitates the dissociation process. The combination of the dynamic equilibrium of monochelate and bischelate copper(I) species in solution and the reaction of copper(I) species with dioxygen reveals the complexity of the occurring reaction mechanism. Canton, Vetrone and co-workers showed an increasing interaction of the halides with the metal with the increasing ion size and polarizability from chloride to iodide, thus influencing the structure and properties of copper indium sulfide quantum dots.[200] Nevertheless, the scarcity of reported studies on the halide influence on metal complexes and especially Cu_2O_2 species in the presence of halide species complicates the investigation of the reaction mechanism. The full details of the activation of dioxygen with copper(I) halide complexes remains unclear and needs to be further studied.

In the next step, DFT calculations were performed by Dr. Alexander Hoffmann to evaluate the influence of the iodide on the bis(μ-oxido) species [**O1I**]$^+$. The iodide ligand is expected to form a bridge between the two copper(III) centers, thus stabilizing the bis(μ-oxido) species by reducing the charge of the cation. Simulations are based on the hybrid meta GGA functional TPSSh[157–159] combined with the triple-valence basis set def2-TZVP[160–163] and empirical dispersion corrections with the Becke-Johnson damping GD3BJ.[164–167] Calculated geometric parameters of the theoretical bis(μ-oxido) species [**O1I**]$^+$ are summarized in Table 21 and compared to obtained data of bis(μ-oxido) species [**O1**]$^{2+}$ (see Table 7). Simulations confirm the presence of an iodide-bridged bis(μ-oxido) species (Figure 40), enforcing a slight fold of the normally planar Cu_2O_2 center along the O···O axis. The distortion results in a butterfly-shaped Cu_2O_2 core, which stabilizes the bis(μ-oxido) species (see Table 21 for comparison). This structure motif was also observed in the bis(μ-alkoxido) dicopper(II) complex of another guanidine system.[132]

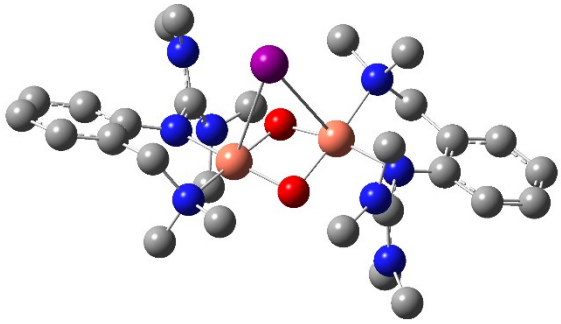

Figure 40: Calculated structure of [**O1I**]$^{+}$ (TPSSh/def2-TZVP, GD3BJ, THF-PCM).

Selected geometric parameters of bis(μ-oxido) species [**O1I**]$^{+}$ and [**O1**]$^{2+}$ show small discrepancies upon introduction of the iodide-bridge. The butterfly distortion of [**O1I**]$^{+}$ causes a significantly shortened Cu···Cu distance, but comparable Cu–O bond lengths and a similar O···O distance with respect to [**O1**]$^{2+}$. The simulated Cu–N_{gua} and Cu–N_{amine} bond lengths are comparable to other hybrid guanidine amine and bis(guanidine)-supported bis(μ-oxido) species.[47,99,135] While the Cu–N_{amine} bond lengths of both bis(μ-oxido) species [**O1I**]$^{+}$ and [**O1**]$^{2+}$ are nearly identical, the Cu–N_{gua} bond lengths differ significantly. In complex [**O1I**]$^{+}$, the Cu–N_{gua} bond lengths are elongated compared to those in [**O1**]$^{2+}$ which is presumably caused by the additional stabilization of the Cu_2O_2 core in [**O1I**]$^{+}$ by the iodide. As a result, the compression of the Cu_2O_2 core caused by the introduced iodide-bridge is seemingly responsible for the extraordinary stability of bis(μ-oxido) species [**O1I**]$^{+}$.

Table 21: Geometric parameters of the theoretical bis(μ-oxido) complex [**O1I**]$^{+}$ (TPSSh/def2-TZVP, GD3BJ, THF-PCM) in comparison to bis(μ-oxido) complex [**O1**]$^{2+}$ (see section 3.1.3). The calculated structure of the complex [**O1I**]$^{+}$ is illustrated in Figure 40. Bond lengths to the same copper atom are separated by comma, otherwise by semicolon.

	[O1]$^{2+}$	**[O1I]$^{+}$**
Cu···Cu [Å]	2.750	2.689
Cu–O [Å]	1.800, 1.806; 1.801, 1.804	1.810, 1.805; 1.805, 1.803
O···O [Å]	2.331	2.328
Cu–I [Å]	-	3.395; 3.511
Cu–N_{gua} [Å]	1.914; 1.915	1.930; 1.925
Cu–N_{amine} [Å]	1.963; 1.965	1.963; 1.966

TD-DFT simulations were performed by Dr. Alexander Hoffmann to get a deeper insight into the experimentally observed blueshift of the characteristic absorption bands of the bis(μ-oxido) species [**O1I**]$^{+}$ and [**O1**]$^{2+}$ in the UV/Vis spectra. Figure 41 shows the molecular orbital and energy correlation of the bis(μ-oxido) species [**O1**]$^{2+}$ (left) and [**O1I**]$^{+}$ (right), revealing the electronic differences caused by the introduction of the iodide-bridge.

The experimentally found absorption band at 392 nm (TD-DFT: 366 nm) of [**O1**](PF$_6$)$_2$ is caused by the transition of HOMO-8, which results from the bonding interaction of the Cu d orbitals with the σ* orbital, to LUMO+1, which results from the antibonding interaction of the Cu d orbitals with the π_σ* orbital. The experimentally observed transition at 280 nm (TD-DFT: 320 nm) of [**O1**](PF$_6$)$_2$ stems from the transition of HOMO-13 to LUMO. HOMO-13 consists of the bonding interaction of the Cu d orbitals with the π_σ* orbital, whereas the LUMO represents the antibonding interaction of the Cu d orbitals with the σ* orbital. These transitions are characteristic for bis(μ-oxido) species and were also observed for other guanidine-supported bis(μ-oxido) species.[47,201] In addition to these classical transitions, two further transitions from HOMO-9 and HOMO-11 to LUMO were found. HOMO-9 results from the bonding interaction of the Cu d orbitals with the σ orbital (TD-DFT: 400 nm). HOMO-11 is caused by the antibonding interaction of the Cu d orbitals with the σ* orbital (TD-DFT: 342 nm). Weaker transitions of 509 nm, 549 nm and 809 nm can be related to transitions from the lone pair of the N_{amine} to LUMO or LUMO+1 and from the π* orbitals of the ligand to LUMO.

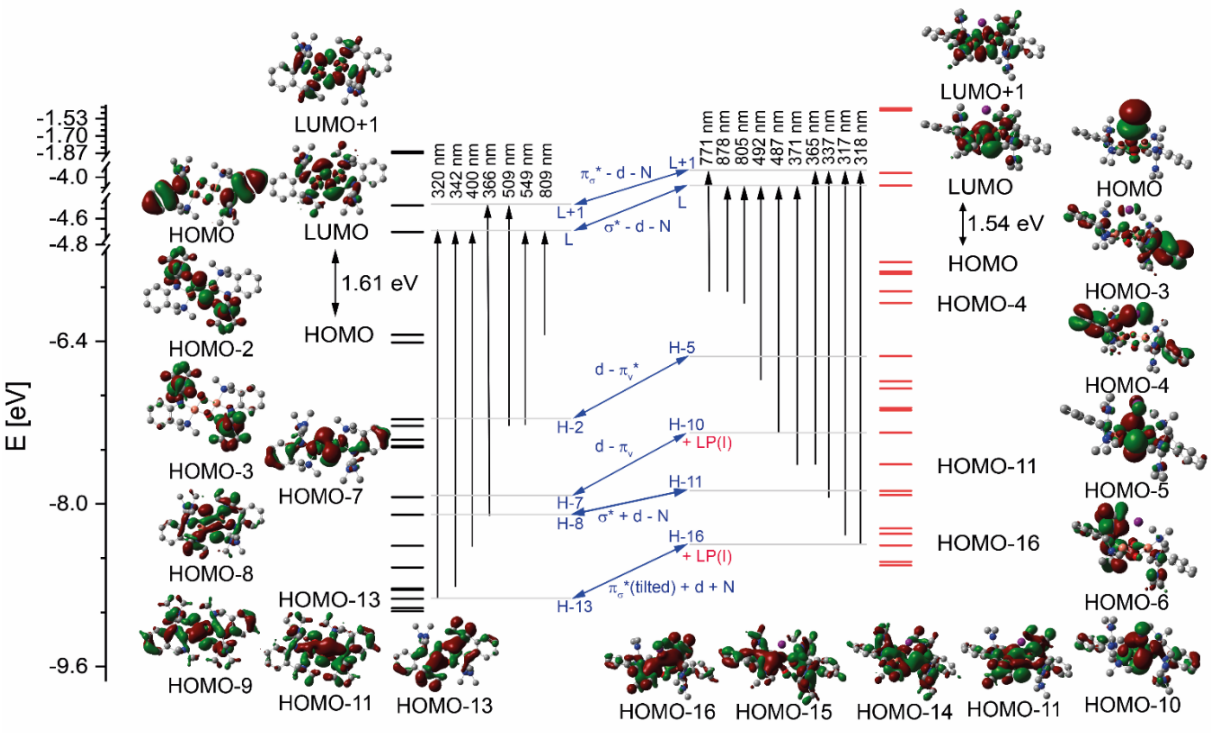

Figure 41: Molecular orbital and energy correlation of the bis(μ-oxido) species [**O1**]$^{2+}$ (left) and [**O1I**]$^{+}$ (right). Main excitations are summarized (calculated by TD-DFT). The corresponding interactions of the MO and the influence of the iodide on the UV/Vis spectra (middle) are presented.

Upon introduction of the iodide-bridge a more complex MO scheme of [**O1I**]$^{+}$ was found due to the involvement of the lone pairs of the iodide. The three lone pairs (HOMO, HOMO-1 and HOMO-2) cause a shift of three orbitals in comparison to the bis(μ-oxido) species [**O1**]$^{2+}$. Therefore, both HOMO-2 in [**O1**]$^{2+}$ and HOMO-5 in [**O1I**]$^{+}$ can be related to the antibonding interaction of the Cu d orbitals and the π_v* orbital of the bis(μ-oxido) moiety (see Table 51 and

Table 52 for comparison). The iodide-bridged species [**O1I**]$^+$ exhibited only one classical transition from HOMO-11 to LUMO+1. HOMO-11 results from the bonding interaction of the Cu d orbitals with the σ^* orbital, whereas LUMO+1 stems from antibonding interactions of Cu d orbitals with the π_σ^* orbital. Iodide contributions were observed in transitions at 318 nm and 337 nm. The intense transition at 318 nm is caused by bonding interactions of the π_σ^* orbital, Cu d orbitals and the LP of the iodide (HOMO-16) with LUMO+1. The transition at 337 nm is evoked by transitions from HOMO-14 and HOMO-16 to LUMO. Additionally, two other transitions in the classical region were found at 317 nm and 371 nm. The transition at 317 nm results from the transition of HOMO-15 (bonding interaction of the linear combination of π_v, π_σ and Cu d orbitals) to the LUMO+1. The transition from HOMO-11 to LUMO causes the transition at 371 nm.

The experimental UV/Vis spectrum showed a tailing around 379 nm which is caused by two transitions: a transition from the HOMO-10 to the LUMO, which stems from antibonding interactions of the Cu d orbitals with the π_v orbital and bonding interactions with the LP of the iodide, and a transition from HOMO-6 to LUMO+1, which originate from π^* orbitals of the guanidine moiety. Transitions at higher wavelengths were also found, which can be redirected to interactions of the ligand **L1**: two interactions of the π^* orbitals (HOMO-3) to LUMO+1 (771 nm) and LUMO (878 nm) as well as one of the π^* orbitals in combination with the LP of the iodide (HOMO-4) to LUMO (805 nm). Thus, the TD-DFT study explains the different UV/Vis spectra of [**O1**]$^{2+}$ and [**O1I**]$^+$ caused by the lone pairs of the iodide-bridge.

The unusual high stability of iodide-bridged bis(μ-oxido) species [**O1I**](CuI_2) at room temperature compared to its very similar relative [**O1**]$(PF_6)_2$ raised the question of a possible interconvertibility of both species. For this purpose, salt metathesis experiments were conducted by titration of the bis(μ-oxido) complex [**O1**]$(PF_6)_2$ with different halide sources Bu_4NX (X^- = I^-, Br^-, Cl^-; Scheme 26). The temperature of the titration reaction was adjusted depending on the least stable species.

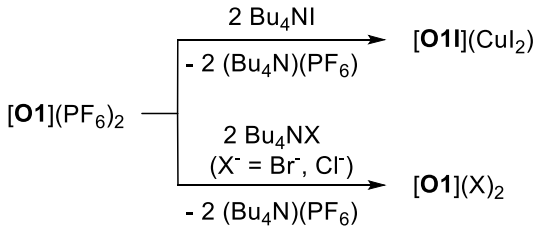

Scheme 26:: Salt metathesis of bis(μ-oxido) complex [**O1**]$(PF_6)_2$ with halide sources Bu_4NX (X^- = I^-, Br^-, Cl^-).

The salt metathesis was tested by using an iodide source to generate the iodide-bridged bis(μ-oxido) species [**O1I**](CuI_2) by exchanging the counterions. Starting from the green

species [**O1**](PF$_6$)$_2$ in tetrahydrofuran at –90 °C, aliquots of tetrabutylammonium iodide were added stepwise and the reaction was followed by UV/Vis spectroscopy (Figure 42).

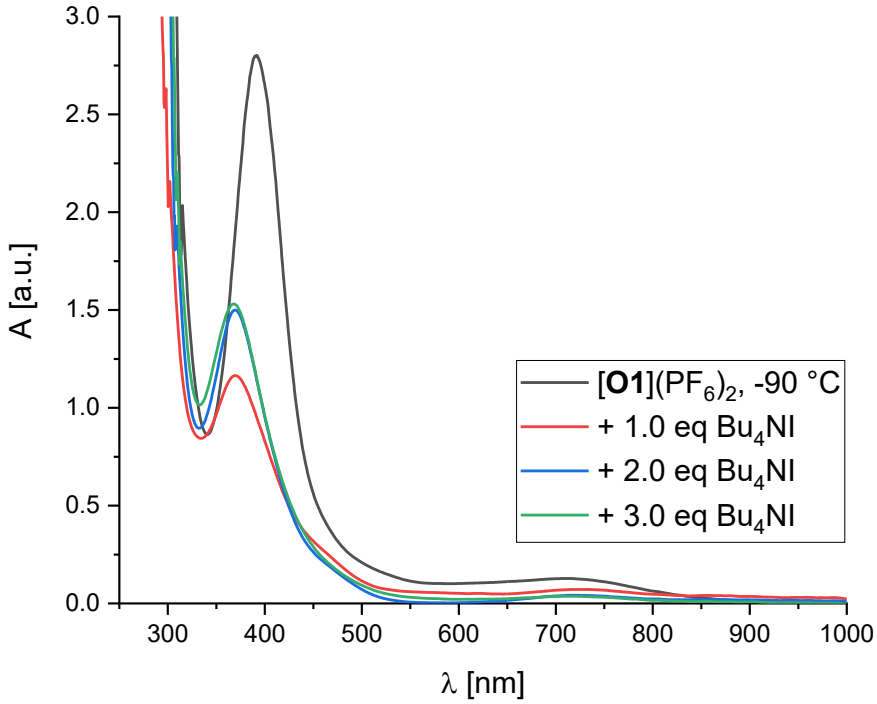

Figure 42: UV/Vis spectra of the salt metathesis of [**O1**](PF$_6$)$_2$ (1.25 mM) with Bu$_4$NI in tetrahydrofuran at –90 °C.

Addition of one equivalent of Bu$_4$NI led to a color change of the reaction solution from green to greenish brown. The LMCT band at 390 nm shifted to 370 nm within minutes under an immense loss in intensity and remained constant after 40 min. Upon the addition of a second equivalent of Bu$_4$NI the reaction solution changes its color to reddish-brown, which is consistent with observations made by the oxygenation of **C10**. The absorption band at 370 nm increased significantly and stabilized after one hour. The addition of a third equivalent of Bu$_4$NI did not show any influence on the color and spectral features of the reaction solution. In addition, the absorption band at 370 nm was resistant to warming up of the reaction solution to room temperature.

The lower intensity of the absorption band at 370 nm shows a partially decayed bis(μ-oxido) species [**O1**](PF$_6$)$_2$, indicating the favored formation of iodidocuprate anions and the more stable iodido-bridged bis(μ-oxido) species over the original bis(μ-oxido) complex [**O1**](PF$_6$)$_2$, as [**O1I**](CuI$_2$) is formed according to a different stoichiometry. The concomitantly observed blueshift is also associated with the formation of [**O1I**](CuI$_2$) (see Figure 36 for comparison). The formed iodidocuprate serves as additional supporting ligand for the reactive bis(μ-oxido) core, which is assumed to be the driving force of the reaction. The interaction of the iodidocuprate and the bis(μ-oxido) core influences the spectral features of the complex cation causing the blueshift. Constant spectral features after the addition of two equivalents of the iodide source indicate a completed salt metathesis. Despite the completed salt metathesis, the

striking difference in intensity of the absorption band at 370 nm compared to that at 390 nm displays the lower quantity of the formed complex [**O1I**](CuI$_2$) in comparison to [**O1**](PF$_6$)$_2$. The loss in quantity is attributed to the missing copper source to achieve the stoichiometry needed for full formation of [**O1I**](CuI$_2$) with respect to [**O1**](PF$_6$)$_2$. Nevertheless, the experiment demonstrates that an easy exchange of the present anions increases the stability of the bis(μ-oxido) species by over 100 °C.

Salt metatheses of [**O1**](PF$_6$)$_2$ were also performed by using halide sources Bu$_4$NX (X$^-$ = Br$^-$, Cl$^-$), leading to the corresponding bis(μ-oxido) species [**O1**]Br$_2$ and [**O1**]Cl$_2$ (see Figure 78 and Figure 79 in the appendix). Both species decayed quickly during the titration due to their low stability (see Figure 38 for comparison). Therefore, the decomposition rate is seemingly higher than the reaction rate of the salt metathesis, which makes salt metatheses for these two species inappropriate.

Next, the competitive formation of the bis(μ-oxido) species [**O1**](PF$_6$)$_2$ and [**O1I**](CuI$_2$) was evaluated due to the significantly different time scales of the oxygenation reactions of **C1** and **C10**. Although the formation of [**O1**](PF$_6$)$_2$ was accomplished within a few minutes at –90 °C, the oxygenation of complex **C10** needed two hours at room temperature for completeness. Hence, copper(I) species **C1** and **C10** were oxygenated simultaneously in tetrahydrofuran at –90 °C to investigate the competitive reactivity towards dioxygen (Figure 43).

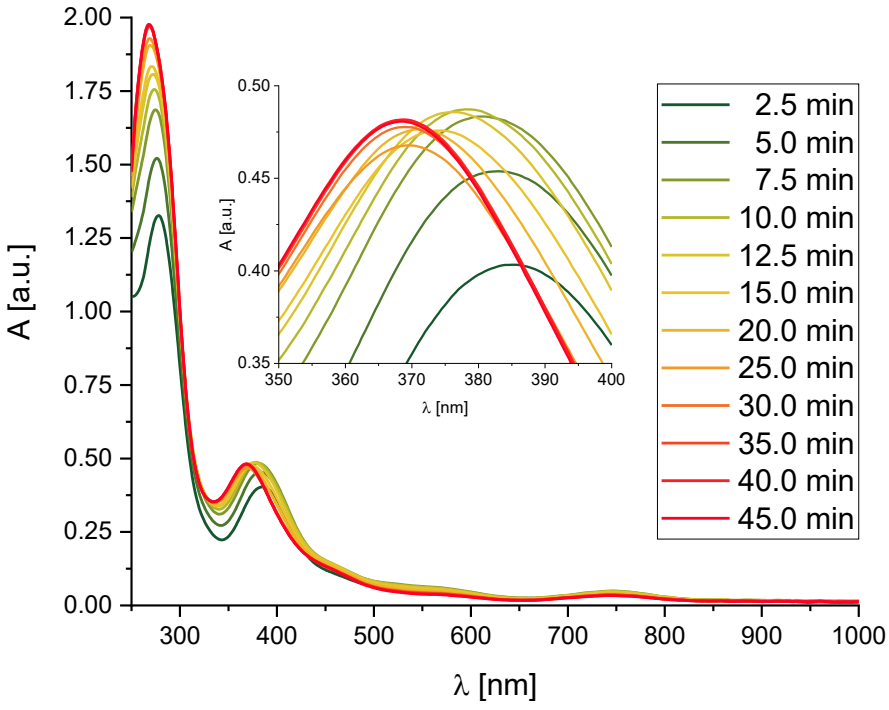

Figure 43: UV/Vis spectra of the competitive formation of [**O1**](PF$_6$)$_2$ and [**O1I**](CuI$_2$) (0.25 mM) in tetrahydrofuran at –90 °C (Inset: expansion of the competitive formation of [**O1**](PF$_6$)$_2$ and [**O1I**](CuI$_2$)).

The initial formation of the absorption band at 390 nm was observed within the first three minutes, which is caused by the formation of [**O1**]$(PF_6)_2$. A slight blueshift to 380 nm, which was stable for a few minutes, indicated the formation of both species [**O1**]$(PF_6)_2$ and [**O1I**](CuI_2). The absorption band shifted further to 370 nm within 25 minutes and remained constant henceforth. Thus, the competitive oxygenation of **C1** and **C10** resulted in the quick formation of [**O1**]$(PF_6)_2$, which slowly undergoes a salt metathesis to form [**O1I**](CuI_2). The observation of the initially formed species [**O1**]$(PF_6)_2$ leads to the assumption that the formation of [**O1**]$(PF_6)_2$ is significantly faster than the formation of the iodidocuprate anions. Thus, the reaction is seemingly driven by both thermodynamic and kinetic effects. The more stable complex [**O1I**](CuI_2) benefits from supporting effects of the formed iodidocuprate anions on the bis(μ-oxido) cation and the followed anion exchange. Nonetheless, a remaining amount of bis(μ-oxido) complex [**O1**]$(PF_6)_2$ is likely as the absorbance remained stable during the shift from 390 nm to 370 nm. Both species are stable at –90°C within the reaction time monitored and therefore, the absorption bands are most likely overlapped to a certain extent.

3.2.4. Catalytic Oxygenation Reactions

Inspired by the broad substrate scope covered by bis(μ-oxido) complex [**O1**]$(PF_6)_2$ (see section 3.1.4), the ability of [**O1I**](CuI_2) to activate C–H bonds in hydroxylation reactions was evaluated with respect to different substrate classes. Only few tyrosinase model systems are able to hydroxylate substrates catalytically and even fewer of them depicted room temperature stability which allows applications under mild reaction conditions.[90]

Since a simple anion exchange accomplished a great leap in stability, bis(μ-oxido) species [**O1I**](CuI_2) was analyzed concerning its reactivity in catalytic hydroxylation reactions of bicyclic aromatic alcohols at room temperature. In this one-pot reaction, a substrate was hydroxylated in *ortho*-position and oxidized. The generated quinones were transformed by 1,2-phenylene-diamine in a condensation reaction to form stable phenazines (Table 22).[82] Bicyclic aromatic alcohols with two product possibilities were chosen from a library of possible substrates to evaluate the influence of the iodide-bridge and the iodidocuprate anion on the selectivity of the oxygenation reaction. The upscaled reaction procedure was carried out according to the protocol described in section 3.1.4., with a change of the reaction temperature from –90 °C to room temperature and varied reaction times.

First, 2-naphthol was converted to compare the hydroxylation abilities of both oxygenated species **C10** (Table 22, entry 1) and **C10**·CuI (entry 2), as [**O1I**](CuI_2) was not formed quantitatively when **C10** was oxygenated due to stoichiometric limitations. The location of the electrophilic attack at 2-naphthol was predicted previously by a large value of the negative Fukui function, leading to the bent phenazine (see section 3.1.4.2). 2-Naphthol was oxygenated within two hours in > 80% conversion and subsequently converted into

benzo[a]phenazine (**P1**). **P1** was purified by column chromatography to produce 37-42% isolated yield (entries 1-2). The oxygenated species **C10**·CuI revealed higher reactivity towards 2-naphthol in the one-pot reaction. Therefore, the bis(μ-oxido) species [**O1I**](CuI_2) generated from **C10**·CuI was evaluated in the following experiments regarding other substrate classes (entries 3-6).

Table 22: Catalytic oxygenation reactions of bicyclic aromatic alcohols mediated by bis(μ-oxido) species [**O1I**](CuI_2).

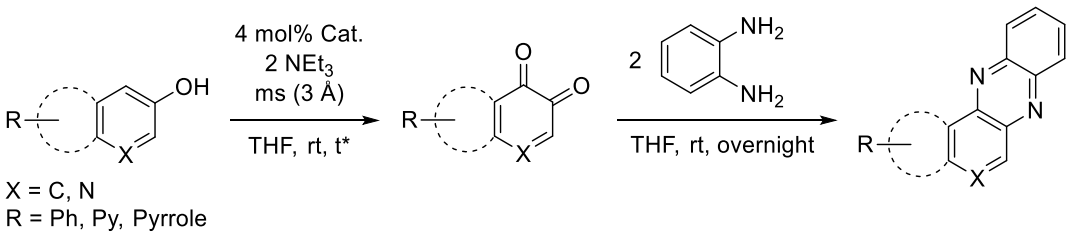

Entry	Cat.	Substrate	t* [h]	Conv.[a] [%]	Product P		Yield[b] [%]
1	[**O1I**](CuI_2)[c]	2-naphthol	2	80	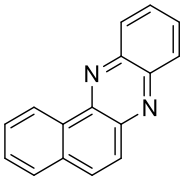	(**P1**)	37
2	[**O1I**](CuI_2)[d]	2-naphthol	2	83		(**P1**)	42
3	[**O1I**](CuI_2)[d]	3-quinolinol	3	> 99	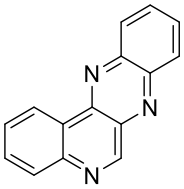	(**P2**)	56
4	[**O1I**](CuI_2)[d]	6-quinolinol	3	> 99	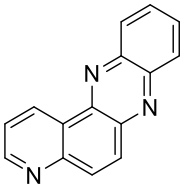	(**P3**)	61
5	[**O1I**](CuI_2)[d]	5-indolol	12	79	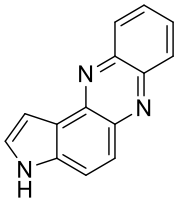	(**P4**)	41
6	[**O1I**](CuI_2)[d]	7-indolol	3	> 99	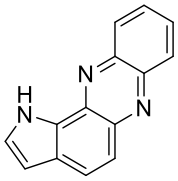	(**P5**)	58

[a] Conversion of the substrate determined by ^{1}H NMR spectroscopy. [b] Isolated yield of the phenazine after column chromatography and/or sublimation. [c] Efficient catalyst concentration of approximately 2 mol% due to oxygenation of **C10**. [d] Catalyst formed by oxygenation of **C10**·CuI.

Full conversion of 3-quinolinol was achieved within three hours at room temperature to give quinolino[3,4-b]quinoxaline (**P2**) after condensation with 1,2-phenylenediamine (entry 3). **P2** was purified by column chromatography as well as by sublimation and isolated in 56% yield. Similarly, 6-quinolinol was converted quantitatively to form pyrido[3,2-a]phenazine (**P3**) in 61% isolated yield (entry 4). C–H bonds of the pyrrole ring of indolols were activated by [**O1I**](CuI_2) to isolate the pyrrolophenazines **P4** and **P5** in 41-58% yield (entries 5-6). Increasing the reaction time of the hydroxylation to 12 hours yielded no undesired side reactions, which underlines the high selectivity of bis(μ-oxido) complex [**O1I**](CuI_2).

In comparison to the related system [**O1**]$(PF_6)_2$, catalyst [**O1I**](CuI_2) revealed an overall higher activity in hydroxylation reactions, as higher yields were achieved. Both catalysts converted bicyclic aromatic alcohols selectively. The mild reaction temperature enabled by using catalyst [**O1I**](CuI_2) maintained the high selectivity. No undesired side reactions were observed as reported by Krohn and co-workers.[190] Moreover, the additional steric demand of the iodide bridge between the two copper centers exhibited no impact on the accessibility of the Cu_2O_2 core regarding exogenous substrates. Instead, the stability of [**O1I**](CuI_2) at room temperature promotes the activity of the catalyst. Consequently, the accessibility of the reactive center from one direction is concluded to be sufficient to successfully perform oxygenation catalysis.

The high activity of bis(μ-oxido) complexes [**O1**]$^{2+}$ and [**O1I**]$^{+}$ in catalytic oxygenation reactions raises the question why the formally bis(μ-oxido) dicopper(III) species is capable of performing electrophilic hydroxylation reactions. The seeming contradiction is illuminated by the theory of inverted ligand field (Figure 44).[202,203]

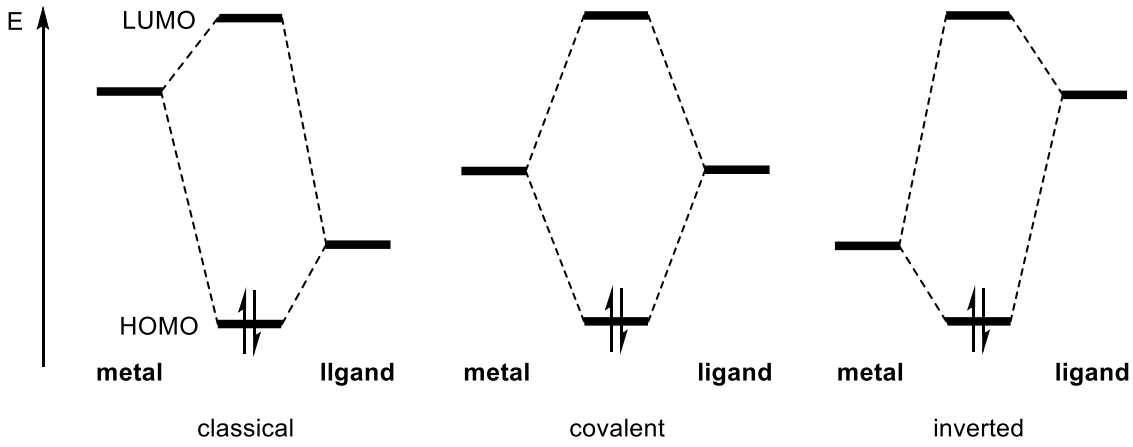

Figure 44: The concept of the classical, covalent, and inverted ligand field.

In a normal ligand field diagram, the metal orbitals are higher in energy compared to the ligand orbitals (Figure 44, left). The molecular orbitals are highly polarized and are mainly found in early 3d transition metal complexes. A more covalent behavior occurs between mid 3d transition metal orbitals and ligand orbitals due to roughly similar energy levels (Figure 44, middle). When the ligand orbitals are energetically higher than the d orbitals of the metal, an

inverted ligand field arises, which is featured in some late 3d transition metal complexes (Figure 44, right). As a result, the HOMO and LUMO of a compound in an inverted ligand field reveal predominant ligand orbital character and the contribution of the metal orbitals is vanishingly small. Thus, the physical oxidation states of the metal-ligand pair are impacted. An inverted ligand field is caused by high oxidation states of the metals (lowering the energy of the metal orbitals) and highly electronegative ligands (increasing the energy of the ligand orbitals). Although an inverted ligand field was mostly observed in the presence of ligands with electron-withdrawing CF_3 moieties[204–209], the two O^{2-} ligands in the formally bis(μ-oxido) dicopper(III) species can also be considered as highly electronegative, leading to a Cu(III) d^8 versus Cu(I) d^{10} discussion, which is only resolvable by full X-ray absorption analysis.[202] The formally bis(μ-oxido) dicopper(III) species [**O1**]$^{2+}$ and [**O1I**]$^{+}$ possess electron holes located at the μ-oxido bridges as both the LUMO and LUMO+1 reveal significant oxygen 2p character (see Figure 41 for comparison). Under the assumption of a prevalent inversion of the ligand field in case of complexes [**O1**]$^{2+}$ and [**O1I**]$^{+}$, the oxygen 2p orbitals are higher in energy than the copper 3d orbitals, leading to primarily oxygen-based redox-active molecular orbitals. Thus, the reactivity of the formally bis(μ-oxido) dicopper(III) species is indicated to be “oxygen-directed”, which apparently correlates with higher electrophilicity and presumably induces greater reactivity towards exogenous substrates. Further evidence for an existing inverted ligand field regarding complexes [**O1**]$^{2+}$ and [**O1I**]$^{+}$ might be drawn from the calculation of the Cu 3d contribution to the LUMOs by using DFT-ROCIS analysis to evaluate the influence of the number of acceptor holes.[202,210]

It is also surprising that the iodide bridge in complex [**O1I**]$^{+}$ is resistant to the formally copper(III) centers, although the oxidation of iodide to iodine seems natural at first glance in the presence of an oxidative species. However, the mechanism of the iodide oxidation would proceed in a radical pathway in the outer-sphere of the bis(μ-oxido) dicopper(III) complex. The given fact, that C–C coupling products (see Scheme 6) were observed in neither case during catalytic oxygenation reactions mediated by complexes [**O1**]$^{2+}$ and [**O1I**]$^{+}$, strengthens the indication of diminished oxidative power in the outer-sphere of both catalysts [**O1**]$^{2+}$ and [**O1I**]$^{+}$, therefore excluding the possibility of radical reaction mechanisms.

3.3. Influence of the Amine Donor on benza-Stabilized Copper Complexes with Weakly Coordinating Anions

Tyrosinase model complexes based on the hybrid guanidine ligand TMGbenza (**L1**) demonstrated impressively their ability to activate and transfer dioxygen in the presence of weakly coordinating anions. However, the systematic study on the oxygenation reactions of [Cu(**L1**)X] (X = I, Br, Cl) revealed an existing equilibrium between the monochelate and bischelate copper(I) species in solution due to the limited bite angle of **L1** (see section 3.2.), which complicates the understanding of O_2 activation due to several occurring processes. Therefore, this chapter focusses on the development of new hybrid guanidine ligand systems with a higher steric demand to avoid the formation of bischelate copper(I) complexes. The corresponding monochelate copper(I) complexes in the presence of different weakly coordinating anions are evaluated regarding their reactivity towards dioxygen by using UV/Vis and resonance Raman spectroscopy, mass spectrometry as well as DFT calculations. The impact of varied amine donor groups on the features of the bis(μ-oxido) complex is discussed and the reactivity in tyrosinase-like oxygenation reactions is investigated.

Parts of this chapter are already published in:

[1] M. Paul, M. Teubner, B. Grimm-Lebsanft, S. Buchenau, A. Hoffmann, M. Rübhausen, S. Herres-Pawlis, *J. Inorg. Biochem.* **2021**, *224*, 111541.

3.3.1. Ligand Synthesis

In relation to the hybrid guanidine ligand system TMGbenza (**L1**), two new ligands were developed in which the amine donor moieties are varied. The modification of the amine donor influences donor strength and steric effects of the ligand system which will impact the activation and transfer of molecular oxygen. Larger alkyl substituents lead to a spatially larger ligand system which is accompanied by weakening of the σ-donor function of the amine unit. Based on ligand **L1**, the permethylated amine moiety is substituted by ethyl and *iso*-propyl groups to form the hybrid guanidine ligands TMGbenzNEt_2 (**L3**, IUPAC: 2-{2-((diethylamino)methyl)phenyl}-1,1,3,3-tetramethylguanidine) and TMGbenzN*i*Pr_2 (**L4**, IUPAC: 2-{2-((di-*iso*-propylamino)methyl)phenyl}-1,1,3,3-tetramethylguanidine).

The synthesis of ligands **L3** and **L4** was performed in a three-step reaction according to Scheme 27 starting from **60** (similar to the synthesis of ligand **L1**, see section 3.1.1.). Both ligands were purified by vacuum distillation and isolated as light-yellow to yellow oils. The overall yield of the ligand synthesis is determined to be 79% for **L3** and 68% for **L4**. Ligands were stored in a glovebox under nitrogen atmosphere due to their moisture-sensitivity.

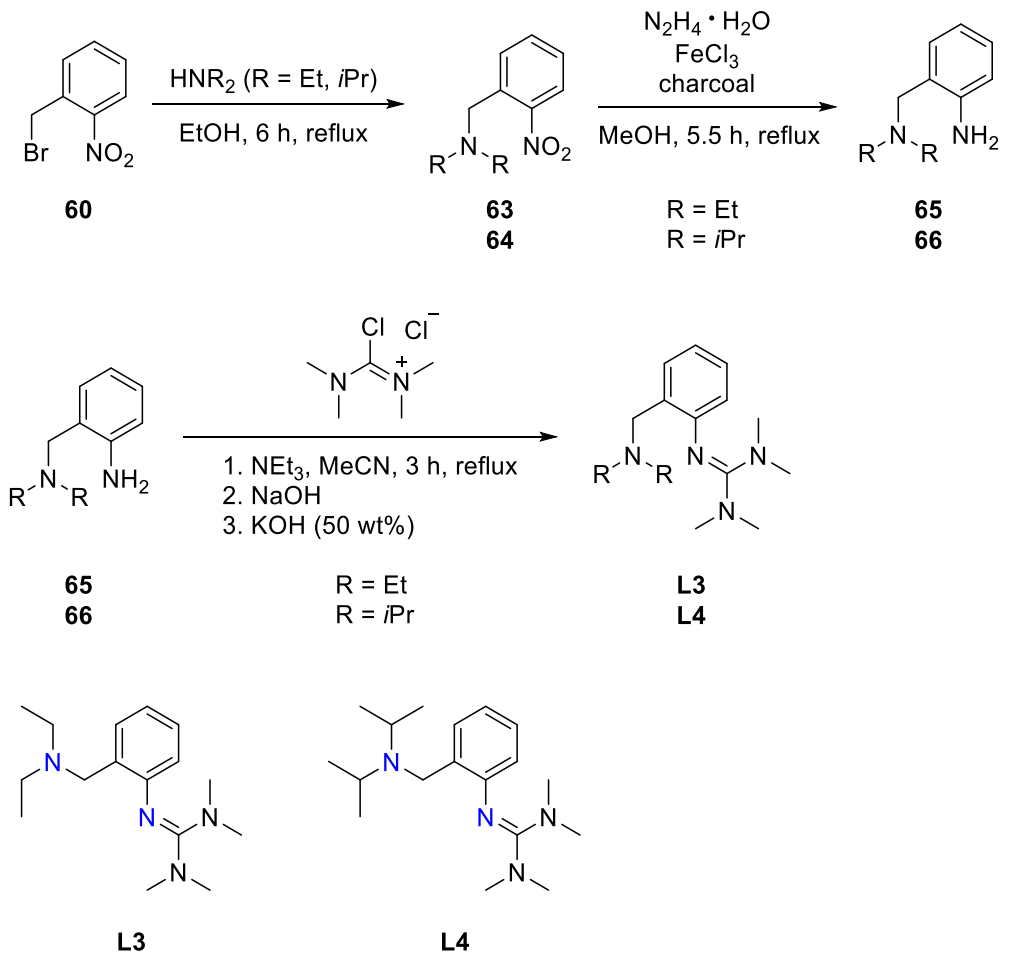

Scheme 27: Synthesis of the bidentate hybrid guanidine ligands **L3** and **L4**.

The hybrid guanidine ligands **L3** and **L4** were analyzed by NMR and IR spectroscopy as well as mass spectrometry and compared to **L1**, as the amine modification from NMe_2 over NEt_2 to $NiPr_2$ influences the electronic properties of the ligand. Major differences of the chemical shifts of **L1**, **L3** and **L4** in the ^{1}H NMR and $^{13}C\{^{1}H\}$ NMR spectra are summarized in Table 23.

Table 23: Selected chemical shifts of the hybrid guanidine ligands **L1**, **L3** and **L4**.

		L1	**L3**	**L4**
^{1}H NMR [ppm]	$C\underline{H}_2$	3.30	3.42	3.51
$^{13}C\{^{1}H\}$ NMR [ppm]	$\underline{C}H_2$	60.6	54.5	45.4
	$CH_2\underline{C}$(Ph)	130.8	131.8	133.8

The variation of the amine donor function is mostly reflected at the methylene group of the ligands. The substitution from NMe_2 over NEt_2 to $NiPr_2$ led to significantly lower chemical shifts of the methylene group in the $^{13}C\{^{1}H\}$ NMR spectrum. Concomitantly, higher chemical shifts of the neighboring protons and carbon atom were observed. This shift is caused by the positive inductive effect of the alkyl substituents, which is most pronounced in the methyl groups and

weakened with increasing chain length. The resulting enlarged electron density of the NMe_2 group compared to the NEt_2 moiety in **L3** and the N*i*Pr_2 moiety in **L4** results in better electron donating properties of the ligand system.

3.3.2. Cu(I) Complexes

Applying equimolar amounts of the ligand **L3** and **L4** and the copper salt $[Cu(MeCN)_4]X$ (X^- = PF_6^-, BF_4^-, OTf^-) in acetonitrile at room temperature resulted in the formation of the monochelate copper(I) complexes **C22**-**C27** (Scheme 28).

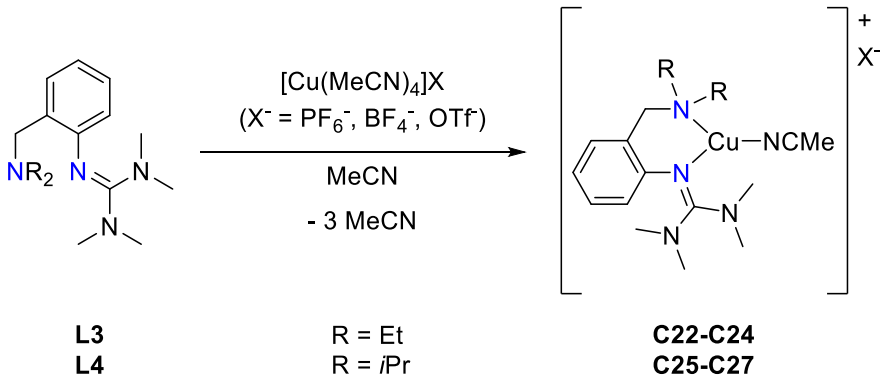

L3 R = Et **C22-C24**
L4 R = *i*Pr **C25-C27**

Scheme 28: Synthesis of copper(I) complexes supported by **L3** and **L4**.

The complexes **C22**-**C27** were investigated by NMR and IR spectroscopy as well as mass spectrometry. ESI-MS measurements show the formation of the desired monochelate copper(I) species. A bischelate copper(I) complex, which was found for **L1**-stabilized copper(I) complexes (see section 3.1.2.), was observed in neither case, which is due to the higher steric encumbrance of the ligands **L3** and **L4**. The NMR spectra of the **L3**-supported species **C22**-**C24** in the presence of different weakly coordinating anions were mainly similar, showing no electronic influence of the weakly coordinating anions on the complex cation. Same observations were made in the **L4**-supported complexes **C25**-**C27**. The comparison of the chemical shifts in the $^{13}C\{^1H\}$ NMR spectra of the carbon atom of the guanidine moiety within the copper(I) complexes stabilized by **L1**, **L3** and **L4** reveals a slight downfield shift upon modification of the amine moiety from NMe_2 over NEt_2 to N*i*Pr_2 independent of the present anion (Table 24). These observations show the electronic influence of the reduced amine donor strength on the guanidine donor moiety. A measurable impact of the present anion was not obtained.

The influence of the amine moiety on the guanidine moiety in the corresponding copper(I) complexes is also visible in the IR spectra (Table 25). The C=N vibration of the guanidine moiety shifted to slightly lower wavenumbers from **L1** to **L3** to **L4**. A similar shift was reported for hybrid guanidine-supported zinc(II) chloride complexes upon variation of the amine donor moiety from NMe_2 to NEt_2 ([Zn(TMGdmap)Cl_2]: 1564 cm^{-1}, [Zn(TMGdeap)Cl_2]: 1560 cm^{-1}; [Zn(TMGdmab)Cl_2]: 1572 cm^{-1}, [Zn(TMGdeab)Cl_2]: 1541 cm^{-1}).[211]

Table 24: Chemical shifts of C_{gua} of the Cu(I) complexes [Cu(L)(MeCN)]X (X^- = PF_6^-, BF_4^-, OTf^-) stabilized by **L1**, **L3** and **L4** in the $^{13}C\{^1H\}$ NMR spectrum [ppm].

	[Cu(L)(MeCN)]PF_6	[Cu(L)(MeCN)]BF_4	[Cu(L)(MeCN)]OTf
L1	164.7	164.7	164.6
L3	165.0	165.0	165.0
L4	165.7	165.7	165.7

Table 25: Frequencies of the C=N stretching mode of the Cu(I) complexes [Cu(L)(MeCN)]X (X^- = PF_6^-, BF_4^-, OTf^-) stabilized by **L1**, **L3** and **L4** in the IR spectra [cm^{-1}].

	[Cu(L)(MeCN)]PF_6	[Cu(L)(MeCN)]BF_4	[Cu(L)(MeCN)]OTf
L1	1555	1557	1549
L3	1555	1554	1546
L4	1551	1550	1543

These observations demonstrate that the guanidine moiety responds to the decreased electron donating abilities of the amine moiety from **L1** to **L3** to **L4** in the copper(I) complexes.

3.3.3. Dioxygen Activation

The oxygenation of the copper(I) species **C22**-**C27** at low temperatures was achieved by bubbling dioxygen through a precooled solution of tetrahydrofuran and injecting copper(I) complexes **C22**-**C27** in acetonitrile (Scheme 29). The addition of the precursor complex solution resulted in an immediate color change. The oxygenation reactions of complexes **C22**-**C27** were followed by UV/Vis spectroscopy (Figure 45). Characteristic UV/Vis features are summarized in Table 26. The reaction of **C22** with dioxygen resulted in the formation of the green bis(μ-oxido) complex [**O3**]$(PF_6)_2$ (Figure 45, left). The complex [**O3**]$(PF_6)_2$ exhibits two characteristic absorption bands at 280 nm (40000 M^{-1} cm^{-1}) and 400 nm (20000 M^{-1} cm^{-1}), which are very similar to the absorption features of [**O1**]$(PF_6)_2$ (absorption bands at 280 nm (40000 M^{-1} cm^{-1}) and 392 nm (21000 M^{-1} cm^{-1})).[212] Comparable UV/Vis characteristics were observed by the oxygenation of **C23** and **C24** leading to the bis(μ-oxido) complexes [**O3**]$(BF_4)_2$ and [**O3**]$(OTf)_2$ (Figure 46, left), showing no influence of the present weakly coordinating anions on the complex cation [**O3**]$^{2+}$. The green bis(μ-oxido) complexes [**O3**]X_2 (X^- = PF_6^-, BF_4^-, OTf^-) were generated within 15-40 min at –100 °C and are stable for at least 90 min at that temperature. Elevated temperatures led to less quantitative formation and faster decay of complex [**O3**]$^{2+}$, which was accompanied by a color change of the reaction solution to yellow.

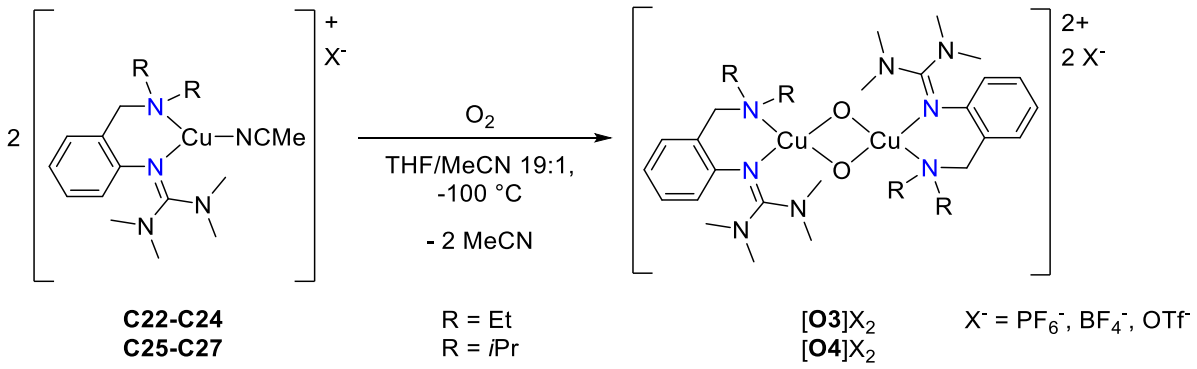

Scheme 29: Reaction of the copper(I) complexes **C22-C27** with dioxygen.

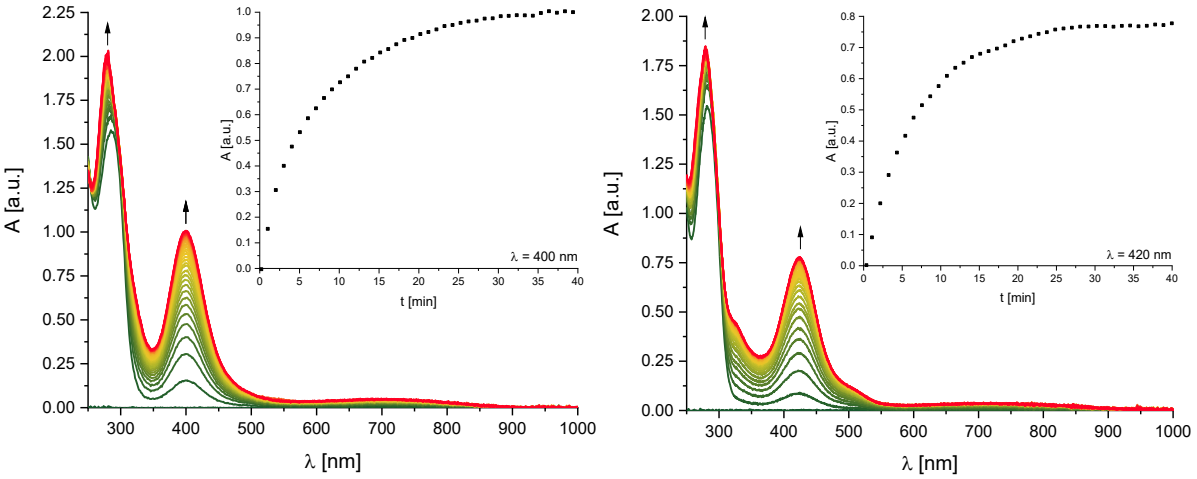

Figure 45: UV/Vis spectra of the formation of [**O3**](PF$_6$)$_2$ (left) and [**O4**](PF$_6$)$_2$ (right, 0.5 mM) in tetrahydrofuran at –100 °C (Insets: time-resolved formation of [**O3**](PF$_6$)$_2$ at 400 nm and [**O4**](PF$_6$)$_2$ at 420 nm).

The orange bis(μ-oxido) species [**O4**](PF$_6$)$_2$ (Figure 45, right) exhibits two UV/Vis features at 280 nm (38000 M^{-1} cm^{-1}) and 423 nm (18000 M^{-1} cm^{-1}) along with an additional absorption band at 330 nm (9000 M^{-1} cm^{-1}). In comparison to the complexes [**O1**]$^{2+}$ and [**O3**]$^{2+}$, the transition at higher wavelength of [**O4**]$^{2+}$ is redshifted (see Figure 47 for comparison). The weak UV/Vis feature at 500 nm was more pronounced upon **L4**-stabilization with respect to **L3** and **L1**, which is responsible for the orange color of [**O4**]$^{2+}$ due to the increased red contribution. The oxygenation reactions of **C26** and **C27** resulted in similar UV/Vis features (Figure 46, right). The bis(μ-oxido) species [**O4**]X$_2$ (X$^-$ = PF$_6^-$, BF$_4^-$, OTf$^-$) were synthesized within 25-40 min at –100 °C and are stable for at least 60 min at that temperature. Higher temperatures resulted in lower quantity and a faster decay of the bis(μ-oxido) species [**O4**]$^{2+}$, followed by the discoloration of the reaction solution to yellow.

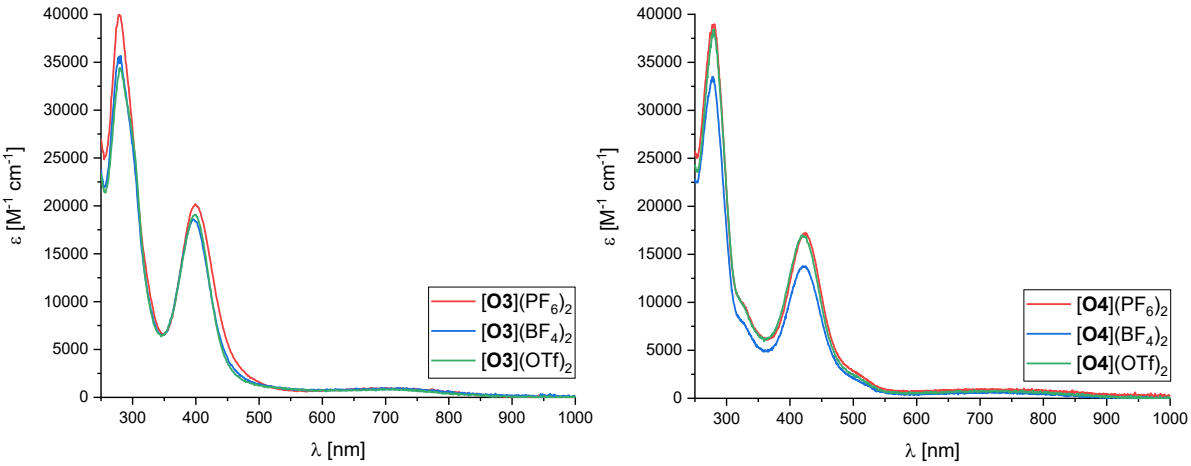

Figure 46: UV/Vis spectra of [**O3**]X_2 (left) and [**O4**]X_2 (right, X^- = PF_6^-, BF_4^-, OTf^-) in tetrahydrofuran.

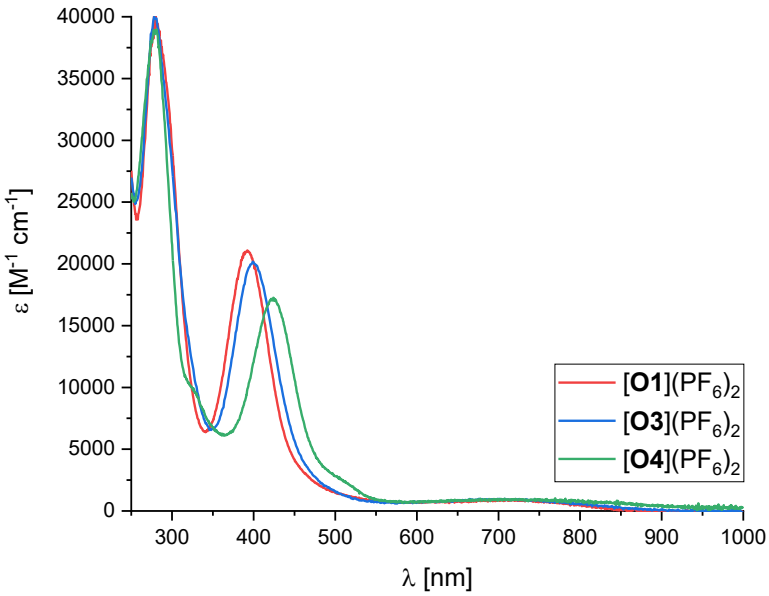

Figure 47: UV/Vis spectra of [**O1**]$(PF_6)_2$, [**O3**]$(PF_6)_2$, and [**O4**]$(PF_6)_2$ (0.5 mM) in tetrahydrofuran.

Table 26: Experimental UV/Vis features of the bis(μ-oxido) complexes [**O1**]X_2, [**O3**]X_2 and [**O4**]X_2 (X^- = PF_6^-, BF_4^-, OTf^-, see also Figure 47).

[O]X_2	λ [nm] (ε [M^{-1} cm^{-1}])	λ [nm] (ε [M^{-1} cm^{-1}])
[**O1**]$(PF_6)_2$	392 (21000)	280 (40000)
[**O1**]$(BF_4)_2$	392 (21000)	280 (40000)
[**O1**]$(OTf)_2$	396 (21000)	284 (39000)
[**O3**]$(PF_6)_2$	400 (20000)	280 (40000)
[**O3**]$(BF_4)_2$	399 (19000)	279 (36000)
[**O3**]$(OTf)_2$	397 (19000)	280 (35000)
[**O4**]$(PF_6)_2$	423 (17000)	280 (38000)
[**O4**]$(BF_4)_2$	422 (14000)	277 (33000)
[**O4**]$(OTf)_2$	421 (17000)	280 (38000)

Theoretical investigations were performed to provide more information about the influence of electronic factors on the bis(μ-oxido) dicopper(III) core. DFT calculations were conducted by Dr. Alexander Hoffmann, which are based on the hybrid meta GGA functional TPSSh[157–159] combined with the triple-valence basis set def2-TZVP[160–163] and empirical dispersion correction with Becke-Johnson damping GD3BJ.[164–167] The experimentally observed redshift of the absorption band at higher wavelength is well reproduced with time-dependent DFT calculations of the bis(μ-oxido) species ([**O1**]$^{2+}$: 375 nm; [**O2**]$^{2+}$: 382 nm; [**O3**]$^{2+}$: 398 nm; see Figure 86 in the appendix).

Table 27: Calculated geometric parameters of the bis(μ-oxido) species [**O1**]$^{2+}$, [**O3**]$^{2+}$ and [**O4**]$^{2+}$ (TPSSh/def2-TZVP, GD3BJ).

	[O1]$^{2+}$	[O3]$^{2+}$	[O4]$^{2+}$
Bond lengths [Å]			
Cu–N_{gua}	1.917, 1.917	1.921, 1.928	1.928, 1.934
Cu–N_{amine}	1.967, 1.967	1.985, 1.991	1.996, 2.006
Cu–O	1.802, 1.807	1.805, 1.807	1.807, 1.810
	1.802, 1.807	1.803, 1.809	1.809, 1.811
O···O	2.326	2.309	2.296
Cu···Cu	2.759	2.777	2.793
Dihedral angle [°]			
∢(Cu_2O_2, CuN_2)	5.0	8.4	17.3

The calculated geometric parameters of the theoretical Cu_2O_2 species are summarized in Table 27. The Cu–N_{gua} bond lengths are shorter compared to the Cu–N_{amine} bond lengths in all three bis(μ-oxido) complexes, showing the higher donor strength of the guanidine moiety over the amine moiety. Also, both the Cu–N_{gua} and the Cu–N_{amine} bond lengths as well as the Cu···Cu distances increase with increasing steric demand of the amine moiety. In addition, a decreased O···O distance and slightly elongated Cu–O bond lengths result from the larger steric encumbrance, leading to an elongated Cu_2O_2 rhomb. Moreover, the angle between the Cu_2O_2 plane and the CuN_2 plane is significantly enlarged with higher steric demand of the amine moiety, which indicates a more pronounced twist of the Cu_2O_2 rhomb and the hybrid guanidine ligands. These effects cause a poorer orbital overlap of the copper ions and the N-donor atoms.

In the next step, natural population analysis (NBO) was performed by Dr. Alexander Hoffmann to investigate the donor properties of the hybrid guanidine ligands in the bis(μ-oxido) species [**O1**]$^{2+}$, [**O3**]$^{2+}$ and [**O4**]$^{2+}$ (Table 28).[106,213–215]

Table 28: NBO charges and charge transfer (CT) energies for selected atoms of the bis(μ-oxido) species [**O1**]$^{2+}$, [**O3**]$^{2+}$ and [**O4**]$^{2+}$ (NBO7.0; TPSSh/def2-TZVP, GD3BJ).

	[O1]$^{2+}$	[O3]$^{2+}$	[O4]$^{2+}$
NBO charges [e$^-$ units]			
Cu	1.35	1.36	1.37
N_{gua}	-0.70, -0.70	-0.71, -0.72	-0.72, -0.72
N_{amine}	-0.40, -0.40	-0.40, -0.40	-0.42, -0.42
O	-0.96, -0.96	-0.96, -0.96	-0.97, -0.98
CT energies [kcal mol^{-1}]			
N_{gua} → Cu	31.9, 31.9	22.0, 27.8	27.1, 29.3
N_{amine} → Cu	20.1, 20.1	17.5, 18.3	14.5, 15.3

The NBO charges of the guanidine moiety are significantly more negative than those of the amine moiety, revealing the more basic character of the N-donor atom of the guanidine moiety. With increasing steric hindrance of the amine donor moiety, a slightly more negative value for the N-donor atom of both the guanidine and the amine moiety is observed. The charge transfer (CT) energies, which were obtained by 2nd order perturbation theory, reveal larger values for the guanidine moiety compared to the amine moiety, demonstrating again the higher donating abilities of the guanidine unit. Also, the CT energies of the amine moiety diminish from [**O1**]$^{2+}$ to [**O3**]$^{2+}$ to [**O4**]$^{2+}$, which is correlated to the decreasing amine donor strength.

A natural transition orbital (NTO) analysis was performed by Dr. Alexander Hoffmann to elucidate the bonding and antibonding interactions of the bis(μ-oxido) species [**O1**]$^{2+}$ and [**O4**]$^{2+}$ in relation to their spectroscopic characteristics (Figure 48).[216]

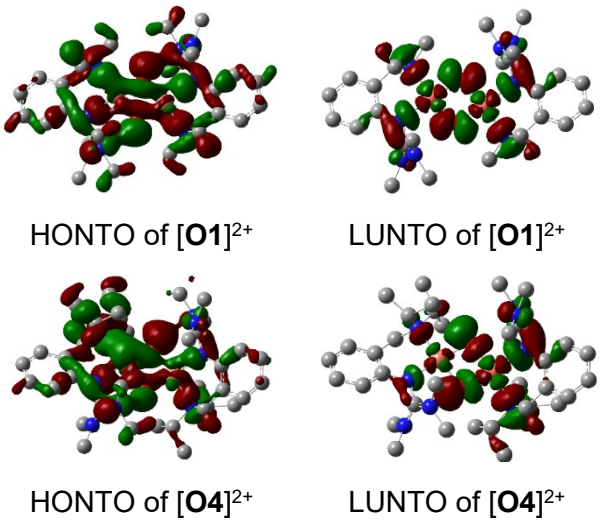

HONTO of [**O1**]$^{2+}$ LUNTO of [**O1**]$^{2+}$

HONTO of [**O4**]$^{2+}$ LUNTO of [**O4**]$^{2+}$

Figure 48: NTO representations of the HONTOs and LUNTOs of the bis(μ-oxido) species [**O1**]$^{2+}$ and [**O4**]$^{2+}$ in the characteristic transition at higher wavelength.

The experimentally observed UV/Vis feature at 280 nm (see Table 26) results from an in plane transition from the bonding interaction of the π_σ* orbital of the oxido ion and a d orbital of the copper ion (highest occupied NTO = HONTO, Figure 48; see also Figure 87 in the appendix) to the antibonding interaction of the σ* orbital of the oxido ion and a d orbital of the copper ion (lowest unoccupied NTO = LUNTO, Figure 48; see also Figure 88 in the appendix). The experimentally observed absorption band at higher wavelength, which redshifts from 392 nm to 423 nm (from [**O1**]$(PF_6)_2$ to [**O4**]$(PF_6)_2$, see Table 26), originates from an in plane transition from the bonding interaction of the σ* orbital of the oxido ion and a d orbital of the copper ion as well as antibonding to the N-donor moieties (HONTO, Figure 48; see also Figure 89 in the appendix) to the antibonding interaction of the π_σ* orbital of the oxido ion and a d orbital of the copper ion as well as antibonding to the N-donor moieties (LUNTO, Figure 48; see also Figure 90 in the appendix). Both spectral features are characteristic for bis(μ-oxido) species supported by N-donor ligands.[10] The additionally observed shoulder at 330 nm for bis(μ-oxido) species [**O4**]$^{2+}$ (see Figure 46, right) originates from the transition from a linear combination of the π_σ* and π_v* orbital as well as a contribution of the ligand to the antibonding interaction of the copper d orbital with the oxygen σ* orbital and antibonding to the N-donors (see Figure 90 in the appendix). The orbitals are distorted due to the enlarged steric demand of the amine moiety.

The experimentally observed redshift (see Figure 47 for comparison) originates from different effects. The higher steric encumbrance of the amine donor moiety along with the weakening donor strength from NMe_2 to NEt_2 to N*i*Pr_2 causes a higher twist between the Cu_2O_2 plane and the CuN_2 plane (also shown in the NTO representations of the bis(μ-oxido) species in Figure 48) and an elongation of the Cu_2O_2 core. The resulting poorer orbital overlap contributes to the spectral redshift. In conjunction with these effects, the energies of the canonical orbitals differ with respect to the ligand system. The energetic gap between the LUMO+1 and the LUMO decreases from [**O1**]$^{2+}$ to [**O3**]$^{2+}$ to [**O4**]$^{2+}$ (see Table 53 and Table 54 in the appendix), so that the LUMO+1 is more stabilized in energy upon weaker donating abilities of the amine moiety along with a higher twist. The key orbital HOMO-8 for the transition at higher wavelength, which also stems from the antibonding interaction of the N-donor moieties into the Cu_2O_2 core (here denoted by a bonding interaction of the Cu d orbitals and the σ* orbital of the oxido ions), is higher in energy due to the weaker amine donor moiety in relation to the HOMO (see Table 53 and Table 54 in the appendix). Consequently, the energy for the transition decreases from [**O1**]$^{2+}$ to [**O3**]$^{2+}$ to [**O4**]$^{2+}$ which is responsible for the observed redshift in the UV/Vis spectra.

The bis(μ-oxido) complexes [**O3**]$(PF_6)_2$ and [**O4**]$(PF_6)_2$ were further analyzed by resonance Raman spectroscopy in cooperation with the group of Prof. Dr. Michael Rübhausen at the CFEL in Hamburg to get deeper insights into the electronic effects at the Cu_2O_2 core. Raman spectra of copper(I) species **C22** and **C25** and their corresponding bis(μ-oxido) species [**O3**]$(PF_6)_2$ and [**O4**]$(PF_6)_2$ were measured in tetrahydrofuran/acetonitrile (80:20) at low

temperatures below –90 °C upon excitation at 532 nm (see also Figure 80 and Figure 81 in the appendix). The Raman spectra of the bis(μ-oxido) complexes [**O3**](PF$_6$)$_2$ and [**O4**](PF$_6$)$_2$ were correlated with the Raman spectrum of the closely related species [**O1**](PF$_6$)$_2$ (see also Figure 22) to evaluate the influence of modified amine donor moieties on the Raman modes (Figure 49). The Raman modes were assigned with the help of simulated resonance Raman spectra using DFT calculations (Table 29). Figure 49 illustrates the vibrational modes of bis(μ-oxido) complexes [**O1**](PF$_6$)$_2$, [**O3**](PF$_6$)$_2$ and [**O4**](PF$_6$)$_2$ at 620 cm^{-1}, 615 cm^{-1} and 607 cm^{-1}, typically observed for the symmetric expansion of the Cu$_2$O$_2$ core of a bis(μ-oxido) dicopper(III) complex (breathing mode).[9–11] Modification of the amine donor moiety of the hybrid guanidine ligand from NMe$_2$ (**L1**) to NEt$_2$ (**L3**) to N*i*Pr$_2$ (**L4**) led to a slight shift of the breathing mode of the Cu$_2$O$_2$ rhomb to lower frequencies, which agrees well with the calculated resonance Raman spectra (Table 29). This behavior can be redirect to the deformation of the Cu$_2$O$_2$ core. Beside the breathing mode, further vibrations were observed, which were attributed to Cu–N$_{amine}$ and Cu–N$_{gua}$ stretching modes and the aromatic backbone of the ligand system (Table 29). The Cu–N$_{amine}$ stretching mode shifts to lower frequencies from [**O1**](PF$_6$)$_2$ to [**O3**](PF$_6$)$_2$ to [**O4**](PF$_6$)$_2$, which correlates with the weaker donor strength of the amine moiety. The Cu–N$_{gua}$ stretching modes are overlapped by vibrations of the aromatic backbone of the ligand and/or Cu–N$_{amine}$ stretching modes.

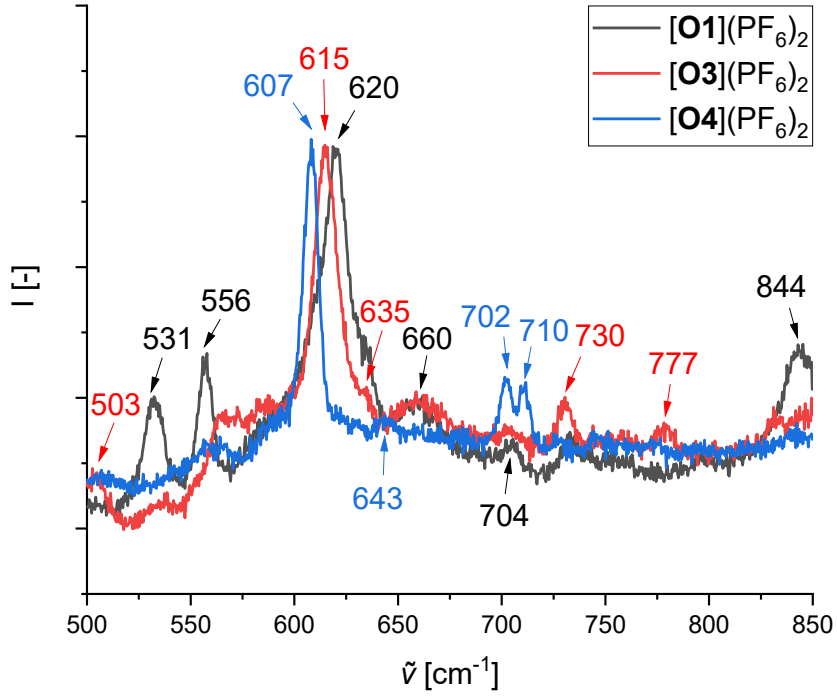

Figure 49: Resonance Raman spectra of [**O1**](PF$_6$)$_2$ (black), [**O3**](PF$_6$)$_2$ (red) and [**O4**](PF$_6$)$_2$ (blue) in a tetrahydrofuran/acetonitrile (80:20) at –90 °C ([**O3**](PF$_6$)$_2$ and [**O4**](PF$_6$)$_2$: ex. at 532 nm, [**O1**](PF$_6$)$_2$: ex. at 420 nm). The spectra were recorded by the group of Prof. Dr. Michael Rübhausen at the CFEL in Hamburg.

Table 29: Assignment of the resonance Raman modes of the bis(μ-oxido) species [**O1**]$^{2+}$, [**O3**]$^{2+}$ and [**O4**]$^{2+}$.

	Wavenumber [cm^{-1}]		**Vibration Type**
	Exp.	**DFT (Intensity)***	
[O1]$^{2+}$		485 (36)	Cu–N_{amine}
	531	509 (84)	Cu–N_{amine}
	556	544 (178)	Cu–N_{gua} and Cu–N_{amine} and benza
	620	602 (426)	asym. Cu_2O_2 and Cu–N_{amine} and benza
		625 (254)	sym. Cu_2O_2 and Cu–N_{amine} and benza
	634	628 (61)	sym. Cu_2O_2 and Cu–N_{gua} and benza
	660		
	704	698 (24)	Cu–N_{gua} and benza
	732	738 (20)	Gua and Cu–N_{amine} and benza
	796	794 (72)	Cu–N_{gua} and benza
	844	832 (120)	Cu–N_{amine}
[O3]$^{2+}$	503	482 (36)	Cu–N_{amine}
	565	540 (19)	Cu–N_{gua} and Cu–N_{amine} and benza
		583 (24)	Cu_2O_2 and Cu–N_{gua} and Cu–N_{amine} and benza
	615	617 (107)	asym. Cu_2O_2 and Cu–N_{amine} and benza
	635	630 (175)	sym. Cu_2O_2 and Cu–N_{amine} and benza
	660	643 (39)	asym. Cu_2O_2 and Cu–N_{amine}
	704	700 (14)	Cu–N_{gua} and benza
		701 (11)	Cu–N_{gua} and benza
	730	737 (7)	Gua and Cu–N_{amine} and benza
	777	760 (16)	Cu–N_{amine}
		798 (21)	Cu–N_{gua} and benza
	830	821 (11)	Cu–N_{amine}
	848	852 (18)	Cu–N_{gua} and benza
[O4]$^{2+}$		399 (29)	Cu–N_{amine}
	560	546 (96)	Cu–N_{gua} and Cu–N_{amine} and benza
		576 (39)	Cu_2O_2 and Cu–N_{gua} and Cu–N_{amine} and benza
	607	600 (74)	asym. Cu_2O_2 and Cu–N_{amine} and Cu–N_{gua} and benza
		609 (46)	asym. Cu_2O_2 and Cu–N_{amine} and Cu–N_{gua} and benza
		617 (146)	sym. Cu_2O_2 and Cu–N_{amine} and Cu–N_{gua} and benza
		630 (140)	sym. Cu_2O_2 and Cu–N_{amine} and Cu–N_{gua} and benza
	643	640 (26)	asym. Cu_2O_2 and Cu–N_{amine}
	702	698 (23)	Cu–N_{gua} and Cu–N_{amine} and benza
		700 (18)	Cu–N_{gua} and Cu–N_{amine} and benza
	710	723 (32)	Cu–N_{amine}

A spectral shift of the absorption bands of the bis(μ-oxido) species in correlation with the stabilizing ligand system was also found in previous studies (see Figure 50 and Table 30). Related to ligand **L1**, the hybrid guanidine system TMGdmap stabilized the bis(μ-oxido) species **RC1** which revealed the characteristic UV/Vis features in the same region.[47,150,217] **RC1** possessed a smaller twist of 1.8 ° between the Cu_2O_2 plane and the CuN_2 plane in comparison with [**O1**]$^{2+}$ (5.0 °), and also a larger Cu···Cu distance (2.747 Å, [**O1**]$^{2+}$: 2.759 Å) and O···O distance (2.336 Å, [**O1**]$^{2+}$: 2.326 Å). Upon modification of the amine unit in TMGdmap from NMe_2 to NEt_2, a redshift from 385 nm to 392 nm was observed for the bis(μ-oxido) species **RC2**, which was redirected to steric effects of the ligand system.[150] The TMG_2tol-supported bis(μ-oxido) species **RC3** also shows a small shift of the absorption band at higher wavelength, which results from the higher twist of 6.9°(av) between the Cu_2O_2 plane and the CuN_2 plane, whereas the Cu···Cu and O···O distances remain constant to **RC1**. The two sterically demanding guanidine moieties lead to two different twist angles of 2.4° and 11.4°.[135]

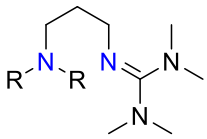

TMGdmap (R = Me)
TMGdeap (R = Et)

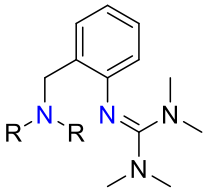

L1 (R = Me)
L3 (R = Et)
L4 (R = *i*Pr)

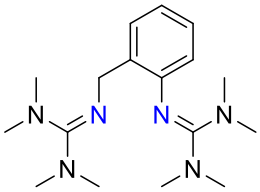

TMG$_2$tol

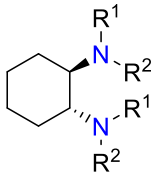

TMCHD (R^1 = R^2 = Me)
MECHD (R^1 = Me, R^2 = Et)
TECHD (R^1 = R^2 = Et)

TMED (R^1 = R^2 = Me)
Me$_2$Et$_2$ED (R^1 = Me, R^2 = Et)
TEED (R^1 = R^2 = Et)

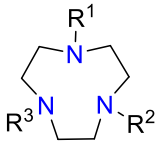

Me$_3$TACN (R^1 = R^2 = R^3 = Me)
Bz$_3$TACN (R^1 = R^2 = R^3 = Bz)
***i*Pr$_2$BzTACN** (R^1 = R^2 = *i*Pr, R^3 = Bz)
***i*Pr$_3$TACN** (R^1 = R^2 = R^3 = *i*Pr)

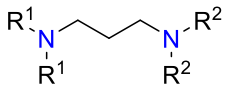

PD (R^1 = R^2 = H)
DMPD (R^1 = H, R^2 = Me)
TMPD (R^1 = R^2 = Me)

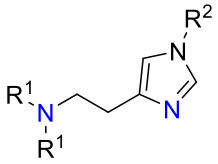

Me$_3$His (R^1 = Me, R^2 = Me)
***n*BuHis** (R^1 = H, R^2 = *n*Bu)

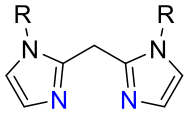

***n*BuBIM** (R = *n*Bu)

Figure 50: Selected N-donor ligand systems for the stabilization of bis(μ-oxido) dicopper(III) complexes.

Stack, Solomon, and co-workers analyzed a huge number of bis(μ-oxido) species, which are based on peralkylated bidentate *trans*-(1R, 2R)-cyclohexane diamine (CHD) (**RC4**-**RC6**) and 1,2-ethanediamine (ED) skeletons (**RC7**-**RC9**), varying from tetramethyl to dimethyl-diethyl to tetraethyl derivatives.[66,218,219] They and the group of Tolman also investigated bis(μ-oxido) species supported by polyazacyclononane (TACN) ligands (**RC16**-**RC19**).[66,178,218,219] For the CHD-stabilized systems **RC4**-**RC6**, a redshift in correlation with higher steric demand of the ligand system was reported, which was attributed to the steric influence of the ligand system on the Cu_2O_2 core, resulting in an elongated Cu_2O_2 rhomb. A possible impact of the twist between the Cu_2O_2 plane and the CuN_2 plane was not ruled out. These observations were also made by using the ED-systems **RC7-RC9** and the TACN-based species **RC16-RC19**.

The variation of ED-supported systems to 1,2-propanediamine (PD)-stabilized systems **RC10-RC12** with N-donor moieties ranging from the primary amine to a hybrid version (NH_2, NMe_2) to the permethylated amine also yielded a redshift of the optical bands.[67] Stack and co-workers observed an elongated Cu···Cu distance due to the steric demand and lower donor strength of the ligands, stating PD as the smallest and strongest ligand.[70] Another systematic study on bis(μ-oxido) species stabilized by the ligands TMPD (**RC12**), N_α,N_α,N_τ-trimethyl-histamine (Me_3His, **RC13**), N_τ-n-butyl histamine (*n*BuHis, **RC14**) and bis(1-*n*-butylimidazol-2-yl)methane (*n*BuBIM, **RC15**) revealed the correlation of the donor character following the trend TMPD < Me_3His < *n*BuHis < *n*BuBIM to a blueshift of the UV/Vis features due to the stronger donation and better orbital overlap of the donors.[69] Moreover, the Cu···Cu distance and the Cu–N bond lengths decreased with higher donor strength of the ligand system. To sum it up, these findings clearly show that the higher the donor strength of the N-donor moieties are, the more blueshifted is the absorption band of the bis(μ-oxido) species and *vice versa*.

The influence of systematically modified N-donor moieties on the spectral features of the bis(μ-oxido) dicopper(III) species in both the UV/Vis and resonance Raman spectra was only reported in a few studies before.[66,218,219] Stack, Solomon and co-workers reported both a redshift in the UV/Vis spectra (from 399 nm to 408 nm to 413 nm) and a slight frequency shift in the resonance Raman spectra (from 605 cm^{-1} to 610 cm^{-1} to 616 cm^{-1}) for the CHD-based bis(μ-oxido) complexes **RC4**-**RC6** when the cyclohexyl-bridged bis(amine) ligand was modified from permethylated over a hybrid version (NMe_2, NEt_2) to perethylated.[66,218,219] They assigned the small frequency shifts in the Raman spectra to be indicative for solely the Cu_2O_2 core as larger frequency shifts were observed regarding smaller perturbations in the ligand system.[219] In addition, Solomon, Stack, and co-workers reported a frequency shift of the Cu–N stretching mode to smaller wavenumbers in the Raman spectrum for sterically demanding ligand systems. For the bis(μ-oxido) species **RC16**-**RC19** stabilized by the tridentate TACN system, the reversed trend was observed (see Table 30), which agrees well with the trend from [**O1**]$(PF_6)_2$ to [**O3**]$(PF_6)_2$ to [**O4**]$(PF_6)_2$.

Table 30: Selected structural and spectroscopic parameters of bis(μ-oxido) species stabilized by bidentate and tridentate ligands.

Oxido[a] species	**ligand system**	**UV/Vis, λ [nm] (ε [mM^{-1} cm^{-1}])**	**rR $\tilde{\nu}$ [cm^{-1}]**	**Cu···Cu [Å]**	**Cu–O[b] [Å]**	**Cu–N[b] [Å]**
[**O1**]$^{2+}$	TMGbenza	392 (21), 280 (40)	620	2.66[c] 2.76[d]	1.89[c] 1.80[d]	2.01, 2.06[c] 1.92, 1.97[d]
[**O3**]$^{2+}$	TMGbenzNEt$_2$	399 (21), 280 (40)	615	2.78[d]	1.81[d]	1.92, 1.99[d]
[**O4**]$^{2+}$	TMGbenzN*i*Pr$_2$	423 (18), 280 (38)	607	2.79[d]	1.81[d]	1.93, 2.00[d]
RC1	TMGdmap[47,150]	385 (18), 297 (20)	617[220]	2.78[c] 2.76[d]	1.82[c] 1.79[d]	1.96, 1.96[c] 1.91, 2.00[d]
RC2	TMGdeap[150]	392 (18), 297 (15)	–	–	–	–
RC3	TMG$_2$tol[135]	395 (12), 290 (38)	600	2.75[d]	1.81[d]	1.92[d]
RC4	TMCHD[66,218,219]	399 (25), 301 (20)	605	–	–	–
RC5	MECHD[66,218,219]	408 (28), 313 (21)	610	2.74[e] 2.73[c]	1.80[e] 1.81[c]	–
RC6	TECHD[66,218,219]	413 (23), 319 (17)	616	–	–	–
RC7	TMED[221]	392 (18)	607	2.74[c] 2.77[d]	1.80[c] 1.81[d]	1.96[c] 1.97[d]
RC8	Me$_2$Et$_2$ED[66]	397 (21), 297 (18)	–	–	–	–
RC9	TEED[66,219]	407 (24), 307 (17)	603	2.74[c]	1.80[c]	
RC10	PD[67]	375 (23), 278 (21)	–	2.77[c] 2.71[d]	1.86[c] 1.80[d]	2.00[c] 1.94[d]
RC11	DMPD[67]	390 (28), 290 (20)	–	2.81[c] 2.78[d]	1.82[c] 1.81[d]	1.96[c] 1.99, 1.91[d]
RC12	TMPD[67]	403 (29), 302 (19)	608	2.85[c] 2.83[d]	1.84[c] 1.81[d]	2.02[c] 2.00[d]
RC13	Me$_3$His[68]	380 (30), 280 (25)	–	2.80[c] 2.77[d]	1.82[c] 1.81[d]	1.97[c] 1.98, 1.91[d]
RC14	*n*BuHis[68]	363 (28), 262 (30)	–	2.78[c] 2.73[d]	1.82[c] 1.81[d]	1.96[c] 1.95, 1.91[d]
RC15	*n*BuBIM[69]	349 (24), 251 (35)	–	2.78[c] 2.69[d]	1.84[c] 1.76[d]	1.94[c] 1.89[d]
RC16	Me$_3$TACN[218]	412 (18), 307 (16)	604	2.77[c]	–	–
RC17	Bz$_3$TACN[178]	430 (14), 318 (12)	603	2.79[e]	1.81[e]	–
RC18	*i*Pr$_2$BzTACN[178]	436 (16), 322 (12)	594	–	–	–
RC19	*i*Pr$_3$TACN[178]	448 (13), 324 (11)	589	–	–	–

a) RC = reference bis(μ-oxido) complex in the presence of a weakly coordinating anion, b) Cu–O values are averaged; Cu–N values are averaged in some cases, c) Derived from EXAFS data, d) Determined by DFT calculations, e) Derived from X-ray data.

Next, cryo-UHR-ESI measurements were used to resolve the Cu–O_2 stoichiometry of the bis(μ-oxido) complexes [**O3**]$^{2+}$ and [**O4**]$^{2+}$ (Figure 51). The measured isotopic pattern and corresponding m/z values are in good agreement with the simulated spectra of the monocationic species [**O3**]$(PF_6)^+$ and [**O4**]$(PF_6)^+$, depicting a Cu–O_2 ratio of 2:1. Accordingly, the monocationic species [**O3**]$(BF_4)^+$, [**O3**]$(OTf)^+$, [**O4**]$(BF_4)^+$ and [**O4**]$(OTf)^+$ were obtained (Figure 71, Figure 72, Figure 73 and Figure 74 in the appendix). It is worth to mention that, in contrast to **L1**-stabilized complexes, the formation of the bischelate complex $[Cu(L)_2]^+$ using ligands **L3** or **L4** was found in neither case, which was ascribed to an increased steric demand of the ligand system due to the amine modification.

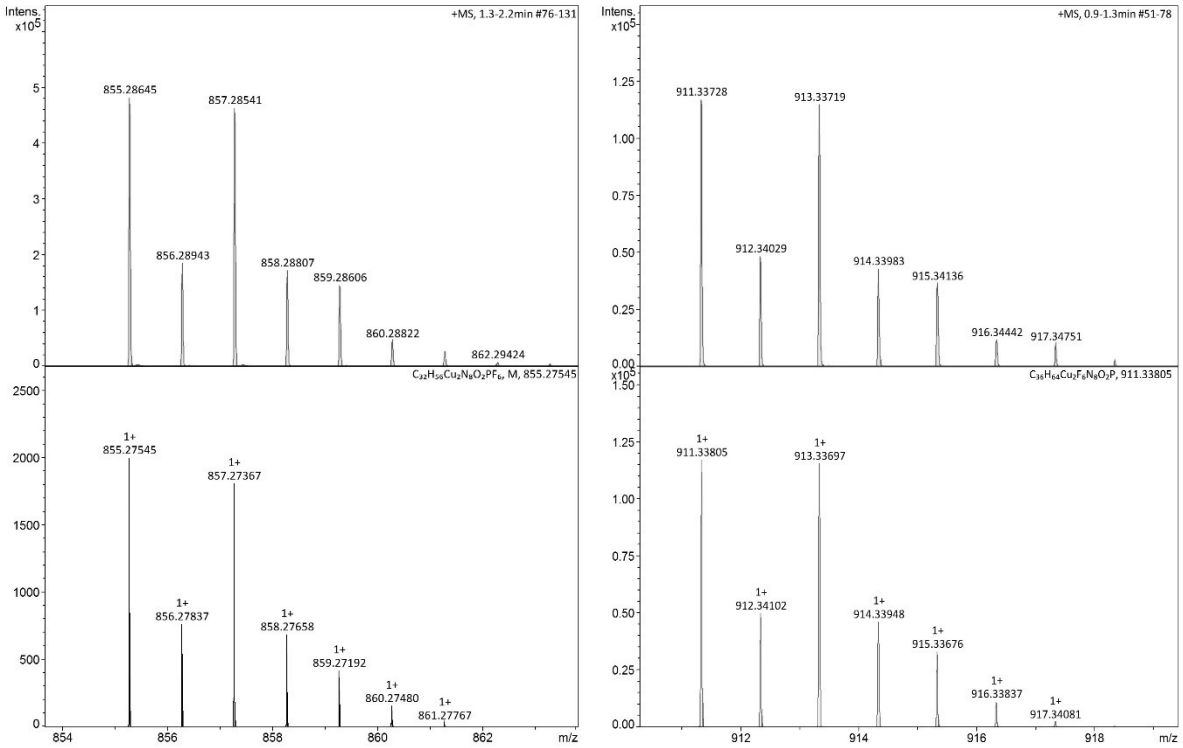

Figure 51: Cryo-UHR-ESI mass spectra of [**O3**]$(PF_6)^+$ (left) and [**O4**]$(PF_6)^+$ (right) in tetrahydrofuran at –80 °C (top: experimental, bottom: calculated spectra).

3.3.4. Catalytic Oxygenation Reactions

The conversion of a library of polycyclic aromatic alcohols by the bis(μ-oxido) complex [**O1**]$(PF_6)_2$ (see section 3.1.4) revealed a beneficial interplay of the sterically demanding, strong N-donor features of the guanidine moiety and the smaller, weaker amine donor moiety regarding the accessibility of the reactive bis(μ-oxido) dicopper(III) core towards external substrates. The variation of the amine donor moiety from NMe_2 to NEt_2 to N*i*Pr_2 increases the steric demand of the ligand shielding the bis(μ-oxido) core. The activity of the bis(μ-oxido) species [**O3**]$(PF_6)_2$ and [**O4**]$(PF_6)_2$ in catalytic oxygenation reactions was evaluated towards polycyclic aromatic alcohols to analyze the impact of the increased shielding of the Cu_2O_2 core on the substrate accessibility (Table 31). Oxygenation reactions were conducted in an

upscaled one-pot setup following the protocol described in section 3.1.4 with adjusted temperature according to the stability of the catalyst. The catalyst concentration was referred to the quantitative formation of the bis(μ-oxido) complex and adapted from the study on complex [**O1**](PF$_6$)$_2$. The duration of the hydroxylation reaction was extended to increase the substrate conversion.

Table 31: Catalytic oxygenation of polycyclic aromatic alcohols mediated by a bis(μ-oxido) species and subsequent condensation of the quinone by using 1,2-phenylenediamine to form phenazines.

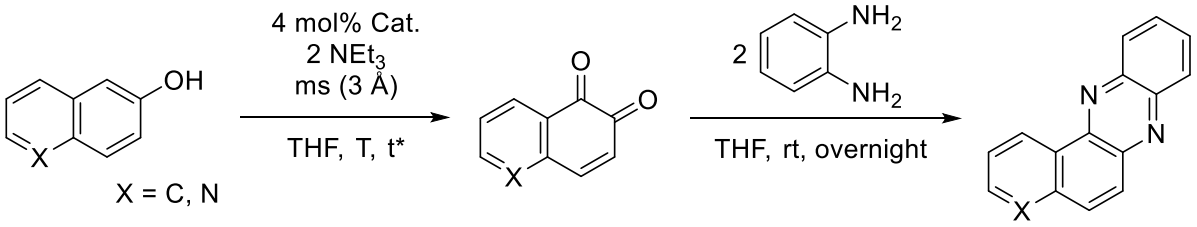

Entry	Cat.	Substrate	T [°C]	t* [h]	Conv.[a] [%]	Product P	Yield[b] [%]
1	[**O1**](PF$_6$)$_2$	2-naphthol	-90	1	89	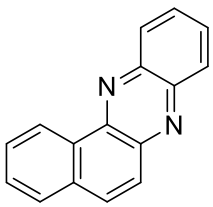 (**P1**)	31
2	[**O3**](PF$_6$)$_2$	2-naphthol	-100	2	82	(**P1**)	28
3	[**O4**](PF$_6$)$_2$	2-naphthol	-100	2	78	(**P1**)	23
4	[**O1**](PF$_6$)$_2$	6-quinolinol	-90	1	> 99	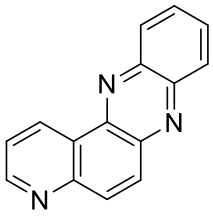 (**P2**)	30
5	[**O3**](PF$_6$)$_2$	6-quinolinol	-100	3	95	(**P2**)	31
6	[**O4**](PF$_6$)$_2$	6-quinolinol	-100	3	> 99	(**P2**)	28

[a] Determined conversion of the substrate by ^{1}H NMR spectroscopy. [b] Isolated yield of the phenazine after column chromatography.

The substrates 2-naphthol and 6-quinolinol were chosen to study the reactivity of the catalysts [**O3**](PF$_6$)$_2$ and [**O4**](PF$_6$)$_2$. Both substrates provide two product possibilities of the quinone formed to investigate the selectivity of the reaction. DFT calculations using the negative Fukui function revealed the preferred hydroxylation position to quinone intermediates which leads exclusively to bent phenazines (see section 3.1.4.2 for further details). 2-naphthol was transformed by [**O3**](PF$_6$)$_2$ within two hours at –100 °C at 82% (entry 2), whereas a smaller conversion of 78% was obtained when using the catalyst [**O4**](PF$_6$)$_2$ (entry 3), which was ascribed to the higher steric encumbrance of the *iso*-propyl groups with respect to the ethyl groups. The higher steric demand shields the Cu_2O_2 core more, thus decelerating the reaction

rate of substrate conversion. This agrees well with the isolated yield of benzo[a]phenazine (**P1**). Catalyst [**O1**]$(PF_6)_2$ achieved a marginally higher substrate conversion in only one hour at –90 °C (entry 1), so that more product **P1** was isolable. 6-quinolinol was nearly fully converted by all three catalysts [**O1**]$(PF_6)_2$, [**O3**]$(PF_6)_2$ and [**O4**]$(PF_6)_2$ (entry 4-6).

The conditions of the oxygenation reactions only differ in temperature, which is caused by the stability of the catalyst, and therefore also in the reaction time required to optimize the substrate conversion. Pyrido[3,2-a]phenazine (**P2**) was obtained in 28-31% isolated yield. The three catalysts exhibited likewise high selectivity without exception during the oxygenation reactions, yielding exclusively bent phenazines (see section 3.1.4.2 for further details). Consequently, the steric effects of the varied amine donor group on the selectivity of the catalyst in catalytic hydroxylation reactions are vanishingly small. The bis(μ-oxido) dicopper(III) core was open to challenging substrate classes despite the enlarged steric demand of the ligand system.

3.4. DMEGanil-stabilized Copper Complexes with Weakly Coordinating and Coordinating Anions

The benza ligands **L1**-**L4** demonstrated their suitability as tyrosinase model systems in the presence of coordinating and/or weakly coordinating anions. This chapter deals with the synthesis and characterization of the counterpart of the described hybrid guanidine ligands– the anil ligands, in which the guanidine moiety is bound to the methylene group. In contrast to the DMEG-based anil ligand, a ligand screening in earlier studies showed that the TMG-based anil ligand did not support the formation of bis(μ-oxido) dicopper(III) species.[154] Therefore, only the DMEG-based ligand was used in the following for further investigations. Hybrid guanidine ligand **L5** possesses a permethylated amine donor bound to the rigid phenyl ring and a dimethylethyleneguanidine (DMEG) moiety bound to the more flexible alkyl chain. The reactivity of **L5**-stabilized copper(I) complexes towards molecular oxygen is investigated in the presence of coordinating and weakly coordinating anions.

Parts of this chapter are already published in:

[1] M. Paul, *Master Thesis* **2017**, RWTH Aachen University.

3.4.1. Ligand Synthesis

Anil ligands are synthesized in a four-step reaction according to Scheme 30.

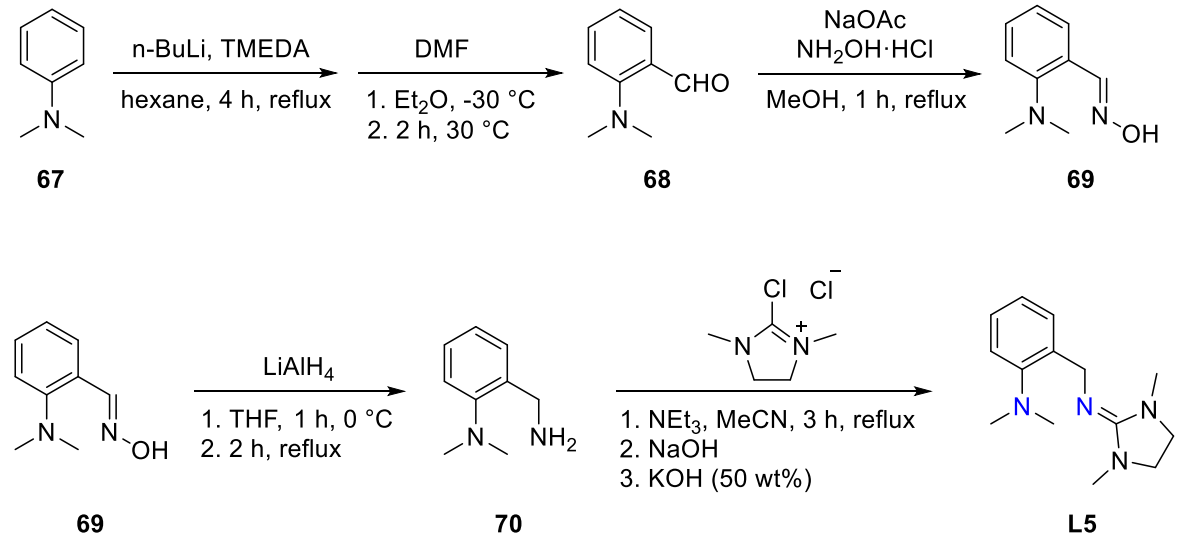

Scheme 30: Synthesis of hybrid guanidine ligand **L5**.

Firstly, *N,N*-dimethyl aniline (**67**) is lithiated in the *ortho*-position with *n*-butyl lithium in the presence of *N,N,N',N'*-tetramethylethylenediamine (TMEDA) and subsequently formylated by dimethyl formamide to form the aldehyde **68**. Secondly, the condensation of the aldehyde **68** with hydroxylamine hydrochloride and sodium acetate leads to the formation of aldoxime **69**. The oxime group is then reduced by lithium aluminum hydride to generate the primary

amine **70**. Finally, the guanidine synthesis is achieved by condensation of the amine with the Vilsmeier salt chlorido-*N,N'*-dimethylethyleneformamidinium chloride. It is noteworthy that the reaction product of all reaction steps was isolated in high yields in the master thesis, except for the *ortho*-formylation of *N,N*-dimethyl aniline (yield 43%).[154] Therefore, the reactants *n*-butyl lithium and TMEDA were adjusted over-stoichiometrically relative to the starting material. The product was purified by fractional vacuum distillation to produce the aldehyde **68** in 66% yield.

The hybrid guanidine ligand **L5** was purified by vacuum distillation to give the free base as a yellow oil. The overall yield of **L5** is determined to be 36%. **L5** was analyzed by NMR and IR spectroscopy as well as mass spectrometry. Ligand **L5** is very prone to protonation which is identified by precipitation of light-green solid. It is recommended to distill **L5** every few months and store the ligand in a glovebox under nitrogen or argon atmosphere.

The ligand **L5** was crystallized from a saturated pentane solution at -32 °C and analyzed by single crystal X-ray diffraction (Figure 52). Crystallographic details are provided in Table 42 in the appendix and key structural parameters are summarized in Table 32. **L5** crystallizes in the orthorhombic space group *P*na2$_1$ with *Z* = 4.

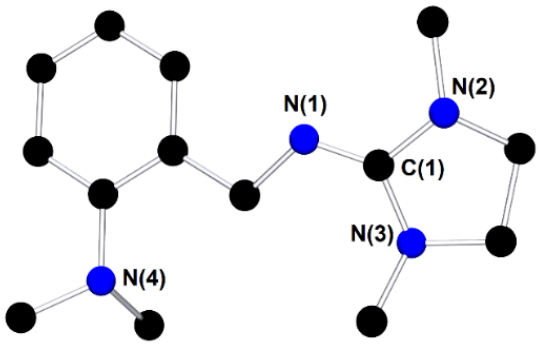

Figure 52: Molecular structure of **L5** in the solid state. Hydrogen atoms were omitted for clarity.

Table 32: Selected bond lengths [Å], angles [°] and the structure parameter ρ of **L5**.

	L5
C(1)–N(1)	1.281(3)
C(1)–N(2)	1.400(3)
C(1)–N(3)	1.392(3)
N(1)–C(1)–N(2)	129.9(2)
N(1)–C(1)–N(3)	122.1(2)
N(2)–C(1)–N(3)	108.0(2)
$\sphericalangle(CN_3;NC_3)_{av}$	10.1
ρ	0.92

ρ = 2a/(b+c)[127] with a = C(1)–N(1), b = C(1)–N(2) and c = C(1)–N(3).

Ligand **L5** possesses C–N single bond lengths ranging from 1.392(3) to 1.400(3) Å, which are closely related to the values of **L1** and **L2** (see section 3.1.1). The C=N double bond of **L5** is significantly shorter than that of **L1** and comparable that to **L2**. The guanidine twist amounts to 10°, which is characteristic for DMEG-based guanidine ligands due to the lack of free rotation of the rigid heterocycle.[99,119,133] Similar to **L2**, the N(2)–C(1)–N(3) angle within the imidazolidine ring of **L5** (108.0(2)°) is shortened in comparison to the ideal 120° bond angle. The structural parameter ρ was determined to 0.92, which is attributed to a good localization of the guanidine double bond.

3.4.2. Dioxygen Activation

Ligand **L5** and a copper salt (copper iodide or $[Cu(MeCN)_4]PF_6$) were dissolved in equimolar amounts in acetonitrile to generate *in-situ* the **L5**-stabilized copper(I) complexes **C28**-**C29** for oxygenation experiments. Activation of dioxygen was achieved by bubbling molecular oxygen through a tetrahydrofuran solution at low temperatures and subsequently injecting a solution of the copper(I) species **C28**-**C29** in acetonitrile (Scheme 31). Both coordinating anions and weakly coordinating anions are used to compare their stabilizing effect upon the oxygenation reaction.

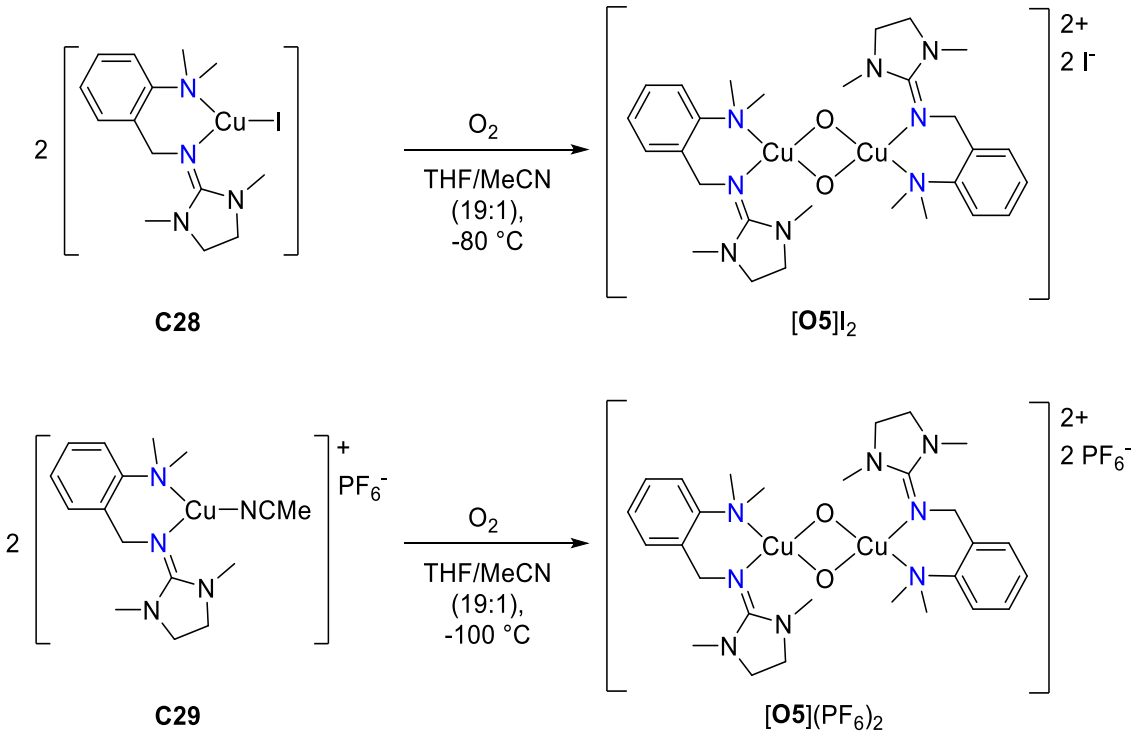

Scheme 31: Oxygenation of **L5**-stabilized copper(I) complexes **C28** and **C29** to generate the bis(μ-oxido) dicopper(III) complexes $[\mathbf{O5}]^{2+}$.

The aliphatic hybrid guanidine ligand DMEGanil (**L5**) was already tested in the oxygenation reactions of the corresponding monochelate copper(I) complexes in the presence of the coordinating anion I^- as a part of the master thesis.[154] Although the oxygenation experiment

was followed by UV/Vis spectroscopy at –80 °C for 20 min, the curve of the absorbance-time plot still revealed an increasing absorption band of the bis(μ-oxido) complex. Therefore, oxygenation of **C28** was repeated in a tetrahydrofuran/acetonitrile mixture at –80 °C for five hours. After the injection of **C28**, a slow coloration from colorless over yellow to green was observed. Selected UV/Vis spectra of the formation of [**O5**]$^{2+}$ are depicted in Figure 53 (left) for clarity.

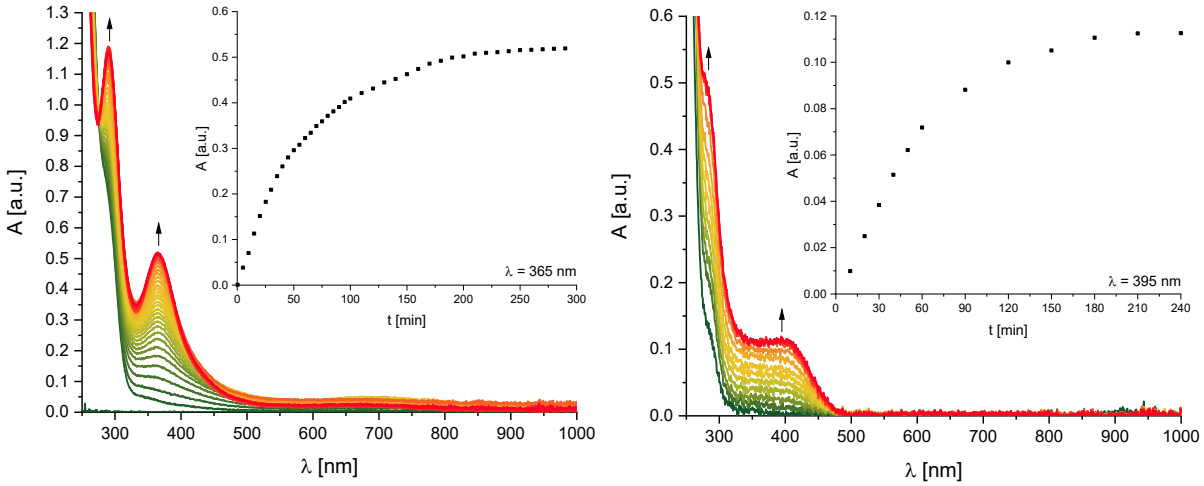

Figure 53: Selected UV/Vis spectra of the formation of [**O5**]I_2 at –80 °C (left) and [**O5**]$(PF_6)_2$ at –100 °C (right) in tetrahydrofuran (0.5 mM; inset: time-resolved formation of [**O5**]I_2 and [**O5**]$(PF_6)_2$ monitored at 365 nm and 395 nm).

The left UV/Vis spectrum exhibits two ligand-to-metal charge transfer bands at 290 nm (9500 M^{-1} cm^{-1}) and 365 nm (4200 M^{-1} cm^{-1}), which are characteristic for bis(μ-oxido) species.[10,11] The band at 365 nm is blueshifted in comparison to normally observed absorption bands at 400 nm, which was also observed for the bis(μ-oxido) species [**O1I**](CuI_2). This is a first hint for the presence of a stabilizing iodide-bridge in complex [**O5**]I_2 as observed for [**O1I**](CuI_2) (see section 3.2.3 for comparison). The higher extinction at 290 nm results from overlapping in-plane π_{σ^*} to d_{xy} and π to π* transitions of the aromatic backbone of **L5**. The weaker CT shoulder at 450 nm (1000 M^{-1} cm^{-1}) was ascribed to the guanidine π-system.[47] The formation of [**O5**]I_2 takes five hours and the extinction coefficients of the absorption bands are considerably low compared to other guanidine-supported bis(μ-oxido) complexes in the presence of coordinating anions.[99,132,135] These findings indicate no quantitative formation of [**O5**]I_2 which could be a result of the concomitant formation of iodidocuprate anions as observed for complex [**O1I**](CuI_2).

For comparison, the **L5**-stabilized copper(I) complex **C29** with weakly coordinating anions PF_6^- was oxygenated at a lower temperature of –100 °C (Figure 53, right), as the presence of these anions is accompanied by a faster formation and lower stability.[10,11] After the addition of **C29** to the oxygenated cooled solvent, a color change to yellow was observed. Although the oxygenation of **C29** was followed by UV/Vis spectroscopy for four hours, it yielded comparable

extinction coefficients of the LMCT bands 280 nm (10000 M^{-1} cm^{-1}) and 395 nm (2300 M^{-1} cm^{-1}) with respect to the oxygenation of **C28**. In addition, the absorption band at 395 nm of [**O5**]$(PF_6)_2$ is comparable to the corresponding band of [**O1**]$(PF_6)_2$ (features at 392 nm (21000 M^{-1} cm^{-1}) and 280 nm (40000 M^{-1} cm^{-1}), see section 3.1.3), but the maximum extinction at 395 nm is reduced by a factor of ten. These findings increase the suspicion of an incomplete formation of both bis(μ-oxido) complexes [**O5**]$(PF_6)_2$ and [**O5**]I_2 independent of the present anion.

Cryo-UHR-ESI measurements in the positive and negative mode were performed to elucidate to stoichiometry of the formed Cu_2O_2 species and its anions. The measurements were performed for both complexes [**O5**]$(PF_6)_2$ and [**O5**]I_2 and recorded approximately two hours after the injection of the Cu(I) complex solution into the preoxygenated, cooled tetrahydrofuran solution. Surprisingly, representative m/z values and isotopic pattern of a bis(μ-oxido) complex with or without one anion was observed in neither case despite several attempts. Upon the oxygenation of **C28** to generate [**O5**]I_2, the predominant m/z values and isotopic pattern obtained in the positive mode were ascribed to the bischelate complex [Cu(**L5**)$_2$]$^+$ (calculated: 555.29849, found: 555.29810). The negative mode exhibited the predominant formation of iodidocuprate anions with the composition of $[CuI_2]^-$ (calculated: 316.73909, found: 316.72938) next to a small signal of iodide (calculated: 126.90502, found: 126.90055), which were also observed during the generation of bis(μ-oxido) species [**O1I**](CuI_2) (see section 3.2.3). Upon the oxygenation of **C29** to generate [**O5**]$(PF_6)_2$, the predominant species is again the bischelate complex [Cu(**L5**)$_2$]$^+$ (calculated: 555.29849, found: 555.30870) in the positive mode. In contrast to the oxygenation of **C28**, a significant amount of the monochelate species [Cu(**L5**)]+ (calculated: 309.11405, found: 309.11928) and a small signal of [Cu(**L5**)(MeCN)]+ (calculated: 350.14060, found: 350.14671), when complex **C29** was oxygenated. Considering that the reaction duration already amounted to two hours, it is surprising that, on the one hand, not even a small signal of the bis(μ-oxido) species was detected although indicated otherwise by UV/Vis spectroscopy. On the other hand, a significant amount of Cu(I) species was monitored although normally very reactive Cu(I) species are prone to reactions with dioxygen when they are exposed to dioxygen. These findings indicate an existing dynamic equilibrium of Cu(I) monochelate and bischelate species, as previously observed with the ligand **L1** (see Scheme 25 for comparison). In case of **L5**-stabilized Cu(I) species, the equilibrium is seemingly shifted towards the dioxygen-resistant species [Cu(**L5**)$_2$]$^+$, which would explain the incomplete formation of [**O5**]$^{2+}$ and the long reaction duration. It is also possible that the amount of formed [**O5**]$^{2+}$ is too small to be detected via cryo-UHR-ESI mass spectrometry as other signals are relatively predominant despite the high sensitivity of the method. Another possible explanation for these findings is based on the properties of the ligand system **L5** itself. The incorporated aromatic spacer ensures the rigidity of the ligand backbone. In contrast to the equivalent

ligands **L1**-**L4**, the strong guanidine donor of **L5** is bound to the more flexible aliphatic chain, which causes a competition between steric constraints and the donor strength of the weaker amine moiety in order to stabilize the copper center. The flexibility of the amine moiety, which is bound to the aromatic ring, is limited by the rigid surrounding. Therefore, the limited range of motion presumably causes no proper orbital overlap of the amine moiety and the copper d orbitals, thus inhibiting the envisioned chelate effect of the ligand system, as observed previously in the molecular structure of **C28** in the solid state (Figure 54).[154]

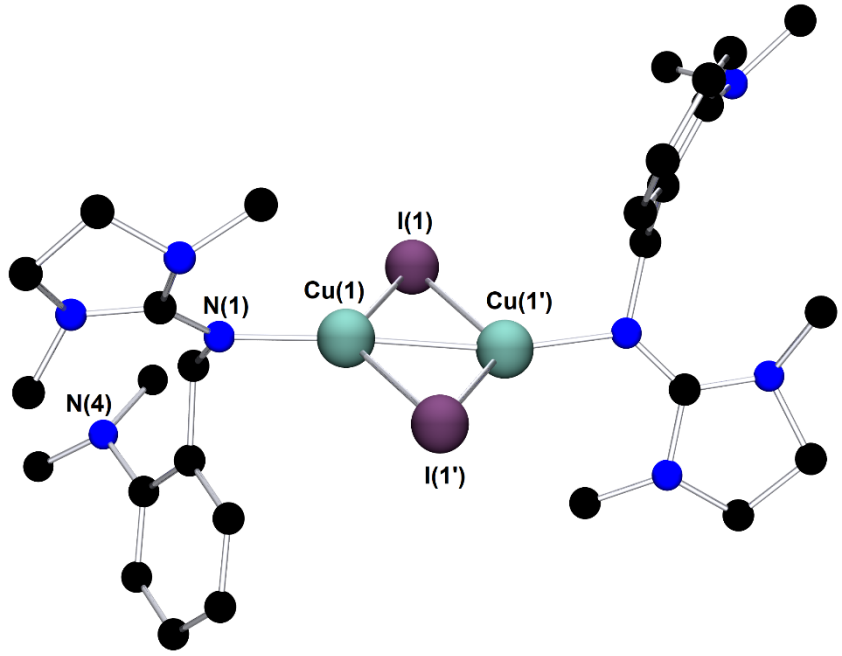

Figure 54: Molecular structure of copper(I) complex **C28**[154] in the solid state. Hydrogen atoms were omitted for clarity.

Complex **C28** showed a dimeric structure, in which the copper centers are only stabilized by the guanidine moiety and bridged by two iodides. As a result, the Cu···Cu distance is shortened to 2.5304(6) Å to saturate the coordination site of the copper atom. Moreover, the amine moiety is oriented in the opposite direction so that there is no stabilizing interaction between the copper(I) center and the intended amine donor moiety. Therefore, it is highly likely that there is also no chelate effect of **L5** in complex **C29**, because the chemical shift in the $^{13}C\{^{1}H\}$ NMR spectrum of the carbon atom adjacent to the amine group of **L5** is only marginally influenced upon complexation (**L5**: 152.6 ppm, **C28**: 153.1 ppm, **C29**: 152.8 ppm). An interaction of the amine group and the Cu(I) center should have an electronic effect which is observable in the NMR spectra. Consequently, ligand **L5** presumably lacks in donor strength to support the formation of a bis(μ-oxido) dicopper(III) complex, which requires a strong chelating ligand system to stabilize the high oxidation state. Future studies should therefore involve the development of a hybrid guanidine ligand with a stronger second N-donor or the incorporation of a different spacer to eliminate the geometric constraints.

4. Conclusion and Outlook

4.1. Conclusion

In this doctoral thesis, copper complexes stabilized by aromatic hybrid guanidine ligands with modified amine donor moieties were introduced as tyrosinase model systems to activate molecular oxygen as catalysts for organic transformation reactions. Correlations between structure and reactivity were evaluated by tuning of the ligand system (Figure 55). Tailored ligand systems were developed benefitting from the interplay of electronic and steric factors to create a toolbox for the application in tyrosinase-like oxygenation and oxidation reactions of aromatic alcohols.

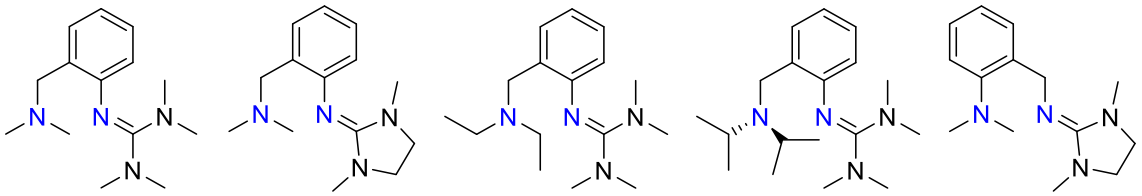

Figure 55: Structures of the synthesized benza and anil ligands **L1**-**L5**: TMGbenza (**L1**), DMEGbenza (**L2**), TMGbenzNEt$_2$ (**L3**), TMGbenzN*i*Pr$_2$ (**L4**) and DMEGanil (**L5**).

The aromatic hybrid guanidine ligands **L1** and **L2** consist of a guanidine and a permethylated amine moiety, which are bridged by an aromatic spacer to enhance the rigidity of the ligand backbone. The related ligands **L3** and **L4** possess a modified amine moiety to enhance the steric demand and simultaneously weaken the donor strength. The guanidines **L1**-**L4** were synthesized in a three-step reaction and isolated in good overall yields. The synthesis of the aliphatic counterpart **L5** was achieved in a four-step reaction starting from *N,N*-dimethyl aniline. The ligand **L5** contains a guanidine moiety bound to a flexible alkyl chain and an amine moiety rigidified to the phenyl ring of the spacer.

The reaction of hybrid guanidine ligands **L1** and copper(I) salts [Cu(MeCN)$_4$]X (X$^-$ = PF_6^-, BF_4^-, OTf^-, ClO_4^-) resulted in the formation of monochelate copper complexes in solution, which exhibited similar spectroscopic properties independent of the weakly coordinating anion. The crystallization of **L1**- and **L2**-stabilized copper(I) complexes in the presence of these anions yielded bischelate complexes, which is caused by the restricted steric demand of the ligand system. In contrast to a second ligand, coordinating acetonitrile molecules are not strong enough to saturate the coordination sites of the copper center. Therefore, neutral organophosphorus compounds were introduced as co-ligand to stabilize monochelate complexes in the solid state, which were characterized by X-ray diffraction. The combination of **L1** and copper(I) halides also resulted in the formation of monochelate copper(I) complexes, whereas ligand **L2** was found to exclusively stabilize dimeric copper(I) structures. Both ligands

L1 and **L2** form monochelate copper(II) complexes by using copper(II) halides. All monochelate copper halide complexes were analyzed crystallographically. The diffusion constants of ligand **L1** and its mono- and bischelate copper iodide complexes were determined by using ^{1}H DOSY NMR spectroscopy, revealing a higher dynamic behavior of the monochelate species due to the smaller molecule size. Therefore, the presence of a dimeric species in solution was ruled out. The guiding principle of the design of **L3** and **L4** was to inhibit the formation of bischelate copper(I) complexes by increasing the steric demand of the ligand, which was confirmed by ESI mass spectrometry, and therefore, exclusively the monochelate species was formed, which allows the activation of dioxygen.

Suitable copper(I) complexes, stabilized by the synthesized hybrid guanidine ligands, were investigated to activate molecular oxygen, leading to the formation of a bis(μ-oxido) dicopper(III) complex. These copper-dioxygen species were analyzed by spectroscopic methods, including UV/Vis, resonance Raman and X-ray absorption spectroscopy, cryo-UHR-ESI mass spectrometry and DFT calculations.

The oxygenation of **L1**-supported copper(I) acetonitrile complexes yielded the bis(μ-oxido) species [**O1**]$^{2+}$ in the presence of weakly coordinating anions PF_6^-, BF_4^-, OTf^- and ClO_4^-. The bis(μ-oxido) complex [**O1**]$^{2+}$ showed two characteristic absorption bands at 280 nm (40000 M^{-1} cm^{-1}) and 390 nm (21000 M^{-1} cm^{-1}) in the UV/Vis spectrum independent of the present anion. The oxygenation reaction required a temperature of –90 °C in tetrahydrofuran to form [**O1**]$^{2+}$ quantitatively after three minutes. The complete formation of [**O1**]$(PF_6)_2$ was confirmed by spectrophotometric titration with ferrocene monocarboxylic acid. Laser excitation at 420 nm resulted in a vibration feature at 620 cm^{-1} which is characteristic for the breathing mode of bis(μ-oxido) dicopper(III) complexes. The $^{16}O_2/^{18}O_2$ isotope exchange measurements on [**O1**]$(PF_6)_2$ exhibited a shift to 591 cm^{-1} which is in good agreement with DFT calculations. XAS measurements revealed an edge position and atom distances typically observed for Cu(III)-centered complexes. Cryo-UHR-ESI mass spectra showed m/z values and respective isotopic pattern of the monocationic species [**O1**]$(PF_6)^+$. Theoretical studies on [**O1**]$(PF_6)_2$ predicted a thermodynamically favored bis(μ-oxido) core over the related μ-η^2:η^2-peroxido core by 10 kcal mol^{-1}. The stability of [**O1**]$(PF_6)_2$ at –90 °C was determined to at least 90 minutes. At higher temperatures, a competitive thermal decay occurred during the formation of [**O1**]$(PF_6)_2$ causing lower quantity. The temperature sensitivity is reflected in the half-life times, which were determined to one hour at –80 °C and five minutes at –74 °C. The decomposition products of [**O1**]X_2 (X^- = PF_6^-, BF_4^-) stabilized by **L1** were analyzed by X-ray diffraction as a dicationic μ-alkoxido μ-hydroxido tricopper(II) complex [**H1**]X_2, which resulted from intramolecular hydroxylation of the supporting ligand system. Upon the decay of [**O2**]$(OTf)_2$, the formation of a bis(μ-hydroxido) dicopper(II) species [**H2**]$(OTf)_2$ was observed, although the two ligands **L1** and **L2** are structurally very similar. A reaction mechanism is proposed to

illustrate possible pathways which are presumably influenced by the coordinating properties of the anions and by the solvent used.

The activation of dioxygen was also achieved by monochelate copper(I) halide complexes stabilized by **L1**. The oxygenation of copper(I) chloride and bromide complexes revealed similar characteristics compared to [**O1**]$(PF_6)_2$, which was ascribed to the more ionic bond character of these anions to the copper(I) center. Cryo-UHR-ESI mass spectra showed the occurrence of the monocationic species [**O1**]$(X)^+$ (X^- = Br^-, Cl^-). A conspicuously different behavior was observed when the copper(I) iodide complex was oxygenated. Cryo-UHR-ESI mass spectra showed besides the monocationic species [**O1I**]$^+$ the occurrence of [**O1**]$(CuI_2)^+$. Moreover, the UV/Vis feature of the bis(μ-oxido) complex documented a blueshift to 370 nm, which is caused by stabilizing effects of an iodide bridge and formed iodidocuprate anions. Therefore, an additional equivalent copper iodide was necessary to achieve the complete formation of [**O1I**](CuI_2), which was confirmed by titration experiments. The iodide bridge and iodidocuprate stabilization provided an extraordinary stability of the bis(μ-oxido) complex, enabling a formation at room temperature. TD-DFT calculations on [**O1**]$^{2+}$ and [**O1I**]$^+$ illuminated the influence of the iodide bridge on the molecular orbitals and spectroscopic properties of the bis(μ-oxido) dicopper(III) species. The complex [**O1I**](CuI_2) was also accessible via salt metathesis from [**O1**]$(PF_6)_2$ and an iodide source, allowing a great leap in stability from –90 °C to room temperature. Even in a competitive oxygenation reaction, the more stable bis(μ-oxido) complex was formed. The complex [**O1I**](CuI_2) showed significantly slower formation kinetics than [**O1**]X_2, (X^- = Br^-, Cl^-), which can be explained by the bonding character of the present halide due to different ionic radii and the occurrence of a dynamic equilibrium between mono- and bischelate copper(I) species. The occurrence of such an equilibrium was examined by oxygenation experiments of bischelate complexes in solution and cryo-UHR-ESI mass spectrometry. A mechanism of the dynamic equilibrium was proposed. Besides the enhanced stability, complex [**O1I**](CuI_2) exhibited a slightly higher extinction coefficient than [**O1**]$(PF_6)_2$, which was redirected to the coordination of iodide as a third bridge between the copper centers, which was also found in other guanidine-stabilized bis(μ-alkoxido) complexes.[132] The complex [**O1I**](CuI_2) displays a rare example of a room temperature stable bis(μ-oxido) complex, providing excellent conditions for applications under mild reaction conditions.

The oxygenation of copper(I) complexes stabilized by ligands **L3** and **L4** led to bis(μ-oxido) complexes in the presence of weakly coordinating anions. The small structural modifications of the ligand system were intended to better understand the structure-function relationship of the reactive Cu_2O_2 species (Figure 56). Both bis(μ-oxido) complexes [**O3**]X_2 and [**O4**]X_2 (X^- = PF_6^-, BF_4^-, OTf^-) required a lower temperature of –100 °C during the formation and exhibited lower stability with respect to [**O1**]X_2, which correlates to the weaker amine donor

moiety following the trend NMe_2 > NEt_2 > N*i*Pr_2. Moreover, the decreased σ-donor character led to a redshift of the characteristic absorption band from 390 nm over 400 nm to 420 nm in the UV/Vis spectrum. The weak absorption feature at 500 nm was more pronounced in [**O4**]$^{2+}$ compared to [**O3**]$^{2+}$ and [**O1**]$^{2+}$, causing the orange color of [**O4**]$^{2+}$ due to the enhanced red contribution, whereas [**O3**]$^{2+}$ and [**O1**]$^{2+}$ are green. All **L3**- and **L4**-supported bis(μ-oxido) complexes were found in cryo-UHR-ESI mass spectra. Resonance Raman studies showed a slight frequency shift of the breathing mode of the Cu_2O_2 core, which presumably originates from the deformation of the Cu_2O_2 core. DFT calculations enabled the assignments of further Raman modes, providing deeper insights into the modified donor strength of the amine in correlation to the Raman mode. Moreover, the higher steric demand and diminished donor strength of the amine donor moiety from NMe_2 to NEt_2 to N*i*Pr_2 result in a larger twist between the Cu_2O_2 plane and the CuN_2 plane and an elongation of the Cu_2O_2 core. These effects cause a poorer orbital overlap, resulting in a redshift of the LMCT feature of the bis(μ-oxido) species.

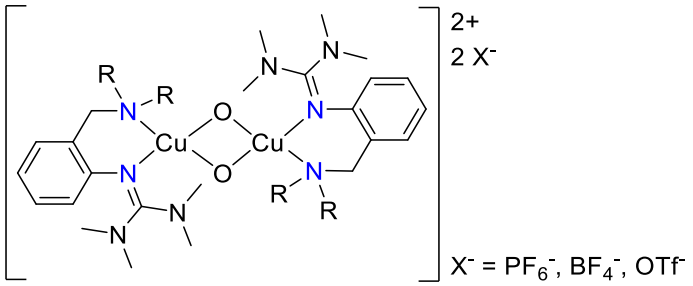

[**O1**]$^{2+}$ (R = Me)	[**O3**]$^{2+}$ (R = Et)	[**O4**]$^{2+}$ (R = *i*Pr)
-	steric demand of the ligand	+
+	amine donor strength	-
+	formation kinetics	-
+	stability	-
390 nm	red shift of the absorption band	420 nm
620 cm^{-1}	shift of the Raman mode	607 cm^{-1}

Figure 56: Influence of the modification of the amine donor moiety on properties of the bis(μ-oxido)dicopper(III) complex in the presence of weakly coordinating anions.

The activation of dioxygen by **L5**-supported copper(I) complexes was performed in the presence of coordinating and weakly coordinating anions. UV/Vis spectra exhibited characteristic absorption bands for a bis(μ-oxido) species [**O5**]$^{2+}$, but the extinction was considerably small in both cases indicating an incomplete formation of [**O5**]$^{2+}$. However, the complex [**O5**]$^{2+}$ was observed by cryo-UHR-ESI measurements in neither case. These findings were ascribed to solely guanidine stabilization, caused by geometric constraints of **L5** inhibiting the chelate effect.

Although the structure of the catalytically active center is still under debate, bis(μ-oxido) dicopper(III) complexes are anticipated to be key intermediates in C–H bond functionalizations of aromatic alcohols in oxygenation reactions.[11,90] The tyrosinase model system [**O1**]$(PF_6)_2$ was tested in catalytic hydroxylation reactions towards a library of substrate classes including phenols, pyridinols, naphthols, quinolinols and indolols. The generated quinones were transformed into more stable phenazine derivatives in a one-pot reaction by using 1,2-phenylenediamine. Simple (substituted) phenols and pyridinols were immediately oxygenated by [**O1**]$(PF_6)_2$, which led to undesired C–O coupling reactions even at –90 °C. More complicated substrates such as bicyclic aromatic alcohols were hydroxylated in a controlled manner. DFT calculations using the Fukui function enabled a prognosis of the preferred position of hydroxylation for substrates with two accessible *ortho*-positions next to the hydroxy group. The electrophilic attack was predicted to be at the C–H bond next to the neighboring aromatic ring, leading exclusively to bent phenazines. The prognosis was validated for all substrates used, yielding the isolated phenazine derivative up to 32% under the applied reaction conditions. Despite the temperature sensitivity of [**O1**]$(PF_6)_2$, the bis(μ-oxido) complex displays an astonishing example of oxidative power towards C–H bonds of aromatic alcohols. The commonly used substrate scope was impressively extended to more challenging substrates classes, to which the enzyme itself revealed no access.

Since a simple salt metathesis enabled room temperature stability of [**O1I**](CuI_2), oxygenation reactions were performed under mild conditions by using [**O1I**](CuI_2) as catalyst. Tested bicyclic aromatic alcohols were transformed into their phenazine derivative in up to 61% isolated yield, showing higher activity of [**O1I**](CuI_2) compared to [**O1**]$(PF_6)_2$. The iodide bridge of [**O1I**](CuI_2) revealed no measurable influence on the accessibility of the Cu_2O_2 core, indicating a sufficient access from one site to perform catalysis. Moreover, the resistant iodide bridge points towards diminished oxidative power of [**O1I**]$^+$ in the outer-sphere as radical mechanisms including C–C coupling reactions were observed in neither case.

The structural changes of the ligand system in **L3** and **L4** were also intended to influence the accessibility of the reactive bis(μ-oxido) core towards exogenous substrates. Both catalysts [**O3**]$(PF_6)_2$ and [**O4**]$(PF_6)_2$ were able to convert bicyclic aromatic alcohols in comparable yields. The bent phenazine derivatives were isolated in up to 31% yield, showing the high selectivity of both catalysts comparable to [**O1**]$(PF_6)_2$. Thus, reaction conditions only differed in temperature and therefore the time needed to achieve high conversions of substrates.

All in all, the catalyst [**O1**]$^{2+}$ displays the best tyrosinase model system in this study. This thesis opens the door to future improvements on tyrosinase model systems by the correlation of ligand design and reactivity of their copper(I) complexes towards dioxygen on the route to atom-economic and efficient C–H functionalization reactions.

4.2. Outlook

The hybrid guanidine ligands demonstrated their suitability as tyrosinase model systems. Especially, the ligand **L1** showed its versatility in stabilizing bis(μ-oxido) complexes depending on the present anion, which provides a powerful toolbox for tailored oxygenation reactions of organic substrates. However, the mechanism of catalytic oxygenation reactions is still not fully understood. Although most applied aromatic alcohols were fully converted by the bis(μ-oxido) complexes, the maximum yield achieved in the one-pot reaction was 61%. Thus, there is still plenty of room for improvement. The one-pot reaction should be analyzed at lower temperatures to enable the observation of reaction intermediates via spectroscopic methods. This could also help to clarify the reaction mechanism of catalyst decomposition, as the **L1**-supported μ-alkoxido μ-hydroxido tricopper(II) complex [**H1**]$^{2+}$ was the first example of a trinuclear decay product, which is seemingly contradictory to the often-observed binuclear bis(μ-hydroxido) and bis(μ-alkoxido) complexes.

The development of suitable ligands, which enable the stabilization of reactive Cu_2O_2 cores under ambient conditions without the help of counterions, represent one major goal in tyrosinase chemistry. Hybrid guanidine ligands with a more rigid aromatic backbone, such as **L1**, have proven to achieve the catalytic reactivity of Cu_2O_2 cores, whereas related ligands with simple aliphatic spacer only supported stoichiometric reactivity.[47] The substitution of the tertiary amine by a secondary amine generating the hybrid guanidine ligand **71** might enable higher thermodynamic stability[68] and a larger steric shield of corresponding Cu_2O_2 species compared to **L1** (Figure 57).

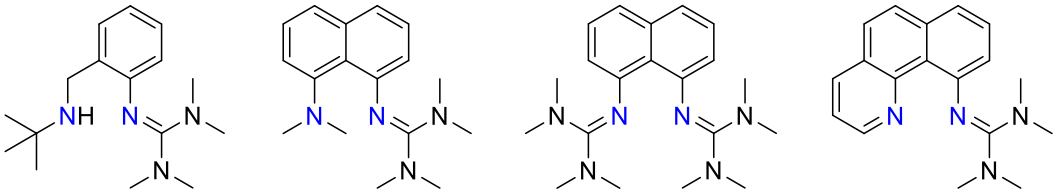

71 **72** **73** **74**

Figure 57: Ligand design of future hybrid guanidine and bis(guanidine) ligands.

Also, the hybrid guanidine and bis(guanidine) ligands **72** and **73** with a naphthalene-based spacer might enforce planarity of the ligand due to the high rigidity. The resulting pre-orientation of the N-donor moieties in a fixed bite angle might facilitate the copper coordination in six-membered ring due to a less flexible, presumably more stable ligand system. Bis(guanidine) ligand **73**[222] was already reported by Sundermeyer in 2002, but there are no reports on its copper(I) complexes and their reactivity towards dioxygen. Benzoquinoline-based hybrid guanidine ligands (**74**) enhance both rigidity and steric demand of the ligand system to prevent additionally the formation of bischelate complexes by shielding of the copper

center. These ligands facilitate the detection with spectroscopic methods due to the larger aromatic spacer.

Regarding the substrate scope of oxygenation reactions mediated by Cu_2O_2 species, new substrate classes should be evaluated. Exploring the limitations of the reaction should help to understand how the molecule size of the substrate and the steric demand of the ligand system correlate. After the successful conversion of bicyclic aromatic alcohols, the next logical step represents even more complicated tricyclic substrates such as anthrols or acridinols, which are envisioned to challenge bis(guanidines) in favor of hybrid guanidines due to steric factors.

5. Experimental Section

5.1. General Remarks

All operations were performed under an inert atmosphere of nitrogen (99.996%) with the use of standard Schlenk or glovebox techniques. Pure nitrogen (nitrogen 5.0) was dried by a column of P_2O_5. Solvents (HPLC grade, Fisher Scientific) were purified under nitrogen atmosphere via distillation from CaH_2, magnesium or sodium/benzophenone ketyl radical. All chemicals were purchased commercially (Table 33) and used without further purification unless otherwise noted. Copper salts $[Cu(MeCN)_4]X$ ($X^- = PF_6^-$, BF_4^-, OTf^-, ClO_4^-) were synthesized by reaction of Cu_2O (99.99%, Sigma Aldrich) and acid HX (Sigma Aldrich) in acetonitrile and recrystallized at least twice from acetonitrile/diethyl ether at -30 °C.[223] Vilsmeier salts chlorido-N,N,N',N'-tetramethylformamidinium chloride and chlorido-N,N'-dimethylethyleneformamidinium chloride were synthesized according to literature procedures.[126,128,222] Ferrocene monocarboxylic acid was recrystallized twice from tetrahydrofuran. Thin-layer chromatography sheets were purchased from Macherey-Nagel (SiO_2, layer thickness 0.20 mm, fluorescent indicator). Column chromatography was performed on Geduran Si 60 (40-63 µm, Merck).

Table 33: Used chemicals.

Chemicals	Supplier
1-methyl 2-naphthol (95%)	abcr
1-naphthol (98%)	Fluka
1,2-phenylenediamine (98%)	Fluka
2-methyl 8-quinolinol (98%)	abcr
2-naphthol (98%)	Sigma-Aldrich
2-nitrobenzyl bromide (97%)	abcr
2,4-di-*tert*-butyl phenol (98%)	Sigma-Aldrich
3-pyridinol (98%)	abcr
3-quinolinol (95%)	abcr
4-indolol (98%)	abcr
4-methoxy phenol (98%)	Sigma-Aldrich
4-pyridinol (97%)	abcr
4-quinolinol (98%)	abcr
4-*tert*-butyl phenol (98%)	abcr
5-indolol (95%)	abcr
6-indolol (95%)	abcr
6-quinolinol (95%)	Sigma-Aldrich
7-indolol (95%)	abcr

8-quinolinol (99%)	Merck
acetonitrile-d_3 (99.8%)	Sigma-Aldrich
calcium hydride (0-2 mm, 93%)	Acros Organics
charcoal	Grüssing
chloroform-d (99.96%)	Euriso-top
Celite 535	Roth
copper(I) bromide (99%)	Fluka
copper(II) chloride (97%)	Fluka
copper(I) iodide (98%)	Fluka
di-*iso*-propyl amine (99%)	Sigma-Aldrich
diethyl amine (99.5%)	Sigma-Aldrich
dimethyl amine (2 M in tetrahydrofuran)	Sigma-Aldrich
dimethyl aniline (99%)	Sigma-Aldrich
dimethyl sulfoxide-d_6 (99%)	Sigma-Aldrich
dimethyl formamide (HPLC grade)	Fisher Scientific
dioxygen 2.5 (99.5 Vol%)	Westfalen AG
ethylenediaminetetraacetic acid (EDTA, 99%)	Fluka
ferrocene monocarboxylic acid (FcCOOH, 97%)	abcr
ferric chloride (99%)	Riedel-de Haën
hydrazine monohydrate (98%)	Tokyo Chemical Industry
hydrochloric acid (37%)	Fisher Scientific
hydroxylammonium chloride (99%)	VWR
lithium aluminum hydride (97%)	Sigma-Aldrich
n-butyl lithium (2.5 M in hexane)	Sigma-Aldrich
phenol (99%)	Merck
potassium hydroxide (85%)	Grüssing
sodium (99.9%)	Sigma-Aldrich
sodium acetate (99%)	Sigma-Aldrich
sodium chloride (99.5%)	Grüssing
sodium hydroxide (99%)	Grüssing
sodium sulfate (99%)	Grüssing
tetrabutylammonium bromide (98%)	abcr
tetrabutylammonium chloride (95%)	abcr
tetrabutylammonium iodide (98%)	abcr
tetramethylethylenediamine (98%)	Fluka
triethylamine (99%)	abcr
trimethylphosphine (1 M in tetrahydrofuran)	Sigma-Aldrich
triphenylphosphine (99%)	abcr

5.2. Physical Methods

5.2.1. Mass Spectrometry

EI mass spectrometry was performed with the use of a Thermo Fisher Scientific Finnigan MAT 95 spectrometer with a source voltage of 5 kV and an electron energy of 70 eV.

ESI mass spectra were recorded on a Thermo Fisher Scientific LTQ Orbitrap XL spectrometer at a source voltage of 4.49 kV and a capillary temperature of 299.54 °C. The voltage of the tube lens was between 100 and 130 V.

Cryospray-ionization mass spectrometry (CSI-MS) measurements, recorded for oxygenation reactions of **C1** and **C3**, were performed by Laura Senft (group of Prof. Dr. Ivana Ivanović-Burmazović, FAU Erlangen-Nürnberg) on an UHR-TOF Bruker Daltonik maXis plus, an ESI-quadrupole time-of-flight (qToF) mass spectrometer capable of a resolution of at least 60.000 FWHM, which was coupled to a Bruker Daltonik Cryospray unit. Detection was in the positive ion mode; the source voltage was 3.8 kV. The flow rate was 4.0 µL min^{-1}. The drying gas (N_2), to achieve solvent removal, and the spray gas were both held at –80 °C. The mass spectrometer was calibrated prior to every experiment via direct infusion of Agilent ESI-TOF low concentration tuning mixture, which provided a m/z range of singly charged peaks up to 2700 Da in both ion modes.

Cryospray-ionization mass spectrometry (CSI-MS) measurements, recorded for oxygenation reactions of **C10**-**C15** and **C22**-**C29**, were performed on an UHR-TOF Bruker Daltonik maXis II, an ESI-quadrupole time-of-flight (qToF) mass spectrometer capable of a resolution of at least 80.000 FWHM, which was coupled to a Bruker Daltonik Cryospray unit. Detection was either in the positive or in the negative ion mode; the source voltage was 3.5 kV. The flow rate was 3.0 µL min^{-1}. The drying gas (N_2), to achieve solvent removal, and the spray gas were both held at –80 °C. The mass spectrometer was calibrated prior to every experiment via direct infusion of Agilent ESI-TOF low concentration tuning mixture, which provided a m/z range of singly charged peaks up to 3000 Da in both ion modes.

5.2.2. Elemental Analysis

Elemental analyses were carried out on an elementar vario EL and an elementar vario EL cube instrument.

5.2.3. NMR Spectroscopy

^{1}H, $^{13}C\{^{1}H\}$, $^{19}F\{^{1}H\}$ and $^{31}P\{^{1}H\}$ NMR spectra were recorded on a Bruker Avance II 400 and Bruker Avance III HD 400 spectrometer at 25 °C in NMR tubes, respectively. Resonances were referenced to the residual solvent signal, relative to TMS. Chemical shifts were assigned

with the use of two-dimensional NMR experiments (COSY, HSQC, HMBC). DOSY NMR measurements were performed using ^{1}H NMR standard processing applied on pseudo-2D datasets (si = 8k, lb = 0.3, xf2, abs2). Self-diffusion constants were evaluated by using the program Dynamics Center of Bruker. Integration areas were defined manually according to the proton shifts, and its diffusion were arithmetically averaged. All NMR data were deposited as original data in Chemotion Repository and are published under an Open Access model. The link to the original data is given in the analytical description.

5.2.4. IR Spectroscopy

FT-IR spectra were recorded on a Shimadzu IR Tracer 100 equipped with a CsI beam splitter in combination with an ATR unit (Quest model from Specac utilizing a robust monolithic crystalline diamond) in a resolution of 2 cm^{-1} and on a ThermoFisher Avatar™ 360 spectrometer with the use of KBr pellets or NaCl plates in a resolution of 2 cm^{-1}.

5.2.5. UV/Vis Spectroscopy

UV/Vis spectroscopy was carried out on a Cary 60 spectrophotometer of Agilent Technologies connected via a Cary 50 fiber optic coupler and combined with a fiber-optic quartz glass immersion probe (Hellma, 1 mm) and a tailored Schlenk cell.

5.2.6. Raman Spectroscopy

Raman measurements were performed and evaluated by the group of Prof. Dr. Michael Rübhausen at the Center for Free Electron Laser Science (CFEL) in Hamburg with a UT-3 Raman spectrometer[224], combined with a frequency doubled Ti:sapphire laser (Tsunami model 3960C-15HP, Spectra Physics Lasers Inc.) to obtain an excitation wavelength of 420 nm with a pulse width of 2.3 ps or a 532 nm diode cw laser (Millennia, Spectra Physics Lasers Inc.). The cryostat was a slightly modified version of a setup described previously[225] with a 1.4 mL or a 3.5 mL screw cap Suprasil® cuvette with septum (117104F-10-40, Hellma) for oxygenation, equipped with a Peltier element (QC-127-1.4-6.0MS, QuickCool) and a cooling copper block which encloses three sides of the cuvette. The laser beam was widened with a spatial filter and then focused on the cuvette inside the cryostat. The focus spot size was around 20 µm or 50 µm in diameter. With a micrometer screw, a focal depth of 30 µm inside the cuvette was adjusted. Raman scattered light was captured with the entrance optics of the UT-3 triple monochromator spectrometer.[224] The complexes **C1** (20 mmol L^{-1}), **C22** and **C25** (10 mmol L^{-1}) in tetrahydrofuran/acetonitrile (80:20) were cooled in the cuvette cryostat to below –90 °C. Dioxygen was added via a cannula through the septum (0.02 bar overpressure for 5 min for a complex concentration of 20 mmol L^{-1} or 10 min for a complex concentration of 10 mmol L^{-1}) until a distinct color change was observed. The used laser power in front of the

entrance optics was 37 mW or 42 mW. Data were accumulated for 3 x 120 s and corrected for the spectral sensitivity of the instrument.

5.2.7. X-ray Absorption Spectroscopy

X-ray absorption spectroscopy was performed and evaluated by the group of Prof. Dr. Michael Rübhausen at the CFEL in Hamburg. The data were collected in fluorescence mode using a Passivated Implanted Planar Silicon (PIPS) detector at beamline P64 (DESY, PETRA III, Hamburg, Germany).[226]

The complex **C1** was prepared under inert conditions (oxygen and water free) and then transferred to a cuvette with septum. The cuvette was cooled in a liquid ethanol bath of liquid ethanol based closed-cycle chiller (Proline RP890, Lauda) to below 183 K. Afterwards oxygen was added for 5 min to form the complex. With a precooled syringe, the solution (~75 µL) was first transferred to the sample holder, which was frozen directly after in a liquid nitrogen bath and put into a closed cycle helium cryostat (SHI-950T, Janis and SHI) afterwards, which was precooled to 150 K. The sample was kept at 150 K during the whole measurement.

The measurement time for a complete scan from 8780 eV to 9880 eV was 300 s. In total, the complex was measured for one hour. Copper foil was measured concomitantly, and the first inflection point energy set to 8979.0 eV. All measurements were calibrated to this shift afterwards. Data processing and analysis were performed with Athena and Artemis.[156]

Data reduction and Analysis:

For each spectrum, a second-order polynomial was fitted to the pre-edge region, extrapolated, and then subtracted from the data using Athena. Normalization was performed starting 150 eV above the edge with a normalization order of 3. For background removal, Rbkg was set to 1.1 and the k-weight to 2. The spline range was 0 to 15.3 $Å^{-1}$ in k and 0 to 894 eV in energy above the edge. Low and high spline clamps were set to “None” and “Strong”, respectively. For EXAFS fitting, the first shell and five additional carbon atoms were used, as they have a similar distance to the copper atom as the other copper atom. Scattering paths were calculated using Demeter 0.9.26 with Ifeffit 1.2.12 and a DFT-calculated structure of the complex.

Parameters:

ΔE_0	= 6.38404822 ± 2.02977590
σ^2 (for Cu–O, Cu–N, Cu–C)	= 0.00014048 ± 0.00074801
σ^2 (for Cu–Cu)	= 0.01341955 ± 0.00512504
delta (for Cu–N, Cu–O)	= 0.05059119 ± 0.00606741
delta2 (for Cu–Cu)	= -0.03150106 ± 0.01810690
delta3 (for Cu–C)	= 0.02573750 ± 0.01541418

5.2.8. Single Crystal X-ray Diffraction

The single crystal diffraction data for **L1**, **L2**, **L5**, [**L1**H_2]$^{2+}$, **C5-C9**, **C11-C12**, **C17-C19**, **C21**, [**H1**]X_2 (X^- = PF_6^-, BF_4^-), [**H2**]$(OTf)_2$, **P3** and **P5** are presented in Tables 34-43 in the appendix. The data were collected with a four-circle goniometer STOE Stadivari with Dectris Pilatus3 R 200 K hybrid pixel detector with the use of GeniX 3D high flux Mo-Kα radiation (0.71073 Å) or Cu–Kα radiation (1.54186 Å) at 100 K. The temperature was controlled by using an Oxford Cryostream 800. Crystals were mounted with grease on glass fibers. Data were collected with X-Area Pilatus and integrated with X-Area Integrate and X-Area Recipe. The absorption correction was performed by Gaussian integration with X-Red32. Scaling of reflections was carried out by using X-Area LANA.[227]

The single crystal diffraction data for **C10**, **C16** and **C20** are presented in Tables 38, 39 and 41 in the appendix. The data were collected by the group of Prof. Dr. Ullrich Englert with a Bruker D8 goniometer with APEX CCD area detector in ω-scan mode with Mo-Kα radiation (0.71073 Å) of an Incoatec microsource. Data reduction and absorption correction was performed by using SAINT and SADABS.[228]

The structures were solved by direct and conventional Fourier methods and all non-hydrogen atoms were refined anisotropically with full-matrix least-squares based on F² (XPREP[229], SHELXT[230], SHELXL[231] and ShelXle[232]). Hydrogen atoms were derived from difference Fourier maps and placed at idealized positions, riding on their parent C atoms, with isotropic displacement parameters U_{iso}(H) = 1.2 U_{eq}(C) and 1.5 U_{eq}(C methyl). All methyl groups were allowed to rotate but not to tip.

In complex **C9** it was not possible to model the disordered solvent molecules of tetrahydrofuran (void with 145 Å^3 and electron content of 38 electrons) in an adequate manner, and the data set was treated with the SQUEEZE routine as implemented in PLATON.[233,234]

Full crystallographic data have been deposited with the Cambridge Crystallographic Data Centre as supplementary no. CCDC – 1950654 for [**H1**]$(PF_6)_2$, CCDC – 1950655 for [**H1**]$(BF_4)_2$, CCDC – 1950656 for **P3,** CCDC – 1950657 for **P5** and CCDC – 1963147 for [**L1**H_2]$(BF_4)_2$, CCDC – 2003620 for **C10**, CCDC – 2003621 for **C11** and CCDC – 2003622 for **C12**. Copies of the data can be obtained free of charge on application to CCDC, 12 Union Road, Cambridge CB2 1EZ, UK (fax: (+44)1223-336-033; e-mail: deposit@ccdc.cam.ac.uk).

5.2.9. Computational Details

DFT calculations were performed, analyzed and interpreted by Dr. Alexander Hoffmann with the program suite Gaussian 16, revision B01.[235] The geometries of bis(μ-oxido) species were optimized by using the nonlocal hybrid meta GGA TPSSh functional[157–159], the triple-zeta basis set def2-TZVP[160–163] as implemented in Gaussian on all atoms and the empirical dispersion

correction with Becke-Johnson damping factors (GD3BJ).[164–167] This combination was found best for the calculation of bioinorganic copper complexes.[201,217,236,237] Furthermore, a PCM solvent model (tetrahydrofuran) was used for the calculations on the bis(μ-oxido) species [**O1**]$^{2+}$ and [**O1I**]$^{+}$. For the theoretical bis(μ-oxido) species [**O3**]$^{2+}$ and [**O4**]$^{2+}$, no solvent model was used in the calculations because no stable minimum was observed. Frequency calculations showed no imaginary values. Additionally, effective core potentials (ECP) obtained from the TURBOMOLE basis set library were used for the heavier atom I for the geometry optimization of bis(μ-oxido) complex [**O1I**]$^{+}$.[238,239] NBO calculations were accomplished using the program suite NBO 7.0 delivering the NBO charges and the charge-transfer energies by second order perturbation theory.[213–215] The condensed Fukui function for an electrophilic attack was calculated using AOMix.[240]

5.3. Synthetic Procedures

Some substances are resynthesized according to literature-known protocols, which were modified. These are marked with the reference.

5.3.1. Synthesis of *N,N*-Dialkyl-(2-nitrophenyl)methanamines

Dialkyl amine (255 mmol, 5.1 eq) was added dropwise to a stirred solution of 2-nitrobenzyl bromide (10.8 g, 50 mmol, 1.0 eq) in ethanol (240 mL). The mixture was refluxed for six hours. The solution was acidified to pH 1 by using concentrated hydrochloric acid. The solvent was removed under reduced pressure. The pH level of the resulting mixture was adjusted to 14 by using aqueous sodium hydroxide solution. The solution was extracted with diethyl ether (4 x 100 mL). The combined organic layers were washed with saturated aqueous sodium chloride solution, dried over sodium sulfate, and evaporated to dryness.

5.3.1.1. Resynthesis of *N,N*-Dimethyl-(2-nitrophenyl)methanamine (61)[241]

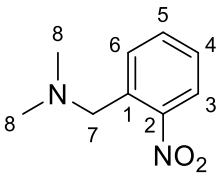

$C_9H_{12}N_2O_2$
180.21 g mol^{-1}

Yellow oil (7.95 g, 44.1 mmol, 88%). **^{1}H NMR** (400 MHz, Chloroform-*d*, 25 °C): *δ* [ppm] = 7.83 (dd, *J* = 8.1, 1.2 Hz, 1H, H3), 7.63 – 7.59 (m, 1H, H5), 7.54 (td, *J* = 7.5, 1.3 Hz, 1H, H4), 7.41 – 7.36 (m, 1H, H6), 3.71 (s, 2H, H7), 2.22 (s, 6H, H8). **^{13}C{^{1}H} NMR** (101 MHz, Chloroform-*d*, 25 °C): *δ* [ppm] = 149.8 (C2), 134.6 (C1), 132.6 (C4), 131.1 (C5), 127.9 (C6), 124.5 (C3), 60.4 (C7), 45.8 (C8). Additional information on the NMR spectra of the target compound including original data files is available via Chemotion Repository: https://dx.doi.org/10.14272/FCAMUPIRWKNASD-UHFFFAOYSA-N.1

5.3.1.2. Synthesis of *N,N*-Diethyl-(2-nitrophenyl)methanamine (63)

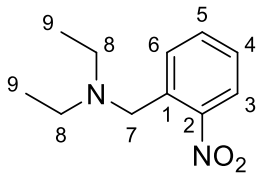

$C_{11}H_{16}N_2O_2$
208.26 g mol^{-1}

Orange oil (10.2 g, 48.9 mmol, 98%). **^{1}H NMR** (400 MHz, Chloroform-*d*, 25 °C): δ [ppm] = 7.80 (dd, *J* = 8.0, 1.2 Hz, 1H, H3), 7.75 – 7.71 (m, 1H, H6), 7.55 – 7.50 (m, 1H, H5), 7.38 – 7.33 (m, 1H, H4), 3.84 (s, 2H, H7), 2.49 (q, *J* = 7.1 Hz, 4H, H8), 0.99 (t, *J* = 7.1 Hz, 6H, H9). **^{13}C{^{1}H} NMR** (101 MHz, Chloroform-*d*, 25 °C): *δ* [ppm] = 149.8 (C2), 136.3 (C1), 132.5 (C5), 131.0 (C6), 127.5 (C4), 124.3 (C3), 54.9 (C7), 47.3 (C8), 11.9 (C9). **HRMS-ESI+** (MeCN): m/z calc. for [($C_{11}H_{16}N_2O_2$)+H]$^+$: 209.12845, found: 209.12850. **IR** (ATR): $\tilde{\nu}$ [cm^{-1}] = 2969 (w, C–H_{arom}), 2935 (vw, C–H_{arom}), 2874 (vw, C–H_{aliph}), 2803 (vw, C–H_{aliph}), 1610 (vw), 1522 (s, N–O), 1446 (w), 1385 (w), 1359 (m), 1345 (m, N–O), 1297 (w), 1240 (vw), 1203 (m), 1167 (m), 1119 (w), 1060 (m), 1043 (w), 994 (vw), 969 (vw), 857 (m) 816 (w), 780 (m), 726 (vs), 704 (vw), 678 (w), 666 (w). Additional information on the NMR spectra of the target compound including original data files is available via Chemotion Repository: https://dx.doi.org/10.14272/ZZLYWHZNBDCOFU-UHFFFAOYSA-N.1

5.3.1.3. Synthesis of *N,N*-Di-*iso*-propyl-(2-nitrophenyl)methanamine (64)

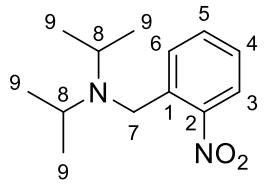

$C_{13}H_{20}N_2O_2$
236.32 g mol^{-1}

Yellow oil (11.3 g, 47.9 mmol, 96%). **^{1}H NMR** (400 MHz, Chloroform-*d*, 25 °C): δ [ppm] = 7.99 – 7.96 (m, 1H, H3), 7.83 (dd, *J* = 8.1, 1.3 Hz, 1H, H6), 7.57 – 7.52 (m, 1H, H4), 7.35 – 7.29 (m, 1H, H5), 3.94 (s, 2H, H7), 3.00 (sept, *J* = 6.6 Hz, 2H, H8), 1.00 (d, *J* = 6.6 Hz, 12H, H9). **^{13}C{^{1}H} NMR** (101 MHz, Chloroform-*d*, 25 °C): *δ* [ppm] = 149.2 (C2), 139.1 (C1), 132.7 (C4), 130.9 (C6), 127.0 (C5), 124.2 (C3), 48.9 (C8), 46.5 (C7), 20.8 (C9). **HRMS-EI**: m/z calc. for [$C_{13}H_{20}N_2O_2$]: 236.1519, found: 236.1513. **IR** (ATR): $\tilde{\nu}$ [cm^{-1}] = 2967 (m, C–H_{arom}), 2932 (w, C–H_{arom}), 1607 (vw), 1577 (vw), 1522 (vs, N–O),1463 (m), 1383 (m), 1366 (m), 1341 (m, N–O), 1296 (w), 1206 (m), 1177 (m), 1159 (m), 1139 (m), 1119 (m), 1053 (w), 1041 (w), 1030 (w), 961 (w), 938 (w), 887 (w), 856 (m), 789 (m), 751 (w), 726 (s), 678 (m), 666 (vw), 610 (vw), 564 (vw), 525 (vw). Additional information on the NMR spectra of the target compound including original data files is available via Chemotion Repository: https://dx.doi.org/10.14272/WHORYBNTUMXXTK-UHFFFAOYSA-N.1

5.3.2. Synthesis of 2-{(Dialkylamino)methyl}anilines

A solution of *N,N*-dialkyl-(2-nitrophenyl)methanamine (44.1 mmol, 1.0 eq) in dried methanol (150 mL) was added to a suspension of ferric chloride (360 mg, 2.20 mmol, 0.05 eq), charcoal (3.0 g) and hydrazine monohydrate (13.3 mL, 273 mmol, 6.2 eq) in two aliquots. The first portion was added dropwise initially. After stirring for 30 min at 65 °C, the remaining portion was added dropwise to the black suspension. The mixture was stirred at 65 °C for additional five hours and then at room temperature overnight. The suspension was filtered, and the filtrate

was evaporated to dryness. The residue was dissolved in methylene chloride, dried over sodium sulfate, and dried under reduced pressure.

*The quantities given are exemplary for the synthesis of compound **62** (see below). Quantities needed for the synthesis of compounds **65** and **66** must be adjusted according to the yield of the respective precursor compound (**63** and **64**).*

5.3.2.1. Resynthesis of 2-{(Dimethylamino)methyl}aniline (62)[241,242]

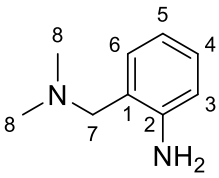

$C_9H_{14}N_2$
150.23 g mol^{-1}

Colorless solid (5.45 g, 36.3 mmol, 82%). **^{1}H NMR** (400 MHz, Chloroform-*d,* 25 °C): *δ* [ppm] = 7.10 (td, *J* = 7.6, 1.5 Hz, 1H, H4), 7.01 – 6.97 (m, 1H, H6), 6.70 – 6.63 (m, 2H, H3+5), 4.62 (s, 2H, NH_2), 3.42 (s, 2H, H7), 2.20 (s, 6H, H8). **^{13}C{^{1}H} NMR** (101 MHz, Chloroform-*d*, 25 °C): *δ* [ppm] = 147.0 (C2), 130.2 (C6), 128.3 (C4), 123.3 (C1), 117.5 (C5), 115.4 (C3), 63.4 (C7), 45.0 (C8). Additional information on the NMR spectra of the target compound including original data files is available via Chemotion Repository: https://dx.doi.org/10.14272/XQWHZHODENELCJ-UHFFFAOYSA-N.1

5.3.2.2. Synthesis of 2-{(Diethylamino)methyl}aniline (65)

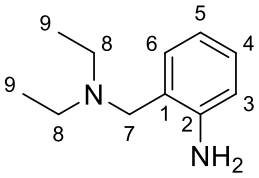

$C_{11}H_{18}N_2$
178.28 g mol^{-1}

Yellow solid (7.51 g, 42.1 mmol, 86%). **^{1}H NMR** (400 MHz, Chloroform-*d*, 25 °C): δ [ppm] = 7.11 – 7.05 (m, 1H, H3), 6.99 (ddt, *J* = 7.4, 1.0, 0.4 Hz, 1H, H5), 6.68 – 6.60 (m, 2H, H4+H6), 4.85 (s, 2H, NH_2), 3.59 (s, 2H, H7), 2.50 (q, *J* = 7.1 Hz, 4H, H8), 1.03 (t, *J* = 7.1 Hz, 6H, H9). **^{13}C{^{1}H} NMR** (101 MHz, Chloroform-*d*, 25 °C): *δ* [ppm] = 147.3 (C2), 130.4 (C5), 128.2 (C3), 123.5 (C1), 117.5 (C6), 115.5 (C4), 57.6 (C7), 46.4 (C8), 11.6 (C9). **HRMS-ESI+** (MeCN): m/z calc. for $[(C_{11}H_{18}N_2)+H]^+$: 179.15427, found: 179.15469. **IR** (ATR): $\tilde{\nu}$ [cm^{-1}] = 3438 (vw, N–H), 3284 (vw, N–H), 2968 (m, C–H_{arom}), 2932 (w, C–H_{arom}), 2874 (w, C–H_{aliph}), 1615 (m, C=C), 1495 (m), 1459 (m), 1384 (m), 1371 (m), 1363 (w), 1314 (w), 1286 (m), 1240 (vw), 1195 (m), 1166 (m), 1118 (w), 1087 (w), 1054 (m), 1037 (m), 980 (w), 966 (w), 928 (w), 912 (w), 778 (w), 746 (vs), 719 (m), 624 (m), 561 (vw), 540 (m). Additional information on the NMR spectra of the target compound including original data files is available via Chemotion Repository: https://dx.doi.org/10.14272/XUNNOCZTJBRTEX-UHFFFAOYSA-N.1

5.3.2.3. Synthesis of 2-{(Di-*iso*-propylamino)methyl}aniline (66)

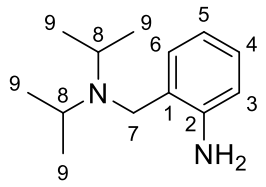

$C_{13}H_{22}N_2$
206.33 g mol^{-1}

Yellow solid (8.11 g, 39.3 mmol, 82%).**^{1}H NMR** (400 MHz, Chloroform-*d,* 25 °C): *δ* [ppm] = 7.09 (td, *J* = 7.7, 1.5 Hz, 1H, H3), 7.04 (d, *J* = 7.4 Hz, 1H, H5), 6.68 (td, *J* = 7.4, 1.2 Hz, 1H, H6), 6.61 (dd, *J* = 7.8, 0.9 Hz, 1H, H4), 4.90 (s, 2H, NH_2), 3.76 (s, 2H, H7), 3.09 (sept, *J* = 6.7 Hz, 2H, H8), 1.09 (d, *J* = 6.7 Hz, 12H, H9). **^{13}C{^{1}H} NMR** (101 MHz, Chloroform-*d*, 25 °C): *δ* [ppm] = 147.5 (C2), 130.5 (C5), 127.9 (C3), 123.9 (C1), 117.5 (C6), 115.4 (C4), 48.9 (C7), 47.0 (C8), 20.2 (C9). **HRMS-ESI+** (MeOH): m/z calc. for $[(C_{13}H_{22}N_2)+H]^+$: 207.18557, found: 207.18501. **IR** (ATR): $\tilde{\nu}$ [cm^{-1}] = 2965 (m, C–H_{arom}), 2927 (vw, C–H_{arom}), 2871 (vw, C–H_{aliph}), 1613 (m, C=C), 1493 (m), 1458 (m), 1383 (w),1363 (m), 1311 (w), 1282 (w), 1244 (vw), 1199 (w), 1175 (m), 1120 (w), 1087 (w), 1014 (w), 952 (w), 927 (w), 872 (vw), 745 (vs), 700 (vw), 628 (w), 544 (w), 526 (w). Additional information on the NMR spectra of the target compound including original data files is available via Chemotion Repository: https://dx.doi.org/10.14272/BHTORDOUUFFJPO-UHFFFAOYSA-N.1

5.3.3. Resynthesis of 2-(Dimethylamino)benzaldehyde (68)[243]

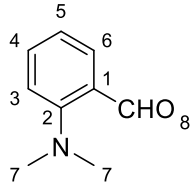

$C_9H_{11}NO$
149.19 g mol^{-1}

N,N-dimethyl aniline (**67**), *N,N,N′,N′*-tetramethylethane-1,2-diamine, and *N,N*-dimethyl formamide were dried over calcium hydride and distilled prior to usage. *N,N,N′,N′*-tetramethylethane-1,2-diamine (18.0 mL, 13.9 g, 120 mmol, 1.2 eq) was added slowly to *n*-butyl lithium (2.5 M in hexane, 48.0 mL, 120 mmol, 1.2 eq). *N,N*-dimethyl aniline (**67**, 12.7 mL, 12.1 g, 100 mmol, 1.0 eq) was added dropwise. The yellow solution was refluxed for four hours until no gas evolution was observed. The brown solution was stirred overnight at room temperature. The resulting suspension was diluted by adding diethyl ether (80 mL) and cooled to -30 °C. *N,N*-dimethyl formamide (9.7 mL, 9.17 g, 125 mmol, 1.25 eq) was added slowly and the reaction mixture was warmed up to room temperature. The suspension was heated to 30 °C for two hours and cooled to room temperature. The yellow solution was diluted in water (800 mL). The solution was extracted with diethyl ether (4 x 150 mL). The combined organic layers were washed with saturated aqueous sodium chloride solution, dried over sodium sulfate, and evaporated to dryness. The product was purified by fractional vacuum distillation (90-110 °C, 9 x 10^{-3} mbar) in combination with a 40 cm Vigreux column to give a yellow oil (9.85 g, 66.0 mmol, 66%). **^{1}H NMR** (400 MHz, Chloroform-*d*, 25 °C): δ [ppm] = 10.23 (s, 1H, H8), 7.76 (dd, *J* = 7.7, 1.8 Hz, 1H, H6), 7.49 – 7.43 (m, 1H, H4), 7.05 (d, *J* = 8.3 Hz, 1H, H5), 7.03 – 6.98 (m, 1H, H3), 2.93 (s, 6H, H7). **^{13}C{^{1}H} NMR** (101 MHz, Chloroform-*d*, 25 °C): δ [ppm] = 191.4 (C8), 155.9 (C2), 134.7 (C4), 131.1 (C6), 127.1 (C1), 120.7 (C3), 117.7 (C5), 45.6 (C7). Additional information on the NMR spectra of the target compound including original

data files is available via Chemotion Repository: https://dx.doi.org/10.14272/DGPBVJWCIDNDPN-UHFFFAOYSA-N.1

5.3.4. Resynthesis of 2-(Dimethylamino)benzaldehyde oxime (69)[244]

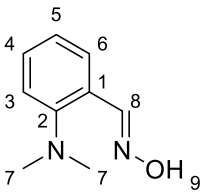

$C_9H_{12}N_2O$
164.21 g mol^{-1}

Aldehyde **68** (9.85 g, 66.0 mmol, 1.0 eq), sodium acetate (6.50 g, 79.2 mmol, 1.2 eq) and hydroxylamine hydrochloride (5.50 g, 79.2 mmol, 1.2 eq) were suspended in methanol (50 mL). The suspension was refluxed for one hour, cooled to room temperature and diluted by adding ethyl acetate (100 mL). Aqueous sodium hydroxide solution (2 M, 40 mL) was added. All volatiles were removed under reduced pressure. The residue was dissolved in water (100 mL). The solution was extracted with ethyl acetate (4 x 80 mL). The combined organic layers were washed with saturated aqueous sodium chloride solution, dried over sodium sulfate, and evaporated to dryness. The product was isolated as a beige solid (9.54 g, 58.1 mmol, 88%). **^{1}H NMR** (400 MHz, Chloroform-*d*, 25 °C): δ [ppm] = 8.46 (s, 1H, H8), 8.41 (s, 1H, H9), 7.68 (ddd, *J* = 7.7, 1.7, 0.5 Hz, 1H, H6), 7.33 (ddd, *J* = 8.2, 7.3, 1.7 Hz, 1H, H4), 7.07 (dd, *J* = 8.2, 1.1 Hz, 1H, H3), 7.03 (ddd, *J* = 7.7, 1.1, 0.5 Hz, 1H, H5), 2.75 (s, 6H, H7). **^{13}C{^{1}H} NMR** (101 MHz, Chloroform-*d*, 25 °C): δ [ppm] = 153.2 (C2), 149.2 (C8), 130.7 (C4), 127.6 (C6), 125.5 (C1), 122.7 (C3), 118.7 (C5), 45.3 (C7). Additional information on the NMR spectra of the target compound including original data files is available via Chemotion Repository: https://dx.doi.org/10.14272/LUVZOATVQRJLMA-JXMROGBWSA-N.1

5.3.5. Resynthesis of 2-(Aminomethyl) *N,N*-dimethyl aniline (70)[244,245]

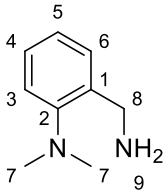

$C_9H_{14}N_2$
150.23 g mol^{-1}

Oxime **69** (9.54 g, 58.1 mmol, 1.0 eq) in tetrahydrofuran (100 mL) was cooled to 0 °C and lithium aluminum hydride (4.84 g, 128 mmol, 2.2 eq) in tetrahydrofuran (60 mL) was added dropwise. The suspension was stirred for one hour at 0 °C and refluxed for two hours. The reaction mixture was cooled to room temperature and diluted with diethyl ether (80 mL). The solution was cooled to 0 °C and acidified by hydrochloric acid (3 M, 120 mL). After warming up to room temperature the pH level of the solution was adjusted to 12 by using aqueous sodium hydroxide solution. The solution was extracted with diethyl ether (4 x 100 mL). The combined organic layers were washed with saturated aqueous sodium chloride solution, dried over sodium sulfate, and evaporated to dryness. The product was isolated as an orange oil (5.93 g, 39.5 mmol, 68%). **^{1}H NMR** (400 MHz, Chloroform-*d*, 25 °C): δ [ppm] = 7.30 (dd, *J* = 7.5, 1.7 Hz, 1H, H4), 7.22 (ddd, *J* = 8.0, 7.3, 1.7 Hz, 1H, H6), 7.12 (dd, *J* = 8.0, 1.4 Hz, 1H, H3), 7.05 (td, *J* = 7.4, 1.3 Hz, 1H, H5), 3.92 (s, 2H, H8), 2.70 (s, 6H, H7), 1.77 (s, 2H, H9). **^{13}C{^{1}H} NMR** (101 MHz, Chloroform-*d*, 25 °C): δ [ppm] = 152.5 (C2), 137.7 (C1), 128.7 (C4), 127.7 (C6), 123.7 (C5), 119.6 (C3), 45.1 (C7), 43.4 (C8). Additional information on the NMR spectra of the

target compound including original data files is available via Chemotion Repository: https://dx.doi.org/10.14272/MMSHDAHNUHLXQD-UHFFFAOYSA-N.1

5.3.6. General Synthesis of Hybrid Guanidine Amine Ligands

To a stirring solution of the primary amine (36.3 mmol, 1.0 eq) in dried acetonitrile (40 mL), triethylamine (5.1 mL, 36.3 mmol, 1.0 eq) was added at room temperature. A solution of Vilsmeier salt chlorido-*N,N,N′,N′*-tetramethylformamidinium chloride or chlorido-*N,N′*-dimethyl-ethyleneformamidinium chloride (36.3 mmol, 1.0 eq) in dried acetonitrile (40 mL) was added dropwise to the reaction mixture. The slightly yellow solution was refluxed for three hours. After cooling the reaction mixture down to room temperature, aqueous sodium hydroxide solution (1.45 g, 36.3 mmol, 1.0 eq, in 15 mL) was added. All volatiles were removed under reduced pressure. Aqueous potassium hydroxide solution (50 wt%, 50 g in 50 mL) was added and the mixture was extracted with acetonitrile (4 x 50 mL). The combined organic layers were dried over sodium sulfate and charcoal, filtered, and evaporated to dryness.

*The quantities given are exemplary for the synthesis of compound **L1** (see below). Quantities needed for the synthesis of ligands **L2**-**L5** must be adjusted according to the yield of the respective precursor compound (**62**, **65**, **66** and **70**).*

5.3.6.1. Synthesis of 2-{2-((Dimethylamino)methyl)phenyl}-1,1,3,3-tetramethyl-guanidine (TMGbenza, L1)

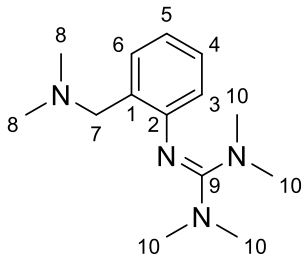

$C_{14}H_{24}N_4$
248.37 g mol^{-1}

The product was purified by vacuum distillation (130 °C, 3 x 10^{-2} mbar) to give a light-yellow oil (7.92 g, 31.9 mmol, 88%). Single crystals, suitable for X-ray diffraction, were grown from a saturated pentane solution of **L1** (0.1 mmol in 1 mL) at -32 °C. After several weeks, colorless blocks were obtained. **^{1}H NMR** (400 MHz, Acetonitrile-d_3, 25 °C): δ [ppm] = 7.24 (dd, J = 7.4, 1.6 Hz, 1H, H3), 7.04 (td, J = 7.5, 1.6 Hz, 1H, H5), 6.78 (td, J = 7.4, 1.3 Hz, 1H, H4), 6.41 (dd, J = 7.9, 1.3 Hz, 1H, H6), 3.30 (s, 2H, H7), 2.62 (s, 12H, H10), 2.16 (s, 6H, H8). **^{13}C{^{1}H} NMR** (101 MHz, Acetonitrile-d_3, 25 °C): δ [ppm] = 159.5 (C9), 151.8 (C2), 130.8 (C1), 130.0 (C3), 127.7 (C5), 122.1 (C6), 120.3 (C4), 60.6 (C7), 46.0 (C8), 39.8 (C10). **CHN anal.** calc. for $C_{14}H_{24}N_4$: C 67.70%; H 9.74%; N 22.56%; found: C 67.58%; H 9.61%; N 23.31%. **HRMS-EI:** m/z calc. for [$C_{14}H_{24}N_4$]: 248.1999, found: 248.1995. **IR** (ATR): $\tilde{\nu}$ [cm^{-1}] = 2936 (w, C–H_{arom}), 2885 (w, C–H_{aliph}), 2850 (w, C–H_{aliph}), 2810 (w), 2764 (w), 1604 (m), 1585 (vs, C=N), 1564 (vs), 1500 (m), 1479 (m), 1447 (m), 1425 (m), 1371 (s), 1234 (w), 1209 (w), 1174 (w), 1135 (s), 1058 (w), 1043 (w), 1016 (vs), 924 (w), 865 (w), 842 (m), 780 (m), 737 (m), 701 (w), 628 (w), 614 (vw), 537 (w), 506 (vw). Additional information on the NMR spectra of the target

compound including original data files is available via Chemotion Repository: https://dx.doi.org/10.14272/WYPRQDLUGJFJCG-UHFFFAOYSA-N.1

5.3.6.2. Synthesis of 1-(2-((1,3-Dimethylimidazolidin-2-yliden)amino)phenyl)-*N,N*-dimethylmethanamine (DMEGbenza, L2)

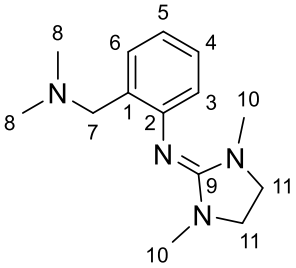

$C_{14}H_{22}N_4$
246.37 g mol^{-1}

The product was purified by vacuum distillation (130 °C, 3 x 10^{-2} mbar) to give a light-yellow oil (8.14 g, 33.0 mmol, 91%). Single crystals, suitable for X-ray diffraction, were grown from a saturated pentane solution of **L2** (0.1 mmol in 1 mL) at -32 °C. After several weeks, colorless blocks were obtained. **^{1}H NMR** (400 MHz, Acetonitrile-d_3, 25 °C): δ [ppm] = 7.26 – 7.23 (m, 1H, H3), 7.06 – 7.01 (m, 1H, H5), 6.81 (m, 1H, H4), 6.70 – 6.66 (m, 1H, H6), 3.30 (s, 2H, H7), 3.21 (s, 4H, H11), 2.52 (s, 6H, H10), 2.17 (s, 6H, H8). **^{13}C{^{1}H} NMR** (101 MHz, Acetonitrile-d_3, 25 °C): δ [ppm] = 155.5 (C9), 150.2 (C2), 131.3 (C1), 129.8 (C3), 127.4 (C5), 123.0 (C6), 120.7 (C4), 60.3 (C7), 49.2 (C11), 45.9 (C8), 35.2 (C10). **CHN anal.** calc. for $C_{14}H_{22}N_4$: C, 68.26%; H, 9.00%; N, 22.74%; found: C, 67.98%; H, 8.91%; N, 23.42%. **MS-EI**: m/z (%) = 246.4 (75) [M^+], 231.4 (94) [M^+-Me], 203.3 (49), 202.3 (88), 188.3 (100), 187.3 (43), 186.3 (62), 147.3 (21), 145.3 (23), 132.2 (28), 131.2 (29), 118.2 (24), 117.2 (31), 98.3 (38), 97.3 (22), 91.2 (25). **HRMS-EI:** m/z calc. for [$C_{14}H_{22}N_4$]: 246.1839, found: 246.1841. **IR** (ATR): $\tilde{\nu}$ [cm^{-1}] = 2972 (w, C–H_{arom}), 2938 (w, C–H_{arom}), 2848 (w, C–H_{aliph}), 2813 (w, C–H_{aliph}), 2765 (w, C–H_{aliph}), 1641 (vs, C=N), 1591 (s), 1568 (m), 1479 (m), 1437 (m), 1414 (m), 1391 (m), 1361 (w), 1277 (m), 1228 (m), 1197 (vw), 1174 (w), 1148 (w), 1121 (vw), 1097 (w), 1073 (w), 1029 (s), 992 (w), 967 (m), 936 (w), 869 (w), 846 (w), 774 (m), 736 (m), 700 (w), 651 (w), 618 (vw), 597 (w), 584 (w), 535 (vw), 496 (vw). Additional information on the NMR spectra of the target compound including original data files is available via Chemotion Repository: https://dx.doi.org/10.14272/QPMZKBLZEHVLOS-UHFFFAOYSA-N.1

5.3.6.3. Synthesis of 2-{2-((Diethylamino)methyl)phenyl}-1,1,3,3-tetramethyl-guanidine (TMGbenzaNEt$_2$, L3)

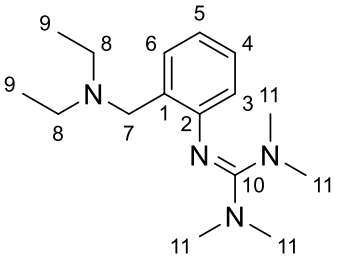

$C_{16}H_{28}N_4$
276.43 g mol^{-1}

The product was purified by vacuum distillation (140 °C, 3 x 10^{-2} mbar) to give a light-yellow oil (10.9 g, 39.6 mmol, 94%). **^{1}H NMR** (400 MHz, Acetonitrile-d_3, 25 °C): δ [ppm] = 7.29 (ddt, J = 7.5, 1.0, 0.4 Hz, 1H, H3), 7.05 – 6.99 (m, 1H, H5), 6.78 (td, J = 7.4, 1.3 Hz, 1H, H4), 6.39 (dd, J = 7.8, 1.2 Hz, 1H, H6), 3.42 (s, 2H, H7), 2.62 (s, 12H, H11), 2.46 (q, J = 7.1 Hz, 4H, H8), 0.99 (t, J = 7.1 Hz, 6H, H9). **^{13}C{^{1}H} NMR** (101 MHz, Acetonitrile-d_3, 25 °C): δ [ppm] = 159.3 (C10), 151.7 (C2), 131.8 (C1), 129.9 (C3), 127.4 (C5), 121.9 (C6), 120.3 (C4), 54.5 (C7), 47.9 (C8), 39.8 (C11), 12.5 (C9). **HRMS-EI:** m/z calc. for [$C_{16}H_{28}N_4$]:

276.2311, found: 276.2308. **IR** (ATR): $\tilde{\nu}$ [cm^{-1}] = 2967 (w, C–H$_{arom}$), 2929 (w, C–H$_{arom}$), 2870 (w, C–H$_{aliph}$), 2791 (w, C–H$_{aliph}$), 1608 (s), 1586 (vs, C=N), 1566 (vs), 1499 (m), 1479 (m), 1447 (m), 1425 (m), 1370 (vs), 1234 (w), 1207 (w), 1166 (w), 1135 (s), 1098 (w), 1057 (w), 1040 (w), 1017 (s), 924 (w), 858 (w), 776 (m), 742 (m), 729 (m), 701 (w), 627 (w), 540 (w). Additional information on the NMR spectra of the target compound including original data files is available via Chemotion Repository: https://dx.doi.org/10.14272/LNVNFNCAAMQZFE-UHFFFAOYSA-N.1

5.3.6.4. Synthesis of 2-{2-((Di-*iso*-propylamino)methyl)phenyl}-1,1,3,3-tetramethylguanidine (TMGbenzaN*i*Pr$_2$, L4)

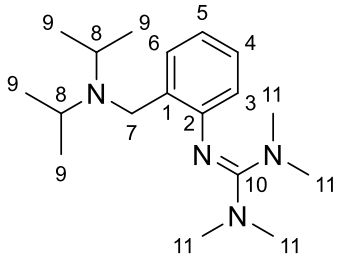

$C_{18}H_{32}N_4$
304.48 g mol^{-1}

The product was purified by vacuum distillation (170 °C, 5 x 10^{-2} mbar) to give a yellow oil (10.4 g, 34.1 mmol, 87%). **^{1}H NMR** (400 MHz, Acetonitrile-d_3, 25 °C): δ [ppm] = 7.41 (ddt, J = 7.6, 1.3, 0.4 Hz, 1H, H3), 7.02 – 6.96 (m, 1H, H5), 6.80 – 6.75 (m, 1H, H4), 6.37 (dd, J = 7.8, 1.3 Hz, 1H, H6), 3.51 (s, 2H, H7), 3.02 (sept, J = 6.6 Hz, 2H, H8), 2.63 (s, 12H, H11), 1.00 (d, J = 6.6 Hz, 12H, H9). **^{13}C{^{1}H} NMR** (101 MHz, Acetonitrile-d_3, 25 °C): δ [ppm] = 159.4 (C10), 151.3 (C2), 133.8 (C1), 129.6 (C3), 127.0 (C5), 121.7 (C6), 120.3 (C4), 48.7 (C8), 45.4 (C7), 39.8 (C11), 21.0 (C9). **HRMS-EI**: m/z calc. for [$C_{18}H_{32}N_4$]: 304.2621, found: 304.2613. **IR** (ATR): $\tilde{\nu}$ [cm^{-1}] = 2961 (m, C–H$_{arom}$), 2929 (m, C–H$_{arom}$), 2875 (w, C–H$_{aliph}$), 2802 (vw, C–H$_{aliph}$), 1607 (m), 1586 (vs, C=N), 1566 (s), 1499 (m), 1479 (m), 1448 (m), 1425 (m), 1372 (vs), 1274 (w), 1251 (w), 1233 (w), 1206 (m), 1174 (m), 1135 (vs), 1106 (m), 1058 (w), 1016 (s), 929 (w), 856 (m), 780 (m), 755 (m), 742 (m),720 (m), 627 (w), 617 (w), 569 (w), 541 (m). Additional information on the NMR spectra of the target compound including original data files is available via Chemotion Repository: https://dx.doi.org/10.14272/QUXYBCGZDQRMFG-UHFFFAOYSA-N.1

5.3.6.5. Synthesis of 2-(((1,3-Dimethylimidazolidin-2-ylidene)amino)methyl)-*N,N*-dimethylaniline (DMEGanil, L5)

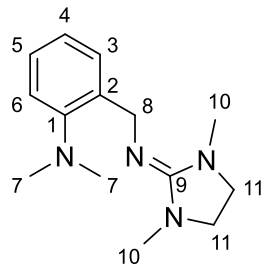

$C_{14}H_{22}N_4$
246.37 g mol^{-1}

The product was purified by vacuum distillation (140 °C, 4 x 10^{-2} mbar) to give a yellow oil (8.17 g, 33.2 mmol, 84%). Single crystals, suitable for X-ray diffraction, were grown from a saturated pentane solution of **L5** (0.1 mmol in 1 mL) at -32 °C. After several weeks, colorless blocks were obtained. **^{1}H NMR** (400 MHz, Acetonitrile-d_3, 25 °C): δ [ppm] = 7.56 (ddd, J = 7.6, 1.3, 0.8 Hz, 1H, H6), 7.18 – 7.13 (m, 1H, H4), 7.06 (dd, J = 8.0, 1.3 Hz, 1H, H3), 7.03 – 6.98 (m, 1H, H5), 4.57 (s, 2H, H8), 3.13 (s, 4H, H11), 2.76 (s, 6H, H10), 2.66 (s, 6H, H7). **^{13}C{^{1}H} NMR** (101 MHz, Acetonitrile-d_3, 25 °C): δ [ppm] = 158.2 (C9), 152.6 (C1), 139.0 (C2), 130.0 (C6), 127.4

(C5), 123.5 (C3), 119.0 (C4), 50.2 (C11), 47.1 (C8), 45.1 (C7), 36.8 (C10). **CHN anal.** calc. for $C_{14}H_{22}N_4$: C, 68.26%; H, 9.00%; N, 22.74%; found: C, 67.67%; H, 8.97%; N, 22.59%. **HRMS-EI:** m/z calc. for [$C_{14}H_{22}N_4$]: 246.1839, found: 246.1839. **IR** (ATR): $\tilde{\nu}$ [cm^{-1}] = 2974 (w, C–H_{arom}), 2935 (w, C–H_{arom}), 2854 (w, C–H_{aliph}), 2826 (m, C–H_{aliph}), 2783 (w, C–H_{aliph}), 1654 (vs, C=N), 1597 (m), 1577 (w), 1486 (m), 1450 (m), 1434 (m), 1412 (w), 1381 (m), 1343 (w), 1263 (m), 1187 (w), 1151 (w), 1098 (w), 1066 (w), 1046 (m), 1022 (w), 955 (m), 945 (m), 860 (vw), 818 (vw), 764 (m), 725 (m), 641 (w), 605 (w), 574 (w), 528 (w), 498 (vw), 457 (w). Additional information on the NMR spectra of the target compound including original data files is available via Chemotion Repository: https://dx.doi.org/10.14272/LOYVSAJIAZWNAB-UHFFFAOYSA-N.1

5.3.7. General Synthesis of Cu(I) and Cu(II) Complexes

The following Cu(I) and Cu(II) complexes were generated in-situ by dissolving the ligand and copper salt in acetonitrile (see below for the stoichiometry and amounts of the components) or isolated for full characterization (and crystallization).

A solution of the ligand (0.10 mmol, 1.0 eq for monochelate complexes and 0.20 mmol, 2.0 eq for bischelate complexes) in dried acetonitrile (2.0 mL) was added dropwise to a stirring solution of the copper salt (0.10 mmol, 1.0 eq) in dried acetonitrile (3.0 mL) during a period of 10 min. The solution was stirred for two hours and evaporated to dryness (Caution! The Cu(I) complexes are very sensitive to dioxygen which is indicated by the partial coloration of the precipitate or oil to light green). The residue was washed with dried pentane (3 x 1.0 mL) and dried *in vacuo*.

5.3.7.1. Synthesis of [Cu(L1)(MeCN)]PF_6 (C1)

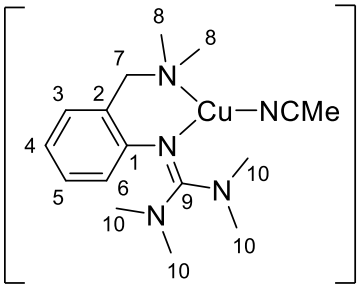

+ PF_6^-

$C_{16}H_{27}CuF_6N_5P$
497.94 g mol^{-1}

Colorless solid (49 mg, 0.098 mmol, 98%). **^{1}H NMR** (400 MHz, Acetonitrile-d_3, 25 °C): δ [ppm] = 7.22 (td, J = 7.7, 1.6 Hz, 1H, H4), 7.14 (dd, J = 7.5, 1.3 Hz, 1H, H6), 6.91 (td, J = 7.4, 1.2 Hz, 1H, H3), 6.48 – 6.42 (dd, J = 7.8, 1.3 Hz, 1H, H5), 3.44 (s, 2H, H7), 2.71 (s, 12H, H10), 2.31 (s, 6H, H8). **^{13}C{^{1}H} NMR** (101 MHz, Acetonitrile-d_3, 25 °C): δ [ppm] = 164.7 (C9), 151.7 (C1), 133.3 (C6), 130.3 (C4), 129.1 (C2), 123.3 (C5), 122.3 (C3), 65.3 (C7), 48.1 (C8), 40.1 (C10). **^{19}F{^{1}H} NMR** (377 MHz, Acetonitrile-d_3, 25 °C): δ [ppm] = -72.94 (d, J = 706.3 Hz, PF_6). **^{31}P{^{1}H} NMR** (162 MHz, Acetonitrile-d_3, 25 °C): δ [ppm] = -144.60 (sept, J = 706.3 Hz, PF_6). **HRMS-ESI+** (MeCN): m/z calc. for [($C_{14}H_{24}N_4$)Cu]$^+$: 311.1297, found: 311.1291, calc. for [($C_{14}H_{24}N_4$)Cu(CH_3CN)]$^+$: 352.1562, found: 352.1557. **IR** (KBr): $\tilde{\nu}$ [cm^{-1}] = 3066 (w, C–H_{arom}), 3008 (w, C–H_{arom}), 2943 (m, C–H_{arom}), 2888 (m, C–H_{aliph}), 2836 (w, C–H_{aliph}),

2800 (w, C–H_{aliph}), 1555 (m, C=N), 1532 (m), 1487 (m), 1471 (m), 1424 (m), 1399 (m), 1332 (w), 1271 (w), 1237 (w), 1161 (w), 1112 (w), 1066 (w), 1036 (m), 999 (w), 839 (vs, PF_6), 752 (m, PF_6), 557 (m, PF_6), 465 (w, PF_6). Additional information on the NMR spectra of the target compound including original data files is available via Chemotion Repository: https://dx.doi.org/10.14272/SXYROFUQPFOADI-UHFFFAOYSA-N.1

5.3.7.2. Synthesis of [Cu(L1)(MeCN)]BF_4 (C2)

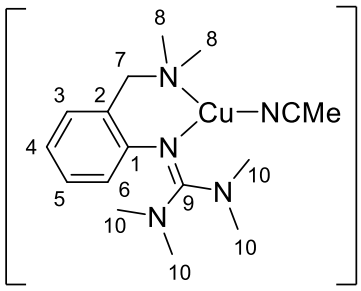

+ BF_4^-

$C_{16}H_{27}BCuF_4N_5$
439.78 g mol^{-1}

The title compound was generated *in-situ*. **^{1}H NMR** (400 MHz, Acetonitrile-d_3, 25 °C): δ [ppm] = 7.20 (td, J = 7.7, 1.6 Hz, 1H, H4), 7.16 (dd, J = 7.5, 1.3 Hz, 1H, H6), 6.91 (td, J = 7.4, 1.2 Hz, 1H, H3), 6.47 (d, J = 7.8 Hz, 1H, H5), 3.44 (s, 2H, H7), 2.70 (s, 12H, H10), 2.28 (s, 6H, H8). **^{13}C{^{1}H} NMR** (101 MHz, Acetonitrile-d_3, 25 °C): δ [ppm] = 164.6 (C9), 151.6 (C1), 133.0 (C6), 130.1 (C4), 129.3 (C2), 123.4 (C5), 122.3 (C3), 64.9 (C7), 47.9 (C8), 40.1 (C10). **^{19}F{^{1}H} NMR** (377 MHz, Acetonitrile-d_3, 25 °C): δ [ppm] = -151.78 (s, BF_4). Additional information on the NMR spectra of the target compound including original data files is available via Chemotion Repository: https://dx.doi.org/10.14272/NLACLAPNGFWSTA-UHFFFAOYSA-N.1

5.3.7.3. Synthesis of [Cu(L1)(MeCN)]OTf (C3)

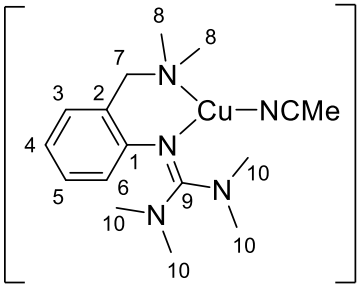

+ OTf^-

$C_{17}H_{27}CuF_3N_5O_3S$
502.04 g mol^{-1}

The title compound was generated *in-situ*. **^{1}H NMR** (400 MHz, Acetonitrile-d_3, 25 °C): δ [ppm] = 7.21 (td, J = 7.6, 1.6 Hz, 1H, H4), 7.14 (dd, J = 7.5, 1.6 Hz, 1H, H6), 6.91 (td, J = 7.4, 1.3 Hz, 1H, H3), 6.45 (dd, J = 7.9, 1.3 Hz, 1H, H5), 3.44 (s, 2H, H7), 2.71 (br s, 12H, H10), 2.31 (s, 6H, H8). **^{13}C{^{1}H} NMR** (101 MHz, Acetonitrile-d_3, 25 °C): δ [ppm] = 164.7 (C9), 151.7 (C1), 133.2 (C6), 130.3 (C4), 129.1 (C2), 126.6 (OTf), 123.3 (C5), 122.3 (C3), 65.3 (C7), 48.1 (C8), 40.1 (C10). **^{19}F{^{1}H} NMR** (377 MHz, Acetonitrile-d_3, 25 °C): δ [ppm] = -79.24 (s, OTf). Additional information on the NMR spectra of the target compound including original data files is available via Chemotion Repository: https://dx.doi.org/10.14272/WOMQOOHUINDJRV-UHFFFAOYSA-M.1

5.3.7.4. Synthesis of [Cu(L1)(MeCN)]ClO$_4$ (C4)

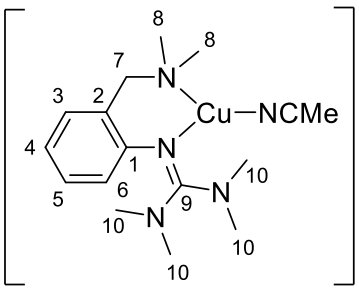

$C_{16}H_{27}ClCuN_5O_4$
452.42 g mol^{-1}

The title compound was generated *in-situ*. **^{1}H NMR** (400 MHz, Acetonitrile-d_3, 25 °C): δ [ppm] = 7.21 (td, J = 7.7, 1.6 Hz, 1H, H4), 7.15 (dd, J = 7.5, 1.4 Hz, 1H, H6), 6.91 (td, J = 7.4, 1.2 Hz, 1H, H3), 6.45 (dd, J = 7.9, 1.4 Hz, 1H, H5), 3.44 (s, 2H, H7), 2.71 (s, 12H, H10), 2.30 (s, 6H, H8). **^{13}C{^{1}H} NMR** (101 MHz, Acetonitrile-d_3, 25 °C): δ [ppm] = 164.6 (C9), 151.7 (C1), 133.1 (C6), 130.2 (C4), 129.1 (C2), 123.3 (C5), 122.3 (C3), 65.1 (C7), 48.1 (C8), 40.1 (C10). Additional information on the NMR spectra of the target compound including original data files is available via Chemotion Repository: https://dx.doi.org/10.14272/SQELSYLGCLCOLU-UHFFFAOYSA-M.1

5.3.7.5. Synthesis of [Cu(L1)$_2$]PF$_6$ (C5)

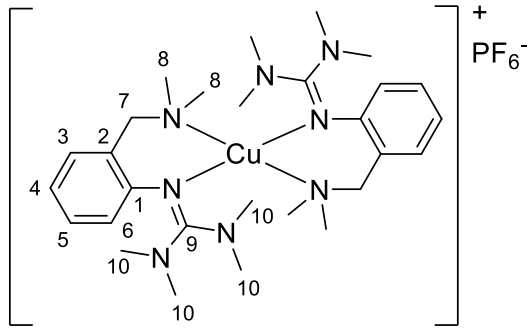

$C_{28}H_{48}CuF_6N_8P$
705.26 g mol^{-1}

Colorless solid (69 mg, 0.098 mmol, 98%). Single crystals, suitable for X-ray diffraction, were grown by slow diffusion of pentane (approx. 4 mL) into the saturated tetrahydrofuran solution of complex **C5** (35 mg, 0.050 mmol in 2 mL) at room temperature. After several weeks, colorless blocks were obtained. **^{1}H NMR** (400 MHz, Acetonitrile-d_3, 25 °C): δ [ppm] = 7.22 – 7.16 (m, 4H, H4+H6), 6.91 (td, J = 7.4, 1.2 Hz, 2H, H3), 6.49 (d, J = 7.5 Hz, 2H, H5), 3.43 (s, 4H, H7), 2.70 (s, 24H, H10), 2.24 (s, 12H, H8). **^{13}C{^{1}H} NMR** (101 MHz, Acetonitrile-d_3, 25 °C): δ [ppm] = 164.3 (C9), 151.4 (C1), 132.6 (C6), 129.8 (C4), 129.6 (C2), 123.4 (C5), 122.3 (C3), 64.3 (C7), 47.6 (C8), 40.1 (C10). **^{19}F{^{1}H} NMR** (377 MHz, Acetonitrile-d_3, 25 °C): δ [ppm] = -72.84 (d, J = 706.6 Hz, PF$_6$). **^{31}P{^{1}H} NMR** (162 MHz, Acetonitrile-d_3, 25 °C): δ [ppm] = -144.58 (sept, J = 706.7 Hz, PF$_6$). **HRMS-ESI+** (MeCN, *in-situ*): m/z calc. for $[(C_{14}H_{24}N_4)_2Cu]^+$: 559.32924, found: 559.32913. **IR** (NaCl plates, *in-situ*): $\tilde{\nu}$ [cm^{-1}] = 2947 (m, C–H$_{arom}$), 2941 (m, C–H$_{arom}$), 2873 (m, C–H$_{aliph}$), 2835 (m, C–H$_{aliph}$), 1549 (s, C=N), 1337 (w), 1271 (m), 1237 (w), 1214 (w), 1194 (vw), 1156 (m), 1112 (m), 1065 (w), 1036 (m), 1030 (s), 999 (m), 924 (vw), 878 (m), 854 (vs, PF$_6$), 792 (w), 754 (m, PF$_6$), 737 (w), 703 (vw). Additional information on the NMR spectra of the target compound including original data files is available via Chemotion Repository: https://dx.doi.org/10.14272/POHVMFXWZCBOFQ-UHFFFAOYSA-N.1

5.3.7.6. Synthesis of $[Cu(L2)_2]PF_6$ (C6)

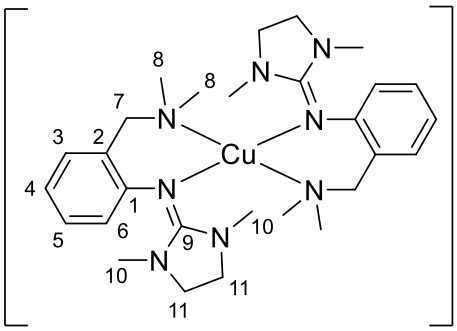

$C_{28}H_{44}CuF_6N_8P$
701.23 g mol^{-1}

Colorless solid (43 mg, 0.061 mmol, 61%). Single crystals, suitable for X-ray diffraction, were grown by slow diffusion of pentane (approx. 5 mL) into the saturated tetrahydrofuran solution of complex **C6** (35 mg, 0.050 mmol in 2 mL) at room temperature. After several weeks, colorless blocks were obtained. **^{1}H NMR** (400 MHz, Acetonitrile-d_3, 25 °C) δ [ppm] = 7.20 (td, J = 7.7, 1.7 Hz, 2H, H6), 7.13 (dd, J = 7.5, 1.3 Hz, 2H, H4), 6.92 (td, J = 7.4, 1.2 Hz, 2H, H5), 6.77 (dd, J = 7.9, 0.9 Hz, 2H, H3), 3.43 (s, 4H, H7), 3.41 (s, 8H, H11), 2.67 (s, 12H, H8), 2.31 (s, 12H, H10). **^{13}C{^{1}H} NMR** (101 MHz, Acetonitrile-d_3, 25 °C) δ [ppm] = 163.1 (C9), 150.6 (C1), 132.9 (C2), 130.1 (C4), 129.8 (C6), 124.5 (C3), 122.5 (C5), 64.7 (C7), 49.4 (C11), 48.2 (C8), 35.7 (C10). **^{19}F{^{1}H} NMR** (377 MHz, Acetonitrile-d_3, 25 °C) δ [ppm] = -72.93 (d, J = 706.4 Hz, PF_6). **^{31}P{^{1}H} NMR** (162 MHz, Acetonitrile-d_3, 25 °C) δ [ppm] = -144.60 (sept, J = 706.3 Hz, PF_6). **HRMS-ESI+** (MeCN, *in-situ*): m/z calc. for $[(C_{14}H_{22}N_4)_2Cu]^+$: 555.29794, found: 555.29927. **IR** (NaCl plates, *in-situ*): $\tilde{\nu}$ [cm^{-1}] = 2966 (m, C–H_{arom}), 2937 (m, C–H_{arom}), 2870 (m, C–H_{arom}), 2835 (m, C–H_{aliph}), 2787 (m, C–H_{aliph}), 1653 (vs, C=N), 1605 (vs, C=N), 1591 (vs), 1569 (vs), 1283 (s), 1226 (m), 1154 (m), 1109 (w), 1073 (w), 1042 (m), 1037 (m), 1033 (m), 1028 (m), 997 (s), 978 (m), 886 (w), 843 (m, PF_6), 804 (m), 779 (vw), 754 (m, PF_6), 732 (w), 702 (vw). Additional information on the NMR spectra of the target compound including original data files is available via Chemotion Repository: https://dx.doi.org/10.14272/VTGIPTDVFRVVHA-UHFFFAOYSA-N.1

5.3.7.7. Synthesis of $[Cu(L2)_2]OTf$ (C7)

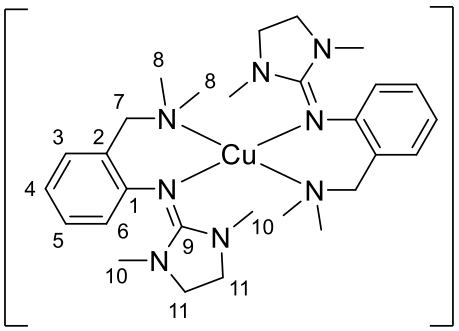

$C_{29}H_{44}CuF_3N_8O_3S$
705.33 g mol^{-1}

Colorless solid (49 mg, 0.069 mmol, 69%). Single crystals, suitable for X-ray diffraction, were grown by slow diffusion of pentane (approx. 5 mL) into the saturated tetrahydrofuran solution of complex **C7** (35 mg, 0.050 mmol in 2 mL) at room temperature. After several weeks, colorless blocks were obtained. **^{1}H NMR** (400 MHz, Acetonitrile-d_3, 25 °C) δ [ppm] = 7.18 – 7.12 (m, 4H, H4+H6), 6.88 (t, J = 7.4 Hz, 2H, H5), 6.76 (d, J = 7.8 Hz, 2H, H3), 3.37 (s, 4H, H7), 3.34 (s, 8H, H11), 2.62 (s, 12H, H8), 2.21 (s, 12H, H10). **^{13}C{^{1}H} NMR** (101 MHz, Acetonitrile-d_3, 25 °C) δ [ppm] = 160.3 (C9), 150.5 (C1), 131.7 (C2), 130.5 (C4), 129.1 (C6), 124.1 (C3), 123.8 (OTf), 121.9 (C5), 63.1 (C7), 49.3 (C11), 47.4 (C8), 35.5 (C10). **HRMS-ESI+**

(MeCN, *in-situ*): m/z calc. for $[(C_{14}H_{22}N_4)_2Cu]^+$: 555.29794, found: 555.29869. **IR** (NaCl plates, *in-situ*): $\tilde{\nu}$ [cm^{-1}] = 2996 (m, C–H_{arom}), 2948 (m, C–H_{arom}), 2941 (m, C–H_{arom}), 2873 (m, C–H_{aliph}), 2836 (m, C–H_{aliph}), 2788 (w, C–H_{aliph}), 1651 (m, C=N), 1604 (vs, C=N), 1589 (vs), 1565 (vs), 1506 (s), 1491 (s), 1477 (s), 1286 (m), 1258 (m), 1243 (m, OTf), 1174 (w, OTf), 1109 (w), 1046 (m), 1030 (m, OTf), 997 (m), 978 (w), 878 (m), 855 (m), 804 (w), 754 (w, OTf). Additional information on the NMR spectra of the target compound including original data files is available via Chemotion Repository: https://dx.doi.org/10.14272/OQUSVZHQZRYDEI-UHFFFAOYSA-M.1

5.3.7.8. Synthesis of $[Cu(L1)(PMe_3)]PF_6$ (C8)

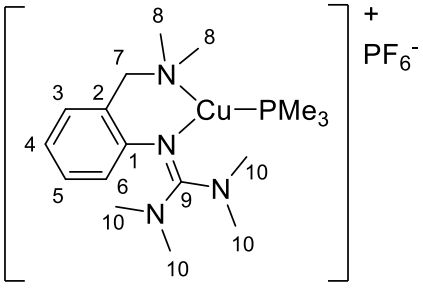

$C_{17}H_{33}CuF_6N_4P_2$
532.96 g mol^{-1}

A solution of **L1** (24.8 mg, 0.1 mmol, 1.0 eq) in dried acetonitrile (2.0 mL) was added dropwise to a stirring solution of $[Cu(MeCN)_4]PF_6$ (37.3 mg, 0.1 mmol, 1.0 eq) in dried acetonitrile (3.0 mL) during a period of 10 min. PMe_3 (1 M in tetrahydrofuran, 0.1 mL, 0.1 mmol, 1.0 eq) was added to the formed complex **C1**. The solution was stirred for two hours and evaporated to dryness. The residue was washed with dried pentane (3 x 1.0 mL) and dried *in vacuo*. Colorless solid (52 mg, 0.098 mmol, 98%). Single crystals, suitable for X-ray diffraction, were grown by slow diffusion of pentane (approx. 6 mL) into the saturated tetrahydrofuran solution of complex **C8** (27 mg, 0.051 mmol in 3 mL) at room temperature. After several days, colorless blocks were obtained. **^{1}H NMR** (400 MHz, Tetrahydrofuran-d_8, 25 °C): δ [ppm] = 7.20 (td, J = 7.7, 1.6 Hz, 1H, H4), 7.14 (dd, J = 7.4, 1.3 Hz, 1H, H6), 6.89 (td, J = 7.4, 1.2 Hz, 1H, H3), 6.47 – 6.42 (m, 1H, H5), 3.57 (s, 2H, H7), 2.78 (s, 12H, H10), 2.41 (s, 6H, H8), 1.36 (d, J = 7.0 Hz, 9H, PMe_3). **^{13}C{^{1}H} NMR** (101 MHz, Tetrahydrofuran-d_8, 25 °C): δ [ppm] = 167.3 (C9), 151.1 (C1), 133.0 (C6), 130.5 (C4), 129.2 (C2), 123.5 (C5), 122.5 (C3), 64.9 (C7), 48.2 (C8), 40.5 (C10), 16.0 (d, J = 24.2 Hz, PMe_3). **^{19}F{^{1}H} NMR** (377 MHz, Tetrahydrofuran-d_8, 25 °C): δ [ppm] = -72.92 (d, J = 711.8 Hz, PF_6). **^{31}P{^{1}H} NMR** (162 MHz, Tetrahydrofuran-d_8, 25 °C): δ [ppm] = -47.17 (PMe_3), -144.28 (sept, J = 712.0 Hz, PF_6). **HRMS-ESI+** (MeCN, *in-situ*): m/z calc. for $[(C_{14}H_{24}N_4)Cu]^+$: 311.12915, found: 311.12945, calc. for $[(C_{14}H_{24}N_4)Cu(PMe_3)]^+$: 387.17388, found: 387.17411. **IR** (NaCl plates, *in-situ*): $\tilde{\nu}$ [cm^{-1}] = 2964 (w, C–H_{arom}), 2927 (w, C–H_{arom}), 2874 (w, C–H_{aliph}), 2836 (w, C–H_{aliph}), 1545 (m, C=N), 1485 (m, PMe_3), 1474 (m), 1368 (m), 1334 (w), 1272 (w), 1158 (m), 1113 (w), 1067 (w), 1046 (m), 1031 (m), 998 (w), 961 (w), 918 (m), 847 (vs, PF_6), 756 (vw, PF_6), 732 (vw), 628 (vw). Additional information on the NMR spectra of the target compound including original data files is available via Chemotion Repository: https://dx.doi.org/10.14272/GGNDXINHPCPWIS-UHFFFAOYSA-N.1

5.3.7.9. Synthesis of [Cu(L1)(PPh$_3$)]PF$_6$ (C9)

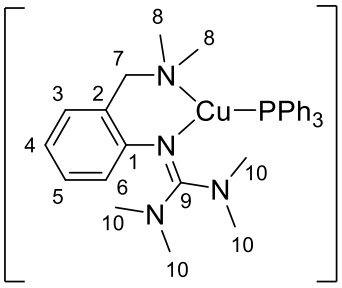

$C_{32}H_{39}CuF_6N_4P_2$
719.18 g mol^{-1}

A solution of **L1** (24.8 mg, 0.1 mmol, 1.0 eq) in dried acetonitrile (2.0 mL) was added dropwise to a stirring solution of [Cu(MeCN)$_4$]PF$_6$ (37.3 mg, 0.1 mmol, 1.0 eq) in dried acetonitrile (3.0 mL) during a period of 10 min. PPh$_3$ (26 mg, 0.1 mmol, 1.0 eq) was added to the formed complex **C1**. The solution was stirred for two hours and evaporated to dryness. The residue was washed with dried pentane (3 x 1.0 mL) and dried *in vacuo*.

Colorless solid (69 mg, 0.096 mmol, 96%). Single crystals, suitable for X-ray diffraction, were grown by slow diffusion of pentane (approx. 6 mL) into the saturated tetrahydrofuran solution of complex **C9** (36 mg, 0.050 mmol in 3 mL) at room temperature. After several days, colorless blocks were obtained. **^{1}H NMR** (400 MHz, Tetrahydrofuran-d_8, 25 °C): δ [ppm] = 7.62 – 7.54 (m, 6H, *ortho*-Ph), 7.51 – 7.44 (m, 9H, *meta-/para*-Ph), 7.26 (td, J = 7.8, 1.6 Hz, 1H, H6), 7.16 (dd, J = 7.5, 1.3 Hz, 1H, H4), 6.94 (td, J = 7.4, 0.9 Hz, 1H, H3), 6.55 – 6.49 (m, 1H, H5), 3.62 (s, 2H, H7), 2.59 (s, 12H, H10), 2.13 (s, 6H, H8). **^{13}C{^{1}H} NMR** (101 MHz, Tetrahydrofuran-d_8, 25 °C): δ [ppm] = 167.4 (C9), 151.4 (C1), 135.0 (d, J = 15.0 Hz, *ortho*-Ph), 133.5 (C2), 133.1 (C4), 131.7 (*ipso*-Ph), 130.7 (C6), 130.3 (d, J = 9.9 Hz, *meta-/para*-Ph), 123.8 (C3), 122.8 (C5), 65.1 (C7), 47.9 (C8), 40.5 (C10). **^{19}F{^{1}H} NMR** (377 MHz, Tetrahydrofuran-d_8, 25 °C): δ [ppm] = -72.93 (d, J = 711.6 Hz, PF$_6$). **^{31}P{^{1}H} NMR** (162 MHz, Tetrahydrofuran-d_8, 25 °C): δ [ppm] = 5.08 (PPh$_3$), -144.11 (sept, J = 711.6 Hz, PF$_6$). **HRMS-ESI+** (MeCN, *in-situ*): m/z calc. for [(C$_{14}$H$_{24}$N$_4$)Cu]$^+$: 311.12915, found: 311.12963, m/z calc. for [(C$_{14}$H$_{24}$N$_4$)Cu(PPh$_3$)]$^+$: 573.22028, found: 573.22303. **IR** (NaCl plates, *in-situ*): $\tilde{\nu}$ [cm^{-1}] = 3006 (m, C–H$_{arom}$), 2946 (m, C–H$_{arom}$), 2941 (m, C–H$_{arom}$), 2871 (w, C–H$_{aliph}$), 2835 (w, C–H$_{aliph}$), 2798 (vw, C–H$_{aliph}$), 1540 (vs, C=N), 1476 (m, PPh$_3$), 1470 (w), 1367 (m), 1338 (w), 1270 (w), 1216 (w), 1157 (m), 1112 (w), 1096 (m), 1064 (vw),1046 (s), 1033 (m), 1030 (s), 998 (w), 929 (vw), 920 (m, PPh$_3$), 878 (m, PPh$_3$), 854 (s, PF$_6$), 791 (vw), 752 (w, PF$_6$), 698 (w), 683 (w). Additional information on the NMR spectra of the target compound including original data files is available via Chemotion Repository: https://dx.doi.org/10.14272/KMTDPTVWKFUSHN-UHFFFAOYSA-N.1

5.3.7.10. Synthesis of [Cu(L1)I] (C10)

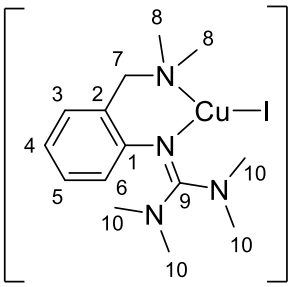

$C_{14}H_{24}CuIN_4$
438.83 g mol^{-1}

Colorless solid (43 mg, 0.099 mmol, 99%). Single crystals, suitable for X-ray diffraction, were grown by slow diffusion of diethyl ether (approx. 4 mL) into the saturated acetonitrile solution of complex **C10** (22 mg, 0.050 mmol in 1 mL) at room temperature. After a few days, colorless blocks were obtained. **^{1}H NMR** (400 MHz, Acetonitrile-d_3, 25 °C): δ [ppm] = 7.23 (ddd, J = 7.8, 7.4, 1.7 Hz, 1H, H6), 7.19 – 7.16 (m, 1H, H4), 6.92 (td, J = 7.4, 1.3 Hz, 1H, H5), 6.47 (dd, J = 7.9, 1.3 Hz, 1H, H3), 3.55 (s, 2H, H7), 2.77 (s, 12H, H10), 2.27 (s, 6H, H8). **^{13}C{^{1}H} NMR** (101 MHz, Acetonitrile-d_3, 25 °C): δ [ppm] = 165.0 (C9), 151.2 (C1), 132.9 (C4), 130.1 (C6), 129.0 (C2), 123.2 (C3), 122.1 (C5), 64.3 (C7), 47.6 (C8), 40.7 (C10). **CHN anal.** calc. for $C_{14}H_{24}CuIN_4$: C, 38.32%; H, 5.51%; N, 12.77%; found: C, 38.25%; H, 5.32%; N, 12.71%. **HRMS-ESI+** (MeCN): m/z calc. for $[(C_{14}H_{24}N_4)Cu]^+$: 311.12915, found: 311.12932. **IR** (KBr): $\tilde{\nu}$ [cm^{-1}] = 3007 (w, C–H$_{arom}$), 2975 (w, C–H$_{arom}$), 2943 (m, C–H$_{arom}$), 2865 (m, C–H$_{aliph}$), 2829 (m, C–H$_{aliph}$), 2797 (m, C–H$_{aliph}$), 2722 (w), 1594 (m), 1542 (s, C=N), 1522 (vs), 1481 (s), 1463 (s), 1449 (m), 1419 (s), 1406 (s), 1392 (s), 1372 (m), 1330 (m), 1267 (m), 1250 (m), 1230 (m), 1208 (m), 1191 (m), 1175 (m), 1154 (m), 1110 (m), 1062 (m), 1029 (m), 1002 (m), 945 (w), 925 (w), 868 (m), 841 (m), 832 (m), 789 (m), 758 (m), 730 (m), 695 (m), 627 (m). Additional information on the NMR spectra of the target compound including original data files is available via Chemotion Repository: https://dx.doi.org/10.14272/DTVVDHUKUBSTJW-UHFFFAOYSA-M.1

5.3.7.11. Synthesis of [Cu(L1)Br] (C11)

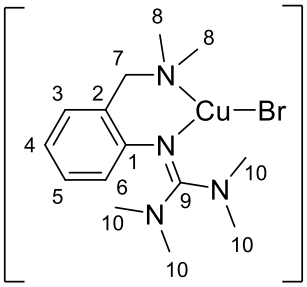

$C_{14}H_{24}BrCuN_4$
391.82 g mol^{-1}

Colorless solid (38 mg, 0.097 mmol, 97%). Single crystals, suitable for X-ray diffraction, were grown by slow diffusion of diethyl ether (approx. 4 mL) into the saturated acetonitrile solution of complex **C11** (20 mg, 0.051 mmol in 1 mL) at room temperature. After a few days, colorless blocks were obtained. **^{1}H NMR** (400 MHz, Acetonitrile-d_3, 25 °C): δ [ppm] = 7.21 – 7.17 (m, 1H, H6), 7.13 (td, J = 7.7, 1.6 Hz, 1H, H4), 6.86 (td, J = 7.4, 1.2 Hz, 1H, H5), 6.44 (dd, J = 8.0, 1.1 Hz, 1H, H3), 3.42 (s, 2H, H7), 2.69 (s, 12H, H10), 2.20 (s, 6H, H8). **^{13}C{^{1}H} NMR** (101 MHz, Acetonitrile-d_3, 25 °C): δ [ppm] = 162.8 (C9), 151.4 (C1), 131.7 (C6), 129.8 (C2), 129.1 (C4), 122.9 (C3), 121.5 (C5), 62.8 (C7), 46.6 (C8), 40.2 (C10). **CHN anal.** calc. for $C_{14}H_{24}CuBrN_4$: C 42.92%; H 6.17%; N 14.30%; found: C 42.81%; H 6.02%; N 14.27%. **HRMS-ESI+** (MeCN): m/z calc. for $[(C_{14}H_{24}N_4)Cu]^+$: 311.12915, found: 311.12902. **IR** (KBr): $\tilde{\nu}$ [cm^{-1}] = 2961 (w, C–H$_{arom}$), 2924 (m, C–H$_{arom}$), 2852 (w, C–H$_{aliph}$), 1543 (m, C=N), 1518 (s), 1481 (m), 1420 (m), 1406 (m), 1391 (m), 1373 (m), 1331 (w), 1261 (m), 1230 (vw),

1154 (m), 1097 (m), 1065 (m), 1029 (s), 1006 (s), 870 (m), 842 (m), 789 (vs), 756 (s), 730 (m), 694 (m), 630 (vw), 554 (w), 484 (m). Additional information on the NMR spectra of the target compound including original data files is available via Chemotion Repository: https://dx.doi.org/10.14272/XYBUOSNKFWKMII-UHFFFAOYSA-M.1

5.3.7.12. Synthesis of [Cu(L1)Cl] (C12)

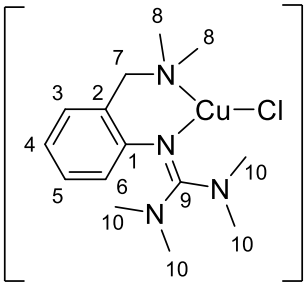

$C_{14}H_{24}ClCuN_4$
347.37 g mol^{-1}

Colorless solid (33 mg, 0.095 mmol, 95%). Single crystals, suitable for X-ray diffraction, were grown by slow diffusion of diethyl ether (approx. 4 mL) into the saturated acetonitrile solution of complex **C12** (18 mg, 0.052 mmol in 1 mL) at room temperature. After a few days, colorless blocks were obtained. **^{1}H NMR** (400 MHz, Acetonitrile-d_3, 25 °C): δ [ppm] = 7.22 – 7.12 (m, 2H, H4+H6), 6.94 – 6.85 (m, 1H, H5), 6.44 (d, J = 7.8 Hz, 1H, H3), 3.48 (s, 2H, H7), 2.74 (s, 12H, H10), 2.24 (s, 6H, H8). **^{13}C{^{1}H} NMR** (101 MHz, Acetonitrile-d_3, 25 °C): δ [ppm] = 164.1 (C9), 151.1 (C1), 132.3 (C6), 129.7 (C2), 129.6 (C4), 123.3 (C3), 122.0 (C5), 63.4 (C7), 46.4 (C8), 40.2 (C10). **CHN anal.** calc. for $C_{14}H_{24}CuClN_4$: C 48.41%; H 6.96%; N 16.13%; found: C 48.30%; H 6.89%; N 15.98%. **HRMS-ESI+** (MeCN): m/z calc. for $[(C_{14}H_{24}N_4)Cu]^+$: 311.12915, found: 311.12938. **IR** (KBr): $\tilde{\nu}$ [cm^{-1}] = 2961 (m, C–H_{arom}), 2922 (m, C–H_{arom}), 2853 (m, C–H_{aliph}), 2811 (w, C–H_{aliph}), 1538 (m, C=N), 1530 (m), 1483 (w), 1417 (m), 1401 (m), 1393 (m), 1370 (w), 1335 (vw), 1259 (m), 1232 (vw), 1149 (w), 1098 (m), 1062 (m), 1028 (s), 1005 (s), 869 (m), 843 (m), 791 (vs), 757 (s), 734 (vw), 700 (vw), 553 (vw), 476 (vw), 458 (vw). Additional information on the NMR spectra of the target compound including original data files is available via Chemotion Repository: https://dx.doi.org/10.14272/DHTDCYWQWFEGRN-UHFFFAOYSA-M.1

5.3.7.13. Synthesis of [Cu(L1)$_2$]I (C13)

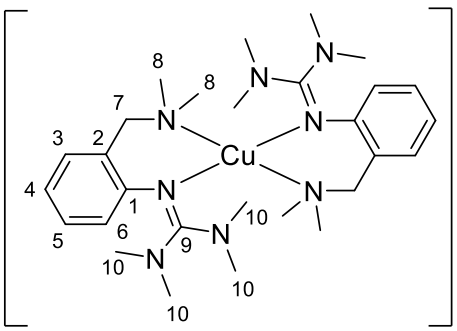

$C_{28}H_{48}CuIN_8$
687.20 g mol^{-1}

The title compound was generated *in-situ*. **^{1}H NMR** (400 MHz, Acetonitrile-d_3, 25 °C): δ [ppm] = 7.18 (d, J = 7.5 Hz, 2H, H6), 7.16 – 7.11 (m, 2H, H4), 6.88 – 6.83 (m, 2H, H5), 6.46 – 6.41 (m, 2H, H3), 3.44 (s, 4H, H7), 2.70 (s, 24H, H10), 2.20 (s, 12H, H8). **^{13}C{^{1}H} NMR** (101 MHz, Acetonitrile-d_3, 25 °C): δ [ppm] = 163.0 (C9), 151.3 (C1), 131.7 (C4), 129.7 (C6), 129.1 (C2), 122.8 (C3), 121.4 (C5), 62.8 (C7), 46.9 (C8), 40.3 (C10). Additional information on the NMR spectra of the target compound including original data files is available via Chemotion Repository: https://dx.doi.org/10.14272/VGPGJDRLIBJZAR-UHFFFAOYSA-M.1

5.3.7.14. Synthesis of [Cu(L1)$_2$]Br (C14)

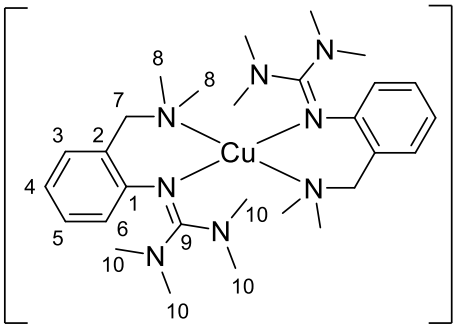

$C_{28}H_{48}BrCuN_8$
640.20 g mol^{-1}

The title compound was generated *in-situ*. **^{1}H NMR** (400 MHz, Acetonitrile-d_3, 25 °C): δ [ppm] = 7.21 – 7.16 (m, 2H, H6), 7.13 (td, J = 7.7, 1.5 Hz, 2H, H4), 6.85 (td, J = 7.4, 1.1 Hz, 2H, H5), 6.44 (dd, J = 7.9, 1.0 Hz, 2H, H3), 3.41 (s, 4H, H7), 2.68 (s, 24H, H10), 2.20 (s, 12H, H8). **^{13}C{^{1}H} NMR** (101 MHz, Acetonitrile-d_3, 25 °C): δ [ppm] = 162.6 (C9), 151.4 (C1), 131.5 (C6), 129.9 (C2), 129.0 (C4), 122.8 (C3), 121.4 (C5), 62.6 (C7), 46.5 (C8), 40.1 (C10). Additional information on the NMR spectra of the target compound including original data files is available via Chemotion Repository: https://dx.doi.org/10.14272/GGYHSQSQRIVBSO-UHFFFAOYSA-M.1

5.3.7.15. Synthesis of [Cu(L1)$_2$]Cl (C15)

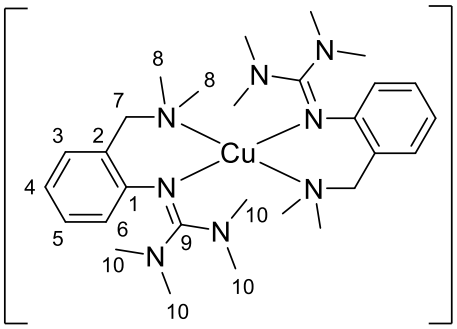

$C_{28}H_{48}ClCuN_8$
595.74 g mol^{-1}

The title compound was generated *in-situ*. **^{1}H NMR** (400 MHz, Acetonitrile-d_3, 25 °C): δ [ppm] = 7.21 – 7.17 (m, 2H, H6), 7.14 (t, J = 7.5 Hz, 2H, H4), 6.89 – 6.82 (m, 2H, H5), 6.43 (d, J = 7.8 Hz, 2H, H3), 3.43 (s, 4H, H7), 2.70 (s, 24H, H10), 2.22 (s, 12H, H8). **^{13}C{^{1}H} NMR** (101 MHz, Acetonitrile-d_3, 25 °C): δ [ppm] = 162.7 (C9), 151.3 (C1), 131.5 (C6), 130.0 (C2), 129.0 (C4), 123.0 (C3), 121.5 (C5), 62.3 (C7), 46.2 (C8), 40.0 (C10). Additional information on the NMR spectra of the target compound including original data files is available via Chemotion Repository: https://dx.doi.org/10.14272/GYQYOCAOCTTZAK-UHFFFAOYSA-M.1

5.3.7.16. Synthesis of [Cu(L2)I]$_2$ (C16)

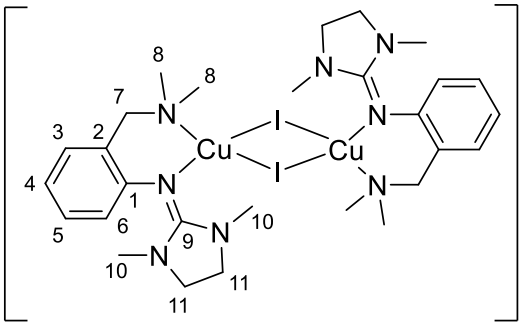

$C_{28}H_{44}Cu_2I_2N_8$
873.62 g mol^{-1}

Colorless solid (39 mg, 0.045 mmol, 90%). Single crystals, suitable for X-ray diffraction, were grown by slow diffusion of pentane (approx. 7 mL) into the saturated tetrahydrofuran solution of complex **C16** (18 mg, 0.021 mmol in 3 mL) at room temperature. After a few weeks, colorless blocks were obtained. **^{1}H NMR** (400 MHz, Acetonitrile-d_3, 25 °C): δ [ppm] = 7.21 (td, J = 7.7, 1.7 Hz, 2H, H6), 7.14 (ddd, J = 7.5, 1.7, 0.4 Hz, 2H, H4), 6.94 (td, J = 7.4, 1.3 Hz, 2H, H5), 6.82 (dd, J = 7.9, 1.1 Hz, 2H, H3), 3.53 (s, 4H, H7), 3.41 (s, 8H, H11), 2.75 (s,

12H, H10), 2.26 (s, 12H, H8). **$^{13}C\{^{1}H\}$ NMR** (101 MHz, Acetonitrile-d_3, 25 °C): δ [ppm] = 162.8 (C9), 149.7 (C1), 132.6 (C4), 130.1 (C2), 130.0 (C6), 124.7 (C3), 122.7 (C5), 63.7 (C7), 49.4 (C11), 47.6 (C8), 36.5 (C10). **CHN anal.** calc. for $C_{28}H_{44}Cu_2I_2N_8$: C, 38.50%; H, 5.08%; N, 12.83%; found: C, 38.16%; H, 5.08%; N, 12.83%. **HRMS-APCI+** (MeCN): m/z calc. for $[(C_{14}H_{22}N_4)Cu]^+$: 309.11405, found: 309.11287, m/z calc. for $[(C_{14}H_{22}N_4)Cu_2I]^+$: 498.94812, found: 498.94647. **IR** (KBr): $\tilde{\nu}$ [cm^{-1}] = 3063 (w, C–H_{arom}), 2987 (w, C–H_{arom}), 2922 (w, C–H_{arom}), 2858 (m, C–H_{aliph}), 2820 (m, C–H_{aliph}), 2773 (m, C–H_{aliph}), 1590 (vs, C=N), 1567 (vs, C=N), 1481 (s), 1455 (m), 1416 (m), 1401 (m), 1361 (m), 1285 (m), 1239 (m), 1201 (w), 1041 (m), 1031 (m), 997 (m), 979 (m), 881 (w), 836 (w), 798 (m), 728 (m), 655 (w). Additional information on the NMR spectra of the target compound including original data files is available via Chemotion Repository: https://dx.doi.org/10.14272/PIFWFHDQDKFJGF-UHFFFAOYSA-L.1

5.3.7.17. Synthesis of $[Cu(L2)Br]_2$ (C17)

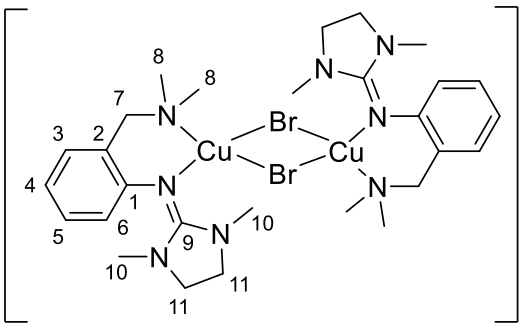

$C_{28}H_{44}Br_2Cu_2N_8$
779.62 g mol^{-1}

Colorless solid (28 mg, 0.036 mmol, 72%). Single crystals, suitable for X-ray diffraction, were grown by slow diffusion of pentane (approx. 6 mL) into the saturated tetrahydrofuran solution of complex **C17** (16 mg, 0.021 mmol in 3 mL) at room temperature. After a few weeks, colorless blocks were obtained. **^{1}H NMR** (400 MHz, Acetonitrile-d_3, 25 °C): δ [ppm] = 7.19 (td, J = 7.7, 1.7 Hz, 2H, H6), 7.14 (dd, J = 7.5, 1.3 Hz, 2H, H4), 6.93 (td, J = 7.4, 1.2 Hz, 2H, H5), 6.82 (dd, J = 7.9, 0.9 Hz, 2H, H3), 3.48 (s, 4H, H7), 3.38 (s, 8H, H11), 2.72 (s, 12H, H10), 2.24 (s, 12H, H8). **$^{13}C\{^{1}H\}$ NMR** (101 MHz, Acetonitrile-d_3, 25 °C): δ [ppm] = 162.3 (C9), 149.6 (C1), 132.4 (C4), 130.2 (C2), 129.8 (C6), 124.7 (C3), 122.7 (C5), 63.5 (C7), 49.3 (C11), 47.0 (C8), 35.9 (C10). **HRMS-APCI+** (MeCN, *in-situ*): m/z calc. for $[(C_{14}H_{22}N_4)Cu]^+$: 309.11405, found: 309.11283, m/z calc. for $[(C_{14}H_{22}N_4)Cu_2Br]^+$: 450.96199, found: 450.96040, m/z calc. for $[(C_{14}H_{22}N_4)_2Cu_2Br]^+$: 697.14643, found: 697.14524. **IR** (NaCl plates, *in-situ*): $\tilde{\nu}$ [cm^{-1}] = 2962 (w, C–H_{arom}), 2938 (m, C–H_{arom}), 2869 (m, C–H_{aliph}), 2833 (m, C–H_{aliph}), 2784 (vw, C–H_{aliph}), 1604 (vs, C=N), 1589 (vs, C=N), 1566 (vs, C=N), 1507 (m), 1486 (vs), 1288 (m), 1173 (vw), 1109 (w), 1046 (m), 1032 (m), 1003 (m), 979 (w), 886 (vw), 842 (w), 806 (w), 755 (m), 731 (vw), 657 (vw). Additional information on the NMR spectra of the target compound including original data files is available via Chemotion Repository: https://dx.doi.org/10.14272/XHJYLLUOTIDGSY-UHFFFAOYSA-L.1

5.3.7.18. Synthesis of {[Cu(L2)Br]·[CuBr]}$_2$ (C18)

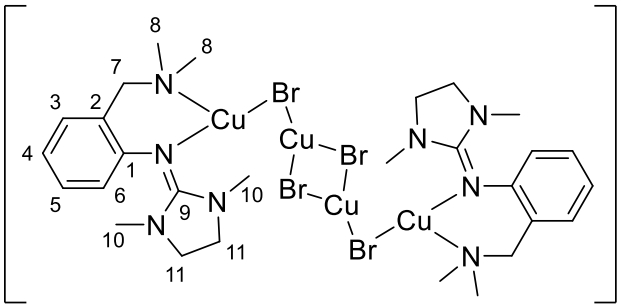

$C_{28}H_{44}Br_4Cu_4N_8$
1066.52 g mol^{-1}

Colorless solid (32 mg, 0.030 mmol, 60%). Single crystals, suitable for X-ray diffraction, were grown by slow diffusion of pentane (approx. 7 mL) into the saturated tetrahydrofuran solution of complex **C18** (11 mg, 0.010 mmol in 4 mL) at room temperature. After a few weeks, colorless blocks were obtained. **^{1}H NMR** (400 MHz, Acetonitrile-d_3, 25 °C): δ [ppm] = 7.19 (td, J = 7.7, 1.6 Hz, 2H, H6), 7.13 (dd, J = 7.5, 1.3 Hz, 2H, H4), 6.92 (td, J = 7.4, 1.2 Hz, 2H, H5), 6.82 – 6.77 (m, 2H, H3), 3.47 (s, 4H, H7), 3.41 (s, 8H, H11), 2.70 (s, 12H, H10), 2.28 (s, 12H, H8). **^{13}C{^{1}H} NMR** (101 MHz, Acetonitrile-d_3, 25 °C): δ [ppm] = 163.0 (C9), 150.0 (C1), 132.7 (C4), 130.0 (C6), 129.8 (C2), 124.6 (C3), 122.5 (C5), 64.2 (C7), 49.3 (C11), 47.7 (C8), 35.8 (C10). **HRMS-APCI+** (MeCN, *in-situ*): m/z calc. for $[(C_{14}H_{22}N_4)Cu]^+$: 309.11405, found: 309.11276, m/z calc. for $[(C_{14}H_{22}N_4)CuBrCu]^+$: 450.96199, found: 450.96050. **IR** (NaCl plates, *in-situ*): $\tilde{\nu}$ [cm^{-1}] = 2965 (w, C–H$_{arom}$), 2942 (m, C–H$_{arom}$), 2872 (w, C–H$_{aliph}$), 2835 (w, C–H$_{aliph}$), 2788 (vw, C–H$_{aliph}$), 1603 (s, C=N), 1589 (vs, C=N), 1567 (vs, C=N), 1506 (m), 1487 (vs), 1476 (m), 1457 (m), 1367 (m), 1287 (m), 1258 (w), 1243 (w), 1174 (w), 1110 (w), 1046 (w), 997 (m), 979 (w), 886 (vw), 843 (w), 805 (w), 755 (w), 731 (vw). Additional information on the NMR spectra of the target compound including original data files is available via Chemotion Repository: https://dx.doi.org/10.14272/WSDKDGLGZMISBF-UHFFFAOYSA-J.1

5.3.7.19. Synthesis of {[Cu(L2)Cl]·[CuCl]}$_2$ (C19)

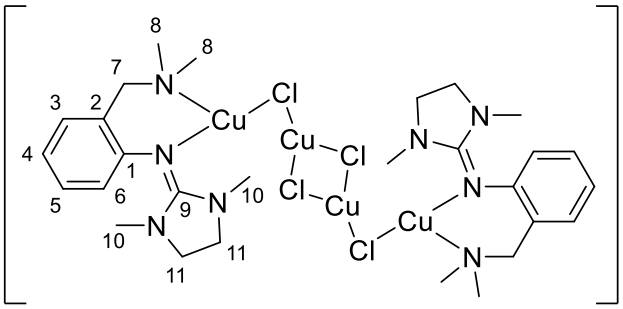

$C_{28}H_{44}Cl_4Cu_4N_8$
888.70 g mol^{-1}

Colorless solid (30 mg, 0.034 mmol, 68%). Single crystals, suitable for X-ray diffraction, were grown by slow diffusion of pentane (approx. 7 mL) into the saturated tetrahydrofuran solution of complex **C19** (11 mg, 0.012 mmol in 4 mL) at room temperature. After a few weeks, colorless blocks were obtained. **^{1}H NMR** (400 MHz, Acetonitrile-d_3, 25 °C): δ [ppm] = 7.23 (t, J = 7.0 Hz, 2H, H6), 7.12 (dd, J = 7.5, 1.5 Hz, 2H, H4), 6.92 (td, J = 7.4, 0.9 Hz, 2H, H5), 6.76 (d, J = 7.8 Hz, 2H, H3), 3.49 (s, 12H, H10), 2.74 (s, 16H, H7+H8), 2.37 (s, 8H, H11). **^{13}C{^{1}H} NMR** (101 MHz, Acetonitrile-d_3, 25 °C): δ [ppm] = 162.9 (C9), 149.4 (C1), 132.4 (C4), 129.8 (C6), 129.4 (C2), 124.5 (C3), 122.1 (C5), 63.3 (C7), 48.9 (C11), 46.7 (C8), 35.1 (C10). **HRMS-APCI+** (MeCN,

in-situ): m/z calc. for $[(C_{14}H_{22}N_4)Cu]^+$: 309.11405, found: 309.11289, m/z calc. for $[(C_{14}H_{22}N_4)CuClCu]^+$: 407.01117, found: 407.01250. **IR** (NaCl plates, *in-situ*): $\tilde{\nu}$ [cm^{-1}] = 2963 (m, C–H_{arom}), 2941 (m, C–H_{arom}), 2872 (m, C–H_{aliph}), 2835 (m, C–H_{aliph}), 2794 (w, C–H_{aliph}), 1603 (s, C=N), 1589 (vs, C=N), 1567 (vs, C=N), 1533 (m), 1506 (m), 1487 (vs), 1367 (m), 1287 (m), 1244 (w), 1175 (vw), 1142 (vw), 1109 (vw), 1047 (m), 1039 (m), 997 (w), 978 (vw), 881 (vw), 862 (vw), 843 (w), 806 (vw), 754 (w), 678 (vw). Additional information on the NMR spectra of the target compound including original data files is available via Chemotion Repository: https://dx.doi.org/10.14272/RKVWKLBBLRKNDP-UHFFFAOYSA-J.1

5.3.7.20. Synthesis of $[Cu(L1)Cl_2]$ (C20)

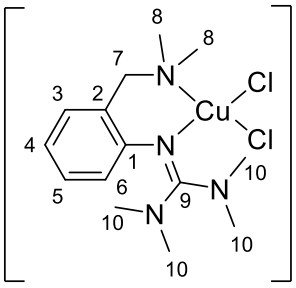

$C_{14}H_{24}Cl_2CuN_4$
382.82 g mol^{-1}

Brown solid (36 mg, 0.094 mmol, 94%). Single crystals, suitable for X-ray diffraction, were grown by slow diffusion of pentane (approx. 14 mL) into the saturated tetrahydrofuran solution of complex **C20** (21 mg, 0.055 mmol in 6 mL) at room temperature. After a few weeks, colorless blocks were obtained. **HRMS-APCI+** (MeCN): m/z calc. for $[C_{14}H_{24}ClCuN_4]^+$: 346.09800, found: 346.09742. **IR** (ATR): $\tilde{\nu}$ [cm^{-1}] = 2965 (vw, C–H_{arom}), 2944 (w, C–H_{arom}), 2921 (w, C–H_{arom}), 2888 (w, C–H_{aliph}), 1584 (w), 1565 (m, C=N), 1521 (vs), 1487 (m), 1449 (m), 1418 (m), 1406 (vs), 1394 (vs), 1329 (m), 1273 (w), 1233 (w), 1162 (m), 1152 (w), 1113 (w), 1067 (w), 1039 (m), 1030 (m), 986 (m), 882 (w), 873 (w), 841 (m), 797 (m), 761 (s), 733 (w), 704 (w), 553 (w).

5.3.7.21. Synthesis of $[Cu(L2)Cl_2]$ (C21)

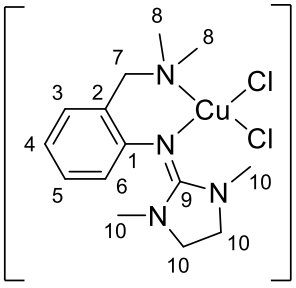

$C_{14}H_{22}Cl_2CuN_4$
380.80 g mol^{-1}

Brown solid (38 mg, 0.099 mmol, 99%). Single crystals, suitable for X-ray diffraction, were grown by slow diffusion of pentane (approx. 15 mL) into the saturated tetrahydrofuran solution of complex **C21** (20 mg, 0.053 mmol in 7 mL) at room temperature. After a few weeks, colorless blocks were obtained. **HRMS-ESI+** (MeCN): m/z calc. for $[C_{14}H_{22}ClCuN_4]^+$: 344.08235, found: 344.08207. **IR** (ATR): $\tilde{\nu}$ [cm^{-1}] = 2962 (vw, C–H_{arom}), 2923 (vw, C–H_{arom}), 2889 (vw, C–H_{aliph}), 2864 (vw, C–H_{aliph}), 2834 (vw, C–H_{aliph}), 1585 (m), 1560 (m, C=N), 1540 (m), 1490 (m), 1476 (m), 1408 (m), 1400 (w), 1380 (m), 1291 (m), 1237 (w), 1027 (m), 994 (w), 892 (w), 840 (m), 807 (m), 770 (vs).

5.3.7.22. Synthesis of [Cu(L3)(MeCN)]PF_6 (C22)

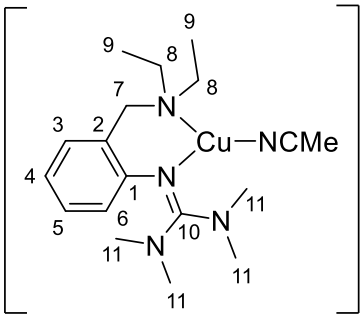

$C_{18}H_{31}CuF_6N_5P$
525.99 g mol^{-1}

Colorless solid (47 mg, 0.089 mmol, 89%). **^{1}H NMR** (400 MHz, Acetonitrile-d_3, 25 °C): δ [ppm] = 7.23 – 7.17 (m, 2H, H4+H6), 6.91 (td, J = 7.4, 1.3 Hz, 1H, H5), 6.44 (dt, J = 7.7, 0.9 Hz, 1H, H3), 3.59 (s, 2H, H7), 2.95 – 2.47 (m, 16H, H8+H11), 1.12 (t, J = 7.1 Hz, 6H, H9). **^{13}C{^{1}H} NMR** (101 MHz, Acetonitrile-d_3, 25 °C): δ [ppm] = 165.0 (C10), 151.6 (C1), 133.2 (C4), 130.2 (C6), 128.5 (C2), 123.1 (C3), 122.3 (C5), 59.2 (C7), 48.2 (C8), 40.1 (C11), 10.0 (C9). **^{19}F{^{1}H} NMR** (377 MHz, Acetonitrile-d_3, 25 °C): δ [ppm] = -72.86 (d, J = 706.5 Hz, PF_6). **^{31}P{^{1}H} NMR** (162 MHz, Acetonitrile-d_3, 25 °C): δ [ppm] = -144.59 (sept, J = 706.4 Hz, PF_6). **HRMS-ESI+** (MeCN): m/z calc. for $[(C_{16}H_{28}N_4)Cu]^+$: 339.16045, found: 339.16591, calc. for $[(C_{16}H_{28}N_4)Cu(CH_3CN)]^+$: 380.18699, found: 380.19176. **IR** (KBr): $\tilde{\nu}$ [cm^{-1}] = 3067 (w, C–H_{arom}), 3023 (m, C–H_{arom}), 3002 (m, C–H_{arom}), 2960 (m, C–H_{arom}), 2935 (m, C–H_{arom}), 2871 (m, C–H_{aliph}), 2844 (m, C–H_{aliph}), 2801 (w, C–H_{aliph}), 1598 (m), 1555 (vs, C=N), 1527 (vs), 1486 (s), 1477 (s), 1447 (s), 1424 (s), 1408 (vs), 1332 (s), 1266 (m), 1238 (m), 1163 (m), 1061 (m), 1037 (s), 838 (vs, PF_6), 750 (s, PF_6), 727 (m), 701 (m), 556 (vs, PF_6), 517 (w), 462 (w, PF_6). Additional information on the NMR spectra of the target compound including original data files is available via Chemotion Repository: https://dx.doi.org/10.14272/FFIOOAUERPRGCO-UHFFFAOYSA-N.1

5.3.7.23. Synthesis of [Cu(L3)(MeCN)]BF_4 (C23)

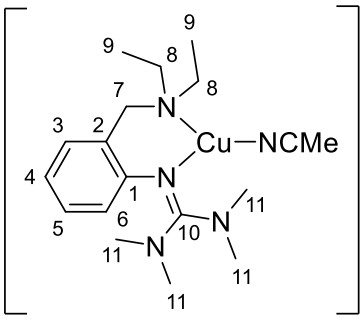

$C_{18}H_{31}BCuF_4N_5$
467.83 g mol^{-1}

Colorless solid (37 mg, 0.079 mmol, 79%). **^{1}H NMR** (400 MHz, Acetonitrile-d_3, 25 °C): δ [ppm] = 7.23 – 7.17 (m, 2H, H4+H6), 6.90 (td, J = 7.4, 1.3 Hz, 1H, H5), 6.44 (dt, J = 7.7, 0.9 Hz, 1H, H3), 3.59 (s, 2H, H7), 2.96 – 2.47 (m, 16H, H8+H11), 1.12 (t, J = 7.1 Hz, 6H, H9). **^{13}C{^{1}H} NMR** (101 MHz, Acetonitrile-d_3, 25 °C): δ [ppm] = 165.0 (C10), 151.6 (C1), 133.2 (C4), 130.2 (C6), 128.5 (C2), 123.1 (C3), 122.3 (C5), 59.2 (C7), 48.3 (C8), 40.1 (C11), 10.0 (C9). **^{19}F{^{1}H} NMR** (377 MHz, Acetonitrile-d_3, 25 °C): δ [ppm] = -151.78 (s, BF_4). **HRMS-ESI+** (MeCN): m/z calc. for $[(C_{16}H_{28}N_4)Cu]^+$: 339.16045, found: 339.16459, calc. for $[(C_{16}H_{28}N_4)Cu(CH_3CN)]^+$: 380.18699, found: 380.19166. **IR** (KBr): $\tilde{\nu}$ [cm^{-1}] = 3062 (w, C–H_{arom}), 2998 (m, C–H_{arom}), 2951 (m, C–H_{arom}), 2883 (m, C–H_{aliph}), 2827 (m, C–H_{aliph}), 1554 (vs, C=N), 1532 (vs), 1483 (s), 1452 (m), 1429 (s), 1408 (s), 1400 (s), 1332 (m), 1267 (m), 1238 (m), 1197 (m), 1164 (m), 1097 (vs, BF_4), 1054 (vs, BF_4), 1034 (vs, BF_4), 913 (m), 864 (m), 824 (w), 782 (m), 753 (m, BF_4), 730 (m), 705 (m), 621 (w), 520 (m, BF_4), 467

(m), 450 (w). Additional information on the NMR spectra of the target compound including original data files is available via Chemotion Repository: https://dx.doi.org/10.14272/PTEOGYLGFQZBHG-UHFFFAOYSA-N.1

5.3.7.24. Synthesis of [Cu(L3)(MeCN)]OTf (C24)

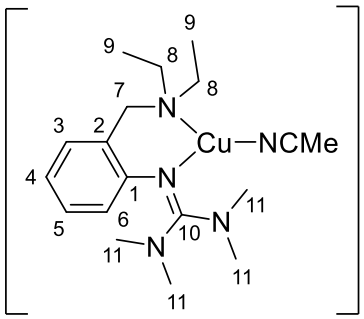

$C_{19}H_{31}CuF_3N_5O_3S$
530.09 g mol^{-1}

Colorless solid (38 mg, 0.071 mmol, 71%). **^{1}H NMR** (400 MHz, Acetonitrile-d_3, 25 °C): δ [ppm] = 7.23 – 7.17 (m, 2H, H4+H6), 6.90 (td, J = 7.4, 1.3 Hz, 1H, H5), 6.44 (dd, J = 7.8, 0.8 Hz, 1H, H3), 3.58 (s, 2H, H7), 2.96 – 2.43 (m, 16H, H8+H11), 1.12 (t, J = 7.2 Hz, 6H, H9). **^{13}C{^{1}H} NMR** (101 MHz, Acetonitrile-d_3, 25 °C): δ [ppm] = 165.0 (C10), 151.6 (C1), 133.2 (C4), 130.2 (C6), 128.5 (C2), 123.8 (OTf), 123.1 (C3), 122.3 (C5), 59.2 (C7), 48.2 (C8), 40.1 (C11), 10.0 (C9). **^{19}F{^{1}H} NMR** (377 MHz, Acetonitrile-d_3, 25 °C): δ [ppm] = -79.23 (s, OTf). **HRMS-ESI+** (MeCN): m/z calc. for $[(C_{16}H_{28}N_4)Cu]^+$: 339.16045, found: 339.16525, calc. for $[(C_{16}H_{28}N_4)Cu(CH_3CN)]^+$: 380.18699, found: 380.18902. **IR** (KBr): $\tilde{\nu}$ [cm^{-1}] = 3058 (w, C–H$_{arom}$), 2969 (m, C–H$_{arom}$), 2936 (m, C–H$_{arom}$), 2873 (m, C–H$_{arom}$), 2803 (w, C–H$_{aliph}$), 1546 (s, C=N), 1528 (s), 1487 (m), 1471 (m), 1423 (m), 1397 (s), 1330 (m), 1267 (vs, OTf), 1223 (m, OTf), 1153 (s, OTf), 1047 (m), 1031 (vs, OTf), 929 (w), 864 (m), 791 (m), 753 (m, OTf), 730 (w), 655 (m), 638 (vs, OTf), 572 (m), 517 (m), 473 (w). Additional information on the NMR spectra of the target compound including original data files is available via Chemotion Repository: https://dx.doi.org/10.14272/PVOWJBLMSRTONC-UHFFFAOYSA-M.1

5.3.7.25. Synthesis of [Cu(L4)(MeCN)]PF$_6$ (C25)

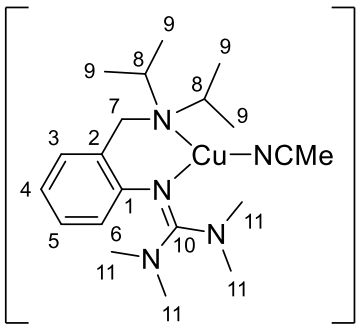

$C_{20}H_{35}CuF_6N_5P$
554.05 g mol^{-1}

Yellow solid (30 mg, 0.054 mmol, 54%). **^{1}H NMR** (400 MHz, Acetonitrile-d_3, 25 °C): δ [ppm] = 7.28 – 7.23 (m, 1H, H6), 7.23 – 7.17 (m, 1H, H4), 6.98 – 6.90 (m, 1H, H5), 6.53 – 6.38 (m, 1H, H3), 3.77 (s, 2H, H7), 3.22 (sept, J = 6.5 Hz, 2H, H8), 2.74 (s, 12H, H11), 1.20 (d, J = 6.6 Hz, 12H, H9). **^{13}C{^{1}H} NMR** (101 MHz, Acetonitrile-d_3, 25 °C): δ [ppm] = 165.7 (C10), 150.7 (C1), 132.7 (C6), 130.1 (C2), 129.9 (C4), 123.0 (C3+C5), 54.1 (C8), 52.1 (C7), 40.3 (C11), 20.9 (C9). **^{19}F{^{1}H} NMR** (377 MHz, Acetonitrile-d_3, 25 °C): δ [ppm] = -72.87 (d, J = 706.6 Hz, PF$_6$). **^{31}P{^{1}H} NMR** (162 MHz, Acetonitrile-d_3, 25 °C): δ [ppm] = -144.59 (sept, J = 706.5 Hz, PF$_6$). **HRMS-ESI+** (MeCN): m/z calc. for $[(C_{18}H_{32}N_4)Cu]^+$: 367.19175, found: 367.19254, calc. for $[(C_{18}H_{32}N_4)Cu(CH_3CN)]^+$: 408.21830, found: 408.21786. **IR** (KBr): $\tilde{\nu}$ [cm^{-1}] = 3058 (m, C–H$_{arom}$), 2966 (m, C–H$_{arom}$), 2938 (m, C–

H_{arom}), 2893 (m, C–H_{aliph}), 2873 (m, C–H_{aliph}), 2800 (m, C–H_{aliph}), 1598 (m), 1551 (s, C=N), 1527 (s), 1488 (m), 1473 (m), 1450 (m), 1424 (m), 1397 (s), 1331 (m), 1269 (m), 1236 (m), 1170 (m), 1159 (m), 1113 (m), 1065 (m), 1034 (m), 988 (w), 839 (vs, PF_6), 751 (m, PF_6), 724 (m), 703 (m), 557 (s, PF_6), 458 (w, PF_6). Additional information on the NMR spectra of the target compound including original data files is available via Chemotion Repository: https://dx.doi.org/10.14272/LKAMFMLEEUDGOQ-UHFFFAOYSA-N.1

5.3.7.26. Synthesis of [Cu(L4)(MeCN)]BF_4 (C26)

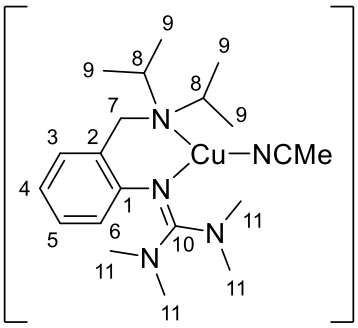

+ BF_4^-

$C_{20}H_{35}BCuF_4N_5$
495.89 g mol^{-1}

Light-yellow solid (34 mg, 0.068 mmol, 68%). **^{1}H NMR** (400 MHz, Acetonitrile-d_3, 25 °C): δ [ppm] = 7.28 – 7.23 (m, 1H, H6), 7.19 (td, J = 7.7, 1.5 Hz, 1H, H4), 6.92 (td, J = 7.4, 1.3 Hz, 1H, H5), 6.44 (d, J = 7.8 Hz, 1H, H3), 3.76 (s, 2H, H7), 3.22 (sept, J = 6.6 Hz, 2H, H8), 2.72 (s, 12H, H11), 1.20 (d, J = 6.6 Hz, 12H, H9). **^{13}C{^{1}H} NMR** (101 MHz, Acetonitrile-d_3, 25 °C): δ [ppm] = 165.7 (C10), 150.6 (C1), 132.7 (C6), 130.2 (C2), 129.9 (C4), 123.1 (C3), 122.8 (C5), 54.2 (C8), 52.2 (C7), 40.3 (C11), 21.0 (C9). **^{19}F{^{1}H} NMR** (377 MHz, Acetonitrile-d_3, 25 °C): δ [ppm] = -151.76 (s, BF_4). **HRMS-ESI+** (MeCN): m/z calc. for $[(C_{18}H_{32}N_4)Cu]^+$: 367.19175, found: 367.19348, calc. for $[(C_{18}H_{32}N_4)Cu(CH_3CN)]^+$: 408.21830, found: 408.21763. **IR** (KBr): $\tilde{\nu}$ [cm^{-1}] = 3062 (w, C–H_{arom}), 2966 (m, C–H_{arom}), 2931 (m, C–H_{arom}), 2891 (m, C–H_{aliph}), 2873 (m, C–H_{aliph}), 2803 (w, C–H_{aliph}), 1550 (vs, C=N), 1534 (vs), 1477 (m), 1449 (m), 1426 (m), 1395 (m), 1327 (m), 1270 (w), 1235 (w), 1208 (m), 1158 (m), 1140 (m), 1050 (vs, BF_4), 866 (w), 827 (w), 760 (m), 749 (m, BF_4), 708 (w), 520 (w, BF_4), 451 (w). Additional information on the NMR spectra of the target compound including original data files is available via Chemotion Repository: https://dx.doi.org/10.14272/XCTDJIMIPLJWIC-UHFFFAOYSA-N.1

5.3.7.27. Synthesis of [Cu(L4)(MeCN)]OTf (C27)

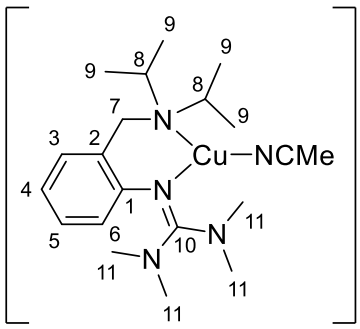

+ OTf^-

$C_{21}H_{35}CuF_3N_5O_3S$
558.14 g mol^{-1}

Light-yellow solid (35 mg, 0.062 mmol, 62%). **^{1}H NMR** (400 MHz, Acetonitrile-d_3, 25 °C): δ [ppm] = 7.27 – 7.23 (m, 1H, H6), 7.19 (td, J = 7.7, 1.6 Hz, 1H, H4), 6.92 (td, J = 7.4, 1.3 Hz, 1H, H5), 6.43 (d, J = 7.8 Hz, 1H, H3), 3.76 (s, 2H, H7), 3.22 (sept, J = 6.5 Hz, 2H, H8), 2.72 (s, 12H, H11), 1.20 (d, J = 6.6 Hz, 12H, H9). **^{13}C{^{1}H} NMR** (101 MHz, Acetonitrile-d_3, 25 °C): δ [ppm] = 165.7 (C10), 150.6 (C1), 132.8 (C6), 130.2 (C2), 129.9 (C4), 123.8 (OTf), 123.1 (C3), 122.8 (C5), 54.2 (C8), 52.3 (C7), 40.3 (C11), 21.0 (C9). **^{19}F{^{1}H} NMR** (377 MHz, Acetonitrile-d_3, 25 °C): δ [ppm] = -79.24 (s, OTf). **HRMS-ESI+**

(MeCN): m/z calc. for $[(C_{18}H_{32}N_4)Cu]^+$: 367.19175, found: 367.19506, calc. for $[(C_{18}H_{32}N_4)Cu(CH_3CN)]^+$: 408.21830, found: 408.21837. **IR** (KBr): $\tilde{\nu}$ [cm^{-1}] = 3059 (w, C–H_{arom}), 2966 (m, C–H_{arom}), 2934 (m, C–H_{arom}), 2892 (m, C–H_{aliph}), 2876 (m, C–H_{aliph}), 2799 (w, C–H_{aliph}), 1543 (vs, C=N), 1530 (vs), 1472 (s), 1424 (s), 1396 (s), 1330 (m), 1267 (vs, OTf), 1223 (m, OTf), 1156 (vs, OTf), 1064 (m), 1048 (s, OTf), 1031 (vs, OTf), 930 (w), 866 (w), 842 (w), 826 (w), 790 (w), 753 (m, OTf), 656 (m), 638 (vs, OTf), 572 (m), 547 (w), 517 (m). Additional information on the NMR spectra of the target compound including original data files is available via Chemotion Repository: https://dx.doi.org/10.14272/HNRHNIXGNDHWER-UHFFFAOYSA-M.1

5.3.7.28. Synthesis of $[Cu(L5)I]_2$ (C28)

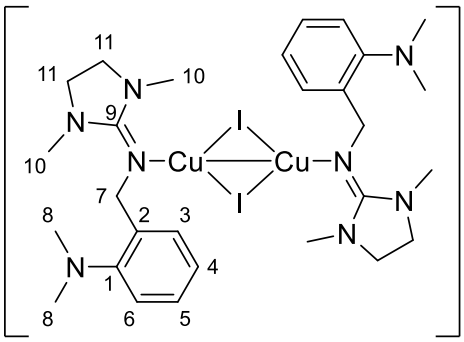

$C_{28}H_{44}Cu_2I_2N_8$
873.62 g mol^{-1}

Light-yellow solid (31 mg, 0.072 mmol, 72%). **^{1}H NMR** (400 MHz, Acetonitrile-d_3, 25 °C): δ [ppm] = 7.35 (dd, J = 7.2, 1.3 Hz, 2H, H5), 7.25 (td, J = 8.0, 1.6 Hz, 2H, H3), 7.15 (dd, J = 8.1, 1.3 Hz, 2H, H6), 7.03 (td, J = 7.4, 1.3 Hz, 2H, H4), 4.53 (s, 4H, H7), 3.31 (s, 8H, H11), 2.86 (s, 12H, H10), 2.68 (s, 12H, H8). **^{13}C{^{1}H} NMR** (101 MHz, Acetonitrile-d_3, 25 °C): δ [ppm] = 164.4 (C9), 153.1 (C1), 137.2 (C2), 131.0 (C5), 128.9 (C3), 124.4 (C6), 120.2 (C4), 50.7 (C7), 50.2 (C11), 45.9 (C8), 37.4 (C10). **CHN anal.** calc. for $C_{14}H_{22}N_4CuI$: C, 38.50%; H 5.08%; N 12.83%; found: C, 38.40%; H, 5.01%; N, 12.78%. **HRMS-ESI+** (MeCN): m/z calc. for $[(C_{14}H_{22}N_4)Cu]^+$: 309.11350, found: 309.11822. **IR** (KBr): $\tilde{\nu}$ [cm^{-1}] = 2985 (vw, C–H_{arom}), 2941 (w, C–H_{arom}), 2856 (w, C–H_{aliph}), 2832 (w, C–H_{aliph}), 2793 (vw, C–H_{aliph}), 2772 (vw, C–H_{aliph}), 1612 (s, C=N), 1594 (s, C=N), 1570 (m), 1487 (m), 1455 (m), 1423 (m), 1395 (m), 1353 (w), 1319 (w), 1285 (m), 1276 (m), 1186 (w), 1153 (w), 1144 (w), 1050 (m), 967 (m), 947 (m), 866 (w), 804 (vw), 763 (s), 724 (m), 718 (m), 664 (w), 594 (w), 559 (m), 529 (w), 459 (m). Additional information on the NMR spectra of the target compound including original data files is available via Chemotion Repository: https://dx.doi.org/10.14272/BMWSYHMPJNUPRV-UHFFFAOYSA-L.1

5.3.7.29. Synthesis of [Cu(L5)(MeCN]PF_6 (C29)

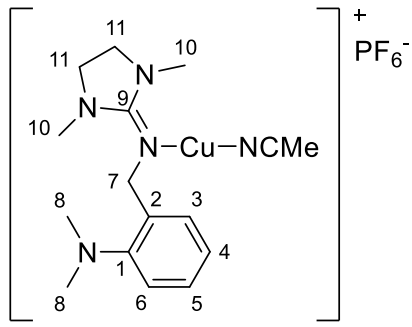

$C_{16}H_{25}CuF_6N_5P$
495.92 g mol^{-1}

The title compound was generated *in-situ*. **^{1}H NMR** (400 MHz, Acetonitrile-d_3, 25 °C): δ [ppm] = 7.30 – 7.22 (m, 2H, H3+H5), 7.15 (dd, J = 8.0, 1.0 Hz, 1H, H4), 7.03 (td, J = 7.5, 1.2 Hz, 1H, H6), 4.45 (s, 2H, H7), 3.35 (s, 4H, H11), 2.80 (s, 6H, H10), 2.65 (s, 6H, H8). **^{13}C{^{1}H} NMR** (101 MHz, Acetonitrile-d_3, 25 °C): δ [ppm] = 165.1 (C9), 152.8 (C1), 135.8 (C2), 130.6 (C5), 128.9 (C3), 124.1 (C6), 119.9 (C4), 50.3 (C7), 49.8 (C11), 45.2 (C8), 36.4 (C10). **^{19}F{^{1}H} NMR** (377 MHz, Acetonitrile-d_3, 25 °C) δ [ppm] = -72.87 (d, J = 706.6 Hz, PF_6). **^{31}P{^{1}H} NMR** (162 MHz, Acetonitrile-d_3, 25 °C) δ [ppm] = -144.60 (sept, J = 706.3 Hz, PF_6). **HRMS-ESI+** (MeCN): m/z calc. for $[(C_{14}H_{22}N_4)Cu]^+$: 309.11350, found: 309.11413, calc. for $[(C_{14}H_{22}N_4)Cu(CH_3CN)]^+$: 350.14004, found: 350.14069. **IR** (NaCl plates): $\tilde{\nu}$ [cm^{-1}] = 2947 (m, C–H_{arom}), 2941 (m, C–H_{arom}), 2871 (m, C–H_{aliph}), 2833 (m, C–H_{aliph}), 2794 (m, C–H_{aliph}), 1598 (vs, C=N), 1506 (m), 1491 (s), 1476 (m), 1474 (w), 1446 (w), 1437 (w), 1427 (w), 1398 (w), 1382 (w), 1376 (w), 1367 (m), 1349 (vw), 1293 (m), 1232 (vw), 1216 (vw), 1154 (vw), 1126 (vw), 1103 (vw), 1046 (m), 1037 (m), 1033 (m), 963 (vw), 946 (m), 877 (m), 854 (vs, PF_6), 771 (w, PF_6), 680 (vw). Additional information on the NMR spectra of the target compound including original data files is available via Chemotion Repository: https://dx.doi.org/10.14272/HINXWGFOFQTPTK-UHFFFAOYSA-N.1

5.3.8. Synthesis of Bis(μ-oxido) Dicopper(III) Complexes

For the generation of the bis(μ-oxido) species [**O1**]$^{2+}$-[**O5**]$^{2+}$ (0.005 mmol, 1.0 eq) dried and degassed tetrahydrofuran (9.5 mL) was saturated with molecular oxygen at the corresponding temperature according to Table 34.

Table 34: Formation temperature of the bis(μ-oxido) species [**O1**]$^{2+}$-[**O5**]$^{2+}$.

bis(μ-oxido) species	temperature [°C]
[**O1**]X_2 (X^- = PF_6^-, BF_4^-, OTf^-, ClO_4^-)	–90
[**O1I**](CuI_2)	rt
[**O1**]X_2 (X^- = Br^-, Cl^-)	–100
[**O3**]X_2 (X^- = PF_6^-, BF_4^-, OTf^-)	–100
[**O4**]X_2 (X^- = PF_6^-, BF_4^-, OTf^-)	–100
[**O5**]X_2 (X^- = I^-)	–80
[**O5**]X_2 (X^- = PF_6^-)	–100

The corresponding copper(I) complex (0.010 mmol, 2.0 eq) in acetonitrile (0.5 mL) was prepared under inert conditions and added rapidly via a Hamilton syringe. For the generation of bis(μ-oxido) species [**O1I**]$^+$, the precursor species **C10** or **C10**·CuI (0.010 mmol, 2.0 eq) was used. The formation of the bis(μ-oxido) complex (0.5 mM) was followed by UV/Vis spectroscopy.

5.3.8.1. General Procedure of Titration Experiments

The bis(μ-oxido) species [**O1**]$^{2+}$ or [**O1I**]$^+$ was synthesized at the respective temperature according to the protocol described above. The excess of O_2 was removed by three cycles of evacuation and purging with N_2. A tenfold stock solution of the required amount of the titrant was prepared and one-tenth of it positioned in a Hamilton syringe. The titrant was added stepwise. The titration experiment was followed by UV/Vis spectroscopy. After stabilization of the optical spectrum the next aliquot of the titrant was injected.

Spectrophotometric Titration of [**O1**]$(PF_6)_2$ with FcCOOH[47]:
Complex **C1** was oxygenated at –90 °C to give [**O1**]$(PF_6)_2$ (0.5 mM). Titrant ferrocene monocarboxylic acid (2.8 mg, 0.012 mmol, 2.4 eq) in tetrahydrofuran (1.2 mL) was added in 0.1 mL (0.2 eq) steps.

Titration of [**O1**]$(PF_6)_2$ with Halide Source Bu_4NX (X= I, Br, Cl):
Complex **C1** was oxygenated at –90 °C to give [**O1**]$(PF_6)_2$ (0.5 mM). Titrant Bu_4NX (50.0 μmol, 10.0 eq) in acetonitrile (1.0 mL) was added stepwise in 0.1 mL (1.0 eq) steps.

Titration of [**O1I**](CuI_2) with **L1:**
Complex **C10** was oxygenated at room temperature to give [**O1I**](CuI_2) (1.25 mM). Titrant **L1** (15.5 mg, 2.5 μmol, 5.0 eq) in acetonitrile (0.5 mL) was added stepwise in 0.1 mL (1.0 eq) steps.

Titration of [**O1I**](CuI_2) with Iodide Source Bu_4NI:
Complex **C10** was oxygenated at room temperature to give [**O1I**](CuI_2) (0.5 mM). Titrant Bu_4NI (18.5 mg, 50.0 μmol, 10.0 eq) in acetonitrile (1.0 mL) was added stepwise in 0.1 mL (1.0 eq) steps.

Titration of [**O1I**](CuI_2) with Copper Sources CuI and $[Cu(MeCN)_4]PF_6$:
Complex **C10** was oxygenated at –80 °C to give [**O1I**](CuI_2) (0.5 mM). Titrant (50.0 μmol, 10.0 eq) in acetonitrile (1.0 mL) was added stepwise in 0.1 mL (1.0 eq) steps.

5.3.8.2. Competitive Oxygenation of C1 and C10

Dried and degassed tetrahydrofuran (9.5 mL) was saturated with molecular oxygen at –90 °C. The precursor complexes **C1** (0.005 mmol, 2.0 eq) and **C10** (0.005 mmol, 2.0 eq) each in

acetonitrile (0.25 mL) were prepared under inert conditions and added simultaneously via a Hamilton syringe. The competitive oxygenation of **C1** and **C10** was followed by UV/Vis spectroscopy.

5.3.9. Decomposition Kinetics

The bis(μ-oxido) species [**O**]$^{2+}$ (0.5 mM) was synthesized at the respective temperature according to the protocol described above. The excess of O_2 was removed by three cycles of evacuation and purging with N_2. The decomposition kinetics were followed by UV/Vis spectroscopy at constant temperature.

5.3.9.1. Synthesis of Decomposition Products

For the generation of the μ-alkoxido μ-hydroxido tricopper(II) species [**H1**](X)$_2$ (X$^-$ = PF_6^-, BF_4^-), dried and degassed tetrahydrofuran (9.0 mL) was saturated with molecular oxygen at –90 °C. The copper(I) complex **C1** or **C2** (60.0 μmol) in acetonitrile (1.0 mL) was prepared under inert conditions and added rapidly via a Hamilton syringe. The formed bis(μ-oxido) complex [**O1**]X$_2$ (X$^-$ = PF_6^-, BF_4^-) was warmed up to room temperature and evaporated to dryness. The green residue was dissolved in acetonitrile and filtered afterwards under ambient conditions. Single crystals of [**H1**](X)$_2$ (X$^-$ = PF_6^-, BF_4^-), suitable for X-ray diffraction, were grown by slow diffusion of diethyl ether into the acetonitrile solution or by slow diffusion of acetonitrile out into toluene. The crystallization of blue and light-yellow blocks in a ratio of 1:1 in a greenish solution was observed after several days. The blue crystals revealed the molecular structure of the trinuclear species [**H1**](X)$_2$ (X$^-$ = PF_6^-, BF_4^-) and the light-yellow crystals showed the molecular structure of the protonated ligand [**L1**H$_2$]$^{2+}$ in the solid state (see Scheme 15 for further details).

[Cu$_3$(μ-OL1)$_2$(μ-OH)$_2$](PF$_6$)$_2$ · 2 thf ([H1](PF$_6$)$_2$)

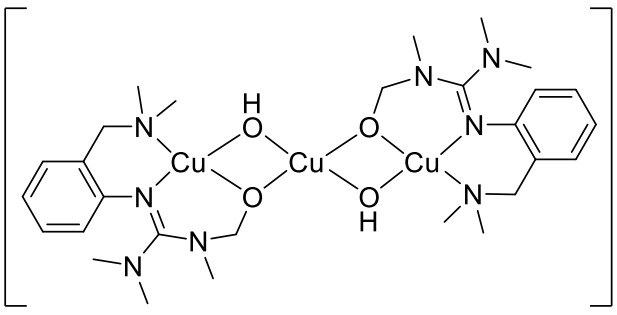

$C_{36}H_{64}Cu_3F_{12}N_8O_6P_2$
1185.53 g mol^{-1}

The title compound was isolated as blue crystalline blocks (19 mg, 18.2 μmol, 30% referred to the amount of the Cu(I) complex). **HRMS-ESI+** (MeCN): m/z calc. for [$C_{28}H_{48}O_4N_8Cu_3$]$^{2+}$: 375.5830, found: 375.5831, m/z calc. for [($C_{28}H_{48}N_8Cu_3O_4$)(PF_6)]$^+$: 896.1479, found: 896.1319. **IR** (ATR): $\tilde{\nu}$ [cm^{-1}] = 2957 (vw, C–H$_{arom}$), 2923 (vw, C–H$_{arom}$), 2862 (vw, C–H$_{aliph}$), 1554 (w, C=N), 1514 (w), 1489 (w), 1457 (w), 1423 (w), 1399 (w), 1381 (m), 1344 (vw), 1277 (vw), 1231 (vw), 1183 (w), 1077 (m), 1038 (m), 983 (w), 908 (vw), 873 (vw), 830 (vs, PF_6), 760 (m, PF_6), 708 (m), 556 (s, PF_6), 504 (w), 462 (w, PF_6).

$[Cu_3(\mu\text{-}OL1)_2(\mu\text{-}OH)_2](BF_4)_2 \cdot 2$ thf ($[H1](BF_4)_2$)

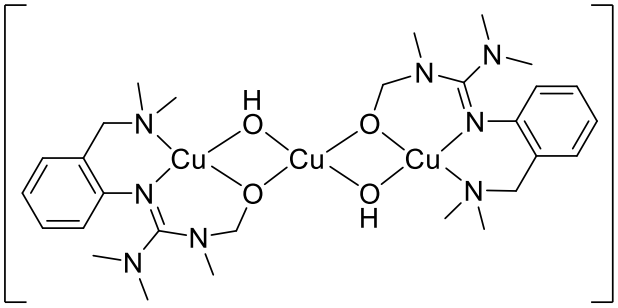

$C_{36}H_{64}B_2Cu_3F_8N_8O_6$
1069.20 g mol^{-1}

The title compound was isolated as blue crystalline blocks (16 mg, 17.3 µmol, 29% referred to the amount of the Cu(I) complex). **HRMS-ESI+** (MeCN): m/z calc. for $[C_{28}H_{48}N_8Cu_3O_4]^{2+}$: 375.5834, found: 375.5857, m/z calc. for $[(C_{28}H_{48}N_8Cu_3O_4)(BF_4)]^{+}$: 838.1693, found: 838.1694. **IR** (ATR): $\tilde{\nu}$ [cm^{-1}] = 2960 (vw, C–H_{arom}), 2927 (w, C–H_{aliph}), 2858 (vw, C–H_{aliph}), 1763 (m), 1654 (m), 1648 (m), 1637 (m), 1624 (m), 1594 (m, C=N), 1555 (m, C=N), 1490 (w), 1473 (w), 1458 (w), 1453 (w), 1424 (w), 1405 (w), 1378 (w), 1170 (m), 1056 (s, BF_4), 1033 (vs, BF_4), 989 (m), 930 (w), 870 (w), 839 (vw), 797 (w), 762 (m, BF_4).

$[Cu_2(L2)_2(\mu\text{-}OH)_2](OTf)_2 \cdot 4$ benzene ($[H2](OTf)_2$)

For the generation of the bis(µ-hydroxido) dicopper(II) species [**H2**]$(OTf)_2$, the bis(µ-oxido) complex [**O2**]$(OTf)_2$ (1.0 eq) was synthesized first at –80 °C by the oxygenation of equimolar amounts of **L2** (24.6 mg, 0.1 mmol, 2.0 eq) and $[Cu(MeCN)_4]OTf$ (37.8 mg, 0.1 mmol, 2.0 eq) in tetrahydrofuran/acetonitrile (9.5 mL/0.5 mL) according to the protocol described above. Then, the solution was warmed up to room temperature and evaporated to dryness. The dark green residue was dissolved in benzene and filtered afterwards under ambient conditions. Single crystals of [**H2**]$(OTf)_2$, suitable for X-ray diffraction, were grown after a few hours by slow diffusion of diethyl ether into the benzene solution.

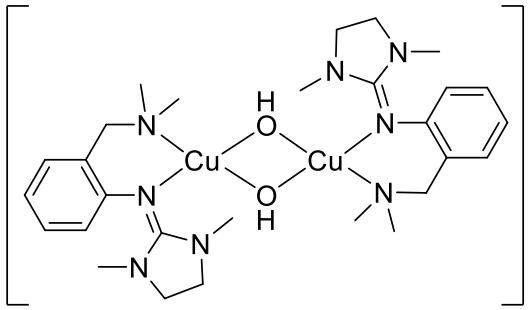

$C_{56}H_{70}Cu_2F_6N_8O_8S_2$
1264.41 g mol^{-1}

The title compound was isolated as green crystalline needles and used for X-ray diffraction analysis. No further analysis is available due to the low amount of the sample.

5.3.10. Catalytic Oxygenation Reactions of Aromatic Alcohols

The catalytic oxygenation reactions of aromatic alcohols were performed in two different scales: in small scale for UV/Vis measurements within the Lambert-Beer law (which provide a first indication of the conversion of the substrate) as well as for cryo-UHR-ESI measurements (which provide insights into the crude oxygenation reaction solution and its catalysis products), and in larger scale to enable the isolation of a possible phenazine for qualitative analyses.

General protocol of the catalytic oxygenation reaction:

The used bis(μ-oxido) species (0.5 mM, 0.005 mmol, 1 eq) was synthesized in a tetrahydrofuran/acetonitrile mixture (9.5 mL/0.5 mL) according to the protocol described above. The substrate solutions were prepared by dissolving the respective substrate (0.125 mmol, 25 eq) in the dried solvent according to Table 35 and adding triethylamine (35 μL, 0.250 mmol, 50 eq) to the solution. The solution was injected in one portion into the reaction mixture and stirred at the respective temperature for the respective duration. 1,2-Phenylenediamine solution (27.0 mg, 0.250 mmol, 50 eq) was prepared by dissolving it in dried tetrahydrofuran (0.2 mL) and then added to the reaction mixture. The reaction mixture was stirred overnight at room temperature.

For cryo-UHR-ESI measurements:

The substrate solution was injected into the solution of the bis(μ-oxido) species and a first mass spectrum was measured immediately. After several scavenging processes, a second mass spectrum was monitored after approximately five minutes.

For the upscaled reaction:

Flame-dried molecular sieve (400 mg, 3 Å) was placed in a flask prior to the reaction. The oxygenation reaction was performed according to the general protocol described above upscaled by a factor of ten. For the work-up of the reaction solution, hydrochloric acid (0.5 M, 50 mL) and EDTA (one spatula) were added. The organic solvents were removed under reduced pressure. The aqueous phase was extracted with methylene chloride (4 x 100 mL). The combined organic layers were dried over sodium sulfate and evaporated to dryness. The crude product was purified via column chromatography on Geduran Si 60 and/or by sublimation.

Table 35: Substrate solutions (0.125 mmol) used for the oxygenations of aromatic alcohols in small scale. For the upscaled reaction, the amount of the substrate and the volume of the solvent were adjusted by a factor of ten.

substrate	solvent	volume [mL]
1-methyl 2-naphthol	tetrahydrofuran	0.1
1-naphthol	tetrahydrofuran	0.2
2-methyl 8-quinolinol	tetrahydrofuran	0.1
2-naphthol	tetrahydrofuran	0.2
2,4-di-*tert*-butyl phenol	tetrahydrofuran	0.1
3-pyridinol	methanol	0.1
3-quinolinol	methanol	1.0
4-indolol	tetrahydrofuran	0.2
4-methoxy phenol	tetrahydrofuran	0.1
4-pyridinol	methanol	0.1
4-quinolinol	methanol	0.3
4-*tert*-butyl phenol	tetrahydrofuran	0.1
5-indolol	tetrahydrofuran	0.2
6-indolol	tetrahydrofuran	0.4
6-quinolinol	methanol	0.8
7-indolol	tetrahydrofuran	0.5
8-quinolinol	tetrahydrofuran	0.1
phenol	tetrahydrofuran	0.1

5.3.10.1. Synthesis of Benzo[a]phenazine (P1)

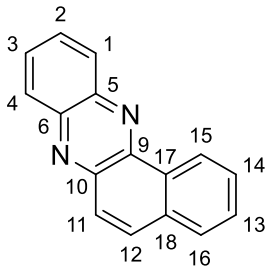

$C_{16}H_{10}N_2$
230.27 g mol^{-1}

Yellow solid. $\mathbf{R_f}$ = 0.44 (ethyl acetate/hexane 5:95). **^{1}H NMR** (400 MHz, DMSO-d_6, 25 °C): δ [ppm] = 9.29 – 9.23 (m, 1H, H15), 8.38 – 8.31 (m, 1H, H1), 8.30 – 8.25 (m, 1H, H4), 8.20 (d, J = 9.3 Hz, 1H, H11), 8.11 – 8.06 (m, 1H, H16), 8.02 – 7.93 (m, 3H, H2+H3+H12), 7.90 – 7.82 (m, 2H, H13+H14). **^{13}C{^{1}H} NMR** (101 MHz, DMSO-d_6, 25 °C): δ [ppm] = 143.1 (C10), 142.2 (C9), 141.7 (C6), 141.1 (C5), 133.4 (C11), 132.9 (C17), 130.5 (C2), 130.5 (C3), 130.2 (C18), 130.1 (C13), 129.2 (C1), 128.9 (C4), 128.5 (C16), 128.1 (C14), 126.8 (C12), 124.6 (C15). **HRMS-EI**: m/z calc. for $C_{16}H_{10}N_2$: 230.0838, found: 230.0837. **IR** (ATR): $\tilde{\nu}$ [cm^{-1}] = 2960 (w), 2923 (m), 2851 (w), 1735 (w), 1536 (w), 1494 (w), 1472 (w), 1355 (m), 1260 (m), 1220 (vw), 1198 (vw), 1136 (w), 1118 (w), 1101 (m), 1010 (m), 974 (w), 959 (m), 909 (w), 877 (m), 836 (m), 806 (m),

795 (m), 776 (m), 764 (m), 759 (vs), 753 (vs), 697 (m), 650 (m), 607 (m), 570 (m), 551 (vs), 536 (m), 503 (m), 485 (w), 404 (s). Analytical data matches those reported in literature.[190] Additional information on the NMR spectra of the target compound including original data files is available via Chemotion Repository: https://dx.doi.org/10.14272/SEXRCKWGFSXUOO-UHFFFAOYSA-N.1

Table 36: Obtained isolated yield of **P1** in dependence of the used catalyst (based on 1.25 mmol of the substrate).

Used catalyst	m [mg]	n [mmol]	Y [%]
[**O1**](PF$_6$)$_2$	89	0.387	31
[**O1I**](CuI$_2$)	121	0.525	42
[**O3**](PF$_6$)$_2$	81	0.350	28
[**O4**](PF$_6$)$_2$	66	0.287	23

5.3.10.2. Synthesis of Quinolino[3,4-b]quinoxaline (P2)

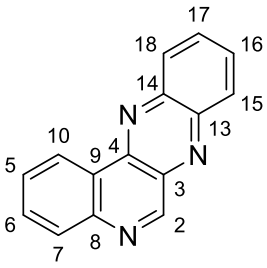

$C_{15}H_9N_3$
231.26 g mol^{-1}

Yellow solid. **R$_f$** = 0.50 (ethyl acetate/hexane 20:80). **^{1}H NMR** (400 MHz, DMSO-*d*$_6$; 25 °C): *δ* [ppm] = 9.60 (s, 1H, H2), 9.16 (ddd, *J* = 8.0, 1.6, 0.6 Hz, 1H, H10), 8.44 – 8.40 (m, 2H, H15+H18), 8.26 – 8.19 (m, 1H, H7), 8.17 – 8.06 (m, 2H, H16+H17), 8.01 (ddd, *J* = 8.1, 7.2, 1.6 Hz, 1H, H6), 7.94 – 7.89 (m, 1H, H5). **^{13}C{^{1}H} NMR** (101 MHz, DMSO-*d*$_6$, 25 °C): *δ* [ppm] = 155.5 (C2), 145.0 (C8), 143.8 (C13), 142.9 (C14), 142.2 (C4), 136.6 (C3), 133.0 (C17), 131.7 (C6), 131.5 (C16), 129.9 (C18), 129.7 (C7), 129.3 (C15), 128.6 (C5), 124.0 (C10), 123.9 (C9). **HRMS-EI**: m/z calc. for $C_{15}H_9N_3$: 231.0791, found: 231.0795. **IR** (ATR): $\tilde{\nu}$ [cm^{-1}] = 2963 (w), 2921 (w), 2852 (vw), 1585 (w), 1534 (w), 1487 (w), 1464 (w), 1363 (w), 1258 (m), 1085 (m), 1011 (vs), 921(w), 881 (m), 794 (s), 777 (s), 769 (s), 704 (m), 649 (m), 611 (m), 592 (w), 571 (m), 550 (m), 511 (w), 410 (s). Additional information on the NMR spectra of the target compound including original data files is available via Chemotion Repository: https://dx.doi.org/10.14272/JJGCDLVZJZGHBZ-UHFFFAOYSA-N.1

Table 37: Obtained isolated yield of **P2** in dependence of the used catalyst (based on 1.25 mmol of the substrate).

Used catalyst	m [mg]	n [mmol]	Y [%]
[**O1**](PF$_6$)$_2$	92	0.398	32
[**O1I**](CuI$_2$)	162	0.700	56

5.3.10.3. Synthesis of Pyrido[3,2-a]phenazine (P3)

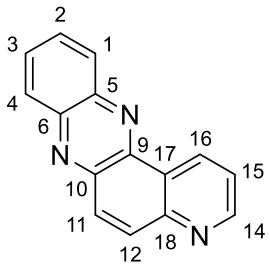

$C_{15}H_9N_3$
231.26 g mol^{-1}

Orange solid. Single crystals of **P3**, suitable for X-ray diffraction, were grown from a concentrated DMSO solution. $\mathbf{R_f}$ = 0.26 (ethyl acetate/hexane 20:80). **^{1}H NMR** (400 MHz, DMSO-d_6, 25 °C): δ [ppm] = 9.51 (dd, J = 8.2, 1.7 Hz, 1H, H14), 9.12 (dd, J = 4.5, 1.7 Hz, 1H, H16), 8.39 – 8.29 (m, 2H, H1+H4), 8.23 (s, 2H, H11+H12), 8.05 – 8.00 (m, 2H, H2+H3), 7.86 (dd, J = 8.2, 4.5 Hz, 1H, H15). **^{13}C{^{1}H} NMR** (101 MHz, DMSO-d_6, 25 °C): δ [ppm] = 152.3 (C16), 149.3 (C18), 142.5 (C9), 142.5 (C10), 141.3 (C6), 140.9 (C5), 134.2 (C12), 132.5 (C14), 131.2 (C2), 131.1 (C3), 130.8 (C11), 129.3 (C1), 129.2 (C4), 126.0 (C17), 123.1 (C15). **HRMS-EI**: m/z calc. for $C_{15}H_9N_3$: 231.0791, found: 231.0792. **IR** (ATR): $\tilde{\nu}$ [cm^{-1}] = 2962 (w), 1585 (w), 1484 (w), 1434 (w), 1355 (w), 1258 (m), 1086 (m), 1006 (vs), 848 (m), 792 (vs), 774 (s), 760 (s), 650 (w), 610 (w), 574 (w), 553 (w), 502 (w), 486 (w), 476 (w), 423 (w). Additional information on the NMR spectra of the target compound including original data files is available via Chemotion Repository: https://dx.doi.org/10.14272/ODJOHIWKLOPSFF-UHFFFAOYSA-N.1

Table 38: Obtained isolated yield of **P3** in dependence of the used catalyst (based on 1.25 mmol of the substrate).

Used catalyst	m [mg]	n [mmol]	Y [%]
[**O1**](PF_6)$_2$	87	0.376	30
[**O1I**](CuI_2)	177	0.765	61
[**O3**](PF_6)$_2$	89	0.387	31
[**O4**](PF_6)$_2$	81	0.350	28

5.3.10.4. Synthesis of Pyrrolo[3,2-a]phenazine (P4)

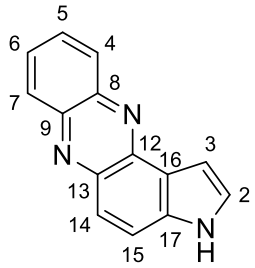

$C_{14}H_9N_3$
219.25 g mol^{-1}

Yellow solid. $\mathbf{R_f}$ = 0.64 (ethyl acetate/hexane 75:25). **^{1}H NMR** (400 MHz, DMSO-d_6, 25 °C): δ [ppm] = 12.08 (s, 1H, NH), 8.30 – 8.22 (m, 2H, H4+H7), 8.06 (dd, J = 9.2, 0.9 Hz, 1H, H14), 7.93 – 7.84 (m, 2H, H5+H6), 7.79 (dd, J = 9.2, 0.4 Hz, 1H, H15), 7.58 – 7.55 (m, 1H, H2), 7.34 (ddd, J = 3.0, 2.1, 0.9 Hz, 1H, H3). **^{13}C{^{1}H} NMR** (101 MHz, DMSO-d_6, 25 °C): δ [ppm] = 141.8 (C12), 141.3 (C8), 140.7 (C9), 140.0 (C13), 133.8 (C17), 129.8 (C6), 129.2 (C4), 128.6 (C5), 128.6 (C7), 124.4 (C2), 122.2 (C15), 121.4 (C16), 121.4 (C14), 103.9 (C3). **HRMS-ESI+** (MeOH): m/z (%) calc. for [($C_{14}H_9N_3$)+H]$^+$: 220.07965, found: 220.08656. **IR** (ATR): $\tilde{\nu}$ [cm^{-1}] = 3170 (w), 3133 (w), 3113 (w), 3093 (w), 3056 (w), 3002 (w), 2914 (vw), 2840 (vw), 1586 (m), 1541 (m), 1436 (m), 1353 (m), 1339 (m), 1136 (m), 1022 (m), 999 (vs), 893 (m), 828 (m), 729 (vs), 671 (w), 615 (w), 589 (s), 529 (s), 517 (m), 473 (m), 420 (s). Additional information on the NMR spectra

of the target compound including original data files is available via Chemotion Repository: https://dx.doi.org/10.14272/AEFJLSGXOWZNJZ-UHFFFAOYSA-N.1

Table 39: Obtained isolated yield of **P4** in dependence of the used catalyst (based on 1.25 mmol of the substrate).

Used catalyst	m [mg]	n [mmol]	Y [%]
[**O1**]$(PF_6)_2$	71	0.323	26
[**O1I**](CuI_2)	112	0.511	41

5.3.10.5. Synthesis of Pyrrolo[2,3-a]phenazine (P5)

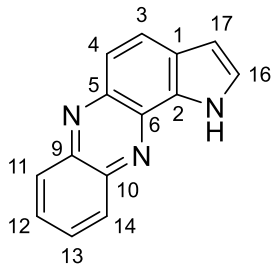

$C_{14}H_9N_3$
219.25 g mol^{-1}

Yellow solid. Single crystals of **P5**, suitable for X-ray diffraction, were grown from a concentrated hexane solution. $\mathbf{R_f}$ = 0.46 (ethyl acetate/hexane 50:50). **^{1}H NMR** (400 MHz, DMSO-d_6, 25 °C): δ [ppm] = 12.88 (s, 1H, NH), 8.30 – 8.23 (m, 2H, H11+H14), 8.13 (d, J = 9.1 Hz, 1H, H4), 7.91 (m, 2H, H12+H13), 7.70 (d, J = 9.0 Hz, 1H, H3), 7.57 (t, J = 2.7 Hz, 1H, H16), 6.80 – 6.77 (m, 1H, H17). **^{13}C{^{1}H} NMR** (101 MHz, DMSO-d_6, 25 °C): δ [ppm] = 142.2 (C6), 140.9 (C10), 140.8 (C9), 134.8 (C2), 130.0 (C13), 129.3 (C11), 128.7 (C12), 128.2 (C14), 128.1 (C5), 128.0 (C4), 126.1 (C16), 126.0 (C1), 120.5 (C3), 104.9 (C17). **HRMS-EI**: m/z calc. for $C_{14}H_9N_3$: 219.0791, found: 219.0799. **IR** (ATR): $\tilde{\nu}$ [cm^{-1}] = 2962 (w), 2923 (w), 2854 (vw), 1400 (w), 1359 (w), 1259 (m), 1086 (m), 1011 (s), 896 (w), 866 (m), 790 (vs), 751 (m), 717 (m), 661 (m), 621 (w), 592 (w), 556 (w), 527 (m), 470 (m), 400 (m). Additional information on the NMR spectra of the target compound including original data files is available via Chemotion Repository: https://dx.doi.org/10.14272/BMNLXKVRGRRHKW-UHFFFAOYSA-N.1

Table 40: Obtained isolated yield of **P5** in dependence of the used catalyst (based on 1.25 mmol of the substrate).

Used catalyst	m [mg]	n [mmol]	Y [%]
[**O1**]$(PF_6)_2$	85	0.387	31
[**O1I**](CuI_2)	159	0.725	58

6. References

[1] W. M. Fitch, *J. Mol. Evol.* **1976**, *8*, 13–40.

[2] T.-P. Chou, W. H. Adolph, *Biochem. J.* **1935**, *29*, 476–479.

[3] J. R. Turnlund, *Am. J. Clin. Nutr.* **1998**, *67*, 960–964.

[4] T. R. Halfdanarson, N. Kumar, C.-Y. Li, R. L. Phyliky, W. J. Hogan, *Eur. J. Haematol.* **2008**, *80*, 523–531.

[5] L. M. Gaetke, C. K. Chow, *Toxicology* **2003**, *189*, 147–163.

[6] J. D. Gitlin, *Gastroenterology* **2003**, *125*, 1868–1877.

[7] B. R. Stern, M. Solioz, D. Krewski, P. Aggett, T. Aw, S. Baker, K. Crump, M. Dourson, L. Haber, R. Hertzberg, C. Keen, B. Meek, L. Rudenko, R. Schoeny, W. Slob, T. Starr, *J. Toxicol. Environ. Heal. Part B* **2007**, *10*, 157–222.

[8] R. R. Conry, *Encycl. Inorg. Chem.*, John Wiley & Sons, Ltd, Chichester, UK, **2006**.

[9] E. A. Lewis, W. B. Tolman, *Chem. Rev.* **2004**, *104*, 1047–1076.

[10] L. M. Mirica, X. Ottenwaelder, T. D. P. Stack, *Chem. Rev.* **2004**, *104*, 1013–1046.

[11] C. E. Elwell, N. L. Gagnon, B. D. Neisen, D. Dhar, A. D. Spaeth, G. M. Yee, W. B. Tolman, *Chem. Rev.* **2017**, *117*, 2059–2107.

[12] I. A. Koval, P. Gamez, C. Belle, K. Selmeczi, J. Reedijk, *Chem. Soc. Rev.* **2006**, *35*, 814–840.

[13] W. Kaim, J. Rall, *Angew. Chem. Int. Ed.* **1996**, *35*, 43–60.

[14] E. I. Solomon, U. M. Sundaram, T. E. Machonkin, *Chem. Rev.* **1996**, *96*, 2563–2606.

[15] Y. Xue, M. Ökvist, Ö. Hansson, S. Young, *Protein Sci.* **1998**, *7*, 2099–2105.

[16] G. E. Norris, B. F. Anderson, E. N. Baker, *J. Am. Chem. Soc.* **1986**, *108*, 2784–2785.

[17] A. C. Rosenzweig, *Nat. Chem.* **2009**, *1*, 684–685.

[18] J. P. Klinman, *Chem. Rev.* **1996**, *96*, 2541–2562.

[19] F. Wendt, M. Rolff, W. Thimm, C. Näther, F. Tuczek, *Z. Anorg. Allg. Chem.* **2013**, *639*, 2502–2509.

[20] J. V. Bannister, W. H. Bannister, G. Rotilio, *Crit. Rev. Biochem.* **1987**, *22*, 111–180.

[21] L. Ciano, G. J. Davies, W. B. Tolman, P. H. Walton, *Nat. Catal.* **2018**, *1*, 571–577.

[22] E. I. Solomon, D. E. Heppner, E. M. Johnston, J. W. Ginsbach, J. Cirera, M. Qayyum, M. T. Kieber-Emmons, C. H. Kjaergaard, R. G. Hadt, L. Tian, *Chem. Rev.* **2014**, *114*, 3659–3853.

[23] Decker, Dillinger, Tuczek, *Angew. Chem. Int. Ed.* **2000**, *39*, 1591–1595.

[24] A. Volbeda, W. G. J. Hol, *J. Mol. Biol.* **1989**, *209*, 249–279.

[25] T. Klabunde, C. Eicken, J. C. Sacchettini, B. Krebs, *Nat. Struct. Biol.* **1998**, *5*, 1084–1090.

[26] A. Bijelic, M. Pretzler, C. Molitor, F. Zekiri, A. Rompel, *Angew. Chem. Int. Ed.* **2015**, *54*, 14677–14680.

[27] X. Lai, H. J. Wichers, M. Soler-Lopez, B. W. Dijkstra, *Chem. Eur. J.* **2018**, *24*, 47–55.

[28] H. S. Mason, W. L. Fowlks, E. Peterson, *J. Am. Chem. Soc.* **1955**, *77*, 2914–2915.

[29] J. N. Rodríguez-López, J. Tudela, R. Varón, F. García-Carmona, F. García-Cánovas, *J. Biol. Chem.* **1992**, *267*, 3801–10.

[30] K. Grønskov, J. Ek, K. Brondum-Nielsen, *Orphanet J. Rare Dis.* **2007**, *2*, 43.

[31] Y.-J. Kim, H. Uyama, *Cell. Mol. Life Sci.* **2005**, *62*, 1707–1723.

[32] D. A. Robb, L. W. Mapson, T. Swain, *Nature* **1964**, *201*, 503–504.

[33] G. M. Sapers, F. W. Douglas, *J. Food Sci.* **1987**, *52*, 1258–1285.

[34] Y. Matoba, T. Kumagai, A. Yamamoto, H. Yoshitsu, M. Sugiyama, *J. Biol. Chem.* **2006**, *281*, 8981–8990.

[35] M. Rolff, J. Schottenheim, H. Decker, F. Tuczek, *Chem. Soc. Rev.* **2011**, *40*, 4077–4098.

[36] C. J. Cramer, B. A. Smith, W. B. Tolman, *J. Am. Chem. Soc.* **1996**, *118*, 11283–11287.

[37] J. Cahoy, P. L. Holland, W. B. Tolman, *Inorg. Chem.* **1999**, *38*, 2161–2168.

[38] V. Mahadevan, M. J. Henson, E. I. Solomon, T. D. P. Stack, *J. Am. Chem. Soc.* **2000**, *122*, 10249–10250.

[39] H.-C. Liang, M. J. Henson, L. Q. Hatcher, M. A. Vance, C. X. Zhang, D. Lahti, S. Kaderli, R. D. Sommer, A. L. Rheingold, A. D. Zuberbühler, E. I. Solomon, K. D. Karlin, *Inorg. Chem.* **2004**, *43*, 4115–4117.

[40] L. M. Mirica, M. Vance, D. J. Rudd, B. Hedman, K. O. Hodgson, E. I. Solomon, T. D. P. Stack, *Science* **2005**, *308*, 1890–1892.

[41] S. Itoh, S. Fukuzumi, *Acc. Chem. Res.* **2007**, *40*, 592–600.

[42] B. T. Op't Holt, M. A. Vance, L. M. Mirica, D. E. Heppner, T. D. P. Stack, E. I. Solomon, *J. Am. Chem. Soc.* **2009**, *131*, 6421–6438.

[43] H. Decker, T. Schweikardt, F. Tuczek, *Angew. Chem. Int. Ed.* **2006**, *45*, 4546–4550.

[44] A. Spada, S. Palavicini, E. Monzani, L. Bubacco, L. Casella, *Dalton Trans.* **2009**, 6468–6471.

[45] S. Itoh, H. Kumei, M. Taki, S. Nagatomo, T. Kitagawa, S. Fukuzumi, *J. Am. Chem. Soc.* **2001**, *123*, 6708–6709.

[46] A. Company, S. Palavicini, I. Garcia-Bosch, R. Mas-Ballesté, L. Que, E. V. Rybak-Akimova, L. Casella, X. Ribas, M. Costas, *Chem. Eur. J.* **2008**, *14*, 3535–3538.

[47] S. Herres-Pawlis, P. Verma, R. Haase, P. Kang, C. T. Lyons, E. C. Wasinger, U. Flörke, G. Henkel, T. D. P. Stack, *J. Am. Chem. Soc.* **2009**, *131*, 1154–1169.

[48] I. Kampatsikas, M. Pretzler, A. Rompel, *Angew. Chem. Int. Ed.* **2020**, *59*, 20940–20945.

[49] I. Kampatsikas, A. Rompel, *ChemBioChem* **2021**, *22*, 1161–1175.

[50] Y. Liang, J. Wei, X. Qiu, N. Jiao, *Chem. Rev.* **2018**, *118*, 4912–4945.

[51] T. Dalton, T. Faber, F. Glorius, *ACS Cent. Sci.* **2021**, *7*, 245–261.

[52] R. Trammell, K. Rajabimoghadam, I. Garcia-Bosch, *Chem. Rev.* **2019**, *119*, 2954–3031.

[53] T. D. P. Stack, *Dalton Trans.* **2003**, 1881–1889.

[54] T. Abe, Y. Shiota, S. Itoh, K. Yoshizawa, *Dalton Trans.* **2020**, *49*, 6710–6717.

[55] J. A. Halfen, S. Mahapatra, E. C. Wilkinson, S. Kaderli, V. G. Young, L. Que, A. D. Zuberbuhler, W. B. Tolman, *Science* **1996**, *271*, 1397–1400.

[56] L. Chiang, W. Keown, C. Citek, E. C. Wasinger, T. D. P. Stack, *Angew. Chem. Int. Ed.* **2016**, *55*, 10453–10457.

[57] E. I. Solomon, P. Chen, M. Metz, S.-K. Lee, A. E. Palmer, *Angew. Chem. Int. Ed.* **2001**, *40*, 4570–4590.

[58] S. E. N. Brazeau, L. H. Doerrer, *Dalton Trans.* **2019**, *48*, 4759–4768.

[59] J. K. Elinburg, L. H. Doerrer, *Polyhedron* **2020**, *190*, 114765.

[60] S. E. N. Brazeau, E. E. Norwine, S. F. Hannigan, N. Orth, I. Ivanović-Burmazović, D. Rukser, F. Biebl, B. Grimm-Lebsanft, G. Praedel, M. Teubner, M. Rübhausen, P. Liebhäuser, T. Rösener, J. Stanek, A. Hoffmann, S. Herres-Pawlis, L. H. Doerrer, *Dalton Trans.* **2019**, *48*, 6899–6909.

[61] K. D. Karlin, J. C. Hayes, Y. Gultneh, R. W. Cruse, J. W. McKown, J. P. Hutchinson, J. Zubieta, *J. Am. Chem. Soc.* **1984**, *106*, 2121–2128.

[62] N. Kitajima, K. Fujisawa, Y. Morooka, K. Toriumi, *J. Am. Chem. Soc.* **1989**, *111*, 8975–8976.

[63] G. J. Karahalis, A. Thangavel, B. Chica, J. Bacsa, R. B. Dyer, C. C. Scarborough, *Inorg. Chem.* **2016**, *55*, 1102–1107.

[64] S. Herres-Pawlis, S. Binder, A. Eich, R. Haase, B. Schulz, G. Wellenreuther, G. Henkel, M. Rübhausen, W. Meyer-Klaucke, *Chem. Eur. J.* **2009**, *15*, 8678–8682.

[65] T. A. G. Large, V. Mahadevan, W. Keown, T. D. P. Stack, *Inorg. Chim. Acta* **2019**, *486*, 782–792.

[66] A. P. Cole, V. Mahadevan, L. M. Mirica, X. Ottenwaelder, T. D. P. Stack, *Inorg. Chem.* **2005**, *44*, 7345–7364.

[67] C. Citek, B.-L. Lin, T. E. Phelps, E. C. Wasinger, T. D. P. Stack, *J. Am. Chem. Soc.* **2014**, *136*, 14405–14408.

[68] C. Citek, J. B. Gary, E. C. Wasinger, T. D. P. Stack, *J. Am. Chem. Soc.* **2015**, *137*, 6991–6994.

[69] W. Keown, T. A. G. Large, L. Chiang, E. C. Wasinger, T. D. P. Stack, *Chem. Commun.* **2019**, *55*, 7390–7393.

[70] C. Citek, S. Herres-Pawlis, T. D. P. Stack, *Acc. Chem. Res.* **2015**, *48*, 2424–2433.

[71] B. E. R. Snyder, M. L. Bols, R. A. Schoonheydt, B. F. Sels, E. I. Solomon, *Chem. Rev.* **2018**, *118*, 2718–2768.

[72] D. Magdziak, A. A. Rodriguez, R. W. Van De Water, T. R. R. Pettus, *Org. Lett.* **2002**, *4*,

285–288.

[73] E. J. Land, C. A. Ramsden, P. A. Riley, *Acc. Chem. Res.* **2003**, *36*, 300–308.

[74] K. V. N. Esguerra, Y. Fall, J. P. Lumb, *Angew. Chem. Int. Ed.* **2014**, *53*, 5877–5881.

[75] M. S. Askari, L. A. Rodríguez-Solano, A. Proppe, B. McAllister, J.-P. Lumb, X. Ottenwaelder, *Dalton Trans.* **2015**, *44*, 12094–12097.

[76] M. S. Askari, K. V. N. Esguerra, J.-P. Lumb, X. Ottenwaelder, *Inorg. Chem.* **2015**, *54*, 8665–8672.

[77] B. Herzigkeit, B. M. Flöser, T. A. Engesser, C. Näther, F. Tuczek, *Eur. J. Inorg. Chem.* **2018**, 3058–3069.

[78] B. Cross, C. L. Dunn, D. H. Payne, J. D. Tipton, *J. Sci. Food Agric.* **1969**, *20*, 340–344.

[79] N. Guttenberger, W. Blankenfeldt, R. Breinbauer, *Bioorg. Med. Chem.* **2017**, *25*, 6149–6166.

[80] A. V. Gulevskaya, *Eur. J. Org. Chem.* **2016**, 4207–4214.

[81] F. B. Mortzfeld, J. Pietruszka, I. R. Baxendale, *Eur. J. Org. Chem.* **2019**, 5424–5433.

[82] J. N. Hamann, M. Rolff, F. Tuczek, *Dalton Trans.* **2015**, *44*, 3251–3258.

[83] A. Chaudhary, J. M. Khurana, *Res. Chem. Intermed.* **2018**, *44*, 1045–1083.

[84] Y. Xiao, W. Hu, S. Sun, J.-T. Yu, J. Cheng, *Synlett* **2019**, *30*, 2113–2122.

[85] V. F. de Andrade-Neto, M. O. F. Goulart, J. F. da Silva Filho, M. J. da Silva, M. do Carmo F. R. Pinto, A. V Pinto, M. G. Zalis, L. H. Carvalho, A. U. Krettli, *Bioorg. Med. Chem. Lett.* **2004**, *14*, 1145–1149.

[86] A. Cimmino, A. Evidente, V. Mathieu, A. Andolfi, F. Lefranc, A. Kornienko, R. Kiss, *Nat. Prod. Rep.* **2012**, *29*, 487–501.

[87] S. Banerjee, *Arkivoc* **2016**, 82–110.

[88] A. K. Jana, *J. Photochem. Photobiol. A Chem.* **2000**, *132*, 1–17.

[89] M. Bilal, S. Guo, H. M. N. Iqbal, H. Hu, W. Wang, X. Zhang, *World J. Microbiol. Biotechnol.* **2017**, *33*, 191.

[90] P. Liebhäuser, A. Hoffmann, S. Herres-Pawlis, *Ref. Modul. Chem. Mol. Sci. Chem. Eng.* **2019**, 1–22.

[91] J. N. Hamann, B. Herzigkeit, R. Jurgeleit, F. Tuczek, *Coord. Chem. Rev.* **2017**, *334*, 54–66.

[92] M. Réglier, C. Jorand, B. Waegell, *J. Chem. Soc., Chem. Commun.* **1990**, 1752–1755.

[93] L. Casella, M. Gullotti, R. Radaelli, P. Di Gennaro, *J. Chem. Soc., Chem. Commun.* **1991**, 1611–1612.

[94] M. Rolff, J. Schottenheim, G. Peters, F. Tuczek, *Angew. Chem. Int. Ed.* **2010**, *49*, 6438–6442.

[95] A. Hoffmann, C. Citek, S. Binder, A. Goos, M. Rübhausen, O. Troeppner, I. Ivanović-Burmazović, E. C. Wasinger, T. D. P. Stack, S. Herres-Pawlis, *Angew. Chem. Int. Ed.*

2013, *52*, 5398–5401.

[96] Z. Huang, O. Kwon, H. Huang, A. Fadli, X. Marat, M. Moreau, J. P. Lumb, *Angew. Chem. Int. Ed.* **2018**, *57*, 11963–11967.

[97] C. Wilfer, P. Liebhäuser, A. Hoffmann, H. Erdmann, O. Grossmann, L. Runtsch, E. Paffenholz, R. Schepper, R. Dick, M. Bauer, M. Dürr, I. Ivanovic-Burmazovic, S. Herres-Pawlis, *Chem. Eur. J.* **2015**, *21*, 17639–17649.

[98] C. Wilfer, P. Liebhäuser, H. Erdmann, A. Hoffmann, S. Herres-Pawlis, *Eur. J. Inorg. Chem.* **2015**, 494–502.

[99] F. Strassl, A. Hoffmann, B. Grimm-Lebsanft, D. Rukser, F. Biebl, M. Tran, F. Metz, M. Rübhausen, S. Herres-Pawlis, *Inorganics* **2018**, *6*, 114–136.

[100] J. Schottenheim, N. Fateeva, W. Thimm, J. Krahmer, F. Tuczek, *Z. Anorg. Allg. Chem.* **2013**, *639*, 1491–1497.

[101] J. N. Hamann, F. Tuczek, *Chem. Commun.* **2014**, *50*, 2298–2300.

[102] J. N. Hamann, R. Schneider, F. Tuczek, *J. Coord. Chem.* **2015**, *68*, 3259–3271.

[103] F. Wendt, C. Näther, F. Tuczek, *J. Biol. Inorg. Chem.* **2016**, *21*, 777–792.

[104] B. Herzigkeit, B. M. Flöser, N. E. Meißner, T. A. Engesser, F. Tuczek, *ChemCatChem* **2018**, *10*, 5402–5405.

[105] B. Herzigkeit, R. Jurgeleit, B. M. Flöser, N. E. Meißner, T. A. Engesser, C. Näther, F. Tuczek, *Eur. J. Inorg. Chem.* **2019**, 2258–2266.

[106] P. Liebhäuser, K. Keisers, A. Hoffmann, T. Schnappinger, I. Sommer, A. Thoma, C. Wilfer, R. Schoch, K. Stührenberg, M. Bauer, M. Dürr, I. Ivanović-Burmazović, S. Herres-Pawlis, *Chem. Eur. J.* **2017**, *23*, 12171–12183.

[107] J. Stanek, T. Rösener, A. Metz, J. Mannsperger, A. Hoffmann, S. Herres-Pawlis, *Top. Heterocycl. Chem.*, **2015**, 95–164.

[108] T. Rösener, K. Kröckert, A. Hoffmann, S. Herres-Pawlis, *Z. Anorg. Allg. Chem.* **2018**, *644*, 1317–1328.

[109] T. Rösener, A. Hoffmann, S. Herres-Pawlis, *Eur. J. Inorg. Chem.* **2018**, 3164–3175.

[110] T. Rösener, O. Bienemann, K. Sigl, N. Schopp, F. Schnitter, U. Flörke, A. Hoffmann, A. Döring, D. Kuckling, S. Herres-Pawlis, *Chem. Eur. J.* **2016**, *22*, 13550–13562.

[111] A. Hoffmann, O. Bienemann, I. Vieira, S. Herres-Pawlis, *Polymers* **2014**, *6*, 995–1007.

[112] P. M. Schäfer, M. Fuchs, A. Ohligschläger, R. Rittinghaus, P. McKeown, E. Akin, M. Schmidt, A. Hoffmann, M. A. Liauw, M. D. Jones, S. Herres-Pawlis, *ChemSusChem* **2017**, *10*, 3547–3556.

[113] A. Metz, P. McKeown, B. Esser, C. Gohlke, K. Kröckert, L. Laurini, M. Scheckenbach, S. N. McCormick, M. Oswald, A. Hoffmann, M. D. Jones, S. Herres-Pawlis, *Eur. J. Inorg. Chem.* **2017**, 5557–5570.

[114] A. Metz, J. Heck, C. Gohlke, K. Kröckert, Y. Louven, P. McKeown, A. Hoffmann, M.

Jones, S. Herres-Pawlis, *Inorganics* **2017**, *5*, 85–104.

[115] R. D. Rittinghaus, P. M. Schäfer, P. Albrecht, C. Conrads, A. Hoffmann, A. N. Ksiazkiewicz, O. Bienemann, A. Pich, S. Herres-Pawlis, *ChemSusChem* **2019**, *12*, 2161–2165.

[116] P. M. Schäfer, P. McKeown, M. Fuchs, R. D. Rittinghaus, A. Hermann, J. Henkel, S. Seidel, C. Roitzheim, A. N. Ksiazkiewicz, A. Hoffmann, A. Pich, M. D. Jones, S. Herres-Pawlis, *Dalton Trans.* **2019**, *48*, 6071–6082.

[117] P. M. Schäfer, S. Herres-Pawlis, *ChemPlusChem* **2020**, *85*, 1044–1052.

[118] A. Hoffmann, J. Stanek, B. Dicke, L. Peters, B. Grimm-Lebsanft, A. Wetzel, A. Jesser, M. Bauer, M. Gnida, W. Meyer-Klaucke, M. Rübhausen, S. Herres-Pawlis, *Eur. J. Inorg. Chem.* **2016**, 4731–4743.

[119] J. Stanek, N. Sackers, F. Fink, M. Paul, L. Peters, R. Grunzke, A. Hoffmann, S. Herres-Pawlis, *Chem. Eur. J.* **2017**, *23*, 15738–15745.

[120] B. Dicke, A. Hoffmann, J. Stanek, M. S. Rampp, B. Grimm-Lebsanft, F. Biebl, D. Rukser, B. Maerz, D. Göries, M. Naumova, M. Biednov, G. Neuber, A. Wetzel, S. M. Hofmann, P. Roedig, A. Meents, J. Bielecki, J. Andreasson, K. R. Beyerlein, H. N. Chapman, C. Bressler, W. Zinth, M. Rübhausen, S. Herres-Pawlis, *Nat. Chem.* **2018**, *10*, 355–362.

[121] D. Maiti, D.-H. Lee, K. Gaoutchenova, C. Würtele, M. C. Holthausen, A. A. Narducci Sarjeant, J. Sundermeyer, S. Schindler, K. D. Karlin, *Angew. Chem. Int. Ed.* **2008**, *47*, 82–85.

[122] M. Schatz, V. Raab, S. P. Foxon, G. Brehm, S. Schneider, M. Reiher, M. C. Holthausen, J. Sundermeyer, S. Schindler, *Angew. Chem. Int. Ed.* **2004**, *43*, 4360–4363.

[123] M. P. Coles, *Dalton Trans.* **2006**, 985–1001.

[124] C. Würtele, E. Gaoutchenova, K. Harms, M. C. Holthausen, J. Sundermeyer, S. Schindler, *Angew. Chem. Int. Ed.* **2006**, *45*, 3867–3869.

[125] A. Strecker, *Ann. Chem. Pharm.* **1861**, *118*, 151–177.

[126] W. Kantlehner, E. Haug, W. W. Mergen, P. Speh, T. Maier, J. J. Kapassakalidis, H.-J. Bräuner, H. Hagen, *Liebigs Ann. Chem.* **1984**, 108–126.

[127] V. Raab, K. Harms, J. Sundermeyer, B. Kovacević, Z. B. Maksić, *J. Org. Chem.* **2003**, *68*, 8790–8797.

[128] S. Herres-Pawlis, A. Neuba, O. Seewald, T. Seshadri, H. Egold, U. Flörke, G. Henkel, *Eur. J. Org. Chem.* **2005**, 4879–4890.

[129] H. Wittmann, A. Schorm, J. Sundermeyer, *Z. Anorg. Allg. Chem.* **2000**, *626*, 1583–1590.

[130] S. Pohl, M. Harmjanz, J. Schneider, W. Saak, G. Henkel, *J. Chem. Soc., Dalton Trans.* **2000**, *2*, 3473–3479.

[131] S. Pohl, M. Harmjanz, J. Schneider, W. Saak, G. Henkel, *Inorg. Chim. Acta* **2000**, *311*, 106–112.

[132] S. Herres, A. J. Heuwing, U. Flörke, J. Schneider, G. Henkel, *Inorg. Chim. Acta* **2005**, *358*, 1089–1095.

[133] S. Herres-Pawlis, U. Flörke, G. Henkel, *Eur. J. Inorg. Chem.* **2005**, 3815–3824.

[134] H. Wittmann, V. Raab, A. Schorm, J. Plackmeyer, J. Sundermeyer, *Eur. J. Inorg. Chem.* **2001**, 1937–1948.

[135] F. Strassl, B. Grimm-Lebsanft, D. Rukser, F. Biebl, M. Biednov, C. Brett, R. Timmermann, F. Metz, A. Hoffmann, M. Rübhausen, S. Herres-Pawlis, *Eur. J. Inorg. Chem.* **2017**, 3350–3359.

[136] P. S. Starcher, B. Phillips, *J. Am. Chem. Soc.* **1958**, *80*, 4079–4082.

[137] S. L. Friess, *J. Am. Chem. Soc.* **1949**, *71*, 2571–2575.

[138] C. Bolm, G. Schlingloff, K. Weickhardt, *Tetrahedron Lett.* **1993**, *34*, 3405–3408.

[139] S. I. Murahashi, Y. Oda, T. Naota, *Tetrahedron Lett.* **1992**, *33*, 7557–7560.

[140] M. Paul, F. Strassl, A. Hoffmann, M. Hoffmann, M. Schlüter, S. Herres-Pawlis, *Eur. J. Inorg. Chem.* **2018**, 2101–2124.

[141] J. Sanyal, S. Vásquez, S. Roy, M. P. Dudukovic, *Chem. Eng. Sci.* **1999**, *54*, 5071–5083.

[142] J. M. Van Baten, R. Krishna, *Chem. Eng. Res. Des.* **2004**, *82*, 1043–1053.

[143] D. Schurr, F. Strassl, P. Liebhäuser, G. Rinke, R. Dittmeyer, S. Herres-Pawlis, *React. Chem. Eng.* **2016**, *1*, 485–493.

[144] F. Strassl, J. Timmermann, M. Schlüter, S. Herres-Pawlis, *GIT Labor-Fachzeitschrift* **2016**, *60*, 39–41.

[145] F. Felis, F. Strassl, L. Laurini, N. Dietrich, A.-M. Billet, V. Roig, S. Herres-Pawlis, K. Loubière, *Chem. Eng. Sci.* **2019**, *207*, 1256–1269.

[146] H. B. Gray, J. R. Winkler, *Acc. Chem. Res.* **2018**, *51*, 1850–1857.

[147] A. N. Campbell, S. S. Stahl, *Acc. Chem. Res.* **2012**, *45*, 851–863.

[148] S. D. McCann, S. S. Stahl, *Acc. Chem. Res.* **2015**, *48*, 1756–1766.

[149] L. Yang, D. R. Powell, R. P. Houser, *Dalton Trans.* **2007**, 955–964.

[150] S. Herres-Pawlis, R. Haase, P. Verma, A. Hoffmann, P. Kang, T. D. P. Stack, *Eur. J. Inorg. Chem.* **2015**, 5426–5436.

[151] C. Müller, *Copper(I) Chem. Phosphines, Funct. Phosphines Phosphorus Heterocycles*, Elsevier, **2019**, 1–19.

[152] J. M. Thomas, P. K. Madarasi, C. Sivasankar, A. G. Samuelson, *Copper(I) Chem. Phosphines, Funct. Phosphines Phosphorus Heterocycles*, Elsevier, **2019**, 165–236.

[153] G. Santiso-Quiñones, A. Reisinger, J. Slattery, I. Krossing, *Chem. Commun.* **2007**, 5046–5048.

[154] M. Paul, *Master Thesis* **2017**, RWTH Aachen University.

[155] J. L. DuBois, P. Mukherjee, T. D. P. Stack, B. Hedman, E. I. Solomon, K. O. Hodgson, *J. Am. Chem. Soc.* **2000**, *122*, 5775–5787.

[156] B. Ravel, M. Newville, *J. Synchrotron Radiat.* **2005**, *12*, 537–541.

[157] J. Tao, J. P. Perdew, V. N. Staroverov, G. E. Scuseria, *Phys. Rev. Lett.* **2003**, *91*, 146401–1–146401–4.

[158] V. N. Staroverov, G. E. Scuseria, J. Tao, J. P. Perdew, *J. Chem. Phys.* **2003**, *119*, 12129–12137.

[159] V. N. Staroverov, G. E. Scuseria, J. Tao, J. P. Perdew, *J. Chem. Phys.* **2004**, *121*, 11507.

[160] F. Weigend, R. Ahlrichs, *Phys. Chem. Chem. Phys.* **2005**, *7*, 3297–3305.

[161] A. Schäfer, C. Huber, R. Ahlrichs, *J. Chem. Phys.* **1994**, *100*, 5829–5835.

[162] K. Eichkorn, F. Weigend, O. Treutler, R. Ahlrichs, *Theor. Chem. Accounts Theory, Comput. Model.* **1997**, *97*, 119–124.

[163] F. Weigend, M. Häser, H. Patzelt, R. Ahlrichs, *Chem. Phys. Lett.* **1998**, *294*, 143–152.

[164] S. Grimme, S. Ehrlich, L. Goerigk, *J. Comput. Chem.* **2011**, *32*, 1456–1465.

[165] L. Goerigk, S. Grimme, *Phys. Chem. Chem. Phys.* **2011**, *13*, 6670–6688.

[166] For TPSSh, the values of the original paper have been substituted by the corrected values kindly provided by S. Grimme as private communication and published in [167].

[167] A. Hoffmann, R. Grunzke, S. Herres-Pawlis, *J. Comput. Chem.* **2014**, *35*, 1943–1950.

[168] J. Mukherjee, R. Mukherjee, *Dalton Trans.* **2006**, *6*, 1611–1621.

[169] L. M. Mirica, T. D. P. Stack, *Inorg. Chem.* **2005**, *44*, 2131–2133.

[170] A. Kunishita, M. Kubo, H. Ishimaru, T. Ogura, H. Sugimoto, S. Itoh, *Inorg. Chem.* **2008**, *47*, 12032–12039.

[171] S. Hong, L. M. R. Hill, A. K. Gupta, B. D. Naab, J. B. Gilroy, R. G. Hicks, C. J. Cramer, W. B. Tolman, *Inorg. Chem.* **2009**, *48*, 4514–4523.

[172] M. Taki, S. Teramae, S. Nagatomo, Y. Tachi, T. Kitagawa, S. Itoh, S. Fukuzumi, *J. Am. Chem. Soc.* **2002**, *124*, 6367–6377.

[173] C. Citek, C. T. Lyons, E. C. Wasinger, T. D. P. Stack, *Nat. Chem.* **2012**, *4*, 317–322.

[174] C. C. L. McCrory, A. Devadoss, X. Ottenwaelder, R. D. Lowe, T. D. P. Stack, C. E. D. Chidsey, *J. Am. Chem. Soc.* **2011**, *133*, 3696–3699.

[175] S. Itoh, H. Nakao, L. M. Berreau, T. Kondo, M. Komatsu, S. Fukuzumi, *J. Am. Chem. Soc.* **1998**, *120*, 2890–2899.

[176] S. Itoh, M. Taki, H. Nakao, P. L. Holland, W. B. Tolman, L. Que, Jr., S. Fukuzumi, *Angew. Chem. Int. Ed.* **2000**, *39*, 398–400.

[177] H. Arii, Y. Saito, S. Nagatomo, T. Kitagawa, Y. Funahashi, K. Jitsukawa, H. Masuda, *Chem. Lett.* **2003**, *32*, 156–157.

[178] S. Mahapatra, J. A. Halfen, W. B. Tolman, *J. Am. Chem. Soc.* **1996**, *118*, 11575–11586.

[179] M. Enomoto, T. Aida, *J. Am. Chem. Soc.* **1999**, *121*, 874–875.

[180] J. A. Halfen, V. G. Young, W. B. Tolman, *Inorg. Chem.* **1998**, *37*, 2102–2103.

[181] S. Herres-Pawlis, *Dissertation* **2005**, Paderborn University.

[182] K. Mawai, S. Nathani, F. S. Tuglak Khan, P. Verma, S. Kumari, P. Roy, U. P. Singh, K. Ghosh, *ChemistrySelect* **2020**, *5*, 463–475.

[183] M. Álvarez, F. Molina, M. R. Fructos, J. Urbano, E. Álvarez, M. Sodupe, A. Lledós, P. J. Pérez, *Dalton Trans.* **2020**, *49*, 14647–14655.

[184] S. Mahapatra, S. Kaderli, A. Llobet, Y.-M. Neuhold, T. Palanché, J. A. Halfen, V. G. Young, T. A. Kaden, L. Que, A. D. Zuberbühler, W. B. Tolman, *Inorg. Chem.* **1997**, *36*, 6343–6356.

[185] J. E. Bulkowski, **1985**, Binucleating Ligand-Metal Complexes as Oxidation Catalysts, US Patent 4,545,937.

[186] I. Yavari, Z. Nader, *Dye. Pigment.* **2007**, *75*, 474–478.

[187] K. Fukui, *Science* **1982**, *218*, 747–754.

[188] A. K. Mishra, J. N. Moorthy, *J. Org. Chem.* **2016**, *81*, 6472–6480.

[189] A. Wu, Y. Duan, D. Xu, T. M. Penning, R. G. Harvey, *Tetrahedron* **2010**, *66*, 2111–2118.

[190] H. Hussain, S. Specht, S. R. Sarite, M. Saeftel, A. Hoerauf, B. Schulz, K. Krohn, *J. Med. Chem.* **2011**, *54*, 4913–4917.

[191] J. A. Leitch, Y. Bhonoah, C. G. Frost, *ACS Catal.* **2017**, *7*, 5618–5627.

[192] R. Krug, D. Schröder, J. Gebauer, S. Suljić, Y. Morimoto, N. Fujieda, S. Itoh, J. Pietruszka, *Eur. J. Org. Chem.* **2018**, 1789–1796.

[193] O. Bienemann, R. Haase, A. Jesser, T. Beschnitt, A. Döring, D. Kuckling, I. dos Santos Vieira, U. Flörke, S. Herres-Pawlis, *Eur. J. Inorg. Chem.* **2011**, *2011*, 2367–2379.

[194] P. K. Mehrotra, R. Hoffmann, *Inorg. Chem.* **1978**, *17*, 2187–2189.

[195] M. Hoyer, H. Hartl, *Z. Anorg. Allg. Chem.* **1991**, *598*, 151–162.

[196] M. Hoyer, H. Hartl, *Z. Anorg. Allg. Chem.* **1992**, *612*, 45–50.

[197] A. M. Wheaton, M. E. Streep, C. M. Ohlhaver, A. D. Nicholas, F. H. Barnes, H. H. Patterson, R. D. Pike, *ACS Omega* **2018**, *3*, 15281–15292.

[198] R. Peng, M. Li, D. Li, *Coord. Chem. Rev.* **2010**, *254*, 1–18.

[199] R. D. Shannon, *Acta Crystallogr. Sect. A* **1976**, *32*, 751–767.

[200] R. Marin, A. Skripka, Y.-C. Huang, T. A. J. Loh, V. Mazeika, V. Karabanovas, D. H. C. Chua, C.-L. Dong, P. Canton, F. Vetrone, *Chem. Commun.* **2020**, *56*, 3341–3344.

[201] M. Rohrmüller, A. Hoffmann, C. Thierfelder, S. Herres-Pawlis, W. G. Schmidt, *J. Comput. Chem.* **2015**, *36*, 1672–1685.

[202] I. M. DiMucci, J. T. Lukens, S. Chatterjee, K. M. Carsch, C. J. Titus, S. J. Lee, D. Nordlund, T. A. Betley, S. N. MacMillan, K. M. Lancaster, *J. Am. Chem. Soc.* **2019**, *141*, 18508–18520.

[203] R. Hoffmann, S. Alvarez, C. Mealli, A. Falceto, T. J. Cahill, T. Zeng, G. Manca, *Chem. Rev.* **2016**, *116*, 8173–8192.

[204] J. P. Snyder, *Angew. Chem. Int. Ed.* **1995**, *34*, 80–81.

[205] J. P. Snyder, *Angew. Chem. Int. Ed.* **1995**, *34*, 986–987.

[206] R. C. Walroth, J. T. Lukens, S. N. MacMillan, K. D. Finkelstein, K. M. Lancaster, *J. Am. Chem. Soc.* **2016**, *138*, 1922–1931.

[207] S. N. MacMillan, K. M. Lancaster, *ACS Catal.* **2017**, *7*, 1776–1791.

[208] K. M. Carsch, I. M. DiMucci, D. A. Iovan, A. Li, S.-L. Zheng, C. J. Titus, S. J. Lee, K. D. Irwin, D. Nordlund, K. M. Lancaster, T. A. Betley, *Science* **2019**, *365*, 1138–1143.

[209] M. Paeth, S. B. Tyndall, L.-Y. Chen, J.-C. Hong, W. P. Carson, X. Liu, X. Sun, J. Liu, K. Yang, E. M. Hale, D. L. Tierney, B. Liu, Z. Cao, M.-J. Cheng, W. A. Goddard, W. Liu, *J. Am. Chem. Soc.* **2019**, *141*, 3153–3159.

[210] M. Roemelt, D. Maganas, S. DeBeer, F. Neese, *J. Chem. Phys.* **2013**, *138*, 204101.

[211] A. Metz, R. Plothe, B. Glowacki, A. Koszalkowski, M. Scheckenbach, A. Beringer, T. Rösener, J. Michaelis de Vasconcellos, R. Haase, U. Flörke, A. Hoffmann, S. Herres-Pawlis, *Eur. J. Inorg. Chem.* **2016**, 4974–4987.

[212] M. Paul, M. Teubner, B. Grimm-Lebsanft, C. Golchert, Y. Meiners, L. Senft, K. Keisers, P. Liebhäuser, T. Rösener, F. Biebl, S. Buchenau, M. Naumova, V. Murzin, R. Krug, A. Hoffmann, J. Pietruszka, I. Ivanović-Burmazović, M. Rübhausen, S. Herres-Pawlis, *Chem. Eur. J.* **2020**, *26*, 7556–7562.

[213] E. D. Glendening, C. R. Landis, F. Weinhold, *J. Comput. Chem.* **2019**, *40*, 2234–2241.

[214] E. D. Glendening, J. K. Badenhoop, A. E. Reed, J. E. Carpenter, J. A. Bohmann, C. M. Morales, P. Karafiloglou, C. R. Landis, F. Weinhold, Theoretical Chemistry Institute, NBO 7.0., University of Wisconsin, Madison, WI, USA, **2018**.

[215] F. Weinhold, C. Landis, Valency and Bonding – A Natural Bond Orbital Donor–Acceptor Perspective, Cambridge University Press, New York, USA, **2005**.

[216] R. L. Martin, *J. Chem. Phys.* **2003**, *118*, 4775–4777.

[217] A. Hoffmann, M. Wern, T. Hoppe, M. Witte, R. Haase, P. Liebhäuser, J. Glatthaar, S. Herres-Pawlis, S. Schindler, *Eur. J. Inorg. Chem.* **2016**, 4744–4751.

[218] V. Mahadevan, Z. Hou, A. P. Cole, D. E. Root, T. K. Lal, E. I. Solomon, T. D. P. Stack, *J. Am. Chem. Soc.* **1997**, *119*, 11996–11997.

[219] M. J. Henson, P. Mukherjee, D. E. Root, T. D. P. Stack, E. I. Solomon, *J. Am. Chem. Soc.* **1999**, *121*, 10332–10345.

[220] B. Grimm-Lebsanft, M. Teubner, M. Paul, S. Buchenau, A. Hoffmann, S. Herres-Pawlis, M. A. Rübhausen, **2021**, manuscript in preparation.

[221] P. Kang, E. Bobyr, J. Dustman, K. O. Hodgson, B. Hedman, E. I. Solomon, T. D. P. Stack, *Inorg. Chem.* **2010**, *49*, 11030–11038.

[222] V. Raab, J. Kipke, R. M. Gschwind, J. Sundermeyer, *Chem. Eur. J.* **2002**, *8*, 1682–1693.

[223] G. J. Kubas, B. Monzyk, A. L. Crumbliss, *Inorg. Synth.* **1979**, *19*, 90–92.

[224] B. Schulz, J. Bäckström, D. Budelmann, R. Maeser, M. Rübhausen, M. V. Klein, E. Schoeffel, A. Mihill, S. Yoon, *Rev. Sci. Instrum.* **2005**, *76*, 073107–1–073107–12.

[225] B. Grimm-Lebsanft, C. Brett, F. Strassl, D. Rukser, M. Biednov, F. Biebl, M. Naumova, A. Hoffmann, L. Akinsinde, D. Brückner, S. Herres-Pawlis, M. Rübhausen, *Inorg. Chim. Acta* **2018**, *481*, 176–180.

[226] W. A. Caliebe, V. Murzin, A. Kalinko, M. Görlitz, in *AIP Conf. Proc.*, **2019**, p. 060031.

[227] a) Stoe & Cie GmbH, *X-Area Pilatus3_SV 1.31.131.0*, Darmstadt, Germany, **2017**; b) Stoe & Cie GmbH, *X-Area Recipe 1.33.0.0*, Darmstadt, Germany, **2015**; c) Stoe & Cie GmbH, *X-Area Integrate 1.71.0.0*, Darmstadt, Germany, **2016**; d) Stoe & Cie GmbH, *X-Area LANA 1.71.4.0*, Darmstadt, Germany, **2017**.

[228] Bruker AXS Inc., *SAINT* and *SADABS*, Madison, WI, USA, **2008**.

[229] Bruker AXS Inc., *XPREP 5.1*, Madison, WI, USA, **1997**.

[230] G. M. Sheldrick, *Acta Crystallogr. Sect. A* **2015**, *71*, 3–8.

[231] G. M. Sheldrick, *Acta Crystallogr. Sect. C* **2015**, *71*, 3–8.

[232] C. B. Hübschle, G. M. Sheldrick, B. Dittrich, *J. Appl. Crystallogr.* **2011**, *44*, 1281–1284.

[233] A. L. Spek, *Acta Crystallogr. Sect. D Biol. Crystallogr.* **2009**, *65*, 148–155.

[234] A. L. Spek, PLATON, A Multipurpose Crystallographic Tool, Utrecht University, Utrecht, The Netherlands, **2008**.

[235] M. J. Frisch, G. W. Trucks, H. B. Schlegel, G. E. Scuseria, M. A. Robb, J. R. Cheeseman, G. Scalmani, V. Barone, G. A. Petersson, H. Nakatsuji, X. Li, M. Caricato, A. V. Marenich, J. Bloino, B. G. Janesko, R. Gomperts, B. Mennucci, H. P. Hratchian, J. V. Ortiz, A. F. Izmaylov, J. L. Sonnenberg, D. Williams-Young, F. Ding, F. Lipparini, F. Egidi, J. Goings, B. Peng, A. Petrone, T. Henderson, D. Ranasinghe, V. G. Zakrzewski, J. Gao, N. Rega, G. Zheng, W. Liang, M. Hada, M. Ehara, K. Toyota, R. Fukuda, J. Hasegawa, M. Ishida, T. Nakajima, Y. Honda, O. Kitao, H. Nakai, T. Vreven, K. Throssell, J. A. Montgomery, Jr., J. E. Peralta, F. Ogliaro, M. J. Bearpark, J. J. Heyd, E. N. Brothers, K. N. Kudin, V. N. Staroverov, T. A. Keith, R. Kobayashi, J. Normand, K. Raghavachari, A. P. Rendell, J. C. Burant, S. S. Iyengar, J. Tomasi, M. Cossi, J. M. Millam, M. Klene, C. Adamo, R. Cammi, J. W. Ochterski, R. L. Martin, K. Morokuma, O. Farkas, J. B. Foresman, D. J. Fox, Gaussian Inc., Gaussian 16, Revision B.01, Wallingford, CT, USA, **2016**.

[236] M. Rohrmüller, S. Herres-Pawlis, M. Witte, W. G. Schmidt, *J. Comput. Chem.* **2013**, *34*, 1035–1045.

[237] A. Hoffmann, S. Herres-Pawlis, *Phys. Chem. Chem. Phys.* **2016**, *18*, 6430–6440.

[238] K. A. Peterson, D. Figgen, E. Goll, H. Stoll, M. Dolg, *J. Chem. Phys.* **2003**, *119*, 11113–11123.

[239] A. Baldes, Turbomole basis set library II. Accessed December 22, 2019.

https://cosmologic-services.de/basis-sets/basissets.php

[240] S. I. Gorelsky, A. B. P. Lever, *J. Organomet. Chem.* **2001**, *635*, 187–196.

[241] M. V. Barybin, P. L. Diaconescu, C. C. Cummins, *Inorg. Chem.* **2001**, *40*, 2892–2897.

[242] R. L. Danheiser, R. F. Miller, R. G. Brisbois, S. Z. Park, *J. Org. Chem.* **1990**, *55*, 1959–1964.

[243] A. Gao, Y. Mu, J. Zhang, W. Yao, *Eur. J. Inorg. Chem.* **2009**, 3613–3621.

[244] D. Gale, J. Wilshire, *Aust. J. Chem.* **1975**, *28*, 2447–2458.

[245] S. Thomas, C. J. Collins, J. R. Cuzens, D. Spiciarich, C. T. Goralski, B. Singaram, *J. Org. Chem.* **2001**, *66*, 1999–2004.

[246] M. Paul, A. Hoffmann, S. Herres-Pawlis, *J. Biol. Inorg. Chem.* **2021**, *26*, 249–263.

[247] M. Paul, M. Teubner, B. Grimm-Lebsanft, S. Buchenau, A. Hoffmann, M. Rübhausen, S. Herres-Pawlis, *J. Inorg. Biochem.* **2021**, *224*, 111541.

7. Appendix

7.1. Crystallographic Data

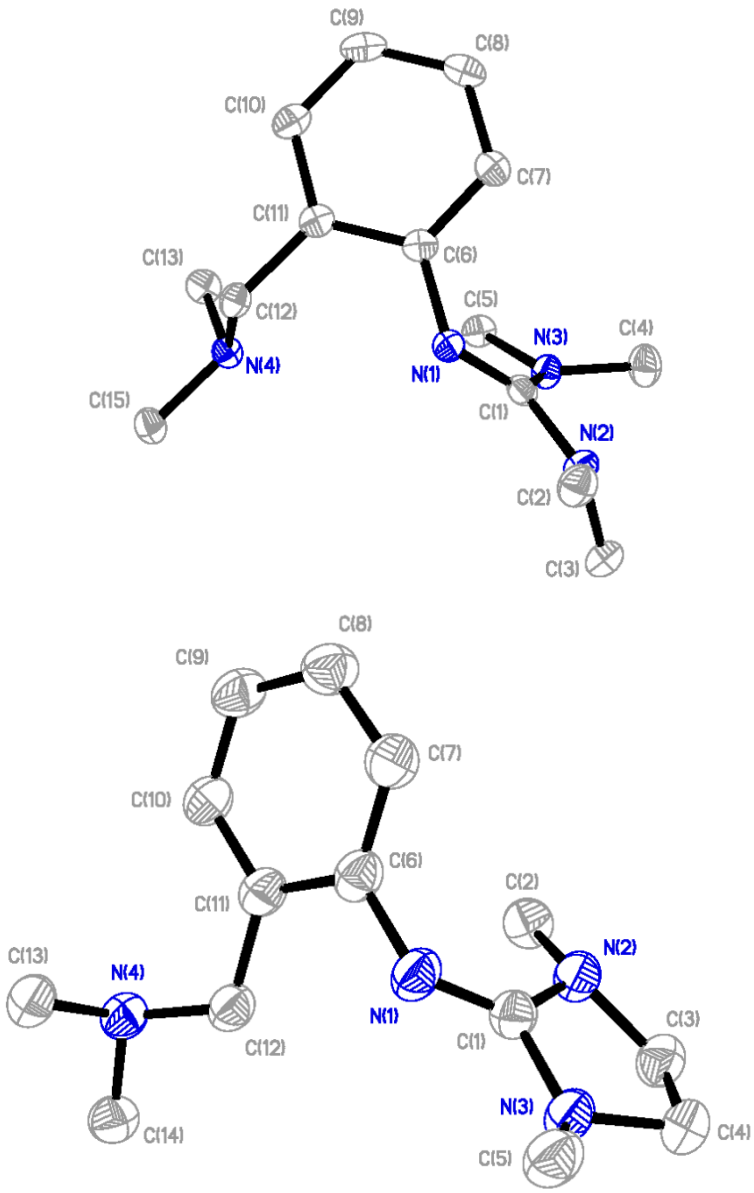

Figure 58: Molecular structures of the ligands **L1** (top) and **L2** (bottom) in the solid state. Hydrogen atoms were omitted for clarity. Displacement ellipsoids represent the 50% probability level.

Table 41: Crystallographic data and parameters of **L1** and **L2**.

	L1	**L2**
Empirical formula	$C_{14}H_{24}N_4$	$C_{14}H_{22}N_4$
Formula weight [g mol^{-1}]	248.37	246.35
T [K]	100	100
λ [Å]	1.54186	1.54186
Crystal system	Monoclinic	Monoclinic
Space group	$P2_1/n$	$P2_1/n$
a [Å]	9.993(2)	10.262(2)
b [Å]	11.144(2)	9.967(2)
c [Å]	13.279(3)	14.191(3)
α [°]	90	90
β [°]	104.99(3)	110.02(3)
γ [°]	90	90
V [Å^3]	1428.4(5)	1363.9(5)
Z	4	4
ρ_{calc} [g cm^{-3}]	1.155	1.200
μ [mm^{-1}]	0.551	0.576
F(000)	544	536
Crystal size [mm]	0.240 x 0.180 x 0.050	0.210 x 0.140 x 0.100
hkl range	–11 ≤ h ≤ 10 –13 ≤ k ≤ 12 –15 ≤ l ≤ 11	–11 ≤ h ≤ 12 –11 ≤ k ≤ 11 –13 ≤ l ≤ 16
Reflections collected	11767	11134
Independent reflections	2420	2317
R_{int}	0.0150	0.0152
Number of parameters	169	168
R1 [I≥2σ(I)]	0.0321	0.0507
wR_2 (all data)	0.0814	0.1381
Goodness-of-fit	1.047	1.062
Largest diff. peak hole [eÅ^{-3}]	0.126, –0.205	0.252, –0.220
Identification code	SH_00658	SH_01038

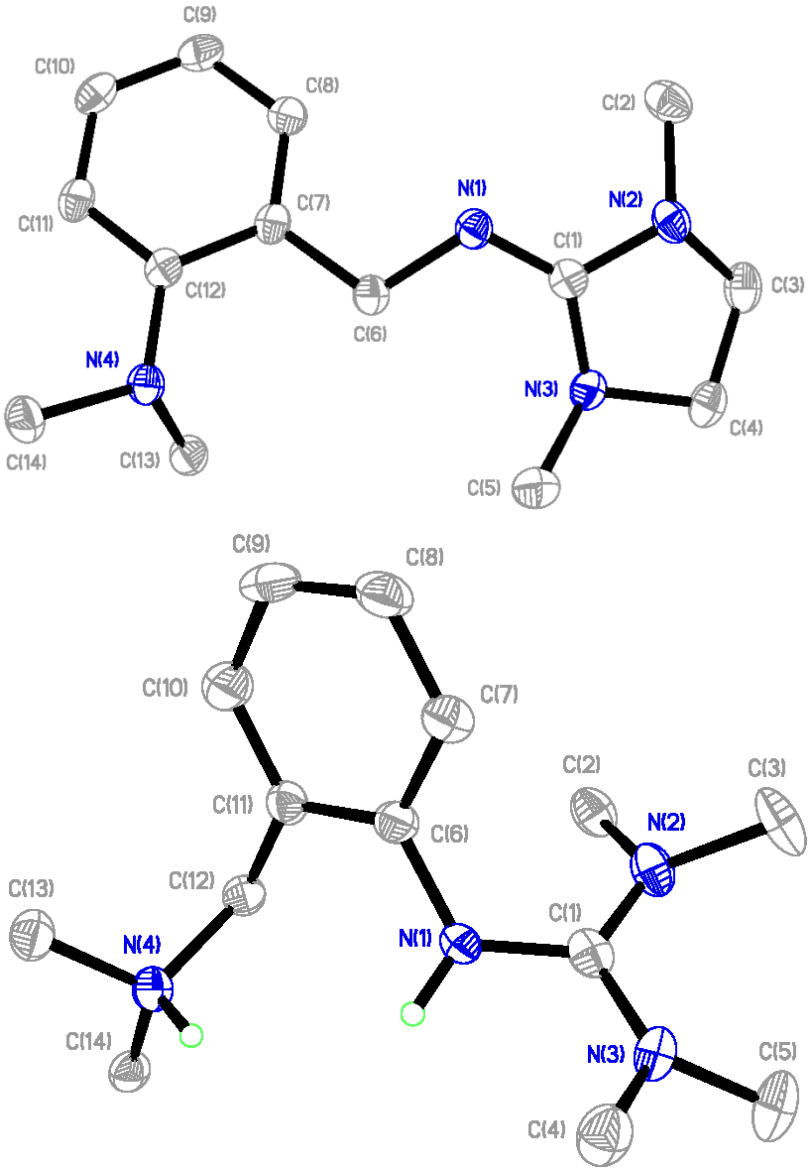

Figure 59: Molecular structures of the ligand **L5** (top) and the protonated ligand $[\mathbf{L1}H_2]^{2+}$ in crystals of $[\mathbf{L1}H_2]_2(F)(BF_4)_3$ (bottom) in the solid state. Hydrogen atoms except for NH groups were omitted for clarity. Displacement ellipsoids represent the 50% probability level.

Table 42: Crystallographic data and parameters of **L5** and [**L1**H_2](F)(BF_4).

	L5	**$[L1H_2]_2(F)(BF_4)_3$**
Empirical formula	$C_{14}H_{22}N_4$	$C_{28}H_{52}B_3F_{13}N_8$
Formula weight [g mol^{-1}]	246.35	780.20
T [K]	100	100
λ [Å]	1.54186	0.71073
Crystal system	Orthorhombic	Tetragonal
Space group	*P*na2_1	$P4_32_12$
a [Å]	14.199(3)	12.3090(17)
b [Å]	11.459(3)	12.3090(17)
c [Å]	8.2906(17)	24.986(5)
α [°]	90	90
β [°]	90	90
γ [°]	90	90
V [Å^3]	1348.9(5)	3785.6(13)
Z	4	4
ρ_{calc} [g cm^{-3}]	1.213	1.369
μ [mm^{-1}]	0.583	0.127
F(000)	536	1632
Crystal size [mm]	0.210 x 0.170 x 0.100	0.220 x 0.190 x 0.130
hkl range	–16 ≤ h ≤ 14 –10 ≤ k ≤ 13 –9 ≤ l ≤ 8	–14 ≤ h ≤ 14 –14 ≤ k ≤ 14 –30 ≤ l ≤ 30
Reflections collected	9463	44583
Independent reflections	2277	3523
R_{int}	0.0563	0.0410
Number of parameters	168	251
R1 [I≥2σ(I)]	0.0296	0.0622
wR_2 (all data)	0.0752	0.1394
Goodness-of-fit	1.070	1.108
Largest diff. peak hole [eÅ^{-3}]	0.152, –0.151	0.675, –0.605
Absolute structure parameter	-	–0.5(4)*
Identification code	SH_00936	SH_00870

* The chiral space group does not originate from a true chirality of the molecule. However, the conformational arrangement of the molecules in the structure generates a chiral axis. The crystallization of the conglomerate appears to occur by chance. The corresponding enantiomer necessarily crystallizes concomitantly. The chiral axis complies with the two-fold rotation axis on the Wyckoff position 4*a* with the fluorine center located on this axis. The structure contains no elements with sufficiently large resonant scattering to give rise to meaningful differences in intensity of Friedel pairs. Thus, this value is meaningless, and the absolute structure cannot be determined here.

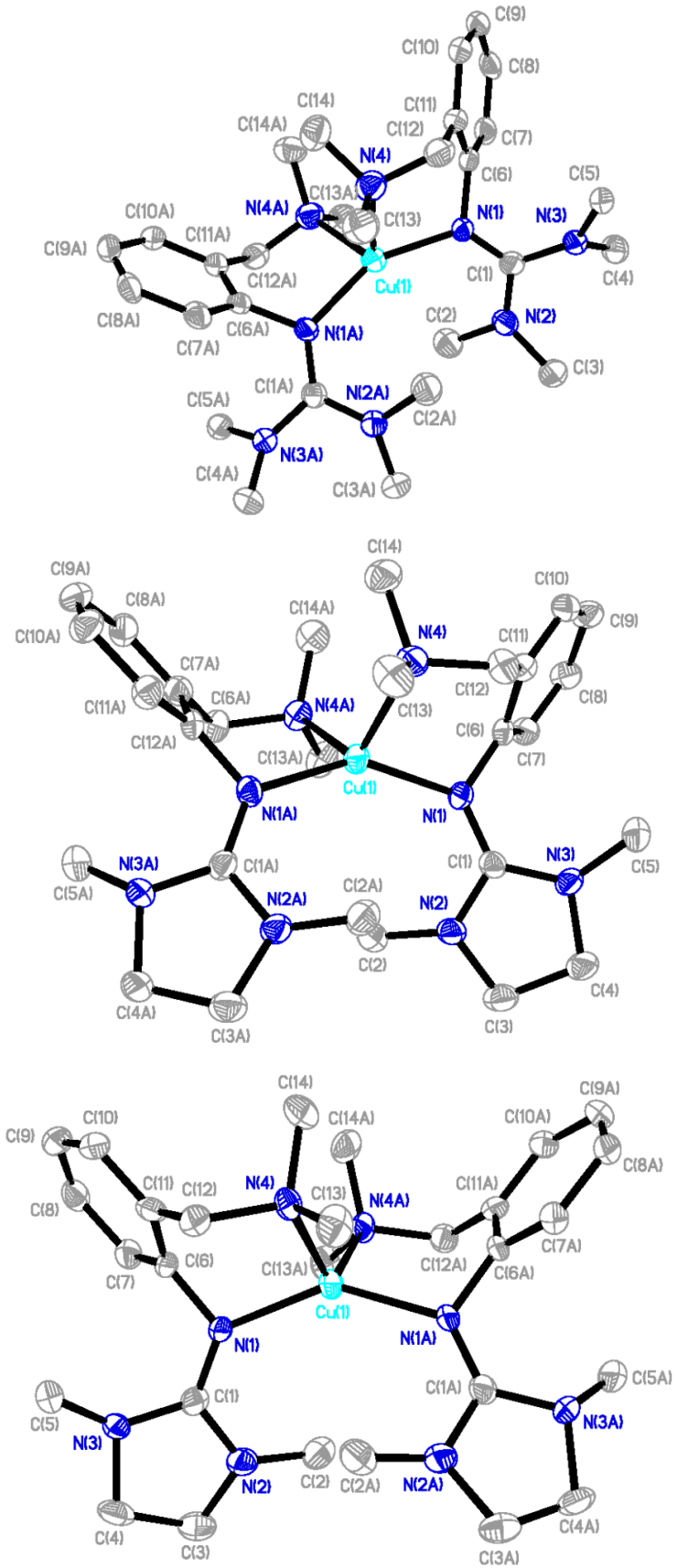

Figure 60: Molecular structures of the complex cations $[Cu(\mathbf{L1})_2]^+$ in crystals of **C5** (top) and $[Cu(\mathbf{L2})_2]^+$ in crystals of **C6** (middle) and **C7** (bottom) in the solid state. Hydrogen atoms and the counterions PF_6^- for **C5** and **C6** as well as OTf^- for **C7** were omitted for clarity. Displacement ellipsoids represent the 50% probability level.

Table 43: Crystallographic data and parameters of **C5**, **C6** and **C7**.

	C5	**C6**	**C7**
Empirical formula	$C_{28}H_{48}CuF_6N_8P$	$C_{28}H_{44}CuF_6N_8P$	$C_{29}H_{44}CuF_3N_8O_3S$
Formula weight [g mol^{-1}]	705.25	701.22	705.32
T [K]	100	100	100
λ [Å]	0.71073	0.71073	0.71073
Crystal system	Orthorhombic	Orthorhombic	Orthorhombic
Space group	*P*ccn	$P2_12_12$	$P2_12_12$
a [Å]	10.428(2)	17.552(4)	9.911(2)
b [Å]	16.610(3)	9.2790(19)	17.329(4)
c [Å]	19.197(4)	9.6660(19)	9.5738(19)
α [°]	90	90	90
β [°]	90	90	90
γ [°]	90	90	90
V [Å^3]	3325.1(11)	1574.3(5)	1644.2(6)
Z	4	2	2
ρ_{calc} [g cm^{-3}]	1.409	1.479	1.425
μ [mm^{-1}]	0.771	0.814	0.788
F(000)	1480	732	740
Crystal size [mm]	0.170 x 0.140 x 0.110	0.160 x 0.110 x 0.100	0.330 x 0.180 x 0.080
hkl range	–13 ≤ h ≤ 13 –21 ≤ k ≤ 21 –25 ≤ l ≤ 13	–20 ≤ h ≤ 23 –12 ≤ k ≤ 11 –9 ≤ l ≤ 12	–13 ≤ h ≤ 13 –22 ≤ k ≤ 23 –9 ≤ l ≤ 12
Reflections collected	26896	12862	13793
Independent reflections	3963	3907	4095
R_{int}	0.0668	0.0438	0.0276
Number of parameters	227	199	246
R1 [I≥2σ(I)]	0.0856	0.0561	0.0619
wR_2 (all data)	0.2380	0.1595	0.1516
Goodness-of-fit	1.100	1.085	1.130
Largest diff. peak hole [eÅ^{-3}]	1.690, –1.318	1.245, –0.881	1.118, –1.995
Absolute structure parameter	-	0.37(2)*	0.07(4)*
Identification code	SH_00310	SH_00181	SH_00251

* The chiral space group does not originate from a true chirality of the molecule. However, the conformational arrangement of the complex generates a chiral axis. The crystallization of the conglomerate appears to occur by chance. The corresponding enantiomer necessarily crystallizes concomitantly. The chiral axis complies with the two-fold rotation axis on the Wyckoff position 2*a* with the Cu center located on this axis. The crystal structure of **C6** was refined as a two-component inversion twin.

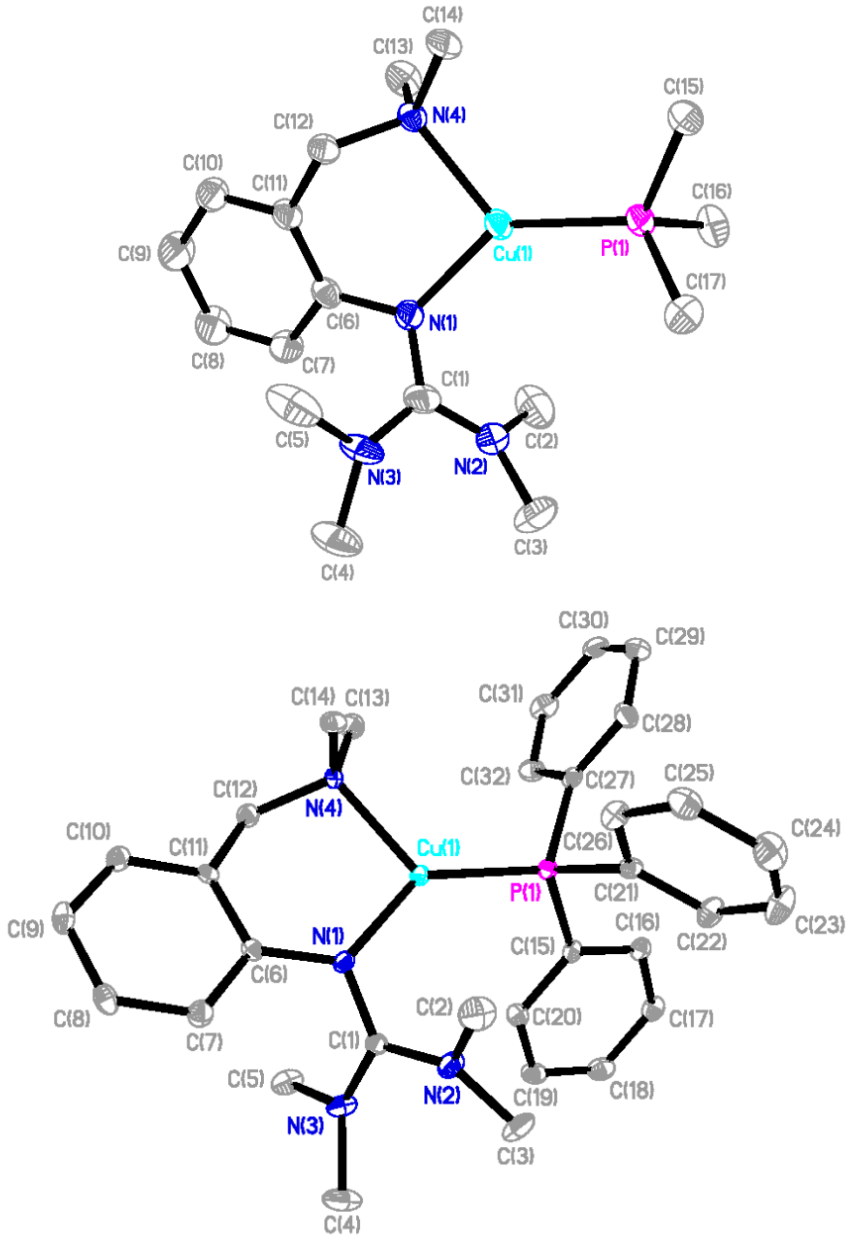

Figure 61: Molecular structures of the complex cations $[Cu(\mathbf{L1})(PMe_3)]^+$ in crystals of **C8** (top) and $[Cu(\mathbf{L1})(PPh_3)]^+$ in crystals of **C9** (bottom) in the solid state. Hydrogen atoms, the counterion PF_6^-, and one tetrahydrofuran molecule in **C9** were omitted for clarity. Displacement ellipsoids represent the 50% probability level.

Table 44: Crystallographic data and parameters of **C8** and **C9**. In **C9** it was not possible to model the disordered tetrahydrofuran molecule (void with 145 Å^3 and electron content of 38 electrons) in an adequate manner, and the data set was treated with the SQUEEZE routine as implemented in PLATON.[233,234]

	C8	**C9**
Empirical formula	$C_{17}H_{33}CuF_6N_4P_2$	$C_{36}H_{47}CuF_6N_4OP_2$
Formula weight [g mol^{-1}]	532.95	791.28
T [K]	100	100
λ [Å]	0.71073	0.71073
Crystal system	Orthorhombic	Triclinic
Space group	*P*bca	$P\bar{1}$
a [Å]	16.648(3)	11.290(2)
b [Å]	14.209(3)	11.504(2)
c [Å]	20.111(4)	14.665(3)
α [°]	90	85.22(3)
β [°]	90	73.62(3)
γ [°]	90	72.87(3)
V [Å^3]	4757.2(16)	1746.5(7)
Z	8	2
ρ_{calc} [g cm^{-3}]	1.488	1.367
μ [mm^{-1}]	1.110	0.776
F(000)	2208	774
Crystal size [mm]	0.220 x 0.180 x 0.120	0.260 x 0.200 x 0.140
hkl range	–24 ≤ h ≤ 24 –20 ≤ k ≤ 13 –29 ≤ l ≤ 28	–17 ≤ h ≤ 13 –17 ≤ k ≤ 17 –22 ≤ l ≤ 19
Reflections collected	49953	30309
Independent reflections	7574	13207
R_{int}	0.0761	0.0259
Number of parameters	280	412
R1 [I≥2σ(I)]	0.0451	0.0314
wR_2 (all data)	0.1205	0.0712
Goodness-of-fit	0.950	0.931
Largest diff. peak hole [eÅ^{-3}]	0.802, –0.652	0.415, –0.471
Identification code	SH_00690	SH_00721

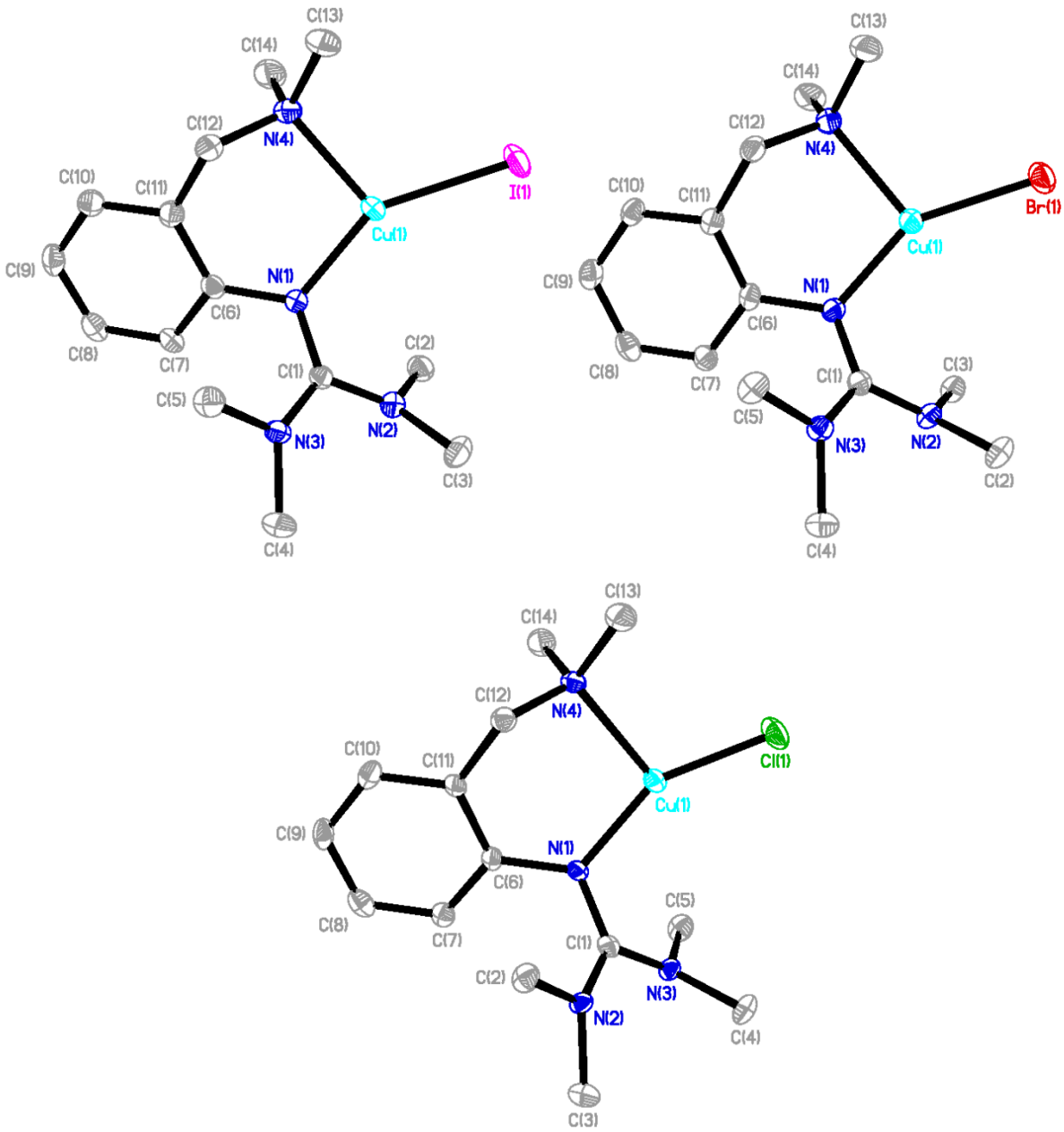

Figure 62: Molecular structures of the complexes **C10**[154] (top left), **C11** (top right) and **C12** (bottom) in the solid state. Hydrogen atoms were omitted for clarity. Displacement ellipsoids represent the 50% probability level.

Table 45: Crystallographic data and parameters of **C10**-**C12**.

	C10[154]	**C11**	**C12**
Empirical formula	$C_{14}H_{24}CuIN_4$	$C_{14}H_{24}CuBrN_4$	$C_{14}H_{24}CuClN_4$
Formula weight [g mol^{-1}]	438.81	391.82	347.36
T [K]	100	100	100
λ [Å]	0.71073	0.71073	0.71073
Crystal system	Orthorhombic	Orthorhombic	Orthorhombic
Space group	*P*bca	*P*bca	*P*bca
a [Å]	16.4039(17)	16.576(3)	16.690(3)
b [Å]	10.8976(11)	10.647(2)	10.502(2)
c [Å]	19.449(2)	18.781(4)	18.476(4)
α [°]	90	90	90
β [°]	90	90	90
γ [°]	90	90	90
V [Å^3]	3476.8(6)	3314.6(11)	3238.6(11)
Z	8	8	8
ρ_{calc} [g cm^{-3}]	1.677	1.570	1.425
μ [mm^{-1}]	3.029	3.725	1.510
F(000)	1744	1600	1456
Crystal size [mm]	0.220 x 0.210 x 0.060	0.260 x 0.160 x 0.080	0.150 x 0.120 x 0.080
hkl range	–22 ≤ h ≤ 22 –14 ≤ k ≤ 14 –26 ≤ l ≤ 26	–22 ≤ h ≤ 14 –13 ≤ k ≤ 14 –25 ≤ l ≤ 25	–22 ≤ h ≤ 15 –11 ≤ k ≤ 14 –23 ≤ l ≤ 24
Reflections collected	69448	16502	13638
Independent reflections	4549	4053	3967
R_{int}	0.0743	0.0631	0.0531
Number of parameters	187	187	187
R1 [I≥2σ(I)]	0.0306	0.0455	0.0365
wR_2 (all data)	0.0808	0.0942	0.0732
Goodness-of-fit	1.014	1.002	0.916
Largest diff. peak hole [eÅ^{-3}]	0.733, –0.868	0.813, –0.495	0.373, –0.331
Identification code	u17_32a	SH_00456	SH_00452

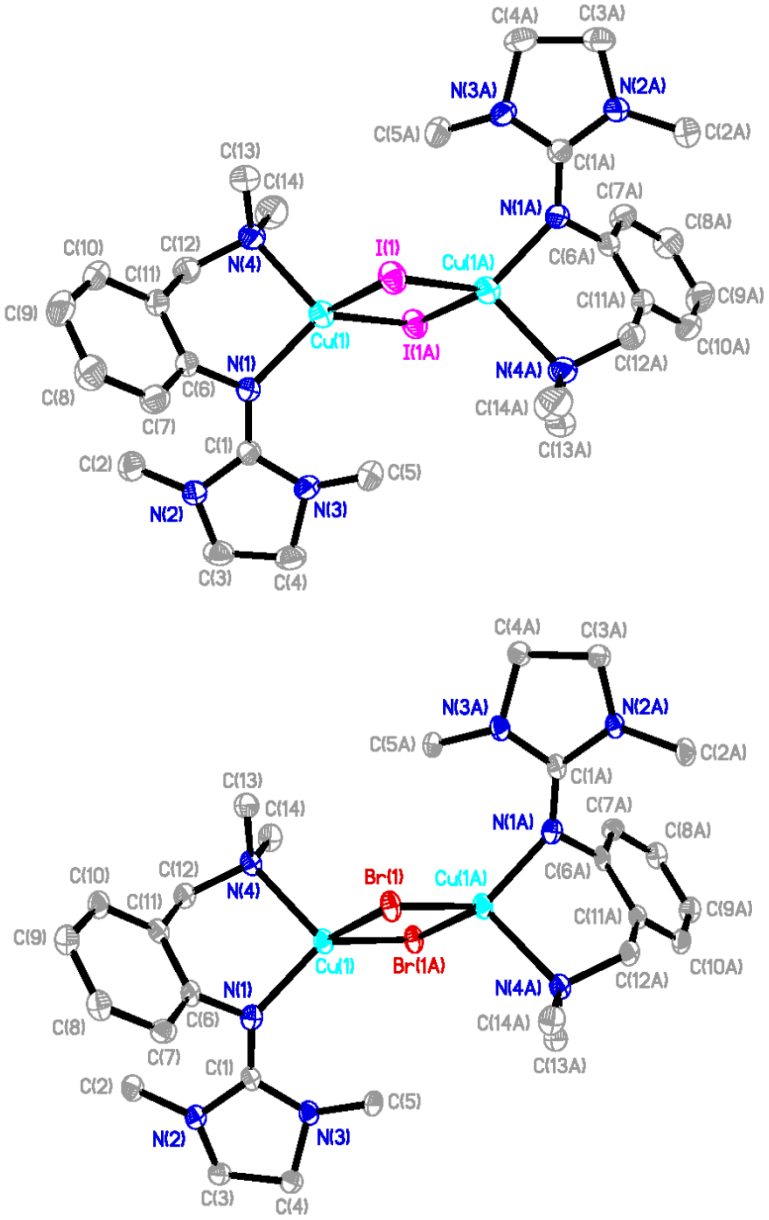

Figure 63: Molecular structures of the complexes **C16**[154] (top) and **C17** (bottom) in the solid state. Hydrogen atoms were omitted for clarity. Displacement ellipsoids represent the 50% probability level.

Table 46: Crystallographic data and parameters of **C16** and **C17**.

	C16[154]	**C17**
Empirical formula	$C_{28}H_{48}Cu_2I_2N_8$	$C_{28}H_{48}Cu_2Br_2N_8$
Formula weight [g mol^{-1}]	873.59	779.61
T [K]	100	100
λ [Å]	0.71073	1.54186
Crystal system	Triclinic	Triclinic
Space group	$P\bar{1}$	$P\bar{1}$
a [Å]	9.1679(16)	8.7744(18)
b [Å]	9.6891(17)	9.954(2)
c [Å]	10.5886(18)	10.372(2)
α [°]	89.543(2)	89.15(3)
β [°]	74.035(2)	73.13(3)
γ [°]	69.357(2)	67.11(3)
V [Å^3]	842.1(3)	793.7(3)
Z	1	1
ρ_{calc} [g cm^{-3}]	1.723	1.631
μ [mm^{-1}]	3.126	4.847
F(000)	432	396
Crystal size [mm]	0.240 x 0.230 x 0.190	0.150 x 0.110 x 0.050
hkl range	–12 ≤ h ≤ 12 –12 ≤ k ≤ 12 –13 ≤ l ≤ 13	–10 ≤ h ≤ 5 –11 ≤ k ≤ 11 –12 ≤ l ≤ 11
Reflections collected	11231	4866
Independent reflections	3992	2627
R_{int}	0.0220	0.0616
Number of parameters	185	185
R1 [I≥2σ(I)]	0.0242	0.0584
wR_2 (all data)	0.0615	0.1586
Goodness-of-fit	1.067	1.127
Largest diff. peak hole [eÅ^{-3}]	0.666, –0.397	1.281, –1.523
Identification code	n17_a99	SH_00444

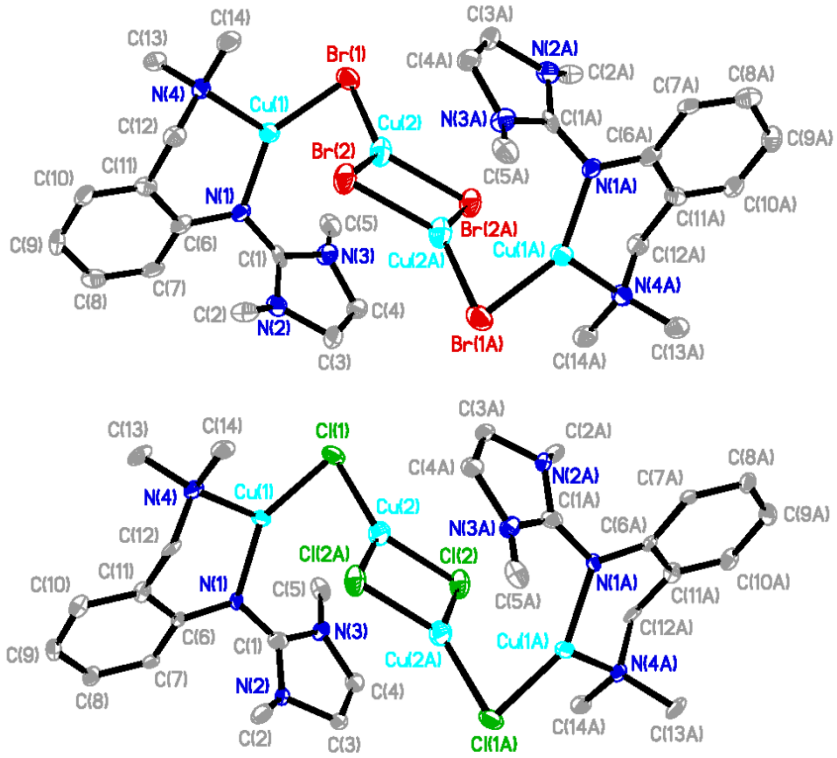

Figure 64: Molecular structures of the complexes **C18** (top) and **C19** (bottom) in the solid state. Hydrogen atoms were omitted for clarity. Displacement ellipsoids represent the 50% probability level.

Table 47: Crystallographic data and parameters of **C18** and **C19**.

	C18	**C19**
Empirical formula	$C_{28}H_{44}Cu_4Br_4N_8$	$C_{28}H_{44}Cu_4Cl_4N_8$
Formula weight [g mol^{-1}]	1066.51	888.67
T [K]	100	100
λ [Å]	0.71073	0.71073
Crystal system	Triclinic	Triclinic
Space group	$P\bar{1}$	$P\bar{1}$
a [Å]	8.9476(18)	8.9064(18)
b [Å]	9.914(2)	9.769(2)
c [Å]	10.677(2)	10.525(2)
α [°]	79.08(3)	79.80(3)
β [°]	74.60(3)	75.08(3)
γ [°]	84.50(3)	85.55(3)
V [Å^3]	895.6(3)	870.4(3)
Z	1	1
ρ_{calc} [g cm^{-3}]	1.977	1.695
μ [mm^{-1}]	6.836	2.750
F(000)	524	452
Crystal size [mm]	0.250 x 0.120 x 0.040	0.130 x 0.110 x 0.070
hkl range	–10 ≤ h ≤ 10 –12 ≤ k ≤ 12 –12 ≤ l ≤ 10	–10 ≤ h ≤ 9 –11 ≤ k ≤ 11 –12 ≤ l ≤ 12
Reflections collected	5872	5932
Independent reflections	3180	3159
R_{int}	0.0530	0.0647
Number of parameters	203	203
R1 [I≥2σ(I)]	0.0750	0.0764
wR_2 (all data)	0.1616	0.2275
Goodness-of-fit	1.176	1.075
Largest diff. peak hole [eÅ^{-3}]	1.298, –0.833	1.343, –1.322
Identification code	SH_00475	SH_00416

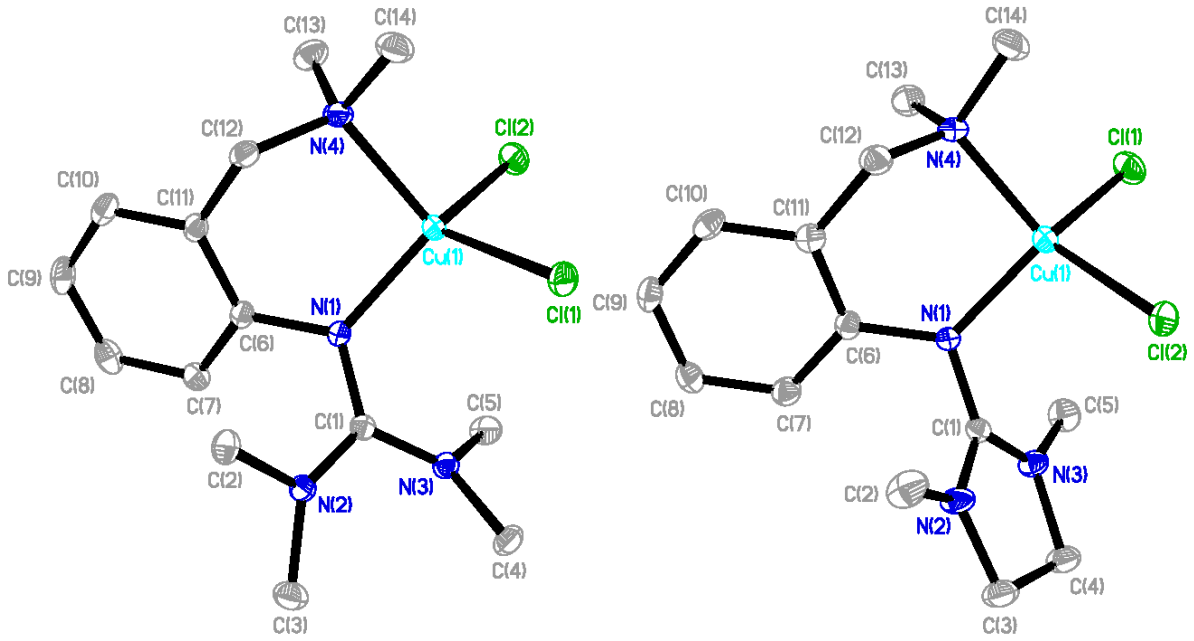

Figure 65: Molecular structures of the complexes **C20** (left) and **C21** (right) in the solid state. Hydrogen atoms were omitted for clarity. Displacement ellipsoids represent the 50% probability level.

Table 48: Crystallographic data and parameters of **C20** and **C21**.

	C20	**C21**
Empirical formula	$C_{14}H_{24}CuCl_2N_4$	$C_{14}H_{22}CuCl_2N_4$
Formula weight [g mol^{-1}]	382.81	380.80
T [K]	100	100
λ [Å]	0.71073	0.71073
Crystal system	Monoclinic	Monoclinic
Space group	$P2_1/c$	$P2_1/n$
a [Å]	10.0998(9)	10.215(2)
b [Å]	15.1423(13)	16.038(3)
c [Å]	12.3745(11)	10.417(2)
α [°]	90	90
β [°]	112.948(2)	93.00(3)
γ [°]	90	90
V [Å^3]	1742.7(3)	1704.4(6)
Z	4	4
ρ_{calc} [g cm^{-3}]	1.459	1.484
μ [mm^{-1}]	1.559	1.593
F(000)	796	788
Crystal size [mm]	0.240 x 0.140 x 0.040	0.140 x 0.110 x 0.090
hkl range	$-12 \le h \le 12$	$-14 \le h \le 7$
	$-18 \le k \le 18$	$-20 \le k \le 22$
	$-15 \le l \le 15$	$-14 \le l \le 14$
Reflections collected	31561	16329
Independent reflections	3586	4853
R_{int}	0.0650	0.0467
Number of parameters	196	194
R1 [I≥2σ(I)]	0.0266	0.0393
wR_2 (all data)	0.0705	0.0817
Goodness-of-fit	1.043	0.873
Largest diff. peak hole [eÅ^{-3}]	0.407, –0.277	0.646, –0.895
Identification code	u17_44	SH_00169

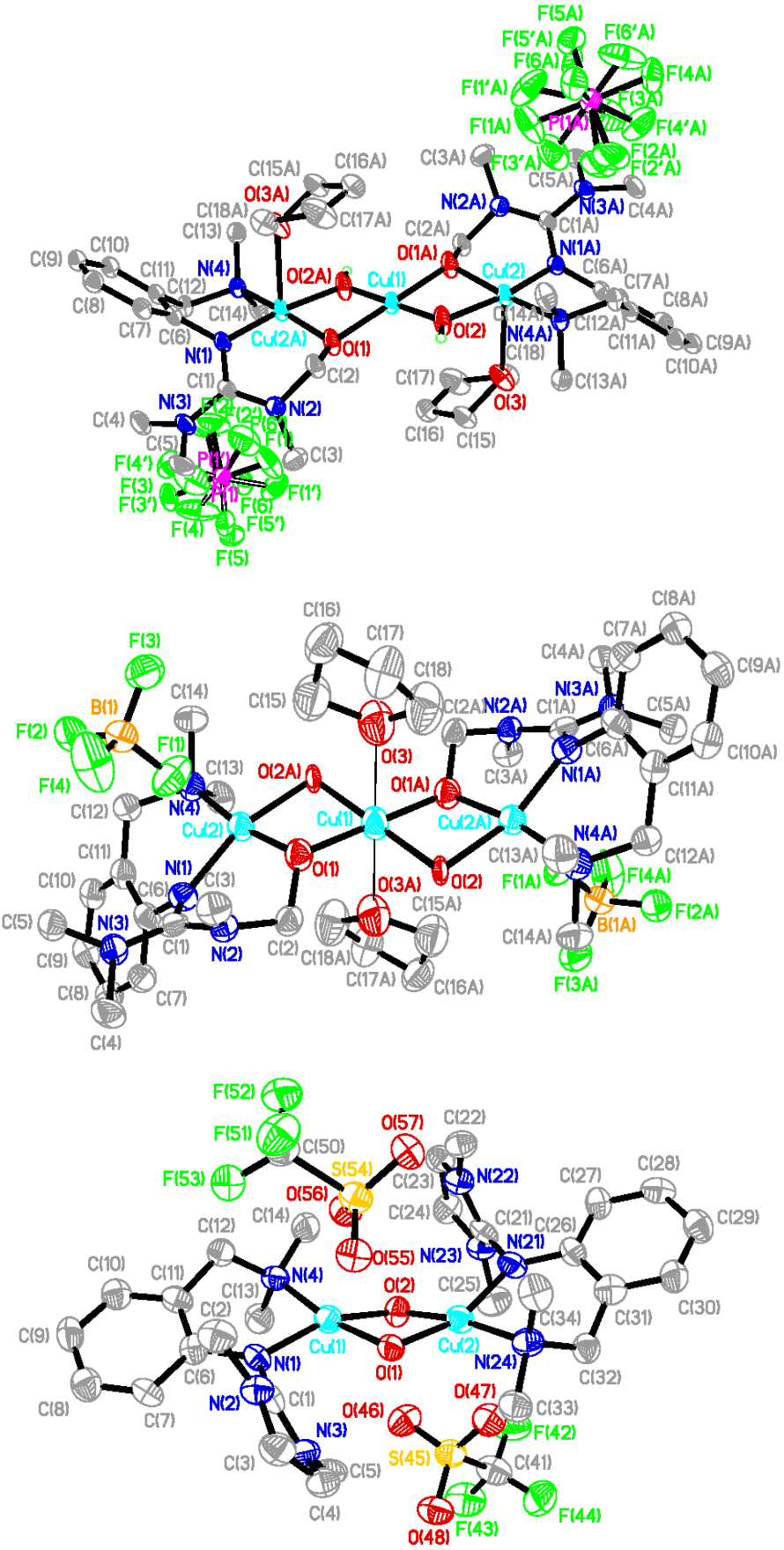

Figure 66: Molecular structures of the complexes [**H1**](PF$_6$)$_2$ (top), [**H1**](BF$_4$)$_2$ (middle) and [**H2**](OTf)$_2$ (bottom) in the solid state. Non-coordinating benzene molecules for [**H2**](OTf)$_2$ and hydrogen atoms were omitted for clarity. Displacement ellipsoids represent the 50% probability level.

Table 49: Crystallographic data and parameters of [**H1**]$(PF_6)_2$, [**H1**]$(BF_4)_2$ and [**H2**]$(OTf)_2$.

	[H1](PF$_6$)$_2$	**[H1](BF$_4$)$_2$**	**[H2](OTf)$_2$**
Empirical formula	$C_{36}H_{64}Cu_3F_{12}N_8O_6P_2$	$C_{36}H_{62}B_2Cu_3F_8N_8O_6$	$C_{54}H_{68}Cu_2F_6N_8O_8S_2$
Formula weight [g mol^{-1}]	1185.51	1067.17	1262.36
T [K], λ [Å]	100, 0.71073	100, 1.54186	100, 1.54186
Crystal system	Monoclinic	Triclinic	Monoclinic
Space group	$P2_1/n$	$P\bar{1}$	$P2_1/c$
a [Å]	9.2369(18)	8.5995(17)	20.498(4)
b [Å]	10.105(2)	8.8545(18)	9.934(2)
c [Å]	26.392(5)	16.097(3)	28.962(6)
α [°]	90	75.67(3)	90
β [°]	97.65(3)	81.55(3)	97.10(3)
γ [°]	90	73.08(3)	90
V [Å^3]	2441.4(9)	1132.4(5)	5852(2)
Z	2	1	4
ρ_{calc} [g cm^{-3}]	1.613	1.565	1.433
μ [mm^{-1}]	1.457	2.381	2.227
F(000)	1218	551	2624
Crystal size [mm]	0.190 x 0.150 x 0.110	0.090 x 0.070 x 0.050	0.17 x 0.08 x 0.03
hkl range	–9 ≤ h ≤ 13 –15 ≤ k ≤ 15 –36 ≤ l ≤ 39	–8 ≤ h ≤ 10 –10 ≤ k ≤ 9 –16 ≤ l ≤ 18	–23 ≤ h ≤ 17 –11 ≤ k ≤ 11 –32 ≤ l ≤ 33
Reflections collected	23367	9014	31430
Independent reflections	8772	3685	9660
R_{int}	0.0419	0.0594	0.1429
Number of parameters	371	291	729
R1 [I≥2σ(I)]	0.0568	0.0699	0.0780
wR_2 (all data)	0.1598	0.1955	0.2177
Goodness-of-fit	1.137	0.944	0.946
Largest diff. peak hole [eÅ^{-3}]	1.199, –1.199	0.851, –0.531	0.680, –0.891
Identification code	SH_00855	SH_00665	SH_00280

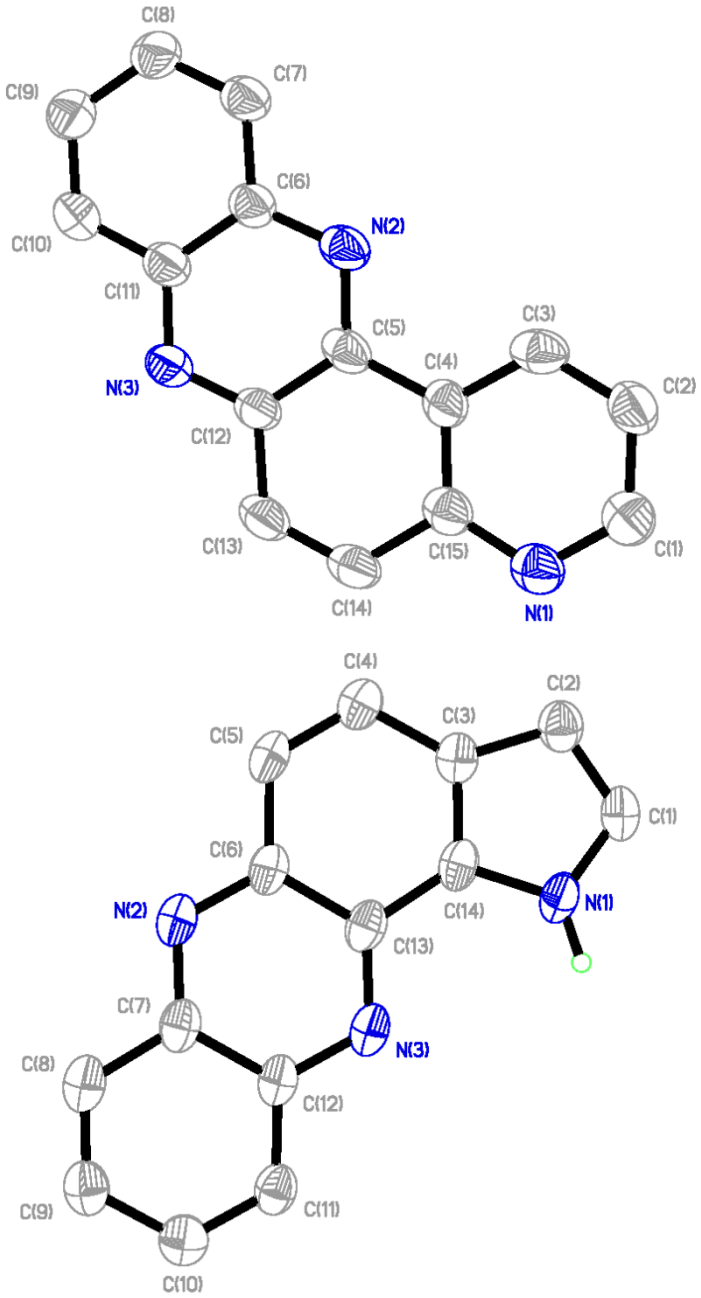

Figure 67: Molecular structures of the phenazines **P3** (top) and **P5** (bottom) in the solid state. Hydrogen atoms except for the NH group were omitted for clarity. Displacement ellipsoids represent the 50% probability level.

Table 50: Crystallographic data and parameters catalysis products **P3** and **P5**.

	P3	**P5**
Empirical formula	$C_{15}H_9N_3$	$C_{14}H_9N_3$
Formula weight [g mol^{-1}]	231.25	219.24
T [K]	100	100
λ [Å]	1.54186	1.54186
Crystal system	Monoclinic	Orthorhombic
Space group	*P*2$_1$/c	*P*bca
a [Å]	15.982(3)	6.9990(14)
b [Å]	4.9914(10)	13.519(3)
c [Å]	13.623(3)	21.134(4)
α [°]	90	90
β [°]	93.90(3)	90
γ [°]	90	90
V [Å^3]	1084.2(4)	1999.6(7)
Z	4	8
ρ_{calc} [g cm^{-3}]	1.417	1.457
μ [mm^{-1}]	0.691	0.714
F(000)	480	912
Crystal size [mm]	0.230 x 0.110 x 0.040	0.170 x 0.140 x 0.080
hkl range	–17 ≤ h ≤ 17	–8 ≤ h ≤ 6
	–5 ≤ k ≤ 5	–15 ≤ k ≤ 12
	–14 ≤ l ≤ 12	–24 ≤ l ≤ 24
Reflections collected	6345	11866
Independent reflections	1546	1689
R_{int}	0.0572	0.0562
Number of parameters	163	154
R1 [I≥2σ(I)]	0.0868	0.0730
wR_2 (all data)	0.2424	0.1713
Goodness-of-fit	1.140	1.207
Largest diff. peak hole [eÅ^{-3}]	0.273, –0.245	0.282, –0.258
Identification code	SH_00832	SH_00969

7.2. Cryo-UHR-ESI Mass Spectra

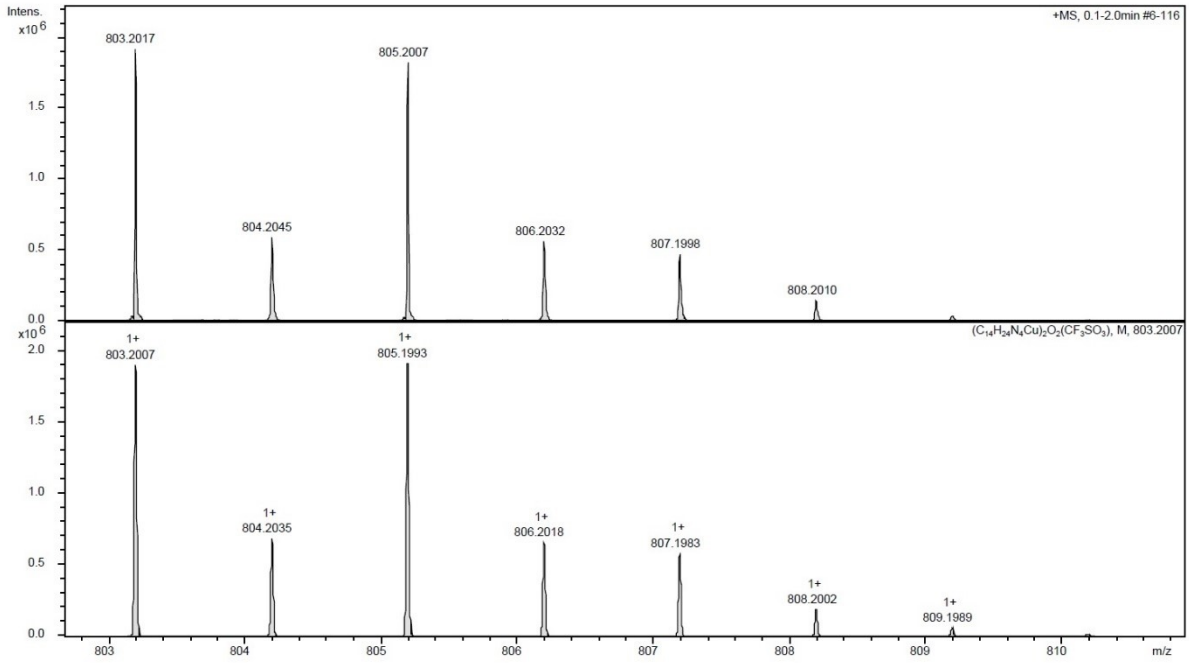

Figure 68: Cryo-UHR-ESI mass spectrometry of [**O1**](OTf)$^+$ in tetrahydrofuran at –80 °C (top: experimental, bottom: calculated spectra). This mass spectrum was recorded on an *UHR-TOF Bruker Daltonik maXis plus* by the group of Prof. Dr. Ivana Ivanović-Burmazović at the University of Erlangen-Nürnberg.

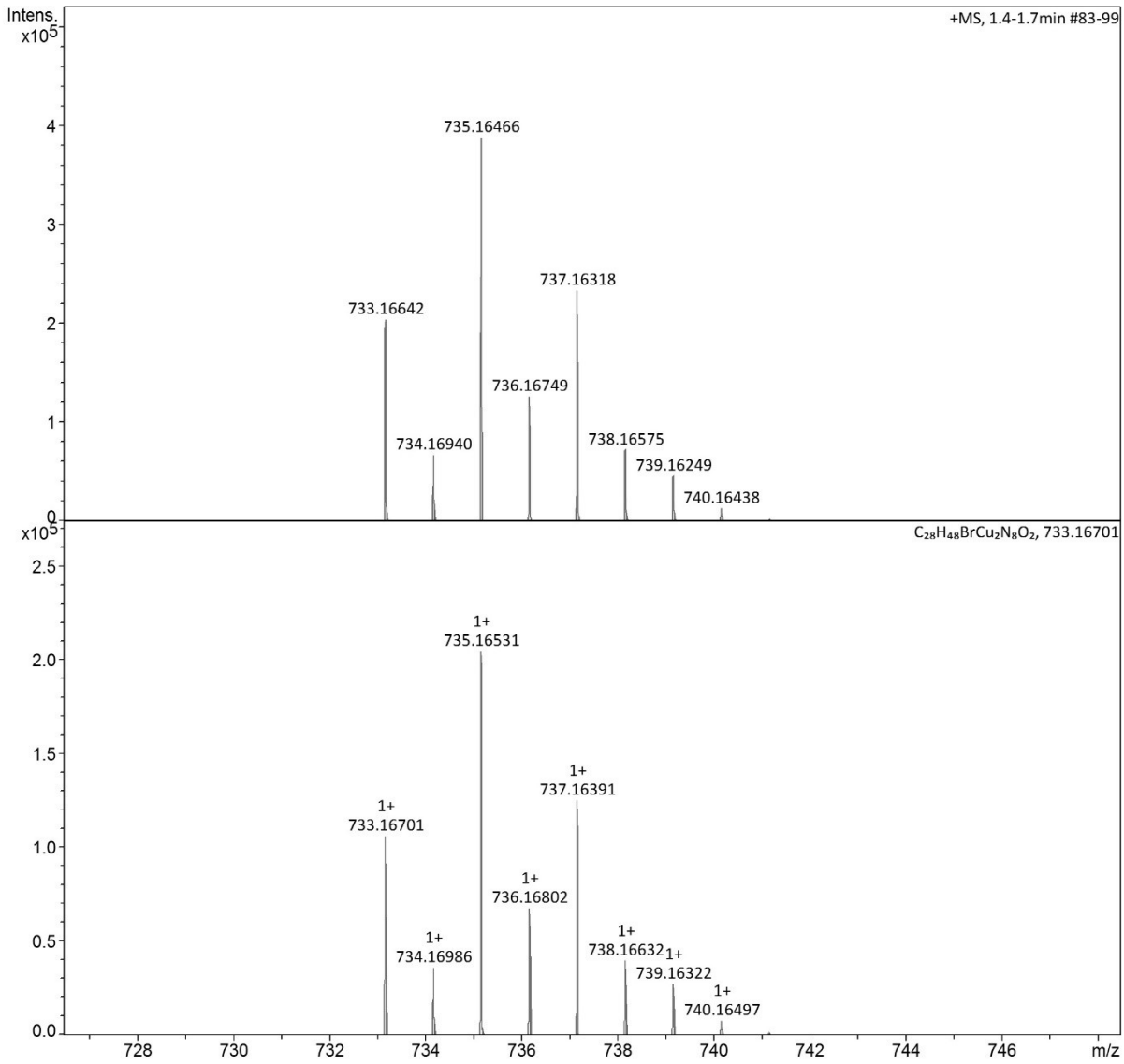

Figure 69: Cryo-UHR-ESI mass spectrometry of [**O1**](Br)$^+$ in tetrahydrofuran at –80 °C (top: experimental, bottom: calculated spectra). This mass spectrum was recorded on an *UHR-TOF Bruker Daltonik maXis II* and was published in literature.[246]

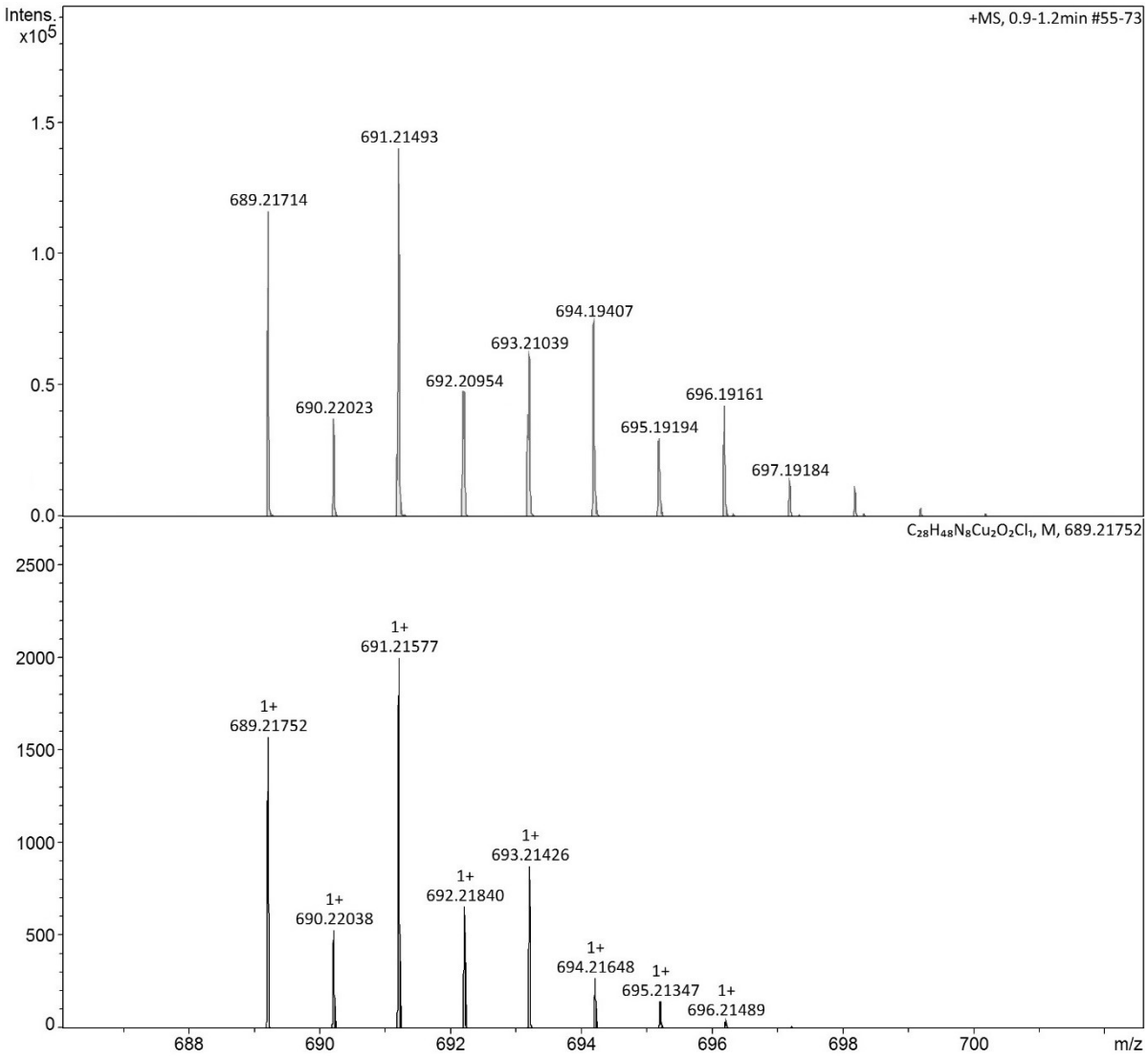

Figure 70: Cryo-UHR-ESI mass spectrometry of [**O1**](Cl)$^+$ in tetrahydrofuran at –80 °C (top: experimental, bottom: calculated spectra). This mass spectrum was recorded on an *UHR-TOF Bruker Daltonik maXis II* and was published in literature.[246]

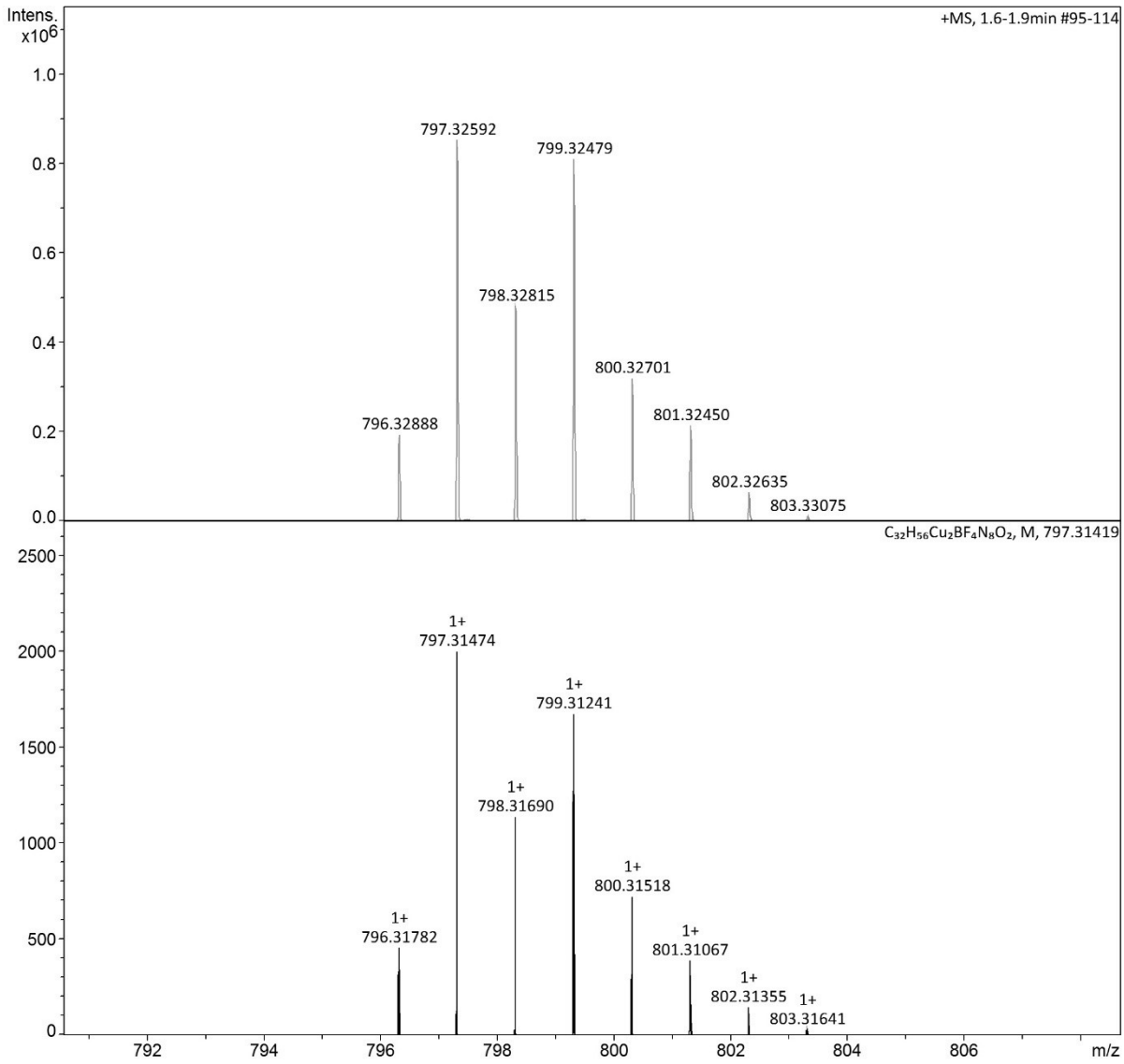

Figure 71: Cryo-UHR-ESI mass spectrometry of [**O3**]$(BF_4)^+$ in tetrahydrofuran at –80 °C (top: experimental, bottom: calculated spectra). This mass spectrum was recorded on an *UHR-TOF Bruker Daltonik maXis II* and was published in literature.[247]

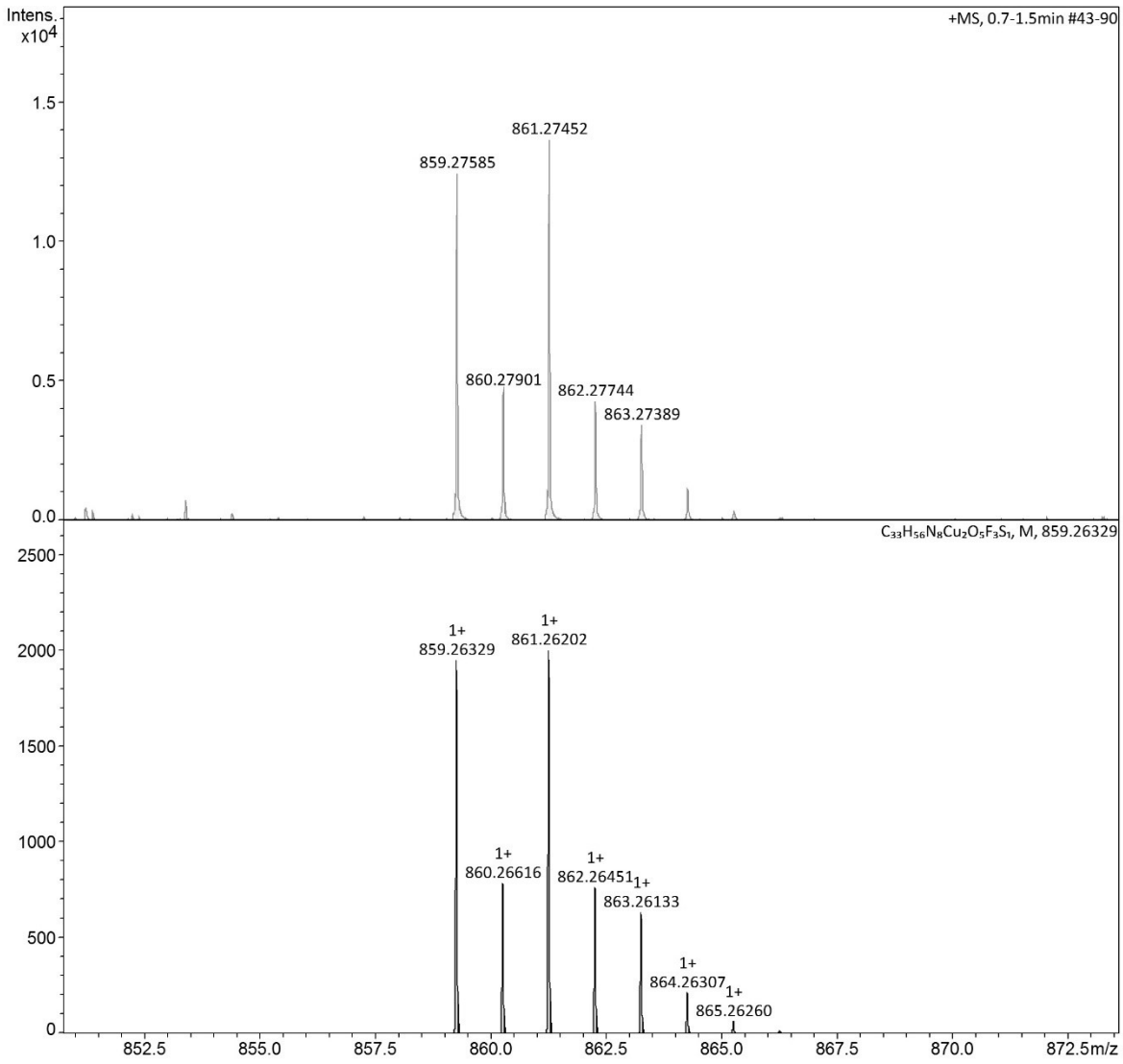

Figure 72: Cryo-UHR-ESI mass spectrometry of [**O3**](OTf)$^+$ in tetrahydrofuran at –80 °C (top: experimental, bottom: calculated spectra). This mass spectrum was recorded on an *UHR-TOF Bruker Daltonik maXis II* and was published in literature.[247]

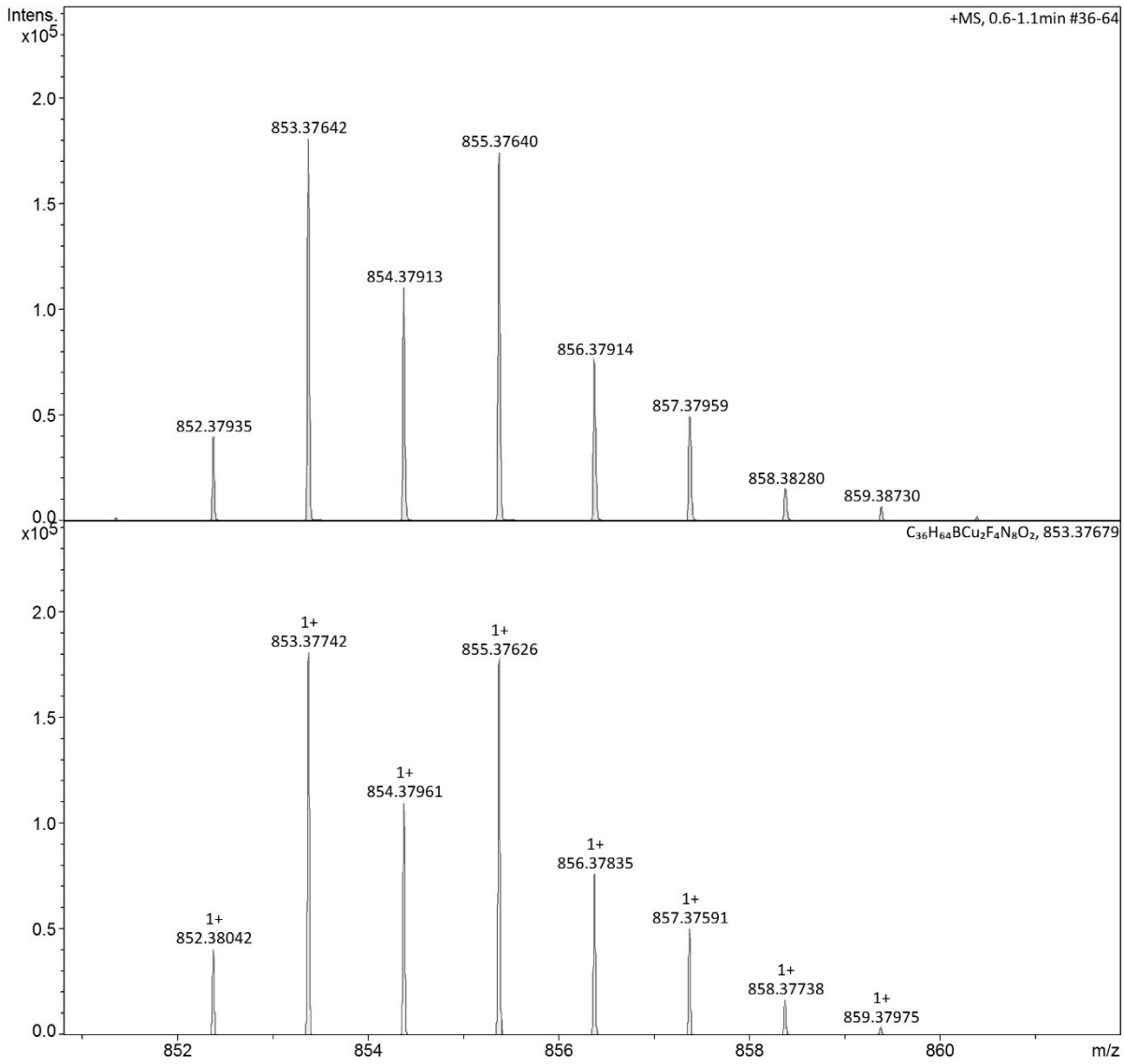

Figure 73: Cryo-UHR-ESI mass spectrometry of [**O4**]$(BF_4)^+$ in tetrahydrofuran at –80 °C (top: experimental, bottom: calculated spectra). This mass spectrum was recorded on an *UHR-TOF Bruker Daltonik maXis II* and was published in literature.[247]

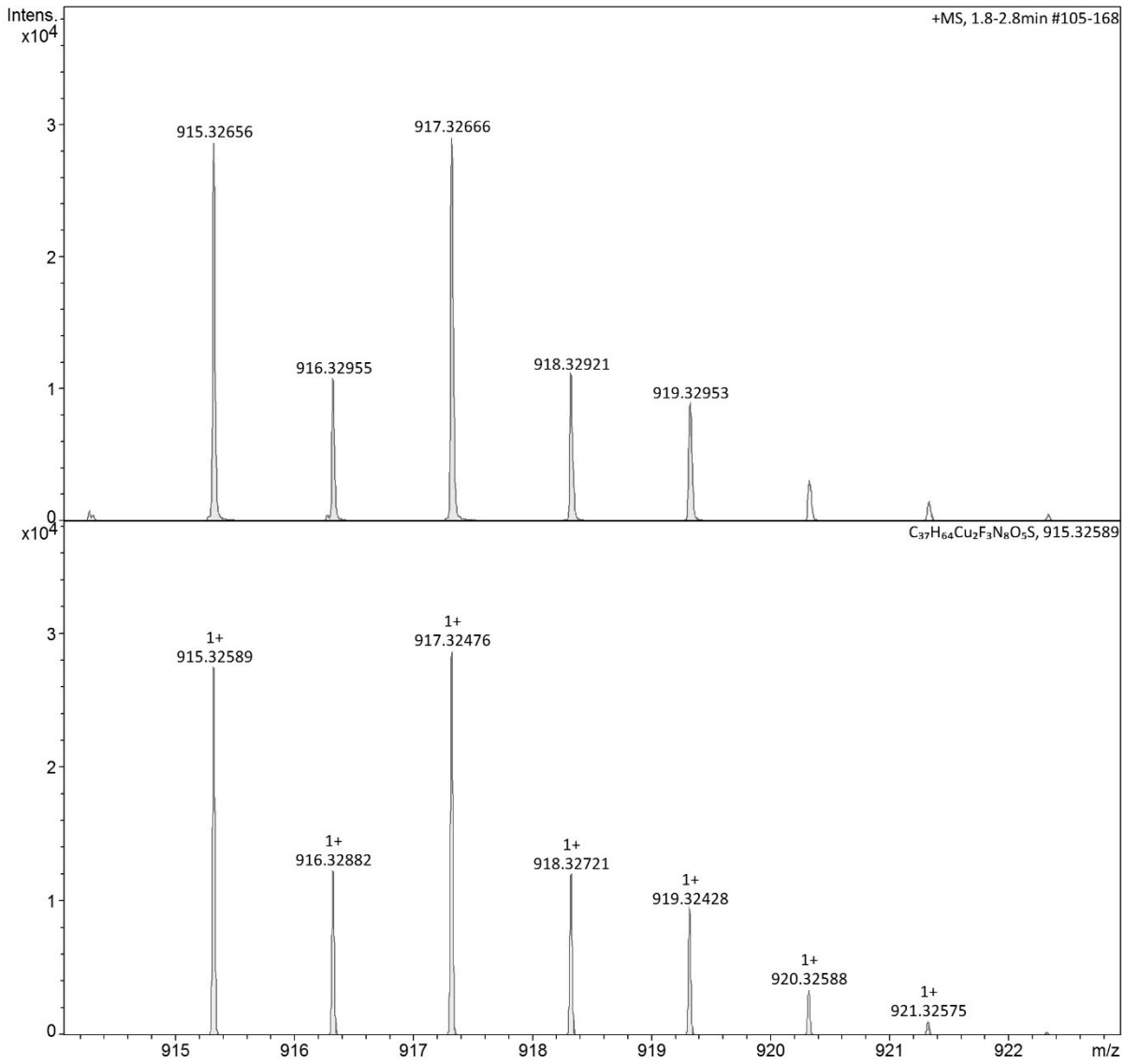

Figure 74: Cryo-UHR-ESI mass spectrometry of [**O4**](OTf)$^+$ in tetrahydrofuran at –80 °C (top: experimental, bottom: calculated spectra). This mass spectrum was recorded on an *UHR-TOF Bruker Daltonik maXis II* and was published in literature.[247]

7.3. UV/Vis Spectra

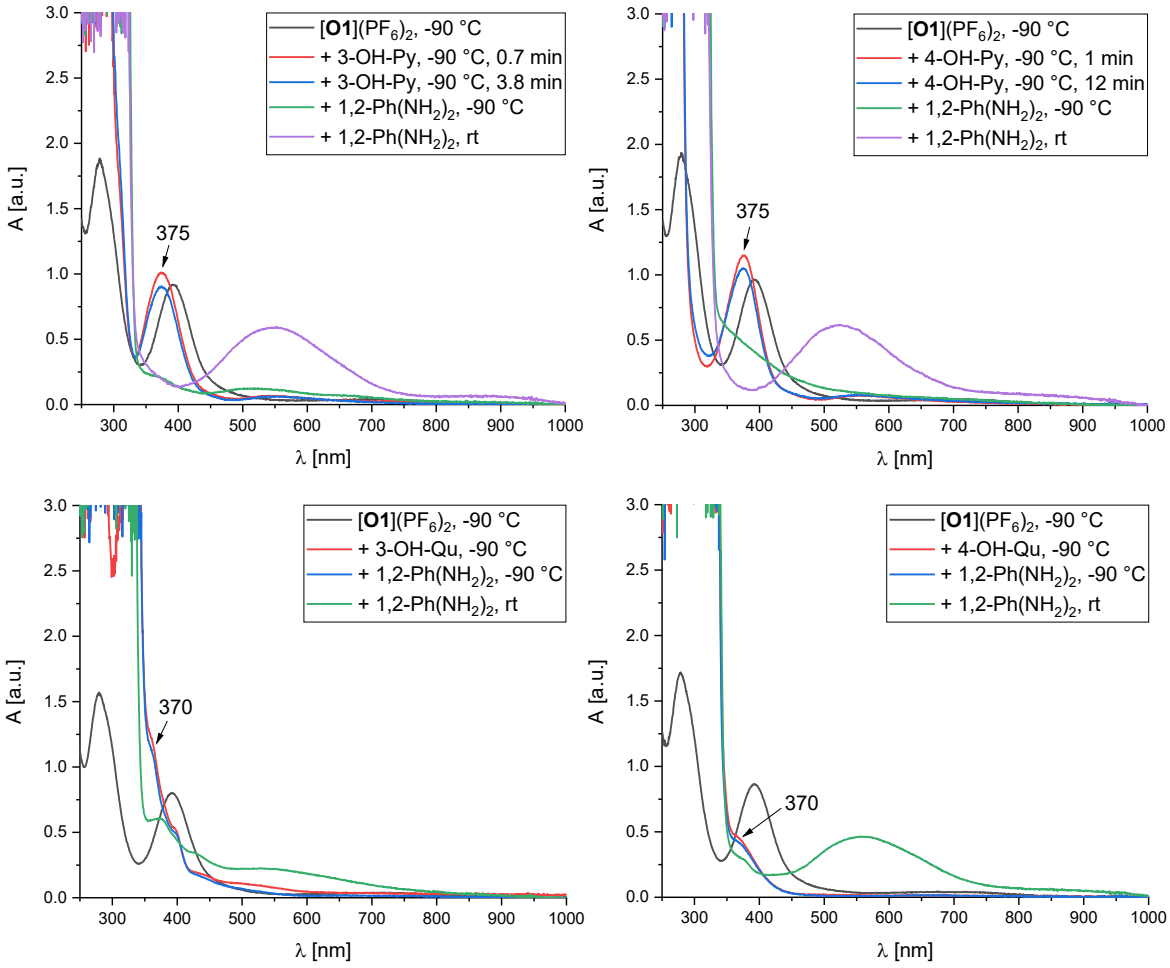

Figure 75: UV/Vis spectra of the oxygenation reactions of 3-pyridinol (top left), 4-pyridinol (top right), 3-quinolinol (bottom left), 4-quinolinol (bottom right) mediated by [**O1**](PF$_6$)$_2$ (0.5 mM) in tetrahydrofuran at –90 °C.

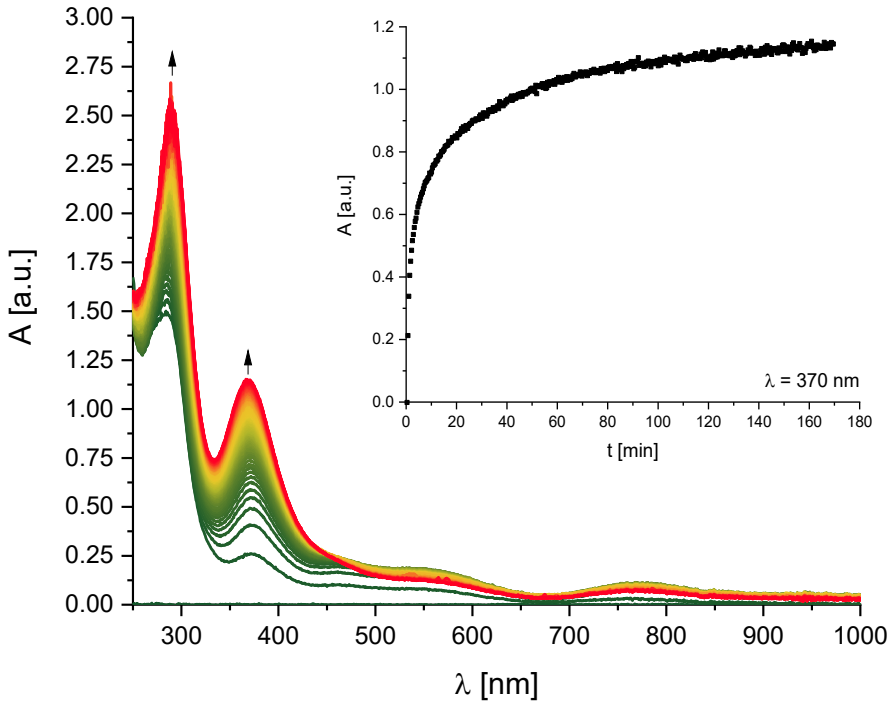

Figure 76: UV/Vis spectra of the oxygenation of **C10**·CuI to form [**O1I**](CuI_2) (0.5 mM) in tetrahydrofuran at room temperature.

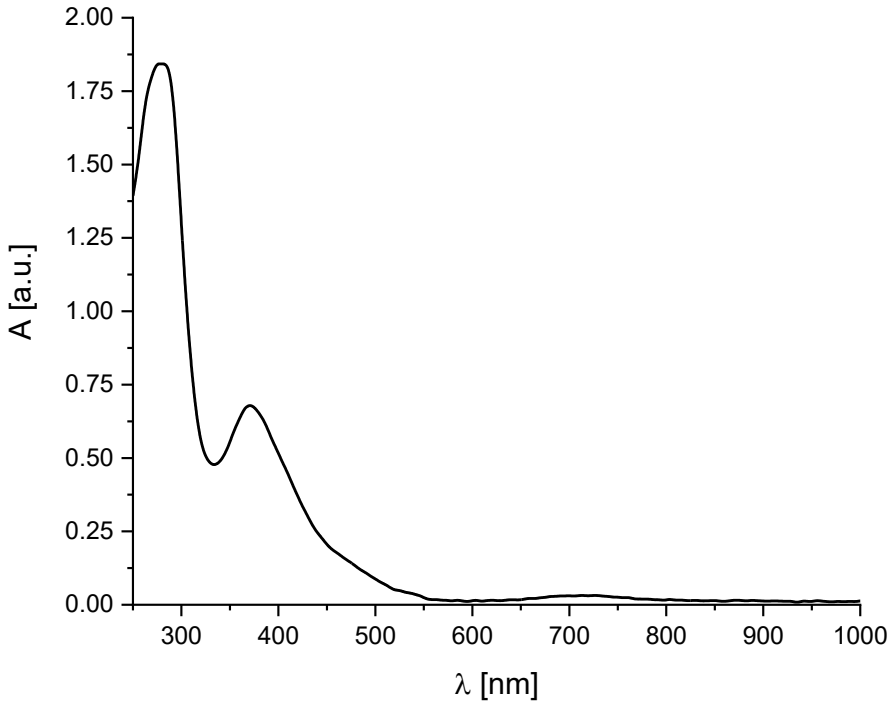

Figure 77: UV/Vis spectrum of the oxygenation of **C10** to form [**O1I**](CuI_2) (0.5 mM) in tetrahydrofuran at –80 °C after two hours.

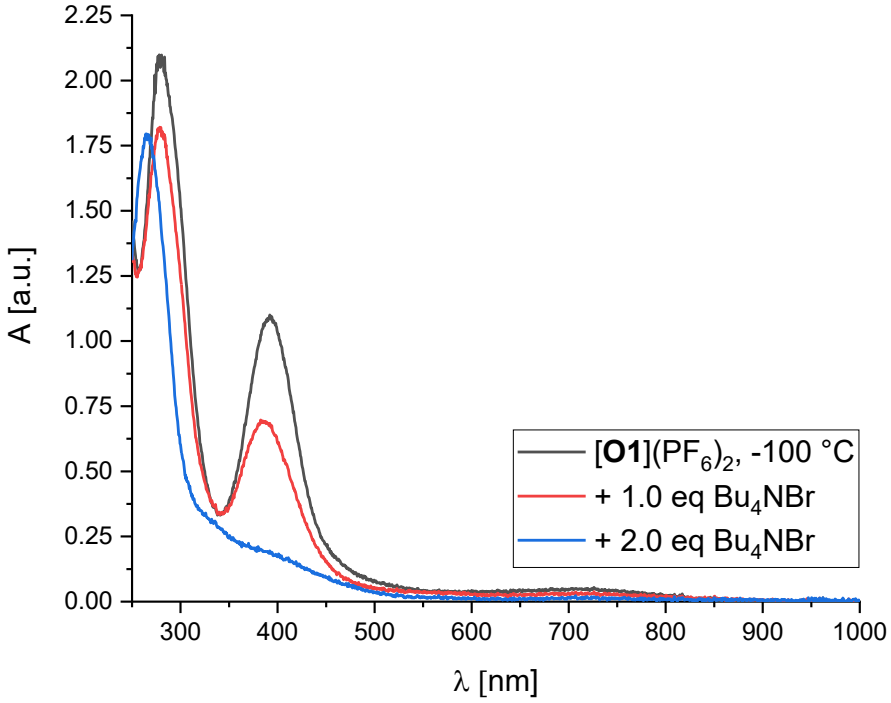

Figure 78: UV/Vis spectra of the salt metathesis of [**O1**]$(PF_6)_2$ (0.5 mM) with Bu_4NBr in tetrahydrofuran at –100 °C.

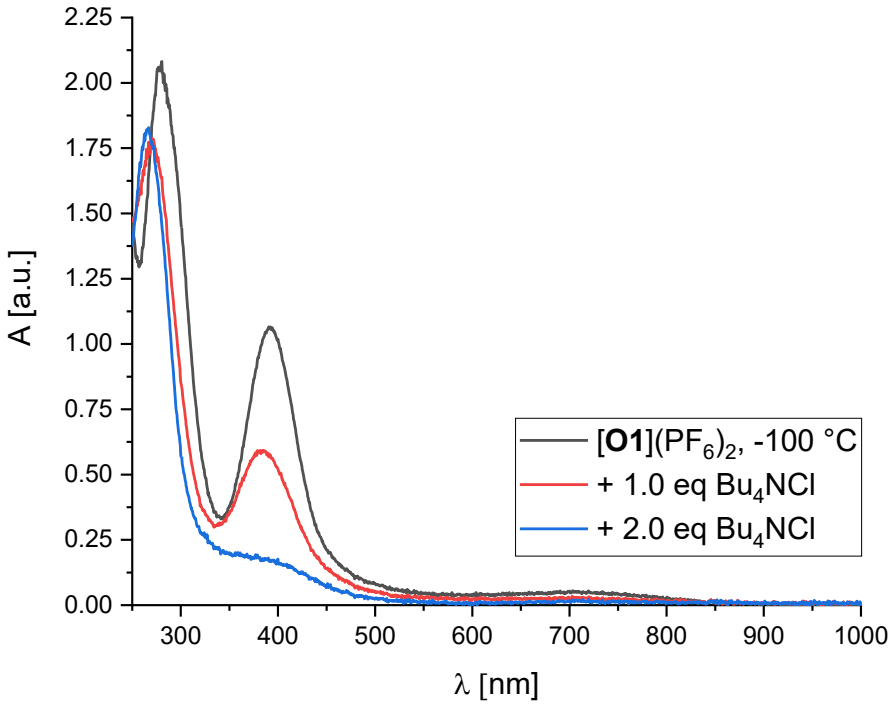

Figure 79: UV/Vis spectra of the salt metathesis of [**O1**]$(PF_6)_2$ (0.5 mM) with Bu_4NCl in tetrahydrofuran at –100 °C.

7.4. Resonance Raman Spectra

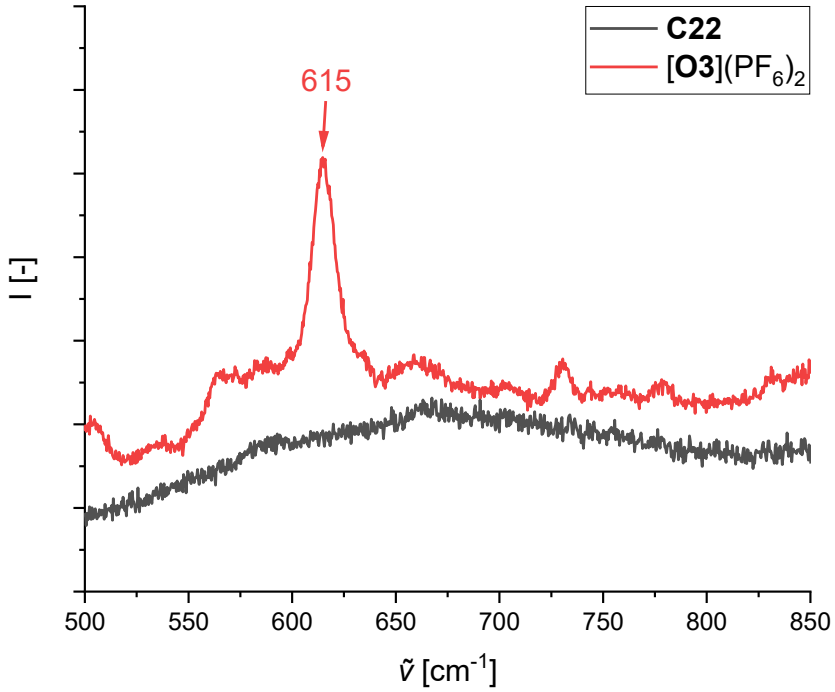

Figure 80: Resonance Raman spectra of copper(I) complex **C22** (black) and bis(μ-oxido) species [**O3**](PF$_6$)$_2$ (red) in a tetrahydrofuran/acetonitrile mixture (80:20) at –90 °C (excitation at 532 nm). The resonance Raman spectrum was recorded by the group of Prof. Dr. Michael Rübhausen at the CFEL in Hamburg.

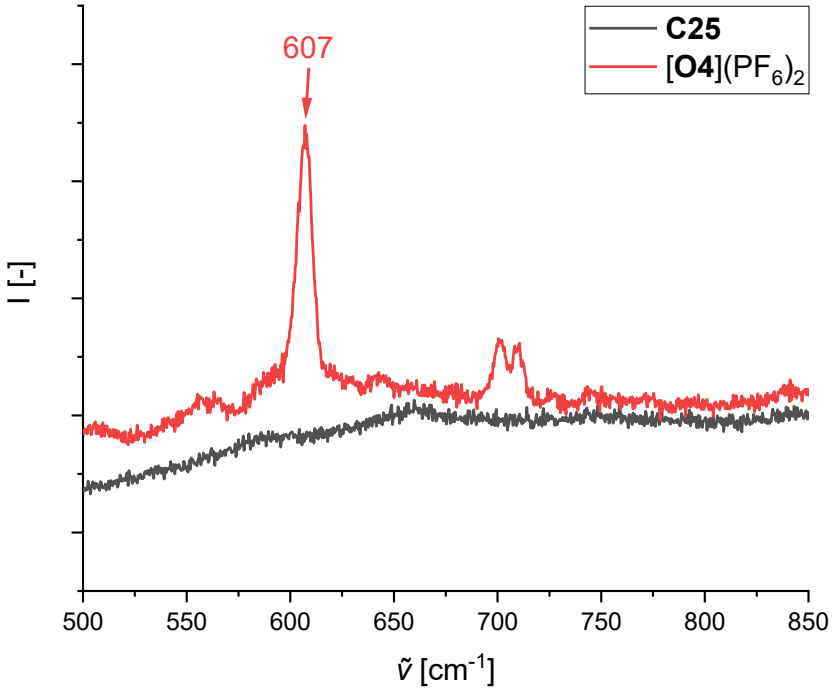

Figure 81: Resonance Raman spectra of copper(I) complex **C25** (black) and bis(μ-oxido) species [**O4**](PF$_6$)$_2$ (red) in a tetrahydrofuran/acetonitrile mixture (80:20) at –90 °C (excitation at 532 nm). The resonance Raman spectrum was recorded by the group of Prof. Dr. Michael Rübhausen at the CFEL in Hamburg.

7.5. NMR Spectra

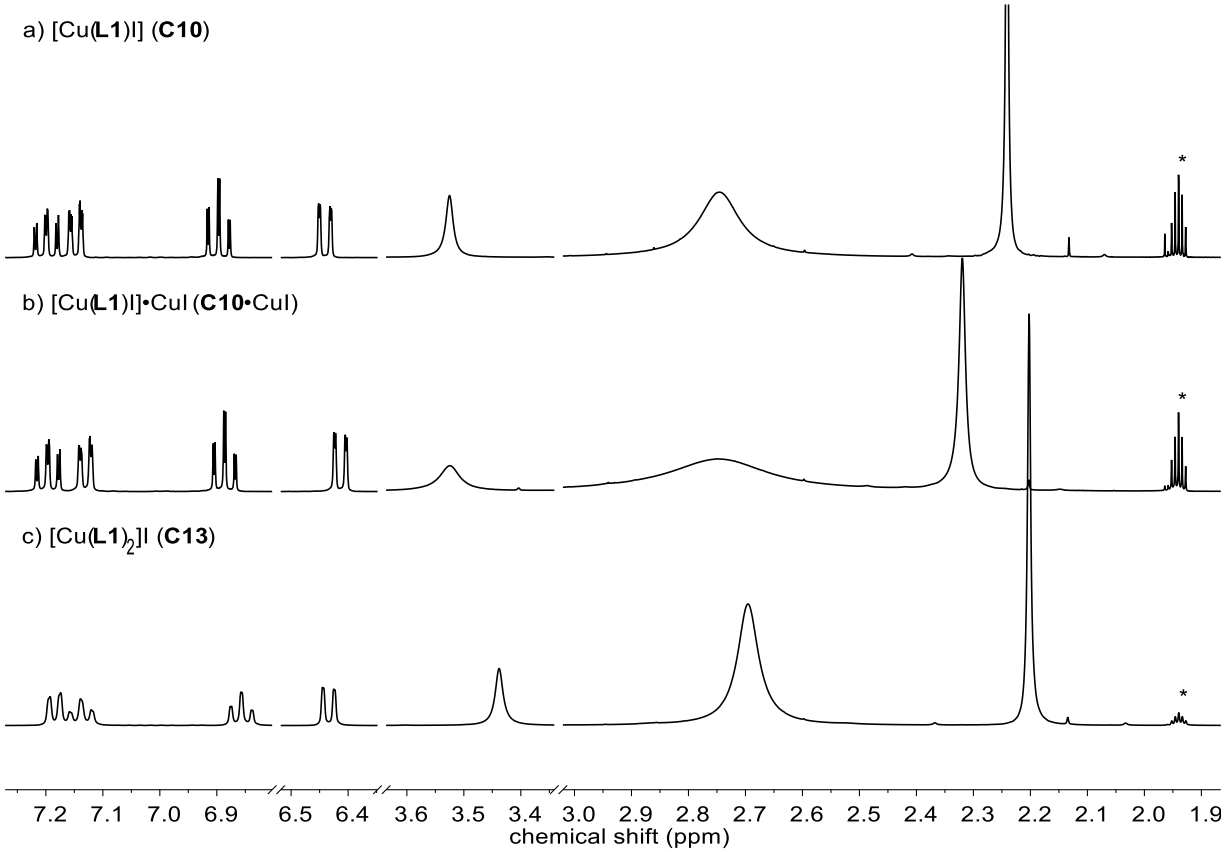

Figure 82: ^{1}H NMR spectra of a) [Cu(**L1**)I] (**C10**), b) [Cu(**L1**)I]·CuI (**C10**·CuI) and c) [Cu(**L1**)$_2$]I (**C13**) (* = CD_3CN).

7.6. DFT and TD-DFT Calculations of $[O1]^{2+}$, $[O1I]^{+}$, $[O3]^{2+}$, and $[O4]^{2+}$

LUMO+3

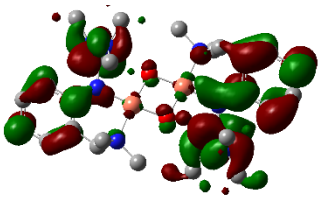

LUMO+2

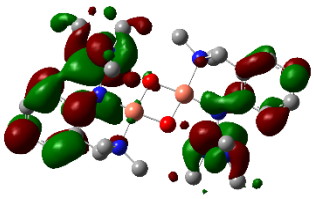

LUMO+1

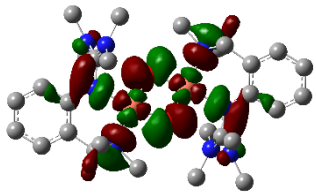

LUMO

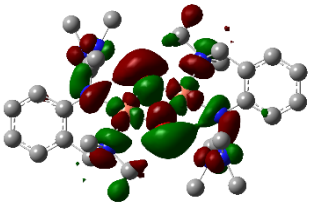

HOMO

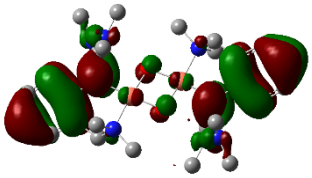

HOMO-1

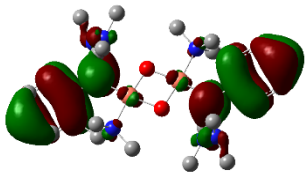

HOMO-2

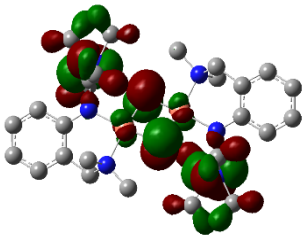

HOMO-3

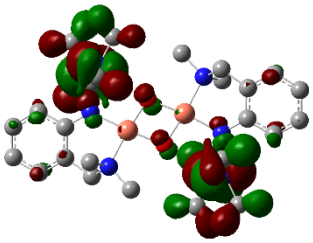

HOMO-4

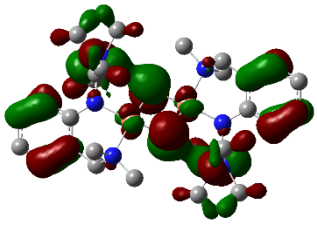

HOMO-5

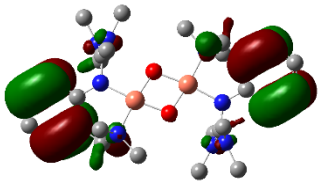

HOMO-6

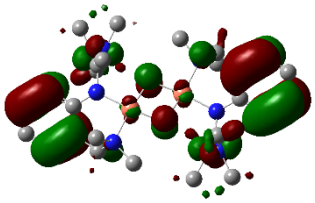

HOMO-7

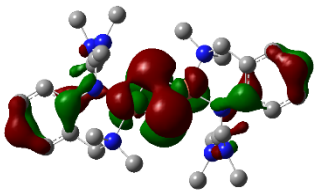

HOMO-8

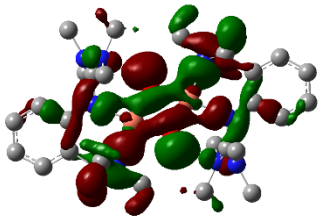

HOMO-9

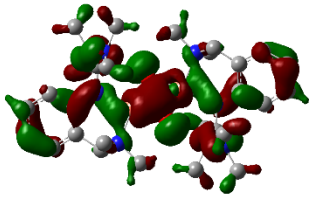

HOMO-10

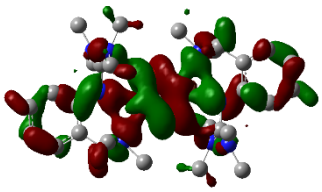

HOMO-11

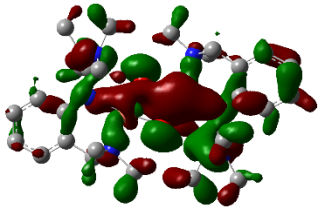

HOMO-12

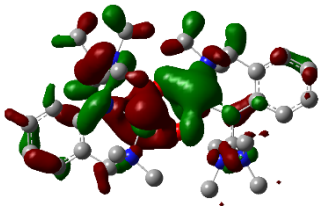

HOMO-13

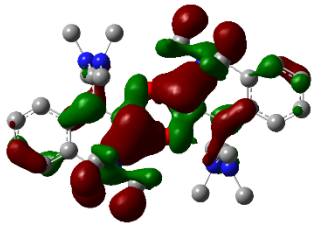

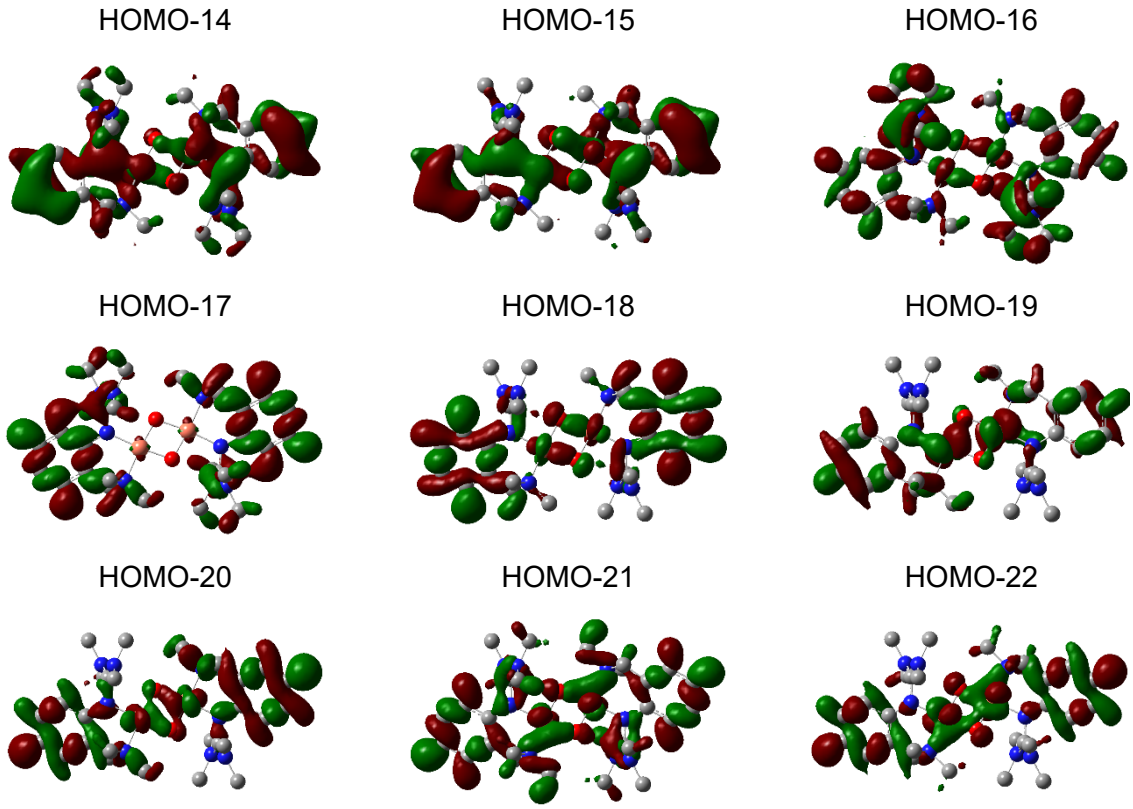

Figure 83: Selected molecular orbitals of [**O1**]$^{2+}$ (TPSSh/def2-TZVP, GD3BJ).

Table 51: MO energies of [**O1**]$^{2+}$ (TPSSh/def2-TZVP, GD3BJ).

MO	E [H]	e [eV]	MO composition
LUMO+3	-0.06817	-1.85500114	π*(benza) and π*(gua)
LUMO+2	-0.06866	-1.86833472	π*(benza) and π*(gua)
LUMO+1	-0.16427	-4.47001668	π_σ* - Cu d - N
LUMO	-0.17384	-4.73042978	σ* - Cu d - N
HOMO	-0.23284	-6.33590238	π*(benza) - π(gua) - π_v (nb)
HOMO-1	-0.23558	-6.41046161	π*(benza) and π*(gua)
HOMO-2	-0.26339	-7.16721065	Cu d - π_v* and LP N(amine)
HOMO-3	-0.26584	-7.23387858	LP N(amine) and π_v (nb)
HOMO-4	-0.27086	-7.3704798	Cu d - π_v* and π*(benza) and LP N(amine)
HOMO-5	-0.27311	-7.43170545	LP(benza)
HOMO-6	-0.27349	-7.44204579	LP(benza) and π_v*
HOMO-7	-0.2915	-7.9321231	Cu d - π_v
HOMO-8	-0.29791	-8.10654817	Cu d + σ* - N
HOMO-9	-0.30912	-8.41158797	Cu d + σ + N
HOMO-10	-0.31692	-8.62383689	Cu d + π_σ + N
HOMO-11	-0.32454	-8.83118776	Cu d - σ*(tilted) + N(gua)
HOMO-12	-0.32508	-8.84588191	Cu d (tilted) + π_σ + N
HOMO-13	-0.32832	-8.93404685	N(amine) + Cu d + π_σ*(tilted)
HOMO-14	-0.33167	-9.02520504	Cu d + N(gua) and benza and π_v*
HOMO-15	-0.3328	-9.05595392	Cu d + N(gua) and π(benza) and π_v*
HOMO-16	-0.35684	-9.71011598	σ(benza) and π(gua) and d - π_σ*(tilted)
HOMO-17	-0.35664	-9.7046737	σ(benza) and σ(gua)
HOMO-18	-0.36021	-9.80181839	σ(benza) and Cu d and tilted π_σ
HOMO-19	-0.36713	-9.99012128	σ(benza) and Cu d
HOMO-20	-0.36875	-10.0342038	σ(benza) and Cu d + π_σ
HOMO-21	-0.36933	-10.0499864	σ(benza) and Cu d - π_σ*
HOMO-22	-0.37183	-10.1180149	σ(benza) and Cu d and σ

LUMO+3

LUMO+2

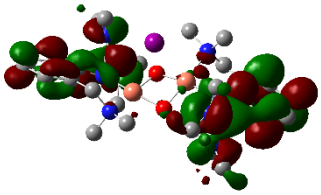

LUMO+1

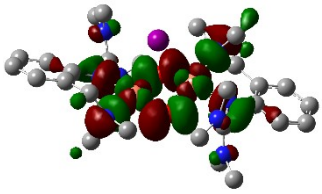

LUMO

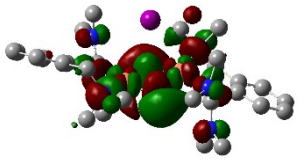

HOMO

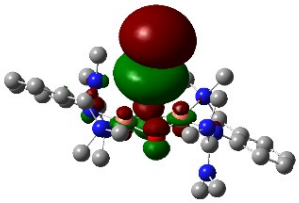

HOMO-1

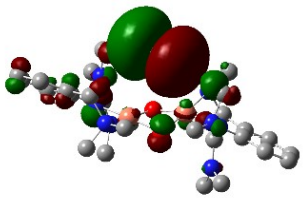

HOMO-2

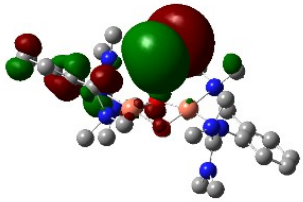

HOMO-3

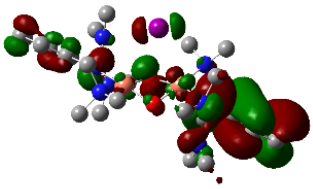

HOMO-4

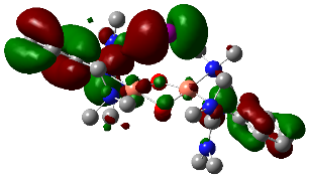

HOMO-5

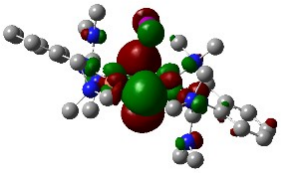

HOMO-6

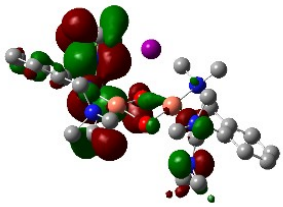

HOMO-7

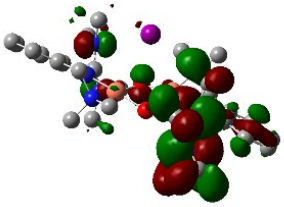

HOMO-8

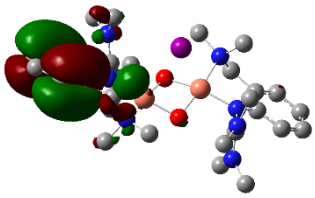

HOMO-9

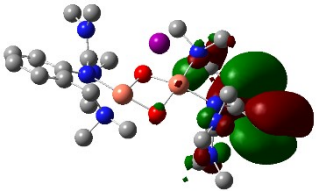

HOMO-10

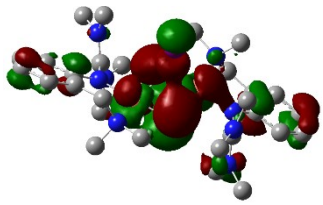

HOMO-11

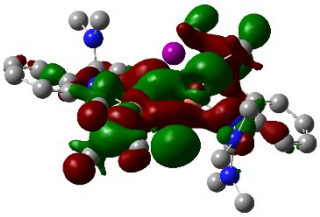

HOMO-12

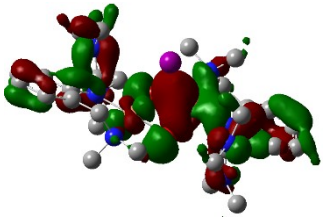

HOMO-13

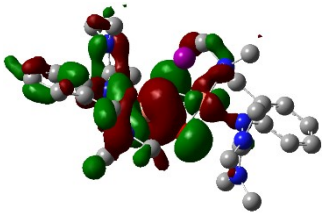

HOMO-14

HOMO-15

HOMO-16

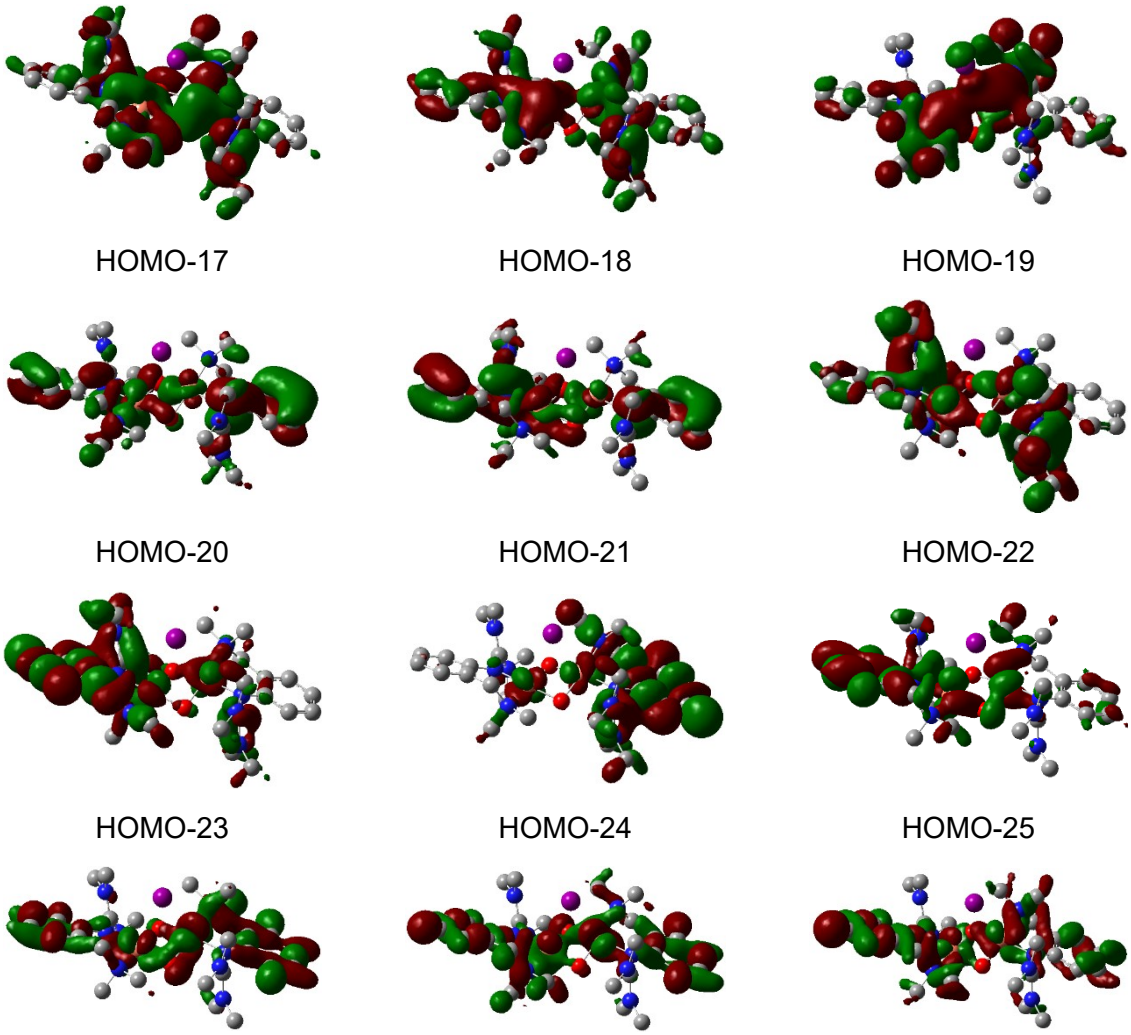

Figure 84: Selected Molecular orbitals of [**O1I**]$^{+}$ (TPSSh/def2-TZVP, GD3BJ).

Table 52: MO energies of [**O1I**]$^+$ (TPSSh/def2-TZVP, GD3BJ).

MO	E [H]	e [eV]	MO composition
LUMO+3	-0.0525	-1.4285985	π*(benza) and π*(gua)
LUMO+2	-0.05323	-1.44846282	π*(benza) and π*(gua)
LUMO+1	-0.14543	-3.9573539	π_σ* - Cu d - N
LUMO	-0.14997	-4.08089366	σ* - Cu d - N
HOMO	-0.20653	-5.61997044	LP(I)
HOMO-1	-0.20996	-5.71330554	LP(I)
HOMO-2	-0.2108	-5.73616312	LP(I)
HOMO-3	-0.2171	-5.90759494	π*(benza) and π(gua)
HOMO-4	-0.22128	-6.02133859	π*(benza) and LP(I)
HOMO-5	-0.24055	-6.54570227	Cu d - π_v*
HOMO-6	-0.24961	-6.79223755	π*(gua)
HOMO-7	-0.25232	-6.86598045	π*(gua)
HOMO-8	-0.25928	-7.05537179	π*(benza)
HOMO-9	-0.26017	-7.07958994	π*(benza)
HOMO-10	-0.26822	-7.29864171	Cu d - π_v + LP(I)
HOMO-11	-0.27974	-7.61211704	Cu d + σ* - N
HOMO-12	-0.28927	-7.87144168	Cu d - π_σ(tilted) + N
HOMO-13	-0.29086	-7.9147078	linear combination of π_σ(tilted) and σ + N
HOMO-14	-0.30291	-8.24260517	Cu d – σ(tilted) + N
HOMO-15	-0.30487	-8.29593952	linear combination π_v and π_σ bonding with Cu d and + N
HOMO-16	-0.30895	-8.40696203	π_σ*(tilted) + N + LP(I) + d
HOMO-17	-0.31488	-8.56832563	N(gua) + Cu d - π_v(tilted) and π(benza)
HOMO-18	-0.31624	-8.60533314	Cu d - π_v(tilted) + N(gua) and π(benza)
HOMO-19	-0.33517	-9.12044494	Cu d - π_v(tilted) + N and π(gua)
HOMO-20	-0.34031	-9.26031153	σ(benza) and Cu d
HOMO-21	-0.3428	-9.32806792	σ(benza) and σ(gua) and Cu d
HOMO-22	-0.34647	-9.42793376	σ(benza) and σ(gua) and Cu d
HOMO-23	-0.34705	-9.44371637	σ(benza) and Cu d
HOMO-24	-0.35065	-9.54167741	σ(benza) and Cu d
HOMO-25	-0.35158	-9.56698401	σ(benza) and Cu d and N

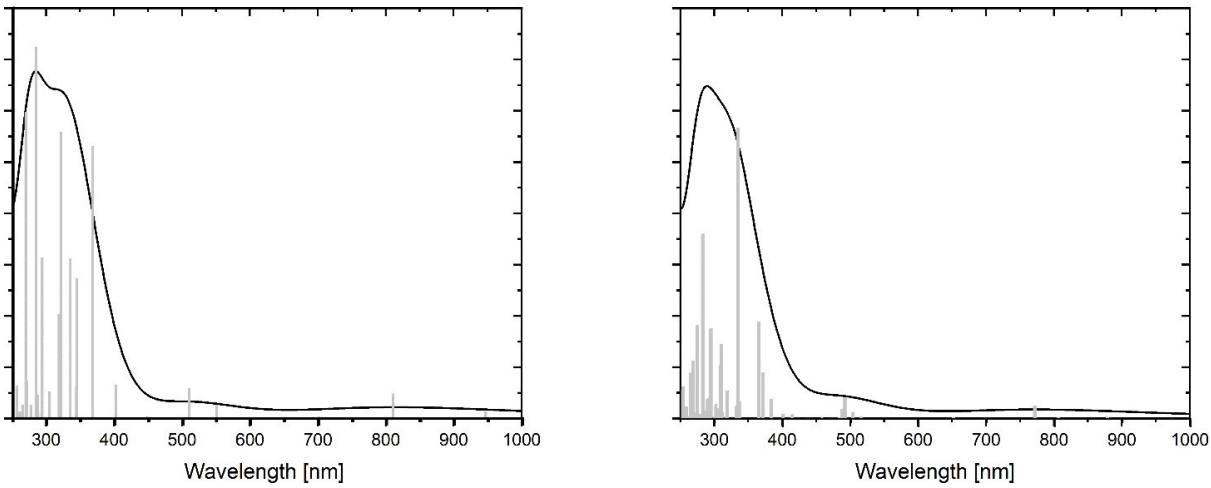

Figure 85: TD-DFT-predicted optical spectra of [**O1**]$^{2+}$ (left) and [**O1I**]$^{+}$ (right) with TPSSh/def2-TZVP with solvent THF and GD3BJ.

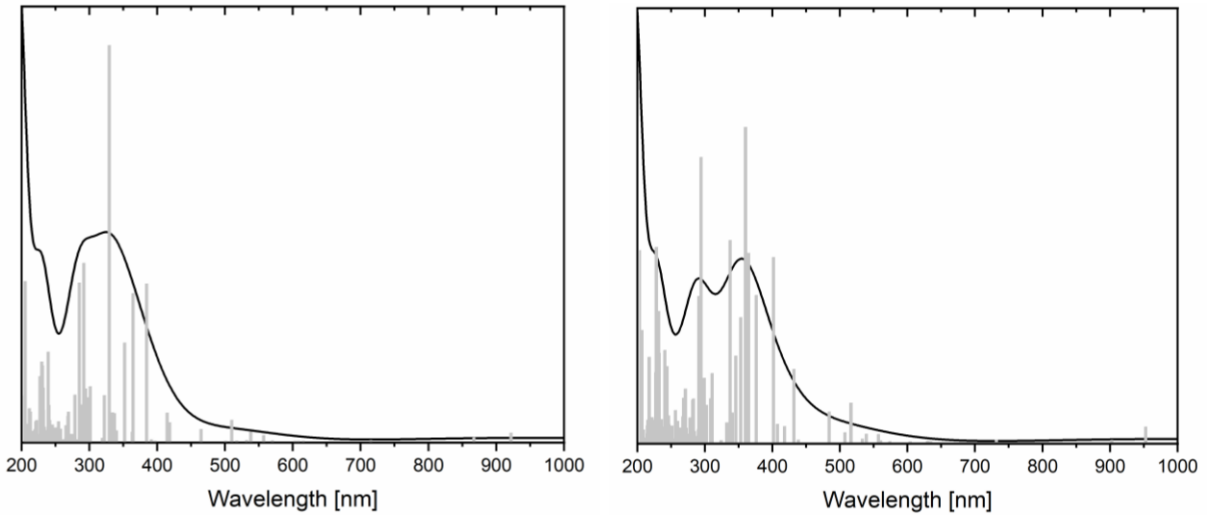

Figure 86: TD-DFT-predicted optical spectra of [**O3**]$^{2+}$ (left) and [**O4**]$^{2+}$ (right) with TPSSh/def2-TZVP and GD3BJ.

Table 53: Selected molecular orbitals of [**O1**]$^{2+}$, [**O3**]$^{2+}$ and [**O4**]$^{2+}$ (TPSSh/def2-TZVP, GD3BJ).

MO	[**O1**]$^{2+}$	[**O3**]$^{2+}$	[**O4**]$^{2+}$
LUMO+3	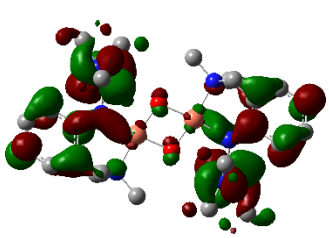	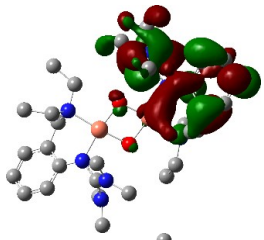	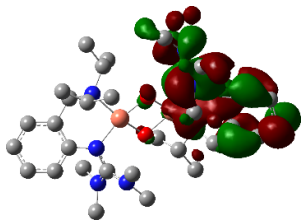
LUMO+2	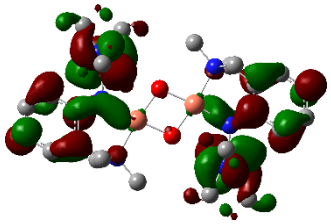	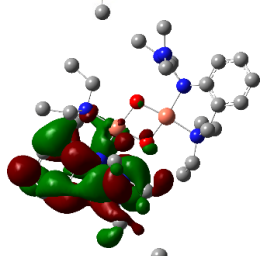	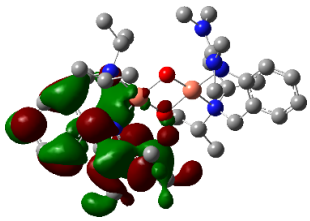
LUMO+1	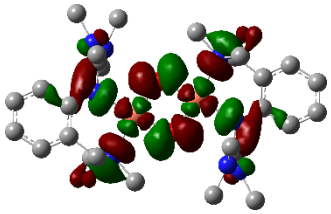	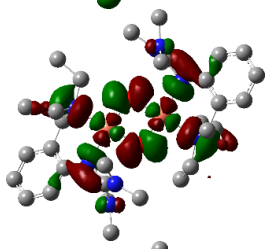	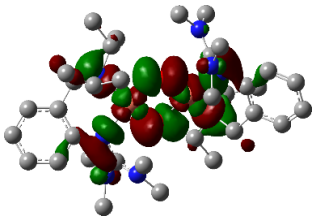
LUMO	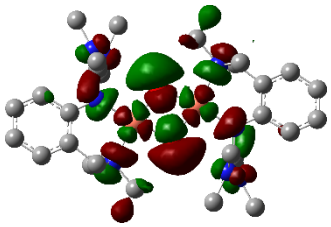	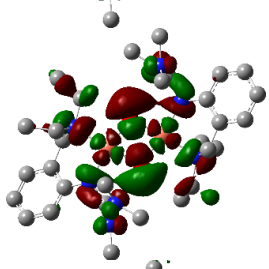	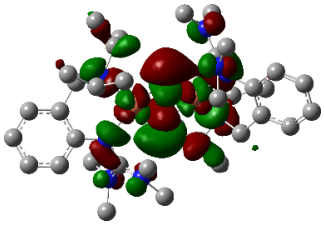
HOMO	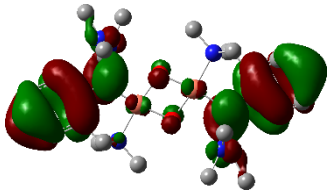	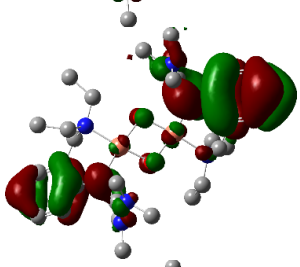	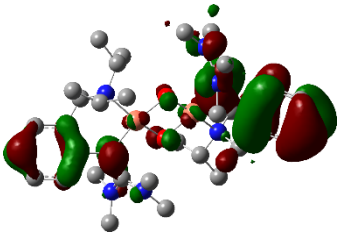
HOMO-1	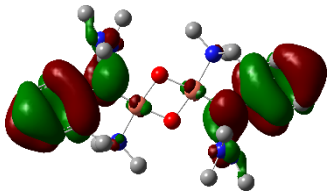	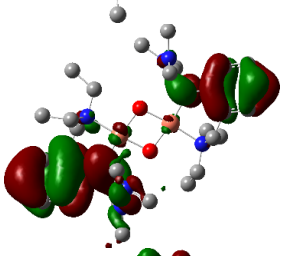	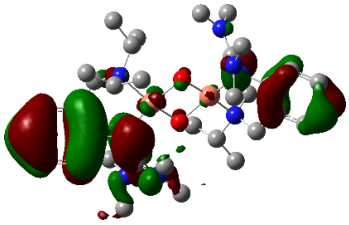
HOMO-2	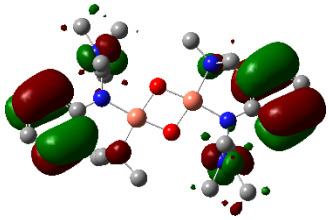	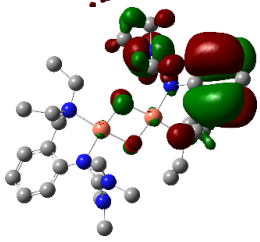	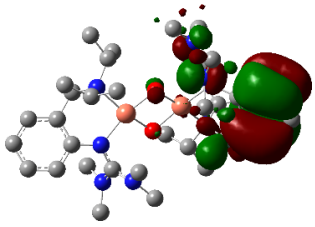

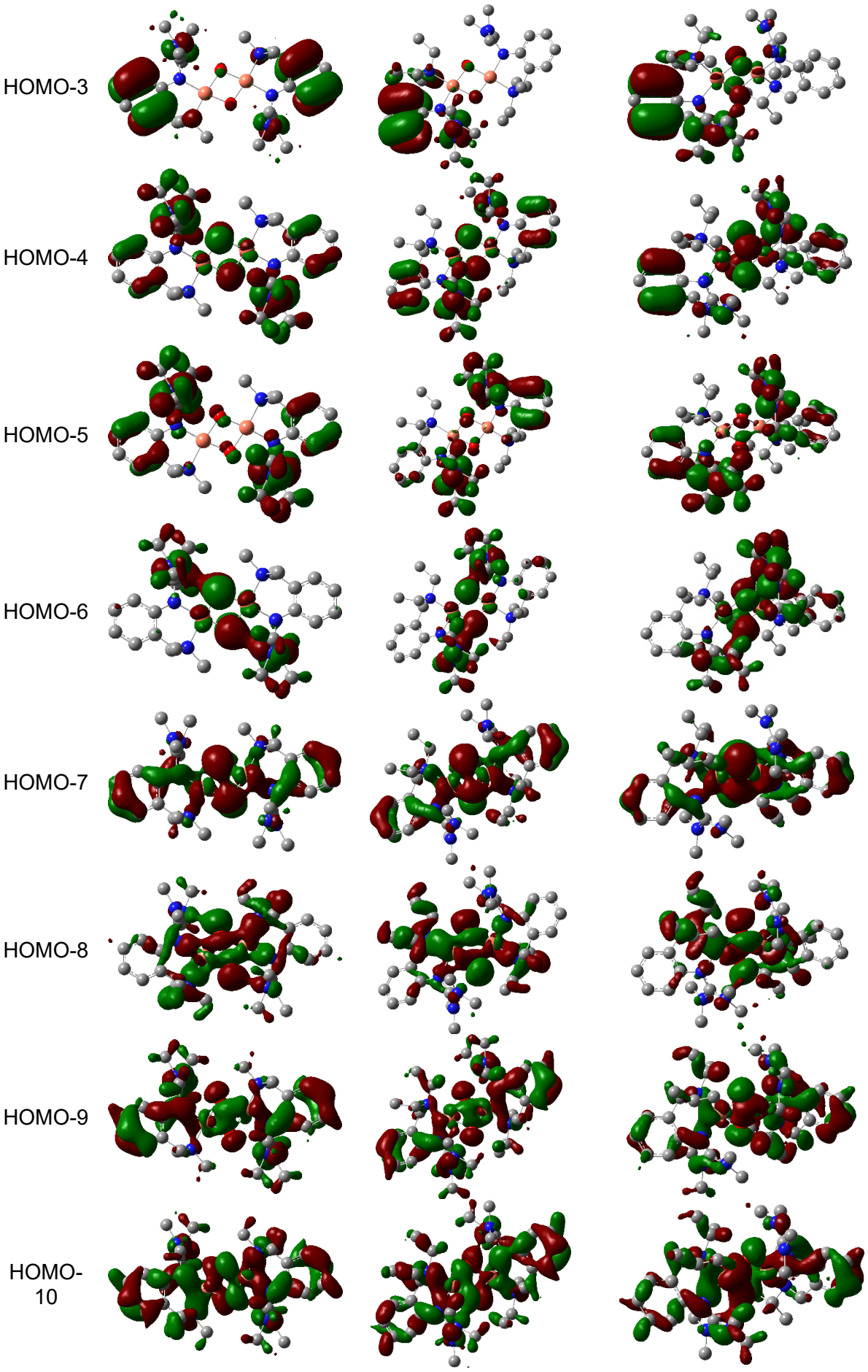
HOMO-3
HOMO-4
HOMO-5
HOMO-6
HOMO-7
HOMO-8
HOMO-9
HOMO-10

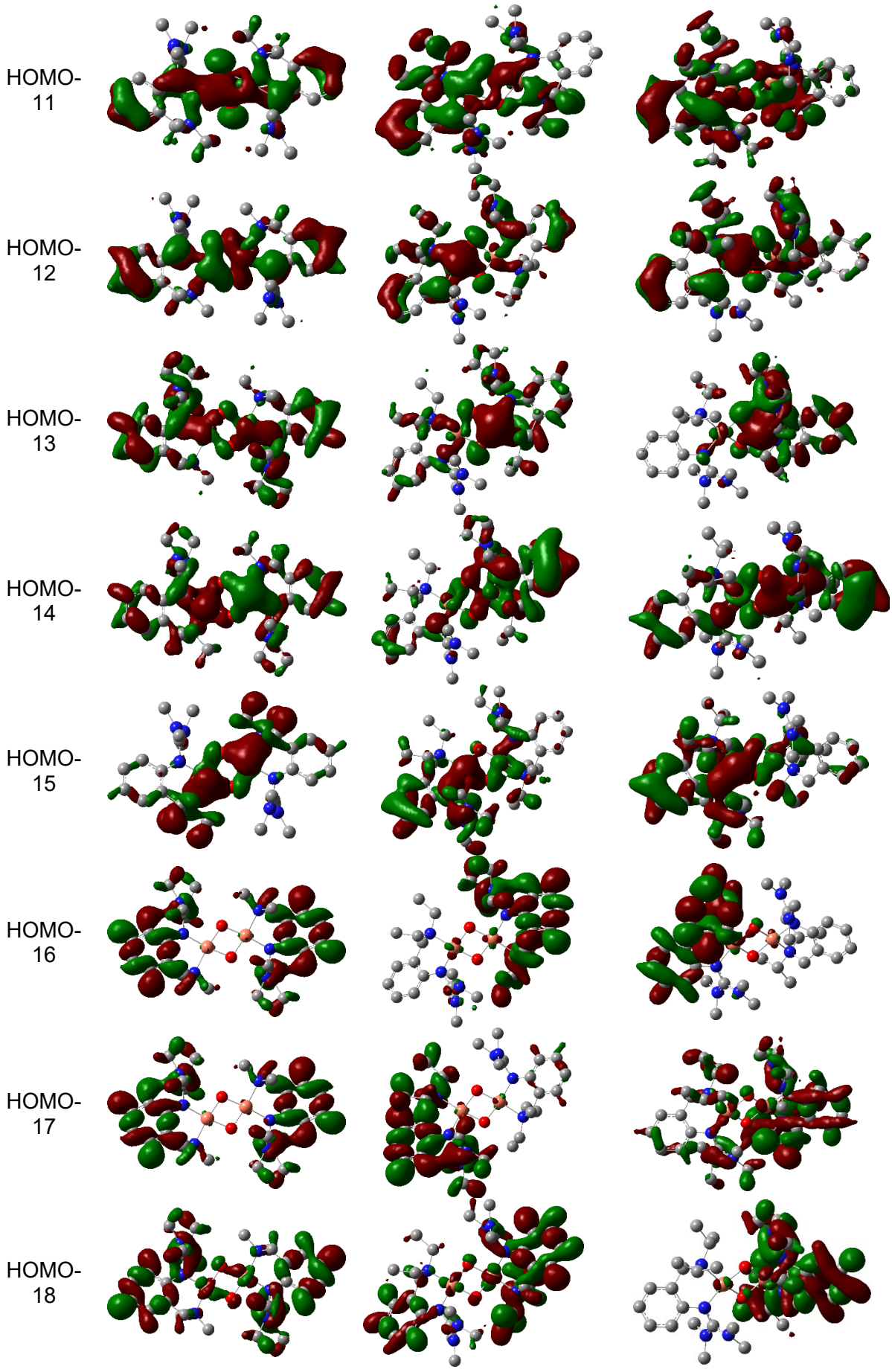
HOMO-11
HOMO-12
HOMO-13
HOMO-14
HOMO-15
HOMO-16
HOMO-17
HOMO-18

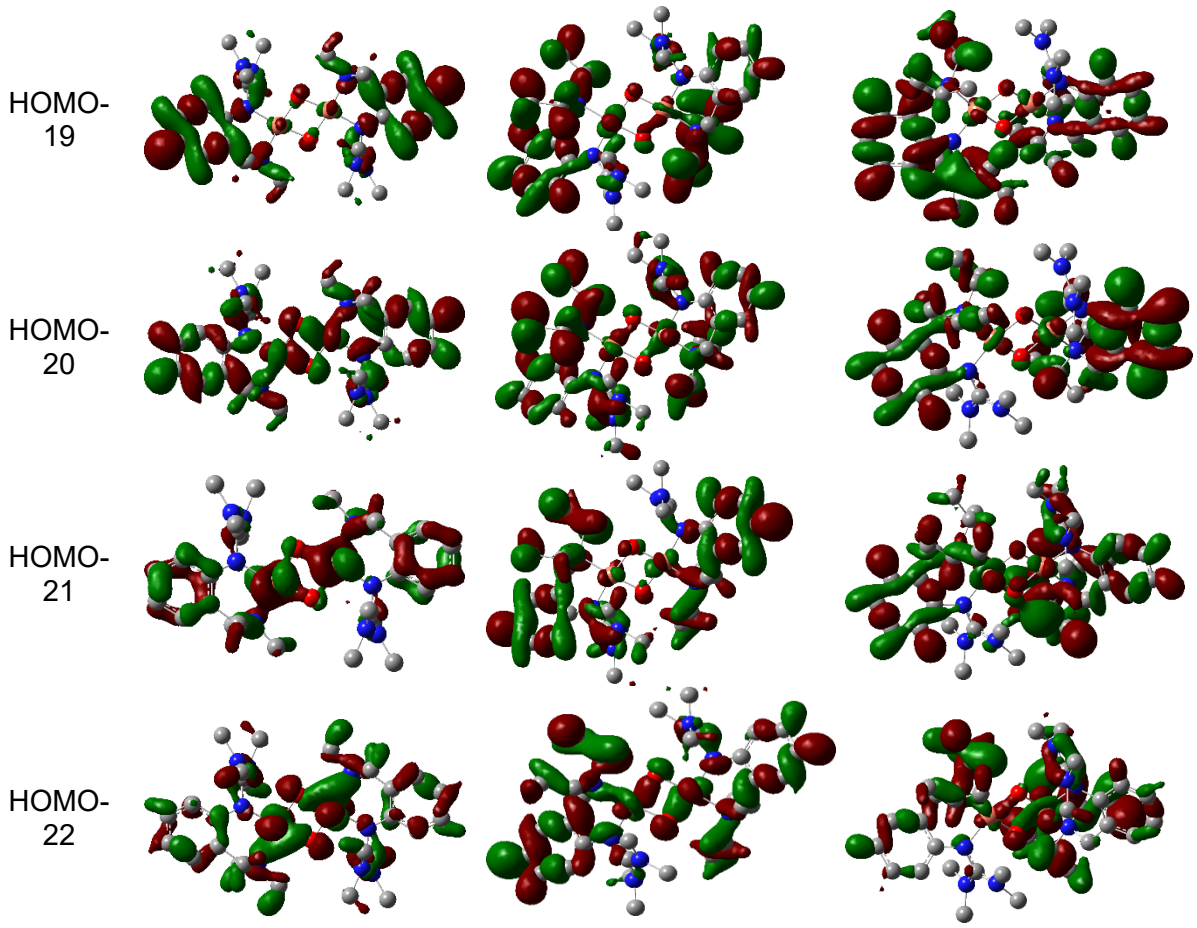
HOMO-19
HOMO-20
HOMO-21
HOMO-22

Table 54: MO energies E [H] of [**O1**]$^{2+}$, [**O3**]$^{2+}$ and [**O4**]$^{2+}$ (TPSSh/def2-TZVP, GD3BJ).

MO	**[O1]$^{2+}$**	**[O3]$^{2+}$**	**[O4]$^{2+}$**
LUMO+3	-0.22193	-0.21866	-0.21552
LUMO+2	-0.22223	-0.21937	-0.21724
LUMO+1	-0.32369	-0.31904	-0.31797
LUMO	-0.33371	-0.3289	-0.32688
HOMO	-0.38222	-0.38096	-0.37812
HOMO-1	-0.3839	-0.38375	-0.38091
HOMO-2	-0.41678	-0.41421	-0.4098
HOMO-3	-0.41683	-0.41492	-0.41237
HOMO-4	-0.42077	-0.41789	-0.4152
HOMO-5	-0.4216	-0.42022	-0.41829
HOMO-6	-0.42772	-0.42496	-0.42227
HOMO-7	-0.44579	-0.44122	-0.43575
HOMO-8	-0.45392	-0.44815	-0.44048
HOMO-9	-0.46241	-0.45714	-0.45167
HOMO-10	-0.47067	-0.4646	-0.45941
HOMO-11	-0.47714	-0.47076	-0.46189
HOMO-12	-0.48231	-0.47483	-0.46799
HOMO-13	-0.48304	-0.47776	-0.47317
HOMO-14	-0.48423	-0.48057	-0.47671
HOMO-15	-0.4859	-0.48157	-0.4798
HOMO-16	-0.50319	-0.50002	-0.49203
HOMO-17	-0.50344	-0.50178	-0.49605
HOMO-18	-0.50919	-0.5048	-0.4967
HOMO-19	-0.51381	-0.50721	-0.49987
HOMO-20	-0.5187	-0.50768	-0.50067
HOMO-21	-0.52263	-0.51095	-0.50203
HOMO-22	-0.52605	-0.51388	-0.50698

7.7. NTO Drawings of HONTO and LUNTO for $[O1]^{2+}$, $[O3]^{2+}$ and $[O4]^{2+}$

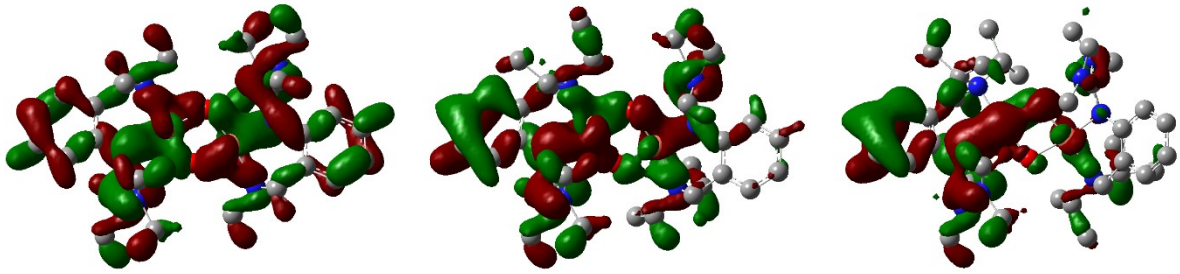

HONTO for [**O1**]$^{2+}$	HONTO for [**O3**]$^{2+}$	HONTO for [**O4**]$^{2+}$
N(amine) + Cu d + π_{σ}^{*} (all tilted) and π^{*}(benzyl)	N(amine) + Cu d + π_{σ}^{*} (all tilted) and π^{*}(benzyl)	N(amine) + Cu d + π_{σ}^{*} (all tilted) and π^{*}(benzyl)
(326 nm)	(327 nm)	(335 nm)

Figure 87: NTO Drawings of the HONTOs for [**O1**]$^{2+}$, [**O3**]$^{2+}$ and [**O4**]$^{2+}$ of the characteristic transition at smaller wavelength.

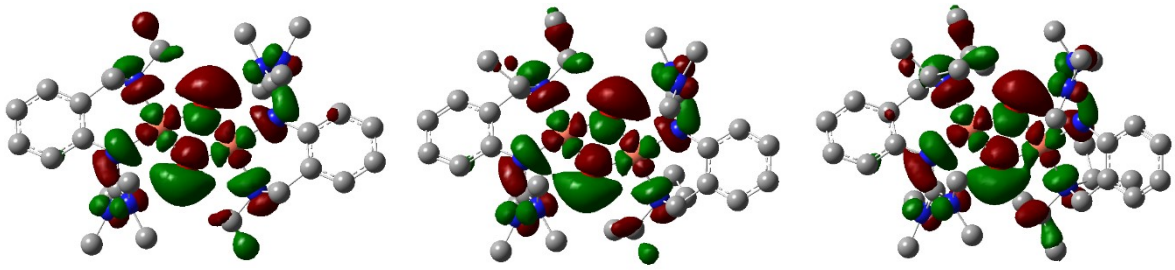

LUNTO for [**O1**]$^{2+}$	LUNTO for [**O3**]$^{2+}$	LUNTO for [**O4**]$^{2+}$
in-plane σ^{*} - Cu d - N	in-plane σ^{*} - Cu d - N	in-plane σ^{*} - Cu d - N
(326 nm)	(327 nm)	(335 nm)

Figure 88: NTO Drawings of the LUNTOs for [**O1**]$^{2+}$, [**O3**]$^{2+}$ and [**O4**]$^{2+}$ of the characteristic transition at smaller wavelength.

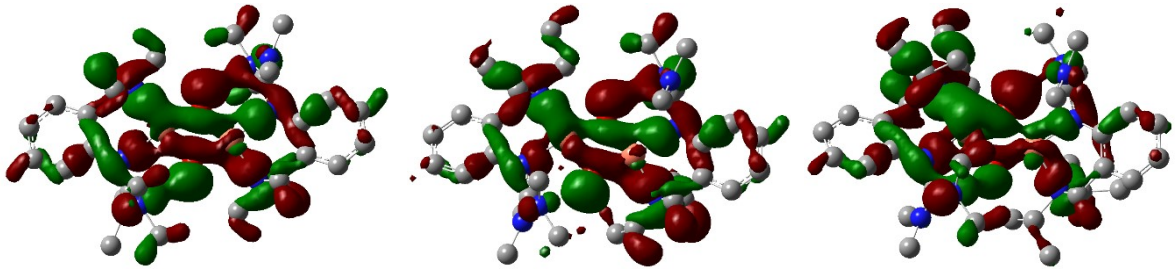

HONTO for [**O1**]$^{2+}$ | HONTO for [**O3**]$^{2+}$ | HONTO for [**O4**]$^{2+}$

in-plane d + σ* - N (375 nm) | in-plane d + σ* - N (382 nm) | in-plane d + σ* - N (398 nm)

Figure 89: NTO Drawings of the HONTOs for [**O1**]$^{2+}$, [**O3**]$^{2+}$ and [**O4**]$^{2+}$ of the characteristic transition at higher wavelength.

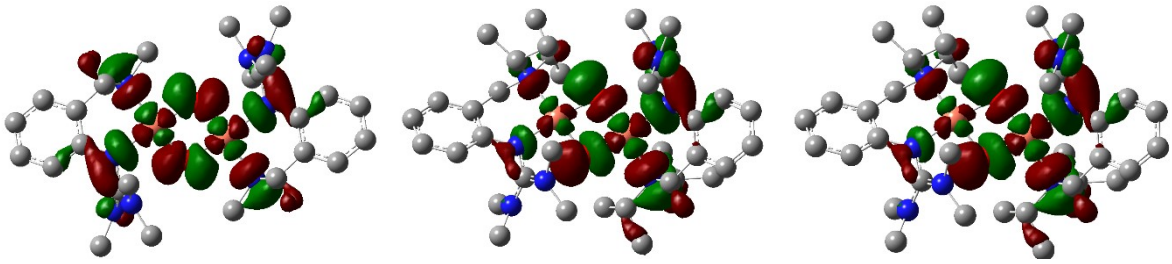

LUNTO for [**O1**]$^{2+}$ | LUNTO for [**O3**]$^{2+}$ | LUNTO for [**O4**]$^{2+}$

in-plane π_σ^* - Cu d - N (375 nm) | in-plane π_σ^* - Cu d - N (382 nm) | in-plane π_σ^* - Cu d - N (398 nm)

Figure 90: NTO Drawings of the LUNTOs for [**O1**]$^{2+}$, [**O3**]$^{2+}$ and [**O4**]$^{2+}$ of the characteristic transition at higher wavelength.

7.8. Fukui Function of Phenolic Substrates

Table 55: Fukui function of phenolic substrates (TPSSh/def2-TZVP, GD3BJ).

phenolic substrate	Fukui function (f_-)
2-naphthol	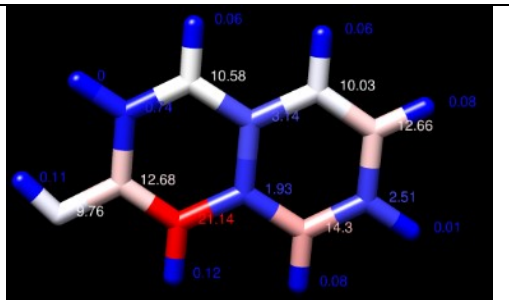
3-quinolinol	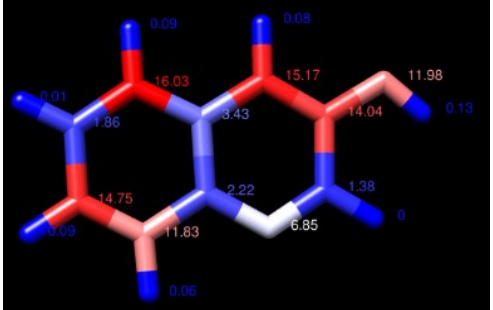
6-quinolinol	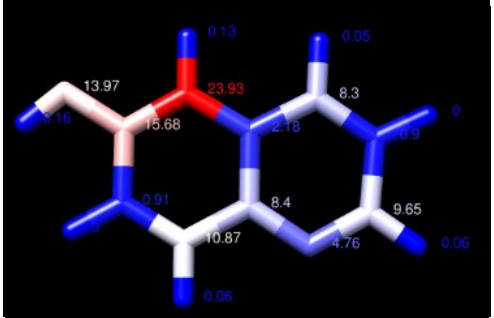
5-indolol	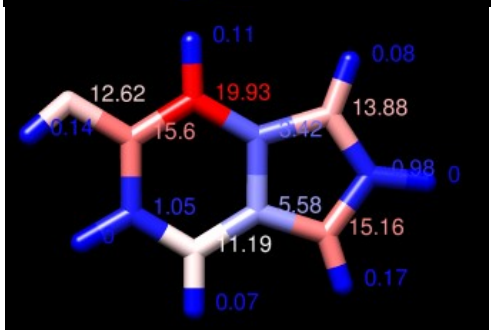
6-indolol	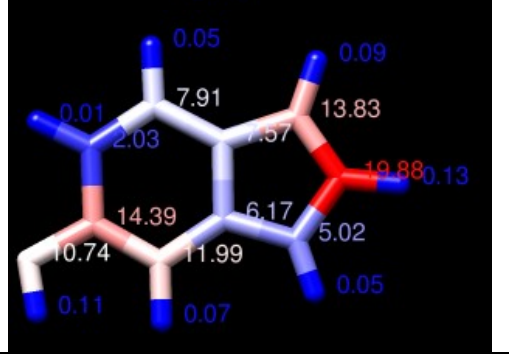

7.9. Fukui Function of the Quinones of the Phenolic Substrates

Table 56: Fukui function of quinones of the phenolic substrates (TPSSh/def2-TZVP, GD3BJ).

quinone	Fukui function (f_+)
quinoline-3,4-dione	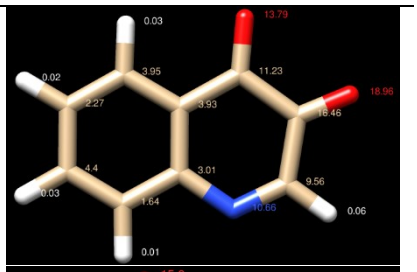
quinoline-5,6-dione	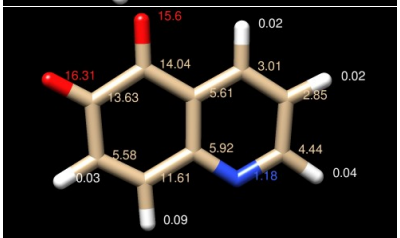
quinoline-7,8-dione	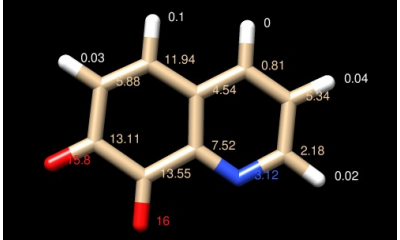
2-methyl quinoline-7,8-dione	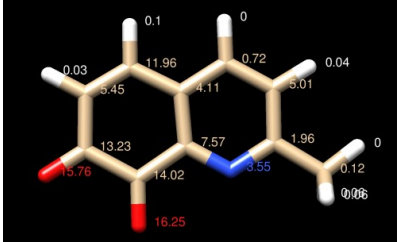
indole-4,5-dione	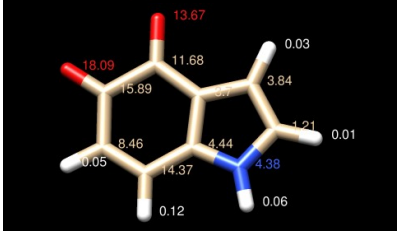
indole-6,7-dione